Impact against X65 offshore pipelines

MARTIN KRISTOFFERSEN

November 20, 2014

NTNU - Norwegian University of Science and Technology
Thesis for the degree of Philosophiae Doctor 2014
Faculty of Engineering Science and Technology
SIMLab - Structural Impact Laboratory
Department of Structural Engineering
Document typeset using LaTeX 2_ε
© Martin Kristoffersen

Preface

This thesis has been submitted in fulfilment of the degree *philosophiae doctor* at the Norwegian University of Science and Technology. The work has been conducted at SIMLab, Centre for Research-based Innovation, housed at the Department of Structural Engineering, under the supervision of Professor Tore Børvik, Professor Odd Sture Hopperstad and Professor Magnus Langseth.

Work with this thesis has hitherto produced two original research articles published in peer-reviewed journals, and another article submitted for possible journal publication, as well as several conference contributions. More publications are in preparation from this endeavor. The chapters herein are thematically structured and can largely be read autonomously. Sorry about the length.

Martin Kristoffersen
Trondheim, Norway
November 20, 2014

Abstract

This thesis presents both experimental and numerical investigations into some of the plethora of parameters influencing pipeline impact behaviour and the potential fracture arising thereof. The seamless pipes studied are made from an X65 offshore steel widely used by the industry. A succinct review of today's valid design codes (and analytical or empirical methods) for problems similar to this one is presented.

Impact tests against empty and water-filled pipes at different velocities were carried out to simulate a collision by trawl gear or an anchor. Subsequent straightening of the pipe representing a rebound after the impact revealed that fracture always presented itself given sufficient stretching (especially if the initial impact velocity had been at the high end of the spectrum). In some cases fracture (not necessarily visible on the surface) was present even after impact only, where in a metallurgical examination cleavage fracture surfaces were observed in the initially ductile material. Equivalent quasi-static three-point bending tests showed no such signs of fracture initiation, meaning that the problem being dynamic is an important factor and the cracking most likely initiates during the rebound after the impact.

Through quasi-static uniaxial tensile tests the X65 steel was characterised as isotropic and homogeneous across the cross-section, with kinematic hardening being present in the material. Testing at elevated strain rates showed that viscous effects caused the flow stress to increase, while the fracture strain remained as for the quasi-static tests. As very high compressive strains were observed in the component tests prior to fracture, a material test using notched specimens was contrived to investigate this further. Specimens were compressed to various levels of plastic strain before being stretched to failure in tension. The tests showed that when the preceding compression increased, the strain to fracture in the following tensile step decreased. Metallurgical studies showed more shallow pores in the compressed specimens and cracked particles were prominent sights, both being indications of earlier onset of fracture. Cleavage fracture was observed in both the material and component tests where large compression preceded tension.

Quasi-static stretch-bending experiments indicated that adding an axial tensile load to the pipe increased its resistance to bending. The same tests were repeated with the addition of internal pressure, which provided further resistance to bending while changing the local deformation significantly.

Finite element simulations of the impact were in general very accurate, whereas in the stretch phase the force was typically overestimated. This was mainly caused by fracture being inadequately described by the numerical model, thereby offering more resistance to straightening compared with the experiments. Fully coupled fluid-structure interaction simulations of the impact against water-filled pipes were also completed with satisfying accuracy, employing a variety of different techniques. The effect of submerging the pipe in water was investigated numerically.

Unit cell simulations with constant triaxiality were used to investigate the fracture mechanisms related to a load cycle of large compression before tension. Results indicated that increasing compression led to an accelerated void growth during tension, but the onset of coalescence appeared to be delayed, contrary to the experimental data. Very high local stresses after compression and load reversal indicate what might initiate cleavage fracture, so making use of a stress based fracture criterion is a natural progression from this thesis. In tension only, the unit cell simulations gave good predictions of the fracture strain given that the triaxiality remained fairly constant in the tests (i.e. notched tests).

In summary the global response of the numerical simulations was very accurate, whereas a small scale phenomenon as initiation of fracture occurs on a scale much smaller than the element size in these global models and is as such not represented with sufficient accuracy and other approaches are needed. Experiments in general, and the advent of the technologies like scanning electron microscopy, are of paramount importance for understanding the physical processes at hand.

Acknowledgements

I want to wholeheartedly thank my main supervisor Professor Tore Børvik, for his able guidance and continuous support and encouragement during the past four years. Your general understanding of the toils and struggles of being a graduate student has been pivotal for this work to see its completion. I would also like to thank my co-supervisors, Professor Odd Sture Hopperstad for helping me gain insight to things that otherwise would surely have eluded me, and Professor Magnus Langseth for unprecedented determination and ability to see the experimental work become a success. I could not have asked for a better team of supervisors.

The work has been financed by the Centre for Research-based Innovation, Structural Impact Laboratory (SIMLab), established by the Research Council of Norway. Håvar Ilstad and Erik Levold at Statoil ASA have supplied the pipes used herein and they have also contributed to the testing of the pipes. Thanks to Dr. Egil Fagerholt for setting up and carrying out the Digital Image Correlation analyses. Further invaluable assistance with the technical setup on the experimental work has been provided by Tore Wisth and Trond Auestad at the Department of Structural Engineering, and by Tore Andre Kristensen at SINTEF.

Dr. Ida Westermann at SINTEF has been very helpful and made significant contributions through her assistance with the metallurgical investigations conducted in the microscopes. Further, working with Dr. Folco Casadei during and after my stay in Italy has been both delightful and beneficial. His experience and competence, along with his composed and patient willingness to teach and share his knowledge, has been an unequivocal positive influence on me.

I want to thank all 11 master students who each have made appreciated contributions despite the incoherent ramblings I passed to you as "guidance". Through your discussions and questions, you have without doubt made this a better thesis. The same applies to all colleagues at the department, especially my fellow PhD candidates, who have definitely made this a great working environment, both educationally and socially.

Thanks also to all my friends for interrupting many late evenings of lucubration, for inviting me to barbecues or football games, for going to concerts with me and for buying me beer – all in all for helping me retain my sanity. I would of course also like to extend my deepest thanks my closest family; my mother for

her unconditional love and support in any endeavor I have chosen to undertake, my late father for teaching me the virtues of rational thinking, lucid expression and curious inquiry, my brother for always providing insightful and encouraging conversations, and my sister for being as cheerful, welcoming and intelligent as only she can be.

Contents

Preface III
Abstract V
Acknowledgements VII
Contents IX

1 Introduction **1**
1.1 Background 1
1.2 Previous work 3
1.3 Objectives 5
1.4 Scope 5
1.5 Outline of thesis 6

2 Standards and analytical/empirical methods **9**
2.1 DNV 9
2.1.1 Introduction 9
2.1.2 Calculating pipe dent 12
2.2 NORSOK N-004 14
2.3 Eurocodes 18
2.4 Analytic approach to dent formation 21
2.4.1 Derivation 21
2.4.2 Evaluation 21
2.5 Empirical estimates of local and global displacement 22
2.5.1 Estimating displacements 23
2.5.2 Separating local and global displacement 27

2.5.3 Comparison with experiments 29

3 Material tests **33**
3.1 Material description 33
3.2 Experimental programme 35
3.3 Quasi-static uniaxial tensile tests 37
3.3.1 Smooth specimens 37
3.3.2 Notched specimens 42
3.4 Dynamic tension tests 44
3.5 Reversed loading tests 48
3.6 Notched compression-tension tests 51
3.7 Discussion 57

4 Component tests **61**
4.1 Introduction 61
4.2 Dynamic impact against empty pipes 67
4.2.1 Setup 67
4.2.2 Results 72
4.3 Dynamic impact against water-filled pipes 80
4.3.1 Setup 80
4.3.2 Results 81
4.4 Quasi-static three-point bending 88
4.4.1 Setup 88
4.4.2 Results 90
4.5 Pipes subjected to stretching, bending and internal pressure . . . 94
4.5.1 Modification of rig 95
4.5.2 Experimental programme 99
4.5.3 Results 104
4.6 Discussion 117

5 Metallurgical investigation **123**
5.1 Overview 123
5.2 Material 124
5.3 Impact and stretching 126
5.4 Impact only 130
5.5 Quasi-static three-point bending 135
5.6 Combined transverse and axial load 136
5.7 Notched compression-tension tests 137
5.7.1 Initial geometry 138

5.7.2 Modified geometry . . . 143
5.8 Notched compression tests . . . 145
5.8.1 Initial geometry . . . 146
5.8.2 Modified geometry . . . 147
5.9 Discussion . . . 148

6 Constitutive relations and fracture criteria 153
6.1 General formulation . . . 153
6.2 Constitutive relations . . . 157
6.2.1 Isotropic hardening only (Johnson-Cook) . . . 157
6.2.2 Combined isotropic/kinematic model . . . 158
6.3 Fracture criteria . . . 159
6.3.1 Johnson-Cook . . . 159
6.3.2 Cockcroft-Latham . . . 160
6.4 Identification of material constants . . . 161
6.4.1 Constitutive relations . . . 161
6.4.2 Fracture criteria . . . 164

7 Numerical simulations 169
7.1 Introduction . . . 169
7.2 Impact and stretch simulations . . . 170
7.2.1 Setup . . . 170
7.2.2 Results . . . 173
7.3 Submodelling . . . 185
7.3.1 Setup . . . 185
7.3.2 Results . . . 187
7.4 Simulations of stretch-bending experiments . . . 189
7.4.1 Setup . . . 190
7.4.2 Results . . . 193
7.5 Discussion . . . 197

8 Fluid-structure interaction 199
8.1 Introduction . . . 199
8.2 About the ALE formulation . . . 200
8.3 Governing equations . . . 202
8.3.1 Structure . . . 202
8.3.2 Fluid . . . 202
8.4 FSI algorithms using ALE in Europlexus . . . 205
8.4.1 Introduction . . . 205

8.4.2 Conforming FE discretisation . . . 206
8.4.3 Non-conforming FE discretisation . . . 208
8.4.4 Node-centered finite volumes (NCFV) . . . 209
8.4.5 Conforming cell-centered finite volumes (C-CCFV) . . . 211
8.4.6 Non-conforming cell-centered finite volumes (NC-CCFV) 212
8.5 Rezoning algorithms . . . 213
8.5.1 Description . . . 213
8.5.2 Simulation attempts . . . 215
8.6 Embedded FSI algorithms . . . 215
8.6.1 Strong coupling in the embedded FSI algorithm . . . 218
8.6.2 Weak coupling in the embedded FSI algorithm . . . 220
8.7 Smoothed particle hydrodynamics (SPH) . . . 221
8.7.1 Introduction . . . 221
8.7.2 SPH formulation . . . 222
8.8 Simulations using fluid-structure interaction . . . 226
8.8.1 Introduction . . . 226
8.8.2 Numerical modelling . . . 226
8.8.3 Numerical results . . . 230

9 Unit cell modelling 243
9.1 Introduction . . . 243
9.2 Description of unit cell . . . 244
9.3 Setup of analyses . . . 246
9.4 Results . . . 249
9.4.1 Tension only . . . 249
9.4.2 Compression-tension from material tests . . . 255
9.4.3 Compression-tension with user-specified triaxiality values 263
9.5 Discussion . . . 268

10 Summary, conclusions and recommandations 273
10.1 Summary . . . 273
10.2 Conclusions . . . 274
10.3 Recommandations for further work . . . 277

Bibliography 279

Appendices 295

A Derivation of analytical pipe dent approach 297

B Material inpection certificate **305**

C Measurements of pipes **311**

D Bulging of circular membrane **333**

E Calibrations for stretch-bending rig **339**

F Drawings for stretch-bending rig **349**

Index **359**

Chapter 1

Introduction

1.1 Background

Today and for all foreseeable future, pipelines are used extensively to convey gas and/or oil over vast distances, often at high pressures and high temperatures [1]. From time to time, such pipelines are subjected to impact loads from anchors, trawl gear or falling objects during installation or maintenance. The Petroleum Safety Authority in Norway (Ptil) has published an elaborate list of all incidents causing damage to load-bearing structures and pipeline systems in the North Sea and the Norwegian Sea [2].

On November 1st 2007, Statoil discovered that the pipeline running from the Kvitebjørn production platform to the Kollsnes gas treatment facility outside Bergen had been damaged [3]. The pipeline had been impacted by an anchor and was subsequently dragged far out of its initial position (approximately 56 m) due to the anchor hooking the pipeline. As the displacement increased the anchor chain eventually gave in, causing the pipeline to rebound towards its origin. The damaged pipeline and the anchor are shown in Fig. 1.1.

Production was shut down temporarily until an inspection in January 2008 deemed the pipeline fit for service until it was to receive permanent repairs during the scheduled maintenance shutdown in 2009. Nevertheless, a gas leak

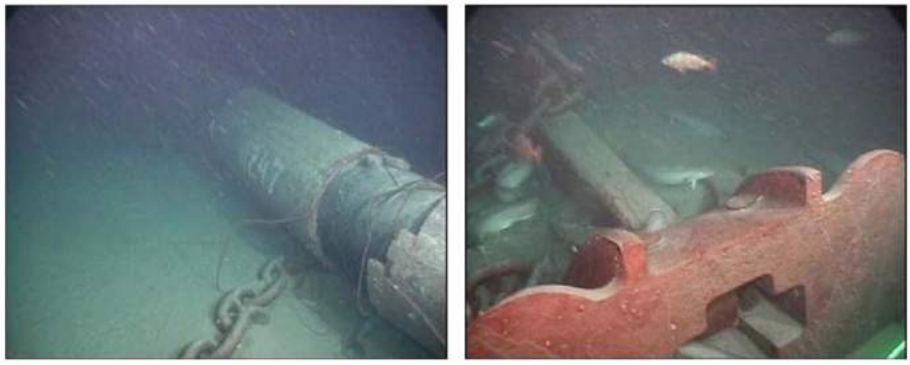

Figure 1.1: *A pipeline impacted by an anchor. On the left the damaged pipeline can be seen, while the right shows the impacting anchor.*

was found in the impacted pipeline during a routine inspection in August 2008, forcing the Kvitebjørn field to close production immediately at immense cost. Repairs were carried out, and the platform resumed operations in January 2009. Such events necessitate an assessment regarding the hazards and potential damage following such an event [4], as failure in a pipeline transporting oil and/or gas could result in severe environmental damage and vast economic losses.

The Kvitebjørn accident spawned a research collaboration between SIMLab and Statoil where strips from an X65 offshore steel pipe were subjected to a similar load sequence as in the actual pipeline [5]: Strips cut from the pipe wall were first exposed to three-point bending, intended to simulate the initial dent from the impact. Next, they were pulled straight in tension in an attempt to recreate the recoil and straightening of the pipeline. Finally, the strips were examined to check if any cracks had formed from such a loading sequence. Of the various setups used, only the one with the smallest punch diameter and shortest span (i.e. causing the largest curvature of the strip) managed to produce indications of fracture. These superficial cracks did not, however, seem to influence the load-displacement curve during stretching [5]. This study is also discussed more elaborately in Chapter 4, where some illustrations from the study have been included.

This background establishes the pretext for the work carried out herein, which will be presented shortly. First, a succinct discussion of some previous work conducted on pipe impact will be laid out.

1.2 Previous work

A brief overview of work available in the open literature related to pipe impact, or impact against tubular structural members (e.g. jacket legs) is presented. First a local dent arises in the pipeline from the impact, an event which may lead to a propagating buckle as investigated experimentally and numerically by Kyriakides and Netto [6], and numerically by Ramasamy and Tuan Ya [7]. The large global deformation due to the subsequent hooking sets up large axial forces, in turn forcing the pipeline back towards its initial position after release, and straightening the bent pipeline to a certain degree. This sequence of events is not particularly well studied in the literature.

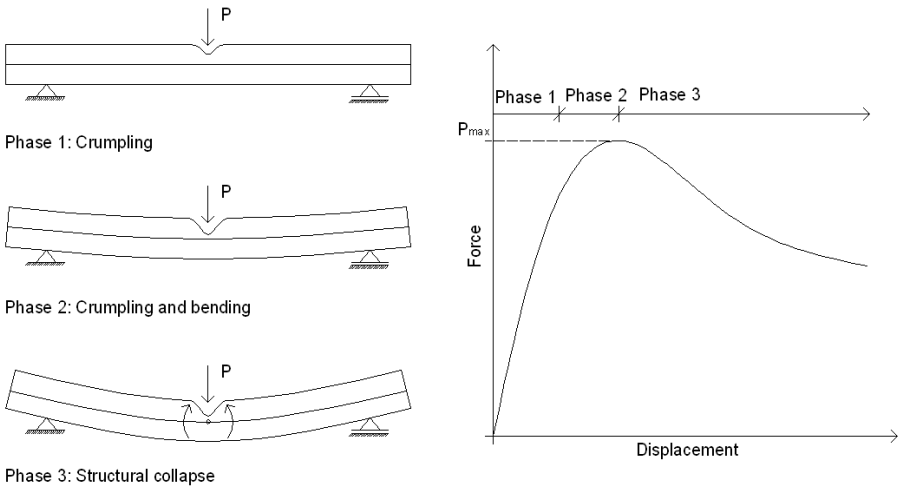

Figure 1.2: *Modes of deformation during pipe impact.*

Pipe impact problems have been studied with many of different approaches, and the open literature provides several studies on pipeline impact. Such problems have been studied for decades, and studies continue until today [8]. Impact against fully clamped pipes have been studied e.g. by Jones et al. [9] and by Chen and Shen [10]. Addition of internal pressure to the pipe during impact was studied by Shen and Shu [11], by Ng and Shen [12] and more recently by Jones and Birch [13], who found a diffence in deformation between empty and pressurised pipes after impact. A defect in the pipe can reduce the pressure capacity significantly [14]. Johnson, Reid and coworkers published a series of

three papers on large transverse deformations of thin walled circular tubes [15–17]. Here, three phases of deformation were identified. As depicted in Fig. 1.2, these are first crumpling, then crumpling and bending, before a final transition is made to global bending and structural collapse as also noted by Soares and Søreide [18]. Thomas et al. [15] also did impact tests where a wedge was dropped onto the pipe's midspan. The energy required to reproduce the same magnitude of deflection quasi-statically was compared to the initial potential energy of the dropped object. Less energy was needed when deforming the mild steel pipes quasi-statically, typically 50% to 70% of the initial potential energy in the wedge. Energy transfer ratio increased with increasing dropping height, occasionally up to 90%. Brittle and ductile fracture surfaces of X80 steel was investigated in detail by Mohseni [19].

Det Norske Veritas (DNV) has given guidelines on certification and verification of pipelines [20], a standard on general design of pipeline systems [21] and specified some recommended practice on interference between pipelines and trawl gear [22] (see Section 2.1 herein for details). A load cycle of impact, hooking, pull-over and release produces a complex stress and strain history which is not well covered in the guidelines. In addition to the simplified analysis provided therein, the guidelines allow for use of numerical analyses – in which boundary conditions are very important [23] – and model tests in the design phase. Further, a novel approach for estimating loads against pipelines due to trawl gear interaction has been suggested by Longva et al. [24].

Fewer studies have been examining the effect of adding liquid to the pipes during impact. Pipe perforation was by Neilson et al. [25] found to be more likely when water was present in the pipe during impact. These tests were performed at much higher impact velocities (46-325 m/s) than in the present study ($<$ 5.2 m/s). Shah [26] conducted experiments and simulations of simply supported water-filled copper pipes at a more relevant impact velocity (6.7 m/s). The pipes were 300 mm long with an outer diameter of 35 mm and wall thickness of 0.7 mm. Rubber membranes were mounted at the ends to restrain the water from escaping, thereby allowing pressure to build up inside the pipe. A difference between empty and water-filled pipes was observed post-impact, where the dent caused by the impact was confined to a smaller surface area of the pipe in the latter case. Similar results were obtained by Jones and Birch [13], in which pressurised pipes correspond to the water-filled pipes in Ref. [26]. These were the most notable studies found, although other relevant literature will be introduced where due.

Heretofore, no study has (at least to the extent of the author's knowledge) carried out full scale impact and stretch tests to simulate the full loading sequence of impact, hooking and release of the pipeline. As described, Manes et al. [5] did this to strips of an X65 pipe, however not to a full pipe cross-section.

1.3 Objectives

This thesis presents experimental and numerical studies on impact against seamless 5 inch X65 steel pipes. The material is chosen as it is widely used in the offshore industry [27], largely due to its relatively high strength and low production costs. The pipes studied were delivered by Statoil as 12 m long pipes, produced by the Argentinian supplier Tenaris [28]. These are full-scale pipes that are intended for transportation of oil and/or gas.

The research objectives are as following:

- Characterise the X65 material and calibrate constitutive models.
- Define and carry out component tests on X65 steel pipes, encompassing both the impact phase and the subsequent stretch phase of an impact, hooking and release event as described above.
- Define and carry out component tests on X65 steel pipes accounting for axial forces and internal pressure.
- Explore capabilities and limitations of numerical simulations using commercially available methods.
- Identify and investigate damage and fracture mechanisms.

More intricate objectives are explained where needed.

1.4 Scope

Due to the plethora of available parameters and branches to investigate regarding pipe impact, some limitations are imposed on the present study:

- Only one material is considered and characterised through material tests.

- The geometry of the pipe in the component tests is kept unaltered[1].
- All testing is carried out at room temperature, no temperature effects are thereby considered.
- Numerical simulations are restricted to what is commercially available.

These are the main boundaries of the study, and other, more detailed ones, are presented where appropriate.

1.5 Outline of thesis

The chapters in this thesis are arranged thematically, with the first few chapters laying the groundwork for the later ones. Each chapter can be read in its own right, as notation and important terms are explained succinctly where due, with internal cross-references when needed.

Chapter 2 reviews prevailing standards and design codes and how they approach the pipe impact problem. Existing analytical/empirical methods are also described. These methods are also discussed in relation to some of the component tests carried out herein.

Chapter 3 elaborates fully on all material tests carried out for the X65 steel.

Chapter 4 provides descriptions and sketches of all component test setups used, and discusses the results obtained. Dynamic vs. quasi-static deformation is explored, along with the influence of pressure and other parameters as well. Results obtained here are also used in Chapter 2.

Chapter 5 includes optical microscope images along with scanning electron microscope images of samples taken from both the material tests and the various component tests. Emphasis here is on fracture and fracture mechanisms.

Chapter 6 explains the constitutive relations and fracture criteria used for the X65 material in the numerical simulations.

Chapter 7 not only includes the results of the numerical simulations, but also the general setup and procedure chosen.

[1] A slight variation in thickness is present, see Chapter 4.

Chapter 8 describes the various fluid-structure interaction techniques used in numerical simulations involving such interaction. Simulation results of this kind are also presented.

Chapter 9 goes down in scale with unit cell modelling in an attempt to understand what happens when a cell composed of a particle and a matrix is compressed before being exposed to a tensile load.

Chapter 10 rounds off the work with some final discussions, some conclusions and suggestions for further work within this topic.

The appendices contain measurements, calibrations and calculations which make the thesis more complete, but may clog the chapters from which they are referenced and thereby ruin the flow and structure of the topics under discussion.

From work on this thesis, several publications have been made. Most notably two peer-reviewed journal articles have been published;

- *Impact against X65 steel pipes — An experimental investigation*, published in the International Journal of Solids and Structures vol. 50 (2013), p. 3430-3445 [29].
- *Impact against empty and water-filled X65 steel pipes — Experiments and simulations*, published in the International Journal of Impact Engineering vol. 71 (2014), p. 73-88 [30].

A third article written by M. Kristoffersen, T. Børvik, M. Langseth and O.S. Hopperstad titled *Dynamic vs. quasi-static loading of X65 offshore steel pipes* has also been submitted for possible journal publication.

Further, several conference contributions have been made, two of which are particularly worth a mention;

- *Damage and failure in an X65 steel pipeline caused by trawl gear impact*, presented at the 32nd ASME International Conference on Ocean, Offshore and Arctic Engineering (OMAE 2013, Nantes, France) [31].
- *Numerical simulations of submerged and pressurised X65 steel pipes*, presented at the XII International Conference on Computational plasticity (COMPLAS 2013, Barcelona, Spain) [32].

Three other conference contributions have been presented, but were not written into a full paper so the details are omitted. Data from some of these may very well be extended and prepared to full journal articles in the future. In addition

several master's theses at NTNU have been produced [33–38] related to this study, all of which have contributed positively in writing this thesis.

The experiments and simulations presented herein should therefore provide valuable insight to how such a system behaves under an extreme load case like this one. Different parameters assumed to influence the behaviour have been investigated, ranging from impact velocity to inclusion of internal pressure. As will be made evident, an elaborate material and component test programme will uncover several interesting features, and provide grounds for conducting advanced numerical simulations. A central part is also a metallurgical study revealing some of the fracture characteristics.

Chapter 2

Standards and analytical or empirical methods

This chapter contains descriptions of various methods for treating accidental interaction between a structure, in this case a pipeline, and an impactor. There are several different approaches, ranging from general impact dynamics and quasi-static approaches to a specific description of pipeline and trawl gear interaction. Throughout this chapter geometric and material data from the full-scale tests, which are elaborated on in Chapter 4, are used in the equations and methods at hand. The most important parameters are the mean nominal thickness of the pipe $t = 4$ mm, the mean nominal diameter $D = 131$ mm (and hence radius $r = 65.5$ mm), and the material's specified yield stress $\sigma_0 = 450$ MPa.

2.1 DNV

2.1.1 Introduction

Det Norske Veritas (DNV) is an independent and autonomous foundation that issues offshore design codes, whose aim is to safeguard life, property and environment both at sea and onshore. DNV undertakes classification, certification,

and other verification and consultancy services relating to quality of ships, offshore units and installations, and onshore industries worldwide, and carries out research in relation to these functions. The DNV standards are by far the most detailed in terms of pipeline impact. A three-level hierarchy of documents comprises the DNV offshore codes:

1. *Offshore Service Specifications (DNV-OSS):* Provide principles and procedures of DNV classification, certification, verification and consultancy services.
2. *Offshore Standards (DNV-OS):* Provide technical provisions and acceptance criteria for general use by the offshore industry as well as the technical basis for DNV offshore services.
3. *Recommended Practices (DNV-RP):* Provide proven technology and sound engineering practice as well as guidance for the higher level Offshore Service Specifications and Offshore Standards.

From each category, these are the most relevant standards for pipeline impact:

DNV-OSS-301 is the parent document for design of pipelines. It provides guidance on and criteria for certifications of complete pipeline systems, and verification of the integrity of parts or phases of pipeline systems [20].

DNV-OS-F101 gives criteria and guidance on concept development, design, construction, operation and abandonment of submarine pipeline systems. The standard defines the design rules for pipeline design [21].

DNV-RP-F111 contains methods for designing pipelines exposed to impact from trawl gear, as well as being a guide to higher level standards (from whence it is referred). The document separates the interaction between the pipe and the trawl gear into two main stages, first *impact* and then *pull-over* or *hooking* as two possible second stages [22]. A further description of the stages follows:

1. Impact is the initial interaction between the pipeline and the impactor. In this stage kinetic energy from the trawl gear towed by a boat is absorbed mostly by local deformation (denting) of the pipeline. The duration of this stage is typically of the order of some hundreths or tenths of a second, seldom larger than one full second.
2. (a) Pull-over is when the trawl board is dragged over the pipeline, and can cause considerable damage to the coating and the pipe

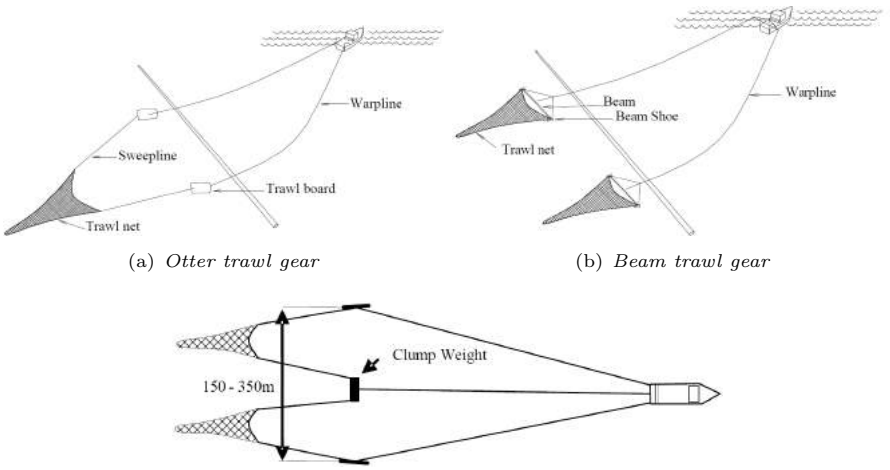

(a) *Otter trawl gear*

(b) *Beam trawl gear*

(c) *Twin trawl with clump weight*

Figure 2.1: *Examples of typical trawl gear used in the North Sea and Norwegian Sea [22].*

itself. Deformations are now on a more global scale. Pull-over usually lasts for a period of 1 s to 10 s.

(b) Hooking is considered a special case, and considers the event where the trawl gear gets stuck under the pipeline. The loads at this stage may become as large as the ultimate strength of the warp line (or anchor chain for an anchor), but this is a much rarer occurrance.

Despite being based on trawl gear data from the North Sea and Norwegian sea, DNV-RP-F111 is intended for worldwide use, although an effort to obtain area-specific data should be made. It gives loads and load effects based on the size, shape, velocity and mass of the trawling gear.

Various trawl gear typically used in the North Sea and Norwegian sea is shown in Fig. 2.1. The otter trawl board in Fig. 2.1(a) utilises hydrodynamic forces to keep the net open. These trawl boards are dragged along the seabed and may represent a hazard to the pipeline. Beam trawl gear uses a steel beam to keep the net open as illustrated in Fig. 2.1(b). Due to the sharp edges, along with a large total kinetic energy, the beam shoes at the end of the beams pose

a substantial threat to a pipeline. Fig. 2.1(c) shows a twin trawl with a clump weight, which has a mass in the range of 2000 to 9000 kg and a plethora of different shapes. Due to the large mass, this may cause a larger impact and pull-over loads compared to trawl boards.

2.1.2 Calculating pipe dent

DNV-RP-F111 suggests that an impact energy should be calculated first, and then determining the dent depth arising from the impact[1]. Establishing the impact energy can be quite an elaborate procedure involving the spring stiffnesses of the trawl gear, the soil and pipe shell. This procedure is omitted herein as the impact energy is well defined in the impact experiments discribed in Chapter 4.

After determining the energy to be absorbed by the system, a dent depth w_l for a bare steel pipeline with outer diameter D_o, thickness t and specified minimum yield strength σ_0 is calculated by

$$w_l = \left(\frac{F_{sh}}{5\alpha_U \sigma_0 t^{3/2}} \right)^2 - \left(\frac{F_{sh} \cdot \sqrt{0.005 D_o}}{5\alpha_U \sigma_0 t^{3/2}} \right) \tag{2.1}$$

where $\alpha_U = 0.96$ is a material strength reduction factor given in DNV-OS-F101 [21]. Here, a rigid a support for the entire pipe length is assumed, i.e. only denting is accounted for and not global bending. Further, the force F_{sh} experienced by the pipe is expressed through

$$F_{sh} = \left(\frac{75}{2} \cdot E_{\text{loc}} \left(\alpha_U \sigma_0 \right)^2 t^3 \right)^{1/3} \tag{2.2}$$

in which E_{loc} is the energy to be absorbed by local denting. When the dent depth has been determined it is evaluated according to a given acceptance criteria, which is based on how often such an event takes place. Definitions of the frequency classes are given in Table 2.1, which also includes the acceptable dent depths. For small and light pipes this method tends to give overly conservative results, and a more elaborate technique is described in Appendix A in DNV-RP-F111 [22]. There the pipe shell can be modelled directly by finite

[1] DNV-RP-F107 [39] suggests a dent vs. absorbed energy relationship, but this is not discussed in detail here.

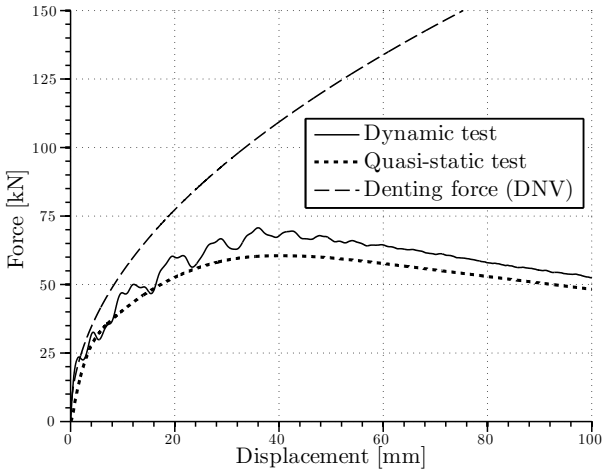

Figure 2.2: *Force vs. dent depth as given in DNV-RP-F111 using the geometric and material properties from the pipe specimens used in this study.*

elements, determined through experimental tests or modelled separately. If no such information is available, the relationship between the force F_{sh} and the dent depth w_l may alternatively be conservatively approximated by

$$F_{sh} = 5\alpha_U \sigma_0 t^{3/2} \cdot \sqrt{w_l} \tag{2.3}$$

Dynamic impact tests and quasi-static three-point bending tests have been carried out for X65 steel pipes (experiments described in detail in Chapter 4) and compared to the estimate from Eq. (2.3). By using the nominal thickness $t = 4$ mm and minimum specified yield strength $\sigma_0 = 450$ MPa, estimates for the resisting denting force F_{sh} is obtained.

Table 2.1: *Frequency classes and associated dent depth acceptance criteria.*

Frequency class	**Impacts per year per km**	**Dent depth** w_d/D
High	> 100	0
Medium	1-100	0.015
Low	< 1	0.035

Fig. 2.2 illustrates the obtained force vs. dent depth. As seen, the initial tangent is estimated quite well, however when global bending starts to take over in the experiments the curves diverge from each other as the DNV method only accounts for local denting. This means that Eq. (2.3) can be used with reasonable accuracy when the prescribed energy produces a small w_l. For large w_l (of the order of half the pipe radius and above), changes in geometry due to global bending should be accounted for. In the dynamic experiment (pipe A from Chapter 4) a total deformation of approximately 132 mm was produced by the impact, while a deformation of about 150 mm was needed to absorb the same amount of energy quasi-statically. Bear in mind that differences in the pipe thickness is important here, as is evident by adjusting the parameter t in the equation and from the experiments presented later. Using the DNV approach, the same energy level is attained after only 74 mm of deformation.

Being a three-point bending test and not a denting test, the tests in this study are arguably not directly comparable to the DNV method. Nevertheless, a comparison is included to see how the method measures up to the experiments, which is a useful exercise in itself.

2.2 NORSOK N-004

To ensure adequate safety, value adding and cost effectiveness for developments and operations, the Norwegian petroleum industry has developed the NORSOK standards. They are based on recognised international standards, and provides additional content where deemed necessary by the industry. The standard NORSOK N-004 specifies guidelines and requirements for design and documentation of offshore steel structures [40]. It is applicable to all types of offshore structures made of steel with a yield strength less than or equal to 500 MPa[2]. Annex A of said standard contains a section (A.3.6) on the force-displacement curve resulting from denting of tubular members for energy dissipation. The method for this estimation will be outlined here.

The resisting force P as function of the dent depth w_l can be estimated either by reading Fig. A.3-7 in NORSOK N-004 [40], or by evaluating the following equation,

[2]The X65 steel studied herein has a nominal yield strength of 450 MPa, and the measured yield strength from tensile tests is 478 MPa.

$$\frac{P}{P_c} = kc_1 \cdot \left(\frac{w_l}{D}\right)^{c_2} \tag{2.4}$$

where c_1 and c_2 are constants based on the width of the contact area B, and the mean diameter of the pipe D,

$$c_1 = 22 + 1.2 \cdot \frac{B}{D} \tag{2.5a}$$

$$c_2 = \frac{1.925}{3.5 + \frac{B}{D}} \tag{2.5b}$$

P_c is given by

$$P_c = \sigma_0 \cdot \frac{t^2}{4} \cdot \sqrt{\frac{D}{t}} \tag{2.6}$$

in which σ_0 is the yield stress of the assumed perfectly plastic material and t is the pipe wall thickness. The factor k is a function of the ratio between the *design* compressive force N_{Sd} acting on the tube, and the compressive *capacity* N_{Rd},

$$k = \begin{cases} 1.0 & \text{if } \dfrac{N_{\mathrm{Sd}}}{N_{\mathrm{Rd}}} \leq 0.2 \\ 1.0 - 2\left(\dfrac{N_{\mathrm{Sd}}}{N_{\mathrm{Rd}}} - 0.2\right) & \text{if } 0.2 < \dfrac{N_{\mathrm{Sd}}}{N_{\mathrm{Rd}}} < 0.6 \\ 0 & \text{if } \dfrac{N_{\mathrm{Sd}}}{N_{\mathrm{Rd}}} \geq 0.6 \end{cases} \tag{2.7}$$

These equations are valid for unstiffened tubes where the indentations should be $w_l > 0.05D$. The intended use is for local energy dissipation via *denting*, and not global deformation.

The NORSOK standard also treats the reduced bending capacity of a dented tubular member, and can be determined through Fig.A.3-10 or Eq. (A.3.12) in Ref. [40]. A sketch of a dented cross-section can be seen in Fig. 2.3(a). This

equation states that the reduced plastic moment capacity due to denting M_{red} can be expressed by

$$\frac{M_{\text{red}}}{M_p} = \cos\frac{\theta}{2} - \frac{1}{2}\sin\theta \tag{2.8}$$

in which $M_p = \sigma_0 D^2 t$ is the moment capacity of the undeformed cross-section, and the angle θ is

$$\theta = \arccos\left(1 - \frac{2w_l}{D}\right) \tag{2.9}$$

The maximum bending moment M_f in a simply supported beam of length ℓ loaded by a point load P_f at midspan is (see Fig. 2.3(a))

$$M_f = \frac{P_f \cdot \ell}{4}$$

By substituting M_f with M_{red} and solving for P_f, an expression for the maximum load as a function of θ (which in turn is a function of w_l) is obtained;

$$P_f = \frac{4M_p}{\ell} \cdot \left[\cos\frac{\theta}{2} - \frac{1}{2}\sin\theta\right]$$

$$P_f = \frac{4M_p}{\ell} \cdot \left[\sqrt{1 - \frac{w_l}{D}} - \frac{1}{2}\sin\left(\arccos\left(1 - \frac{2w_l}{D}\right)\right)\right] \tag{2.10}$$

It is assumed that the entire cross-section plastifies simultaneously,

To obtain an estimate for a load-displacement with both denting and bending parts, Eqs. (2.4) and (2.10) are compared, and the one that for a given w_l is lowest dictates the load-displacement curve. This means that denting is the initial phase, and bending takes over once M_{red} becomes sufficiently low, thereby assuming that no denting and bending take place simultaneously.

Quasi-static three-point bending tests with a span of $\ell = 1000$ mm have been carried out for X65 steel pipes (experiments described in detail in Chapter 4)

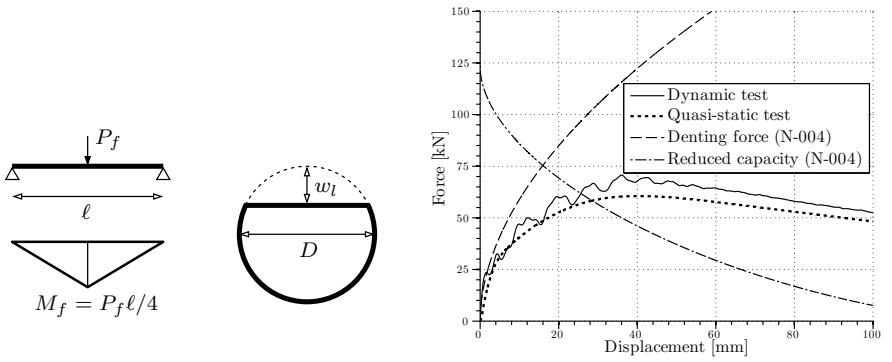

(a) *Beam and dented cross-section* (b) *Force-displacement*

Figure 2.3: *Force-displacement estimates based on NORSOK N-004 using the geometric and material properties from the pipe specimens used in this study.*

and compared to the estimates from this standard. By taking the nominal values of the supplied pipe, $t = 4$ mm, $D = 123$ mm and $\sigma_0 = 450$ MPa, and using the indenter width (20 mm) as B, estimates for the resisting denting force P is obtained from Eq. (2.4). Eq. (2.10) is used to estimate the reduced bending capacity of a dented tubular member.

Fig. 2.3(b) shows the estimated force-displacement curves along with dynamic and quasi-static experimental data. As seen, the initial stiffness is reasonably well predicted, but rapidly diverges from the experimental data as global bending initiates in the test. This is to be expected as denting is compared to three-point bending, and the results are similar to what is seen in Fig. 2.2 from the DNV approach [22]. Where the denting force crosses the bending capacity of the cross-section, global bending is assumed to take over, and no axial strengthening due to membrane forces is assumed. In the test, denting and bending will occur simultaneously, with denting dominating in the beginning and bending gradually taking over, and axial membrane forces being set up as the deformation proceeds.

To absorb the same energy as in the impact experiment (pipe A) using Eq. (2.10) only, a value of about 69 mm is obtained for w_l, compared to 74 mm from the DNV approach (132 mm in the test). If deformation of the cross-section is accounted for, no sensible deformation is obtained as denting and bending are

considered separately. Also, the rapid decline of the cross-sectional capacity in combination with not accounting for axial forces leads to a cap on the amount of energy possible to absorb. This occurs when $w_l = D$ which in theory would produce a complete collapse of the cross-section.

Still, reasonable estimates can be found when w_l of the order of the radius or less. Again the reader is reminded that this approach is intended for an initial denting followed by bending of a reduced cross-section, whereas in the three-point bending setup used in Chapter 4 these processes occur simultaneously. A separate method for accounting for bending of a beam member as part of a truss is included in Section A.3.7 in N-004 [40], but not discussed in detail here.

A more in-depth discussion of the N-004 method applied to ship collision with jacket legs has been carried out by Amdahl et al. [41].

2.3 Eurocodes

The *Eurocode* programme was started in 1975 when the Commission of the European Community decided on undertaking actions to eliminate technical obstacles to trade, and to harmonise technical specifications across Europe. They are the current national standards in Norway, and have been so since March 2010. In Norway, the Eurocodes are maintained by the private independent organisation Standard Norge, which is Norway's member in the European Committee for Standardisation (CEN) and the International Organisation for Standardisation. There are 10 main groups of Eurocodes:

Eurocode 0: Basis of structural design
Eurocode 1: Actions on structures
Eurocode 2: Design of concrete structures
Eurocode 3: Design of steel structures
Eurocode 4: Design of composite steel and concrete structures
Eurocode 5: Design of timber structures
Eurocode 6: Design of masonry structures
Eurocode 7: Geotechnical design
Eurocode 8: Design of structures for earthquake resistance
Eurocode 9: Design of aluminium structures

The Eurocodes do not provide specific details on the particular case of impact against pipelines. EC1 provide actions on structures, while EC3 supplies how

those actions are to be handled. Relevant for the problem at hand are the following:

- NS-EN 1991-1-7: Actions on structures – Accidental actions [42]
- NS-EN 1993-4-3: Design of steel structures – Pipelines [43]

The first standard provides information on how impact is treated in the Eurocode programme. Mainly the impact from, say a ship, is expressed as an "equivalent static load". This load's magnitude depends on the size and velocity of the ship, type of waterway, type of structure and other parameters. It can be distributed over a certain area depending on the ship's size. When the load is determined, the structure is designed to withstand said load.

NS-EN 1997-1-7 also contains an appendix on a simplified dynamic design for impact (neglecting nonlinear material behaviour), where it is distinguished between *hard impact* and *soft impact*. Hard impact is characterised by a situation where the kinetic energy is mainly absorbed by the impacting body. In a soft impact the structure is designed to deform in order to absorb the impact energy, which is the case here. I.e. the impacting body is assumed not to absorb any energy.

Under the assumptions that the structure is linear elastic with stiffness k, and the colliding object is rigid with mass m, a "maximum resulting dynamic interaction force" F is obtained from

$$F = v_0\sqrt{km} \tag{2.11}$$

where v_0 is the object's velocity at impact. F may be considered as a rectangular pulse on the surface of the structure, in which case the pulse duration Δt can be obtained from

$$F\Delta t = mv_0 \qquad \text{or} \qquad \Delta t = \sqrt{\frac{m}{k}} \tag{2.12}$$

A rectangular pulse means that the rise-time of the force is equal to zero, although the code allows for a non-zero rise-time if relevant.

If the structure is designed to absorb energy through plastic deformation, the design code suggests a rigid-plastic material behaviour as a limit case. Then the

following inequality must be upheld to make sure that the structure is sufficiently ductile,

$$\frac{1}{2}mv_0^2 \leq F_0 y_0 \tag{2.13}$$

Here, F_0 is the plastic strength of the structure and y_0 the *deformation capacity*, i.e. the displacement of the point of impact that the structure can undergo without collapsing.

The latter of the two standards gives design rules for the structural design of buried pipelines, in particular for the evaluation of strength, stiffness and deformation capacity. Effects due to earth pressure, internal pressure, shear forces, normal forces (or combinations thereof) and so on are described. In this case where impact is of particular interest, the most interesting information given is the elastic and plastic moment on the pipe cross-section, M_e and M_p respectively,

$$M_e = \pi r^2 t \sigma_{0d} \tag{2.14a}$$

$$M_p = 4r^2 t \sigma_{0d} \tag{2.14b}$$

in which r is the mean radius and t the pipe wall thickness, while σ_{0d} is the *design* value of the nominal yield stress σ_0,

$$\sigma_{0d} = \frac{\sigma_0}{\gamma_M} \tag{2.15}$$

where γ_M is a material factor given in the national annex. The recommended value is $\gamma_M = 1.0$, but for Norway $\gamma_M = 1.05$. From Eqs. (2.14a) and (2.14b) a value for F_0 in Eq. (2.13) can be estimated. NS-EN 1993-4-3 then supplies limits for maximum allowable deformation from which y_0 can be obtained, thus completing Eq. (2.13). The value of y_0 will of course depend on different parameters and considerations, and will not be elaborated on here.

This rather simple engineering type approach is more suitable when doing an estimate for geometric dimensions rather than determining detailed force-displacement curves as the DNV [22] or the NORSOK [40] standards intend to

do. A rectangular pulse, i.e. a constant force, is not able to represent a realistic loading scenario. For that reason, the EC approach is left at that, but kept as a simple method of doing a quick back-of-the-envelope calculation.

2.4 Analytic approach to dent formation

2.4.1 Derivation

Like the NORSOK approach, this is intended for denting of tubular members and not global bending and does not take any dynamic effects into account. Its intention is to estimate load-displacement curves for tubular members of a platform, intended to absorb the kinetic energy of a ship collision. This analytic approach is briefly outlined by Søreide [44], and explained in more detail in Appendix A.

2.4.2 Evaluation

To reiterate, this is meant for dent formation as are the hitherto discussed approaches. A small comparison of the methods is presented here, in terms of energy absorption as function of displacement. This has been chosen as it is clearly defined in the experiments, and the codes typically deal with a specified impact energy to be absorbed. It is also a fairly easy parameter to plot and discuss. Here, the displacement is limited to being equal to the mean pipe radius.

Consider Fig. 2.4, which shows dynamic and quasi-static experimental data (in red) along with the estimates from the discussed approaches (drawn in black). What immediately stands out is the method labelled “analytic”. It has a steep rise in the absorbed energy in the beginning which does not comply with the experiments. This is due to the fact that in the beginning new lengths of the plastic hinge form at a high rate, thereby absorbing considerable amounts of energy. As the denting progresses, the rate falls and less energy is absorbed per length of dent. It is further observed that the “DNV reduced” approaches the “analytic”, and that it is the one most closely resembling the experiments.

As noted earlier, the initial stiffness is well estimated by all methods with the exception of the “analytic”. For small displacements, these methods can give

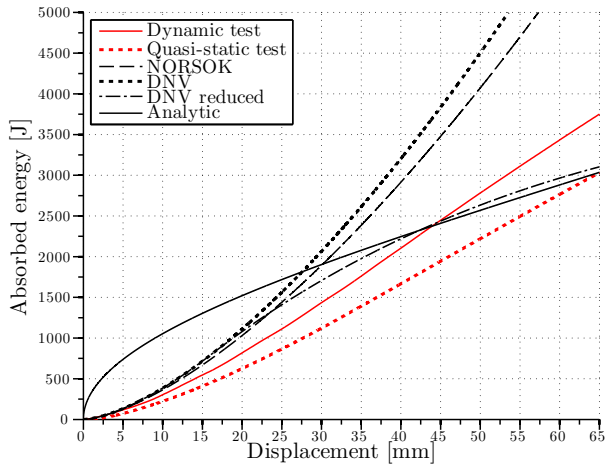

Figure 2.4: *Comparison between experimental data and the different methods discussed up to this point.*

a reasonable estimate for the absorbed energy. More than anything, these results further strengthens the position that experiments are invaluable assets and that advanced numerical simulations are required in order to make reliable predictions.

2.5 Empirical estimates of local and global displacement

A multitude of different empirical formulae for transverse pipe displacements has been developed over the years. Some of them are briefly recapitulated herein, and will be checked against the pipe impact tests performed in Chapter 4. The methods discussed until now has been for denting of tubular members, i.e. only local deformation.

The following methods now account for global deformation as well, assuming a pipe clamped at both ends. This places a rather tight constraint on the system compared to a simply supported beam. Again, a direct comparison with the experiments in Chapter 4 is not entirely reasonable.

2.5.1 Estimating displacements

Three different empirical estimates are considered, namely the ones by

1. Ellinas and Walker [45]
2. de Oliveira, Wierzbicki and Abramowicz [46]
3. Søreide and Amdahl [47]

These three methods will be briefly outlined below, and are discussed e.g. by Jones and Birch [13] and can also be found in online toolboxes [48]. The common traits are that they are all quasi-static methods, intended for impact by an object of mass m and initial velocity v_0 against fully clamped pipes at midspan (span has length 2ℓ). This means that no rate effects are accounted for, and the energy delivered to the system determines the deformation independent of the velocity of the impactor. Further, the pipe is assumed perfectly plastic with yield strength σ_0 and mean radius and thickness R and t, respectively.

Ellinas and Walker [45] (EW)

This method distinguishes between local and global deformation in the sense that once the initial local deformation ceases, global deformation takes over. Alterations in the geometry, and hence strengthening axial membrane forces, are neglected for the global deformations.

The local indentation phase naturally occurs first, and the plastically absorbed energy E_l during this phase is

$$E_l = \frac{1}{3} K R t^2 \sigma_0 \left(\delta^*\right)^{3/2} \quad \text{for} \quad \delta^* \in \left[0, \overline{\delta}^*\right] \tag{2.16}$$

in which K is an empirical factor[3] and $\delta^* = w_l/2R$ is the dimensionless local indentation, which ceases when it attains the limit value $\overline{\delta}^*$, given by

$$\overline{\delta}^* = \left(\frac{32R^2\left(1+\cos\alpha-\alpha\right)}{K\ell t}\right)^2 \tag{2.17}$$

with

[3] A typical value is $K = 150$ [13], and is adopted as default here.

$$\alpha = \left[1 - \frac{2R}{t}\left(\sqrt{\left(\frac{4\overline{\delta}^*}{3}\right)^2 + \left(\frac{t}{2R}\right)^2} - \frac{4\overline{\delta}^*}{3}\right)\right] \cdot \sqrt{\overline{\delta}^*} \tag{2.18}$$

If all the kinetic energy is absorbed by local indentation, the global deformation phase is not initiated and the indentation depth can be found by equating Eq. (2.16) to the initial kinetic energy $mv_0^2/2$ and subsequently solving for w_l,

$$w_l = 2R\left(\frac{3}{2} \cdot \frac{mv_0^2}{KRt^2\sigma_0}\right)^{2/3} \tag{2.19}$$

If the kinetic energy is sufficiently large to produce the maximum dimensionless local indentation $\overline{\delta}^*$ from Eq. (2.17), any excess energy beyond that is absorbed globally. This energy E_g is given as a function of the global deformation w_g,

$$E_g = 8\left(1 + \cos\alpha - \alpha\right) R^2 t\sigma_0 \cdot \frac{w_g}{t} \tag{2.20}$$

Now one simply equates the initial kinetic energy to the sum of the locally and globally absorbed energies with the maximum local indentation and $w_g > 0$ to get

$$\frac{1}{2}mv_0^2 = \frac{1}{3}KRt^2\sigma_0\left(\overline{\delta}^*\right)^{3/2} + 8\left(1 + \cos\alpha - \alpha\right) R^2 t\sigma_0 \frac{w_g}{\ell} \tag{2.21}$$

which completes this method.

de Oliveira et al. [46] (deO)

An initial local indentation is assumed first, after which a global deformation phase commences so no local and global deformation take place simultaneously. The influence of axial forces is retained in the global deformations.

First, the local indentation absorbs the energy E_l

$$E_l = \frac{8\sqrt{\pi}}{3}\sigma_0\left(2Rt\delta^*\right)^{3/2} \tag{2.22}$$

with δ^* being the dimensionless local indentation (equal to $w_l/2R$), which is limited by the maximum value $\overline{\delta}^*$

$$\overline{\delta}^* = 2\left(k - \sqrt{k^2 - 1}\right) \tag{2.23}$$

where

$$k = 1 + \frac{\pi t}{8R} \cdot \left(\frac{\ell}{R}\right)^2 \tag{2.24}$$

For initial kinetic energies producing $\delta^* < \overline{\delta}^*$, Eq. (2.22) is solved for the local indentation w_l

$$w_l = \left(\frac{3}{16\sqrt{\pi}} \cdot \frac{m v_0^2}{t^{3/2}\sigma_0}\right)^{2/3} \tag{2.25}$$

Kinetic energy beyond what produces the maximum dimensionless local indentation $\overline{\delta}^*$ is absorbed by global deformation w, and this energy can be estimated by

$$E_{g1} = \left(16R^3\sigma_0\frac{t}{\ell}\right) \times \left[\frac{8}{\pi^2}\left(1-\overline{\delta}^*\right)\left(2-\overline{\delta}^*\right) \cdot \sin\left(\frac{\pi^2}{8\left(1-\overline{\delta}^*\right)} \cdot \frac{w}{2R}\right) + \frac{\pi^2}{12\left(1-\overline{\delta}^*\right)}\right] \tag{2.26}$$

which absorbs energy until w attains its maximum value $\overline{w}$ given by

$$\overline{w} = \frac{8}{\pi}\left(1-\overline{\delta}^*\right)R \tag{2.27}$$

The sum of the energies absorbed can be solved for $w \in [0, \overline{w}]$ to find the total deformation $w_l + w$.

Kinetic energy surpassing $E_l(\overline{\delta}^*) + E_{g1}(\overline{w})$, i.e. for $w > \overline{w}$, is expressed through

$$E_{g2} = 2\pi R\sigma_0 \frac{t}{\ell}\left(w^2 - \overline{w}^2\right) \tag{2.28}$$

Again, the initial kinetic energy is equated to the energy absorbed by the pipe and a final deformation can be found.

$$\frac{1}{2}mv_0^2 = E_l + E_{g1} + E_{g2} \tag{2.29}$$

Søreide and Amdahl [47] (SA)

Finally, a different approach yet again is described. Here, the initial indentation phase is neglected all together which means that the pipe is assumed to keep a circular cross-section. Global change in the geometry is the only effect accounted for.

As with the previous methods, the initial kinetic energy is set equal to the plastically absorbed energy, giving

$$\begin{aligned}\frac{1}{2}mv_0^2 = 8R^3\sigma_0 \left(\frac{t}{\ell}\right) \times \\ \left[3 \cdot \frac{w}{2R}\sqrt{1 - \left(\frac{w}{2R}\right)^2} + \left(1 + 2\left(\frac{w}{2R}\right)^2\right)\arcsin\left(\frac{w}{2R}\right)\right]\end{aligned} \tag{2.30}$$

which is applicable for $w \in [0, 2R]$. Similarly, for $w \in \langle 2R, \infty \rangle$,

$$\frac{1}{2}mv_0^2 = 4\pi R^3\sigma_0 \left(\frac{t}{\ell}\right)\left[1 + 2\left(\frac{w}{2R}\right)^2\right] \tag{2.31}$$

thereby obtaining an estimate for w. Of the three methods presented here, this one produces the lowest estimates for displacement for a given impact energy.

2.5.2 Separating local and global displacement

After doing impact experiments on pipes, the values typically reported are the *overall permanent displacements* w_f and not the fraction of local indentation (i.e. squashing of the cross-sectional profile) vs. global displacement (overall beam-like displacement). The following equations serve as a means of distinguishing such displacements by an analytic estimate, although some additional measurements for each test specimen will be required due to the complex geometry of the deformed pipe and difficulties related to establishing a reasonable datum for the global deformation. For clarity, this is not another method of estimating the displacements of a pipe due to impact, buth rather an approximation technique for determining the local versus global displacements in an already impacted pipe.

It is assumed by Jones and Shen [49] that the pipes' cross-section (directly in line with the impacting object) is deformed inextensially in the circumferential direction, and that the deformed cross-section is comprised of a circular arc with radius r_0 (seen in Fig. 2.5) closed by with a chord of length D_m as shown in Fig. 2.6. An undeformed but displaced cross-section is used to the define global displacement, and the centre of this undeformed circle is assumed to coincide with the equal area axis of the deformed cross-section (see Fig. 2.5).

Under these assumptions, it is possible, based on the overall permanent displacement w_f along with the "height" T_r and "width" D_m of the deformed

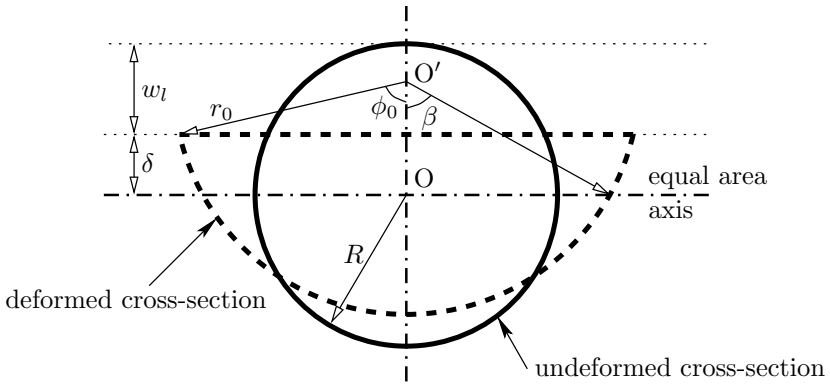

Figure 2.5: *Original and deformed cross-sections of pipe in the plane of impact [49].*

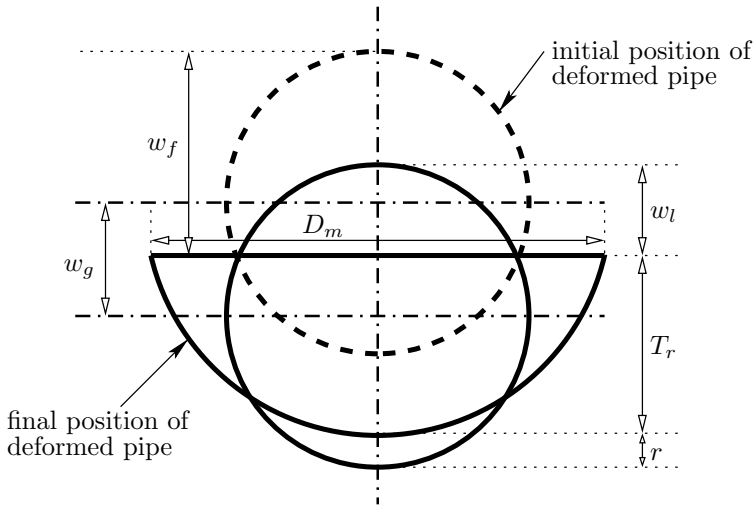

Figure 2.6: *Definitions of local indentation (w_l), global displacement (w_g), and total displacement (w_f) for the idealised cross-section of a pipe in the plane of impact [13].*

cross-section, to distinguish between local and global displacements. All of these values are easily measurable after a pipe impact test.

By rewriting the analysis in [49], an explicit expression for r_0 (see Fig. 2.5) can be obtained;

$$r_0 = \frac{T_r}{2} \cdot \left(1 + \left(\frac{D_m}{2T_r}\right)^2\right) \tag{2.32}$$

Further, the angles ϕ_0 and β can then be found through these expressions [13],

$$\cos\phi_0 = 1 - \frac{T_r}{r_0} \tag{2.33a}$$

$$\beta = \frac{\pi R}{2r_0} \tag{2.33b}$$

The distance from the equal area axis to the top of the deformed cross-section δ is given by

$$\delta = r_0 \left(\cos\beta - \cos\phi_0\right) \tag{2.34}$$

which in turn provides sufficient information to estimate the local displacement w_l as

$$w_l = R - \delta \tag{2.35}$$

From Fig. 2.6 the global displacement is easily calculated;

$$w_g = w_f - w_l \tag{2.36}$$

These equations will be used to estimate local and global deformation in the experimental data, making comparison with the empirical models somewhat more direct.

Not only that, but there is an advantage to estimating the local and global displacements in the experiments themselves. This information can be useful in achieving a better understanding of pipeline failure from a structural mechanics point of view. If an internal pressure was added, this would lead to a smaller local displacement w_l at the expense of an increased global displacement w_g [13]. Jones and Birch [13] further notes that failure in a pipeline tends to occur locally at the site of impact when $w_l > w_g$, while failure at the clamped supports seems more prevalent when $w_g > w_l$. It is, however, hard to make any such generalisations due to the abundance of different parameters associated with pipeline impact. Some of these parameters are explored in this thesis.

2.5.3 Comparison with experiments

As touched upon earlier, pipe impact tests have been carried out (see Chapter 4 for an elaborate description). Estimates based on the three aforementioned empirical equations will be presented along with the experimental values. In addition, the method by Ellinas and Walker [45] will be tested with a different empirical constant K as the boundary conditions are different than its intended use. Being an empirical factor, it can of course be tuned so the results match better with the experiments, and a value of $K = 50$ is chosen here for testing purposes in addition to $K = 150$ as used by Jones and Birch [13]. The

Table 2.2: *Experimental and estimated results for pipe impact test on pipe A.*

Method		**EW**	**EW***	**deO**	**SA**	**Test A**
Initial velocity	[m/s]	3.24	3.24	3.24	3.24	3.24
Impact mass	[kg]	1472	1472	1472	1472	1472
Lenth of span	[mm]	1000	1000	1000	1000	1000
				Results		
w_f	[mm]	63	130	60	35	132
w_g	[mm]	7	25	12	35	86
w_l	[mm]	56	105	48	-	46

*Here, the empirical factor K is changed from 150 to 50.

parameters used for comparison are the total deformation w_f, and the distribution between local indentation w_l and global displacement w_g. In the case of the empirical estimates these are obtained directly, whereas in the experimental case w_l and w_g are obtained through the procedure outlined in Section 2.5.2.

As should have been sufficiently stressed by now, these methods are intended for fully clamped pipes so the estimated deformations are expected to be somewhat lower than the experimental ones as they are obtained through impact against a simply supported pipe, and indeed the results in Table 2.2 reflect that. The table has four columns for the three different methods, with the extra column reserved for the modified EW technique (empirical factor $K = 50$ rather than 150). It is quite clear that the estimates are way too low when the results are compared with test A in Chapter 4. The exception is the EW result with $K = 50$, which estimates the total deformation w_f quite well but misses somewhat on the distribution between w_l and w_g. As the methods have to maximise the local denting before global bending can initiate, $w_l$typically exceeds w_g in this case.

In any case, it is possible to amend these results by various means. The most natural approach concerns the boundary conditions, i.e. fully clamped vs. simply supported. A way to account for this would be to change the span 2ℓ in the equations. A simply supported beam with span $2\ell_1$ and cross-sectional plastic moment capacity M_p subjected to a point load P_f at midpoint experiences a maximum moment $M_{f1} = P_f\ell_1/2$. As P_f is increases to a certain value P_p, M_{f1} will eventually reach M_p which signifies full plastification of the cross-section.

Next, the load P_p is applied to a fully clamped beam with the same M_p, but with a different span, namely $2\ell_2$. The question is then what the fraction ℓ_2/ℓ_1 has to be to ensure full plastification of the cross-section in a fully clamped

Table 2.3: *Experimental and estimated results for pipe impact test on pipe A, after adjusting the span ℓ to twice the original length in the equations.*

Method		**EW**	**EW***	**deO**	**SA**	**Test A**
Initial velocity	[m/s]	3.24	3.24	3.24	3.24	3.24
Impact mass	[kg]	1472	1472	1472	1472	1472
Lenth of span	[mm]	1000	1000	1000	1000	1000
				Results		
w_f	[mm]	94	155	89	67	132
w_g	[mm]	34	73	16	67	86
w_l	[mm]	60	82	73	-	46

*Here, the empirical factor K is changed from 150 to 50.

system. A fully clamped beam of span $2\ell_2$ with a point load at midspan gives a moment $M_{f2} = P_f \ell_2/4$. This leads to the following relation,

$$\frac{\ell_2}{\ell_1} = 2$$

which suggests that a doubling of the length in the equations should provide decent results. Other ameliorations may of course also be reasonable, e.g. specifying the same elastic displacements[4] rather than the same bending moment to plastification, but this is a simple and intuitive approach.

While increasing the span certainly improves the results to some extent, they are still not quite satisfactory as Table 2.3 confirms. Again the modified EW method provides the better result. As this chapter is mainly devoted to existing method for such estimations, no further tinkering will be conducted on these equations. More importantly, this chapter illustrates that more advanced approaches are needed to provide accurate descriptions of the pipe impact scenario.

[4]This would give smaller deformations as the resulting ratio becomes $\ell_2/\ell_1 = \sqrt[3]{4}$.

Chapter 3

Material tests

This chapter contains a description of the pipeline material as delivered, and presents a brief explanation of how the pipes are formed. Basic macroscopic and microscopic properties for the undeformed material are described, being available from the material inspection certificate and from prefatory microscopic investigations. Next, an elaborate material test programme was carried out to obtain a complete material characterisation – vital information for the component tests and for numerical simulations.

3.1 Material description

The material in the pipes used in this thesis is similar to the X65 grade steel used by Manes et al. [5], but the pipes are manufactured in a different manner. Where the pipes in Ref. [5] were formed from rolled plates and welded longitudinally, the current pipes are made seamless. A rough outline of the forming process is as following: By subjecting a solid metal cylinder to radial compression, a cavity forms along the cylinder's longitudinal axis. This is known as the *Mannesmann effect* [50]. The cylinder is then pierced, thus expanding the cavity to form a shell. This shell is then worked to the desired specifications in terms of diameter and thickness (see Fig. 3.1 for an illustration of the process). Production of the

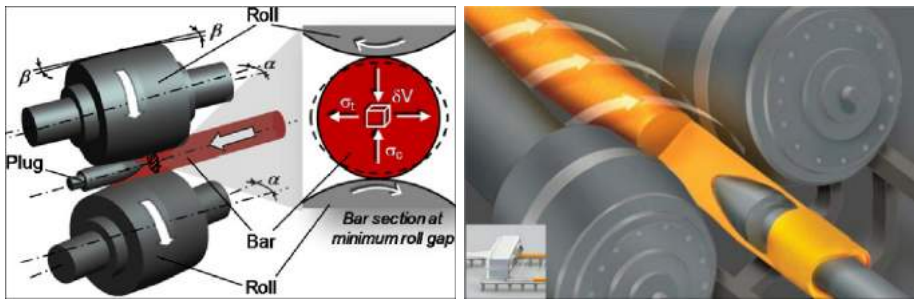

(a) *Illustration by Ghiotti et al. [50]* (b) *Illustration by Tenaris [28]*

Figure 3.1: *Illustrations of the Mannesmann process.*

pipeline has been in accordance with the guidelines in DNV-OS-F101 [21] by the Argentinean supplier Tenaris. Further details can be found in Tenaris' online documentation [28]. A different production method may give rise to different material properties, hence a complete material test programme was conducted as described below.

All specimens used in the material tests (and the component tests presented in Chapter 4) in this thesis were taken from the same batch of pipes. According to the material inspection certificate, the nominal yield stress and the ultimate tensile strength are 450 MPa and 535 MPa, respectively. Young's modulus is 208 000 MPa [33, 34], and the Poisson ratio is 0.3 [51]. The nominal inner diameter of the pipe is 123 mm, and the nominal wall thickness 9.5 mm, making the outer diameter 142 mm and the diameter to thickness ratio approximately 13. Aside from Fe, the main chemical constituents of this alloy are 0.09 C, 0.25 Si, 1.13 Mn, 0.04 Cr, 0.09 Mo, 0.09 Cu and 0.06 V (numbers in weight percentage). The full material certificate, including all chemical components, can be found in Appendix B.

From energy-dispersive X-ray spectroscopy (EDS) of the matrix, it was evident that it contained Fe, Mn and C, as expected from the material inspection card. Scanning electron microscopy (SEM) of the material revealed two types of particles in the material; spherical and angular (both seen in Fig. 3.2). A diameter of about 1 μm to 10 μm was found for the spherical particles, and they were inhomogeneously distributed in the matrix (see Fig. 5.2 for particle size distribution). They consisted mainly of calcium aluminate, and bonded poorly

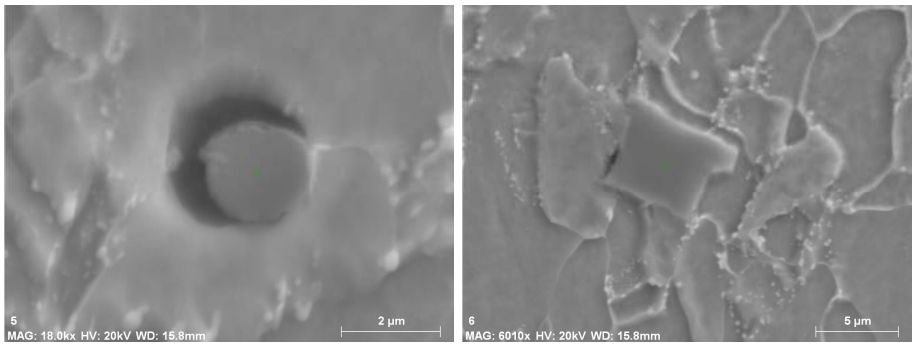

(a) *Spherical particles* (b) *Angular particles*

Figure 3.2: *Pictures from the electron probe microanalysis of the two types of particles found in the material.*

with the matrix. The angular particles, while much less numerous, bonded well with the matrix and their typical size was about 5 μm. Titanium was the main component of these particles, with carbon or nitrogen (inconclusive) second. It will be shown in Chapter 5 that especially the spherical particles are of critical importance for the initiation of both microscopic and macroscopic fracture in the pipe impact problem.

The microstructure of the undeformed material seen in Fig. 3.3 was the same in both the radial and longitudinal direction of the pipe, and it has a ferritic grain structure with grains of size ≤ 10 μm much like that observed by Fragiel et al. [52]. See Section 5.2 for a microstructural elaboration on the material.

3.2 Experimental programme

To characterise the material properties, a broad ranging material test programme was carried out. The pipe material's cross-section homogeneity, possible anisotropic yielding properties, isotropic versus kinematic hardening behaviour, strain rate sensitivity and failure properties were the sought characteristics. To examine the section homogeneity, tensile specimens were cut from different locations – dubbed north, south, east and west – across the cross-section of the pipe. Being seamless, the pipe has no natural reference point on the cross-

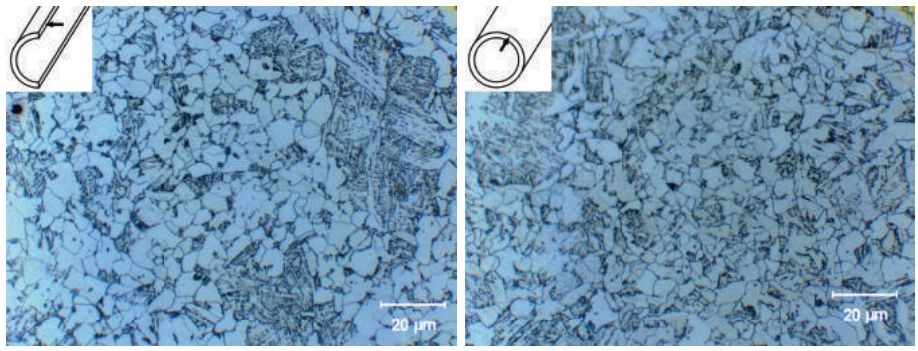

(a) *Radial direction* (b) *Longitudinal direction*

Figure 3.3: *The microstructure of the material in undeformed condition taken from the pipeline, at ×100 magnification.*

section, so one was chosen at random. As the material may have anisotropic properties, specimens were cut in three different directions with respect to the pipe's longitudinal axis; 0°, 45°and 90°. Fig. 3.4 makes evident the positions and directions from where the specimens were cut. These specimens were tested quasi-statically in tension, along with specimens of two different notch root radii. Two specimens from each position and direction were tested, along with three of each notch root radius.

As will be discussed in Section 3.3, the cross-section did indeed appear to be homogeneous, and no anisotropic material behaviour seemed to be present. With this in mind, the location and direction for further material tests became of no significant importance and all future test samples were for simplicity cut so that their longitudinal axis aligned with that of the pipe, not counting those already cut. Tests at elevated strain rates were done on the same specimen geometry as for the quasi-static tension tests, while a slightly different geometry was used for the specimens in the tests involving reversed loading – which included both tension before compression (TC) and compression before tension (CT). Diabolo shaped specimens (see Figs. 3.16(a), 3.17(a) and 3.20(a)) were used to obtain information on how large compressive strain affected the material behaviour (and possibly ductility). Some specimens were compressed before being stretched to failure while others were just compressed for use in the metallurgical study in Chapter 5. An overview of the material test programme is given in Table 3.1.

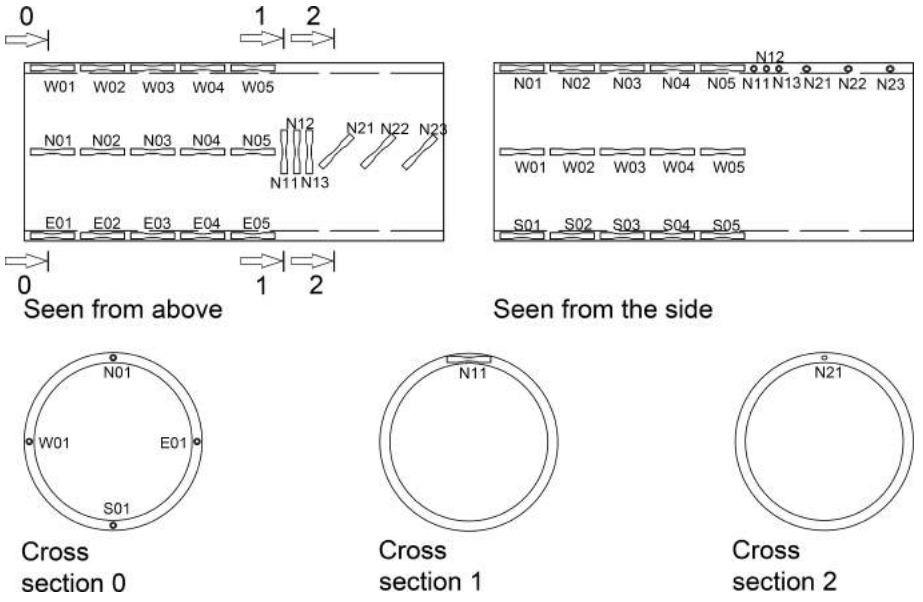

Figure 3.4: *Locations and directions from which smooth axisymmetric test specimens were cut. The notched specimens are not shown here, but were all cut with their axis aligned with the longitudinal axis of the pipe.*

3.3 Quasi-static uniaxial tensile tests

3.3.1 Smooth specimens

Tensile tests were carried out quasi-statically at room temperature on smooth axisymmetric specimens, whose geometry can be seen in Fig. 3.5. The chosen geometry should, based on the microscope images from Fig. 3.3, be large enough to sample a representative portion of the material. A displacement controlled Zwick testing machine was used with a constant deformation rate of 0.3 mm/min. This corresponds to an initial strain rate of $\dot{\varepsilon} = 10^{-3}$ s^{-1} assuming a gauge length of 5 mm as shown in Fig. 3.5.

Two tests from each position across the cross-section (north, south, east and west) were tested to investigate possible heterogenous properties. Specimens cut at different angles with the respect ot the pipe's longitudinal axis and were

Table 3.1: *Overview of material test programme.*

Quasi-static tensile tests (Section 3.3)

Geometry	*Specimens*							
Fig. 3.5	N01 N11	N02 N12	E01 N21	E02 N22	S01	S02	W01	W02
Fig. 3.9(a)	R08-1	R08-2	R08-3	R20-1	R20-2	R20-3		

Dynamic tensile tests (Section 3.4)

Geometry	*Specimens and accompanying true strain rates*					
Fig. 3.5	E04 234 s^{-1}	E05 242 s^{-1}	W04 545 s^{-1}	W05 527 s^{-1}	N04 820 s^{-1}	S04 838 s^{-1}

Reversed loading tests (Section 3.5)

Geometry	*Loading direction and levels of deformation (% strain)*										
Fig. 3.13	Tens-comp	0.0	0.4	1.0	1.5	2.0	4.0	5.0	6.0	8.0	10.0
	Comp-tens	-	-	1.0	1.5	2.0	4.0	5.0	-	-	-

Notched compression-tension tests (Section 3.6)

Geometry	*Levels of compression (% strain)*								
Fig. 3.16(a)	0	10	20	30	40	-	-	-	-
Fig. 3.17(a)	0	10	20	30	40	-	-	-	-
Fig. 3.17(a)*	-	-	20	-	40	60	80	-	-
Fig. 3.20(a)	-	-	-	-	40	60	80	90	100
Fig. 3.20(a)*	-	-	-	-	-	-	80	90	100

*Compression only for metallurgical investigation

used to unravel potential anisotropic behaviour (two of each angle were tested). During testing, the force, the cross-head displacement and the specimen's diameter reduction were measured continuously. Measurement of the diameter at minimum cross-section of the specimen was made possible using an in-house measuring rig with two perpendicular lasers that accurately measures the specimen diameter until fracture. Each laser projects a beam of light with dimension 13×0.1 mm^2 towards the detector on the opposite side of the specimen. Thus, the two orthogonal lasers create a box of laser light measuring $13 \times 13 \times 0.1$ mm^3 around the minimum cross-section of the sample. As the specimen deforms, the continuous change in diameters is observed by the detectors. This dual-axis laser micrometre consists of a high-speed, contact-less AEROEL XLS13XY laser gauge with 1 μm resolution. The gauge is installed on a mobile frame,

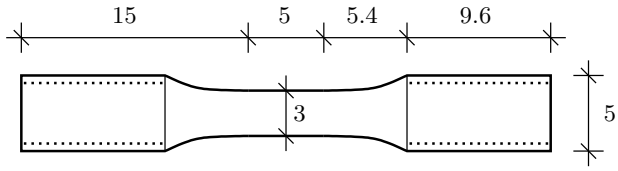

Figure 3.5: *Geometry of specimens (measurements in mm) used in quasi-static and dynamic uniaxial tensile tests.*

making sure that the diameters are always measured at the minimum cross-section. During elongation, the samples were scanned at a frequency of 1200 Hz and the measured data was transferred by the built-in electronics to the remote computer via fast Ethernet. The diameters were measured in the thickness direction of the pipe and in the circumferential direction for the specimens aligned with the pipe's longitudinal axis, to detect potential anisotropy e.g. like in Ref. [53]. As no anisotropy was present, this distinction became unimportant and is hereafter not discussed.

With diameter reduction measurements, it is possible to calculate the true stress σ and the true (logarithmic) strain ε through the well known formulas

$$\sigma = \frac{P}{A} \tag{3.1}$$

$$\varepsilon = \ln\left(\frac{A_0}{A}\right) \tag{3.2}$$

where P is the force measured by the load cell on the Zwick machine and A_0 is the specimen's initial cross-sectional area calculated by $A_0 = (\pi/4)\, D_0^2$, D_0 being the initial diameter. A is the current area of the cross-section, obtained by

$$A = \frac{\pi}{4} D_1 D_2 \tag{3.3}$$

in which D_1 and D_2 are the diameters measured by the two lasers. Assuming additive decomposition of the elastic and plastic strains, the plastic strain ε^p can be found through the relation

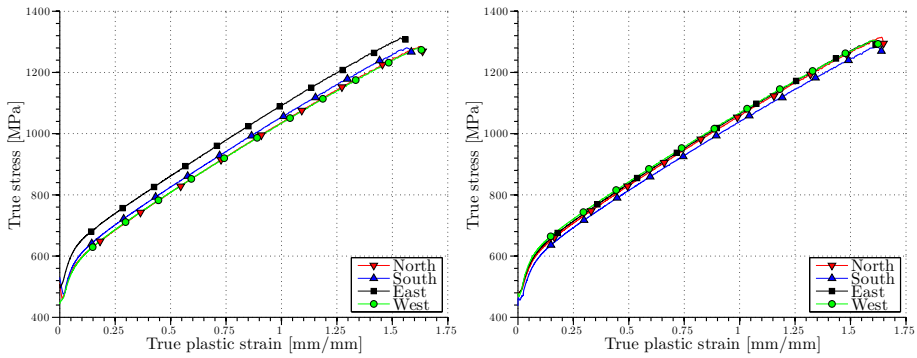

(a) *Series 1* (b) *Series 2*

Figure 3.6: *True stress-true plastic strain curves from quasi-static tensile tests regarding cross-section homogeneity.*

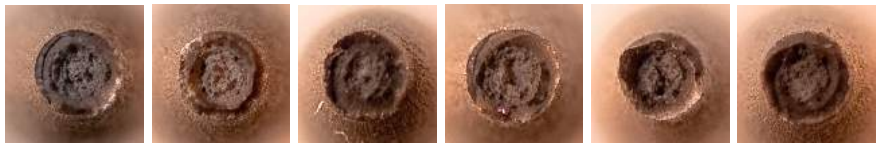

(a) *North 0°* (b) *West 0°* (c) *South 0°* (d) *East 0°* (e) *North 45°* (f) *North 90°*

Figure 3.7: *Fracture surfaces of different tensile test specimens.*

$$\varepsilon^p = \varepsilon - \sigma/E \tag{3.4}$$

where E is Young's modulus. It should be noted that plastic incompressibility and negligible elastic strains are assumed in Eq. (3.2), and that after necking the measured true stress σ and true strain ε represent average values over the minimum cross-section.

Results from the section homogeneity tests are presented in Fig. 3.6, plotted as true stress vs. true strain. These curves are similar in nature to the one for the X65 SAW steel used by Hyde et al. [54] in their study of longitudinal indentation of unpressurised pipes. The material used here has (based on average values from 12 tests) a yield stress σ_0 of 478±15 MPa and an ultimate tensile

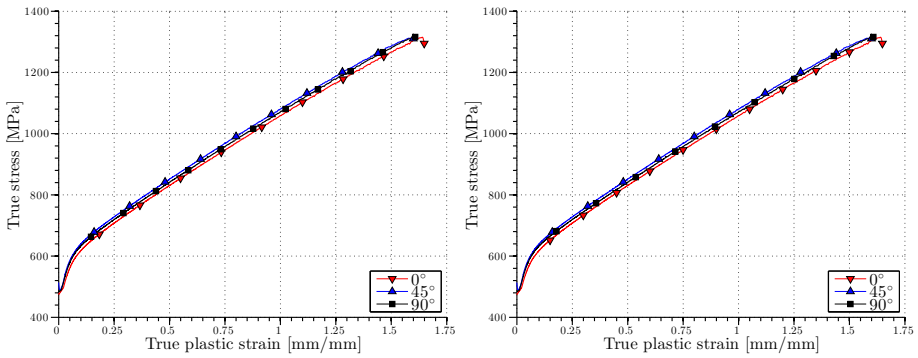

(a) *Series 1* (b) *Series 2*

Figure 3.8: *True stress-true plastic strain curves from quasi-static tensile tests regarding material isotropy.*

strength $S_{\max}$ of 572±14 MPa, at which point the engineering strain $e\,(S_{\max})$ reaches 0.143±0.010. It further strain hardens to a maximum true stress σ_f of 1314±12 MPa and has a true failure strain $\varepsilon_f = 1.613 \pm 0.029$. The average "work per volume" to failure W_{cr}, i.e. the area under the true stress-true strain curve, is 1562±25 Nmm/mm^3. See Table 3.2 for additional details.

The data from the tests, along with the fracture surfaces shown in Figs. 3.7(a)-(d), strongly suggest that for practical and design applications the material properties are homogeneous across the cross-section. True stress-true strain relations from the tests at different directions are displayed in Fig. 3.8, showing the same tendencies; yielding at almost 500 MPa and a peak true stress of about 1300 MPa. The fracture strain was also of the same magnitude, approximately 1.6. Again the data is quite conclusive; no anisotropy appears to be present, as the circular fracture surfaces in Fig. 3.7(a), (e) and (f) also indicate. The ratio of the diameter reduction in the two perpendicular directions remained approximately constant at unity throughout the test, providing strong indications of isotropic behaviour during testing as well, and not just by examining the specimens post-testing.

Based on these results, the material will henceforth be treated as isotropic and homogeneous, in contrast to the quite anisotropic appearance of the X65 steel used by Manes et al. [5], and this difference in properties may be due to the technique by which the pipes were manufactured. As the material may be

Table 3.2: *Experimental data from uniaxial tension tests on smooth axisymmetric specimens.*

ID	Angle	σ_0 [MPa]	$S_{\max}$ [MPa]	$e(S_{\max})$	σ_f [MPa]	ε_f	W_{cr} [MPa]
N01	0°	478	562	0.143	1 314	1.637	1 579
N02	0°	474	562	0.149	1 319	1.650	1 595
S01	0°	475	564	0.150	1 295	1.587	1 518
S02	0°	450	549	0.161	1 292	1.639	1 552
E01	0°	507	603	0.123	1 331	1.560	1 550
E02	0°	476	567	0.146	1 306	1.614	1 557
W01	0°	467	564	0.155	1 310	1.632	1 571
W02	0°	464	574	0.146	1 309	1.625	1 578
N11	90°	480	576	0.139	1 328	1.633	1 598
N12	90°	481	574	0.135	1 320	1.608	1 561
N21	45°	498	588	0.133	1 326	1.557	1 524
N22	45°	486	581	0.137	1 316	1.600	1 564
Avg.	-	478	572	0.143	1 314	1.613	1 562
S.dev.	-	15	14	0.010	12	0.029	25

considered homogeneous and isotropic, all specimens from this point on will therefore for simplicity be cut from the pipe wall in such a way that their longitudinal axis aligns with that of the pipe. Key parameters from the tensile tests are listed in Table 3.2.

3.3.2 Notched specimens

Tests on notched specimens, whose geometries can be seen in Fig. 3.9(a), were also performed. Fracture strain clearly decreased (see Fig. 3.9(b)) when the notch became sharper and the stress triaxiality increased. Stress triaxiality σ^* is defined as the ratio between the hydrostatic stress σ_H and the equivalent von Mises stress σ_{eq},

$$\sigma^* = \frac{\sigma_H}{\sigma_{\mathrm{eq}}} \tag{3.5}$$

An estimate for the initial stress triaxiality σ^*_{init} at the center of the specimen is given by Bridgman's analysis [55] assuming plastic incompressibility and a neck shaped like a circular arc, i.e.

$$\sigma^*_{\mathrm{init}} = \frac{1}{3} + \ln\left(1 + \frac{a}{2R}\right) \tag{3.6}$$

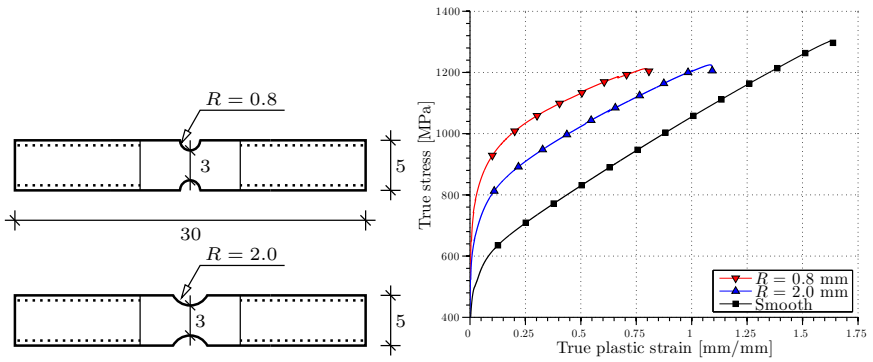

(a) *Specimen geometry in mm* (b) *Results from notched tensile tests*

Figure 3.9: *Notched specimens (a) used in quasi-static tensile tests, and the results (b).*

Table 3.3: *Experimental data from quasi-static tensile tests on notched specimens.*

ID	R [mm]	a [mm]	σ^*_{init}	ε_f	σ_f [MPa]	W_{cr} [MPa]
N01	Smooth	1.515	0.333	1.642	1 314	1 579
N02	Smooth	1.520	0.333	1.655	1 319	1 595
W01	Smooth	1.520	0.333	1.632	1 310	1 571
R20-1	2.0	1.534	0.658	1.018	1 206	1 012
R20-2	2.0	1.538	0.659	1.123	1 209	1 059
R20-3	2.0	1.539	0.659	1.084	1 209	1 017
R08-1	0.8	1.520	1.001	0.762	1 205	820
R08-2	0.8	1.523	1.002	0.761	1 187	739
R08-3	0.8	1.522	1.002	0.792	1 213	821

where a is the radius of the specimen's minimum cross-sectional area and R is the profile radius of the notch at the root.

The stress at fracture, however, appears to be much less affected, which is an interesting characteristic. As different parts of the pipe undergo different types of deformations, the stress triaxiality is bound to vary, thus necessitating data at varying triaxialities. Data from the tests are presented in Fig. 3.9(b), which shows one of each of the notch radii as the scatter between the parallels was very low. Table 3.3 summarises the test data from the notched tension tests, and the triaxiality values listed are initial ones (they change during the

test, see simulations in Fig. 9.4(b) for an estimate). Note also that W_{cr} drops considerably with increasing triaxiality.

3.4 Dynamic tension tests

A split-Hopkinson tension bar (SHTB) was used to obtain stress-strain relations at elevated strain rates [56]. The rig basically consists of two long steel bars, AC and DE in Fig. 3.10, with a diameter of 10 mm. The test specimen is fixed between the two bars and spans from point C to D, and has the same geometry as used in the quasi-static tests (see Fig. 3.5). The bars have a yield stress of approximately 900 MPa. Bar AC is then clamped at point B and given a prescribed tension force[1] N_0 whose magnitude determines the strain rate. The force is applied using a hydraulic jack, and the clamps at point B make sure that the deformation due to N_0 is between points A and B only (part BC is initially stress free).

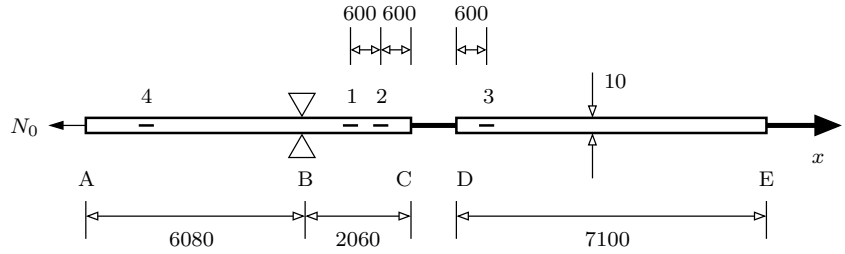

Figure 3.10: *Sketch of split Hopkinson tension bar (not to scale). All measurements in mm.*

There are strain gauges attached to four locations on the rig, each numbered 1 to 4 and marked with a small black line in Fig. 3.10. Two gauges are mounted at each of these four locations, diametrically opposed to each other. This helps eliminate possible bending effects by using the mean value between the two. The sampling rate of the gauges is 1 MHz. The gauges at positions 2 and 3 are used to ascertain the stress, strain and strain rate in the specimen, while the gauges at 4 is used to keep track of the tension force N_0. To check whether any dispersion is present, data from gauges 1 and 2 are considered. The theoretical time lag from the stress wave passes gauge 1 until it reaches gauge 2 is

[1] The applied force should be well below 70 kN to ensure that the deformation in the bar remains elastic.

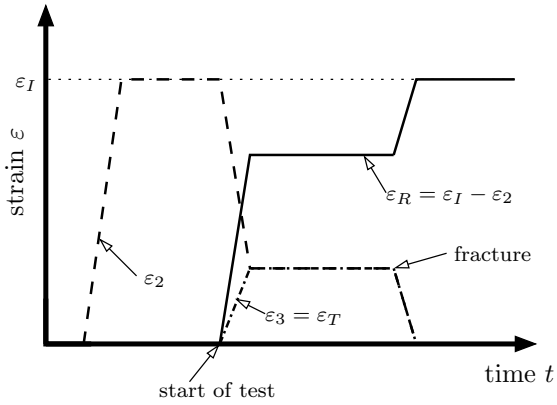

Figure 3.11: *Illustration of strain propagation in the SHTB.*

$$\Delta t = \frac{h_{12}}{c_b} \tag{3.7}$$

where h_{12} is the distance between gauge 1 and gauge 2, and c_b is the wave propagation velocity in the steel bar AC, given by

$$c_b = \sqrt{\frac{E_b}{\rho_b}} \tag{3.8}$$

in which ρ_b and E_b are the density and Young's modulus of steel, respectively. Superimposing the data from gauges 1 and 2 with a lag of Δt for the data from gauge 1 gives an indication to whether any dispersion is present; if the curves are coincident, no dispersion is present. Based on work done by Chen et al. [56] on this rig, the dispersion is assumed negligible and the incoming pulse is assumed to have constant intensity. Chen et al. [56] also provides a more detailed explanation of the rig.

After dispersion has been ruled out, one-dimensional stress wave theory is applicable. When N_0 reaches the prescribed value, the clamps at point B are deactivated and an initial strain wave (ε_I in Fig. 3.11) travels from point B and is captured by strain gauge 2. Upon reaching the specimen, part of the wave is reflected (ε_R) while the remainder is transmitted (ε_T) through the specimen

and measured by the strain gauge at point 3. Using these recorded signals, one-dimensional wave theory can be used to determine the engineering strain e, engineering strain rate $\dot{e}$ and engineering stress S with the following formulae [57]

$$e(t) = 2\frac{c_0}{L_s}\int_0^t \varepsilon_R(\tau)\mathrm{d}\tau \tag{3.9}$$

$$\dot{e}(t) = 2\frac{c_0}{L_s}\varepsilon_R(t) \tag{3.10}$$

$$S(t) = \frac{E_b A_b}{A_s}\varepsilon_T(t) \tag{3.11}$$

where L_s is the length of the specimen's parallel section (5 mm from Fig. 3.5), A_s is the specimen's cross-sectional area, while A_b is the area of the bar's cross-section. The variables ε_R and ε_T are found using the signals ε_2 and ε_3 at strain gauges 2 and 3 respectively as illustrated in Fig. 3.11, based on the assumption that the incoming wave ε_I is constant.

Observations show that the curves for ε_2 and ε_3 coincide largely during the test and that ε_R is fairly constant [56]. The former observation implies that the specimen is in equilibrium during the test, except during the rise of ε_T. The latter shows, based on Eq. (3.10), that the strain rate can be assumed constant during the test.

In Eq. (3.9) the gauge length of the specimen is used to calculate the engineering strain, with the tacit assumption that all deformation takes place in this section. Inspecting the specimens after testing reveals that this is not the case, warranting a correction of the measured strain values. Albertini and Montagnani [58] proposed the following amendment to the strain values

$$e_{\mathrm{corr}} = e_{\mathrm{meas}} - S \cdot \frac{E_{\mathrm{corr}} - E_{\mathrm{meas}}}{E_{\mathrm{corr}} \cdot E_{\mathrm{meas}}} \tag{3.12}$$

where $E_{\mathrm{corr}} = 208\,000$ MPa is the correct Young's modulus for the X65 grade steel and E_{meas} is the slope of the elastic part of the measured nominal stress-

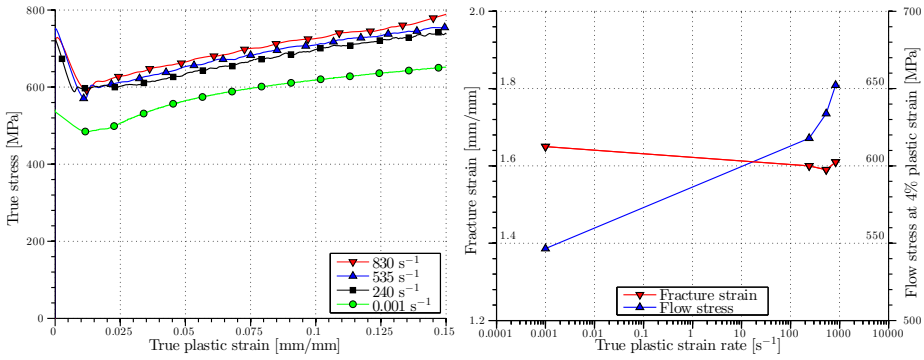

(a) *True stress vs. true strain* (b) *Fracture strain and flow stress vs. strain rate*

Figure 3.12: *Data from dynamic tensile tests on uniaxial specimens.*

Table 3.4: *Experimental data from strain rate sensitivity tests sorted by ascending true strain rates.*

ID	$\dot{\varepsilon}_0$ [s^{-1}]	Meas. $\dot{\varepsilon}$ [s^{-1}]	D_0 [mm]	D_f [mm]	σ_4 [MPa]	σ_{10} [MPa]	ε_f
N01	10^{-3}	10^{-3}	3.03	1.33	547	622	1.642
E04	240	234.2	3.00	1.35	624	701	1.597
E05	240	242.5	3.03	1.36	619	697	1.602
W05	535	527.3	3.00	1.39	634	710	1.627
W04	535	544.8	3.01	1.34	614	694	1.545
N04	830	819.8	3.01	1.34	652	727	1.619
S04	830	837.7	3.00	1.35	645	698	1.597

strain curve. The stress S is determined from Eq. (3.11) while the measured strain e_{meas} comes from Eq. (3.9). By checking the corrected strain e_{corr} against the strain from a strain gauge glued directly on the specimen, Chen et al. [56] showed that this is a viable solution – the agreement between the corrected strain and the strain gauge data was very good until the gauges fell off the specimen. As the specimen is not in equilibrium throughout the entire test, this is an important correction.

Two tests at three different true strain rates $\dot{\varepsilon}_0$ were carried out; 240 s^{-1}, 535 s^{-1} and 830 s^{-1}. The actual true strain rate $\dot{\varepsilon}$ obtained may of course differ somewhat from the intended values (see Table 3.4 for exact values). Fig. 3.12(a) shows that the flow stress increases with increasing strain rate, while the fracture

strain remains of the same order, as seen in Fig. 3.12(b). The component tests presented in Section 4.2 are dynamic in the impact phase, and local strain rates may be quite high during impact, thereby making information on the material's behaviour at elevated strain rates required as modelling of viscoplastic behaviour is of interest. Table 3.4 lists some important results from the dynamic tensile tests, including the flow stress at 4.0% and 10.0% plastic strain (σ_4 and σ_{10} respectively). The fracture strain ε_f was calculated using Eq. (3.13), which is obtained from Eq. (3.2) by inserting the initial diameter D_0 and the diameter at fracture D_f (measured by a micrometer screw) when calculating A_0 and A, making it

$$\varepsilon_f = 2 \ln \left(\frac{D_0}{D_f} \right) \tag{3.13}$$

Again it is referred to Table 3.4 for details.

3.5 Reversed loading tests

To further examine the isotropic and kinematic hardening properties of the material, experiments using reversed loading were performed. During impact, the pipe may in different areas suffer reversed loading with both compression before tension and vice versa. Specimens with geometry as shown in Fig. 3.13 were loaded in tension to a predefined level before the loading was reversed into compressive yielding. Specimens were also loaded oppositely; compression before tension. Compressive strains had to be kept below a certain value to avoid buckling and/or barrelling. Specimens subjected to tension first were loaded to true strain levels ε_{rev} of 0.4%, 1.0%, 1.5%, 2.0%, 4.0%, 5.0%, 6.0%, 8.0% and

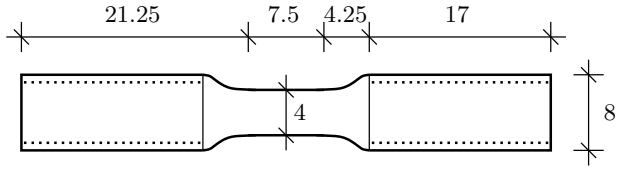

Figure 3.13: *Specimens for reversed loading tests with measurements given in mm. The specimens' longitudinal axis aligns with that of the pipe.*

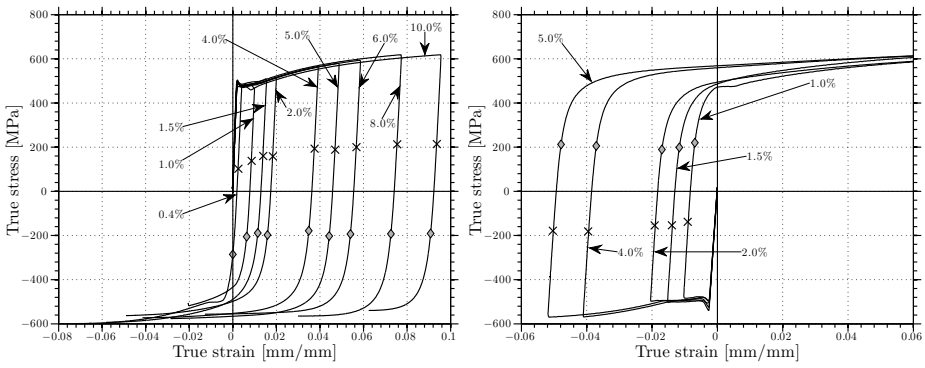

(a) *Tension-compression* (b) *Compression-tension*

Figure 3.14: *Data from quasi-static reversed loading tests on uniaxial specimens.*

10% before the loading was reversed to compression, totalling nine specimens. Five specimens were loaded in compression first, to true strain levels of 1.0%, 1.5%, 2.0%, 4.0%, and 5.0%. In addition, one specimen was loaded to failure in tension only in order to obtain data on the onset of diffuse necking so this could be avoided in subsequent tests. The same laser-based diameter reduction measurement system as used in Section 3.3 was also employed here.

Data from the tests are plotted in Fig. 3.14(a), showing the tension-compression tests, and in Fig. 3.14(b), which shows the compression-tension tests. Kinematic hardening is indeed present in the material, as indicated by the well known Bauschinger effect [59] seen in Fig. 3.14. The diamond shaped markers denote the point of re-yielding after the load is reversed, while the crosses mark the center of the elastic domain. Re-yielding is defined to occur when the plastic strain accumulated after load reversal exceeds 0.0005 – a sketch of an example curve is shown in Fig. 3.15. In addition there seemed to be no difference between which loading direction was applied first when loading to these strain levels, although the initial yield stress $\sigma_{0.2}$ appeared to be slightly higher in compression. On average this was less than 3%, and is therefore not studied further. Right after re-yielding, the two specimens initially loaded to 0.4% in tension and 1.0% in compression displayed a level of constant stress before the strain hardening set in. This is most likely caused by unloading during the Lüders plateu. A more general observation is that all curves appear to converge for large strains. Table 3.5 contains some key data from the reversed loading tests.

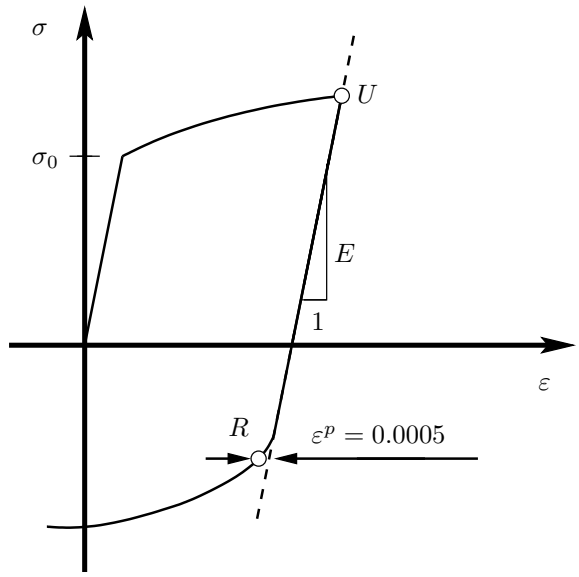

Figure 3.15: *Definition of point of unloading U and point of re-yielding R.*

Table 3.5: *Experimental data from reversed loading tests (see Fig. 3.15).*

ID	ε_{rev}	$\sigma_{0.2}$ [MPa]	U [MPa]	R [MPa]	$\frac{U-R}{2}$ [MPa]	$\frac{U+R}{2}$ [MPa]
T02	0.0100	473	481	-206	343	138
T03	0.0202	478	515	-198	356	159
T04	0.0400	476	565	-179	372	193
T05	0.0604	477	594	-194	394	200
T06	0.0804	486	619	-193	406	213
T07	0.1003	471	618	-191	405	214
T12	0.0500	475	580	-202	391	189
T13	0.0041	472	490	-286	388	102
T14	0.0156	482	510	-189	349	161
C08	-0.0103	-480	-497	220	-359	-138
C09	-0.0204	-482	-498	189	-344	-154
C10	-0.0519	-496	-570	213	-391	-179
C11	-0.0411	-501	-570	206	-388	-182
C15	-0.0152	-489	-507	199	-353	-154

3.6 Notched compression-tension tests

During impact the pipeline suffers large compressive strains in the dent where the impactor hits, before being exposed to tension in the course of the springback directly after impact, and the subsequent quasi-static stretching applied to some of the pipes (component tests described in detail in Chapter 4). To shed some light on the material's behaviour under such loading conditions, experiments on notched specimens (shown in Fig. 3.16(a)) were performed in a deformation controlled Instron 100 kN testing machine. A similar study was conducted by Bao and Treitler [60] on an aluminum alloy, which appeared to display a decrease in ductility with increasing compression. Bouchard et al. [61] concluded with the contrary after exposing two different ductile steel grades to compression-tension loading. Based on the component tests (presented in Chapter 4), the ductility is expected to decrease with increasing compression before tension as a transition from ductile to brittle fracture is observed.

The geometry was chosen in an attempt to prevent or at least minimise buckling and/or barrelling during the compressive phase. First, the specimens in Fig. 3.16(a) were compressed to different levels of large plastic strain – 10%, 20%, 30% and 40% – before being stretched in tension to failure. An additional specimen was stretched to failure without compression for reference, making a

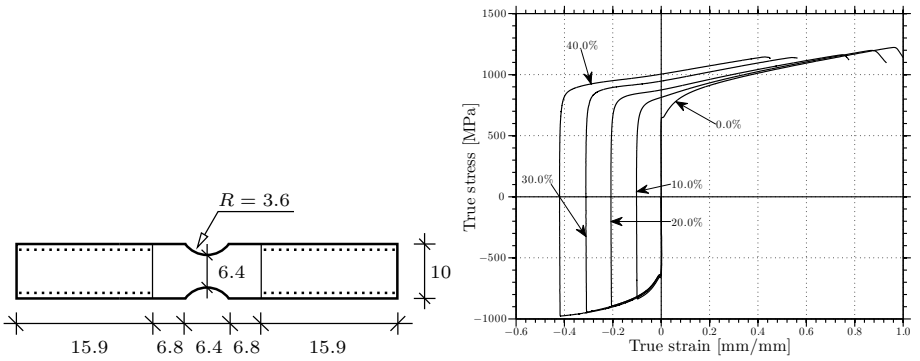

(a) *Specimen geometry in mm* (b) *Test restults*

Figure 3.16: *Specimen geometry (a) and results (b) from the first test series of notched compression-tension tests.*

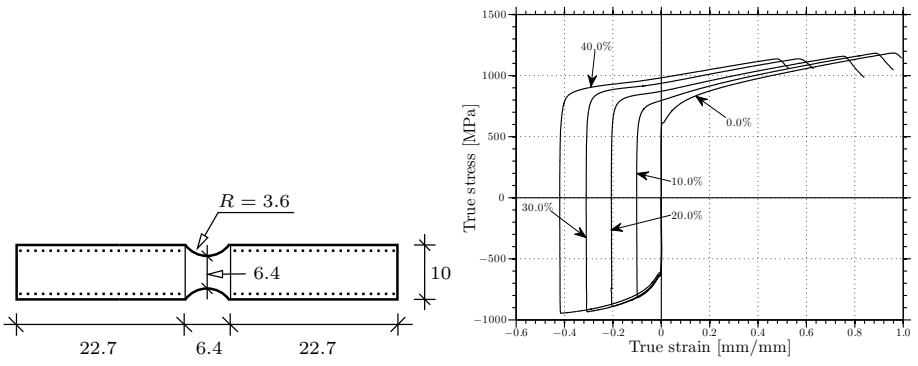

(a) *Specimen geometry in mm* (b) *Test restults*

Figure 3.17: *Specimen geometry (a) and results (b) from the second test series of notched compression-tension tests.*

series of five specimens. Some incipient barrelling between the end of the threads and the notch was observed for the 40% sample, so the threads were extended to the beginning of the notch as seen in Fig. 3.17(a). Another series of five tests was conducted on this geometry. Compression to 60% was also attempted, but barrelling prohibited valid test results from being obtained – the specimen failed in the threads during tension due to the cross-section being widest in the area where the notch had been. Therefore a change was made in the specimen geometry in an attempt to reach higher compressive strains; the diameter at the bottom of the notch was reduced (shown in Fig. 3.20(a)) to avoid this barrelling and a minor eccentricity, both of which were incipient for the 40% test. Once again, the laser-based diameter reduction measurement system was used.

The scatter between the two parallel test series from 0% to 40% compression was low – the stress-strain curves for these are shown in Figs. 3.16(b) and 3.17(b), which are practically identical. In pure tension, the true stress-true strain curve has a clear concave shape. This is not true for the specimens compressed first, which exhibit a slight decrease in work hardening rate before approaching their respective asymptotes. An explanation for this behaviour could be that as the specimens are compressed, dislocations pile up at obstacles and increase the resistance. When the load is reversed, these dislocations have no problem of moving in the opposite direction and offer less resistance. After further increasing the load, more resistance to deformation becomes present and the curves

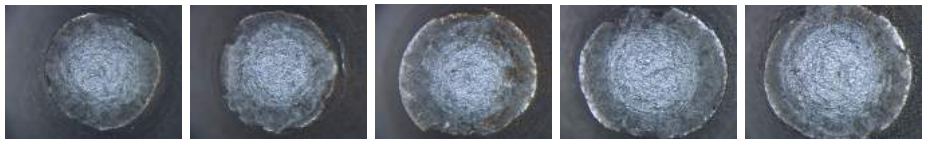

(a) *0%* (b) *10%* (c) *20%* (d) *30%* (e) *40%*

Figure 3.18: *Pictures of fracture surfaces from the notched compression-tension tests.*

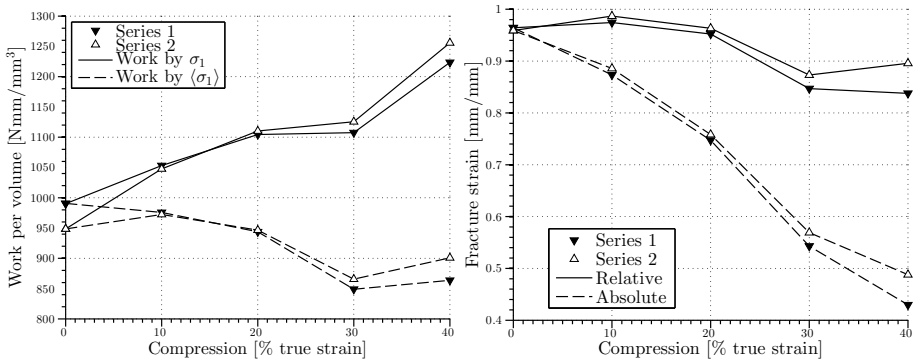

(a) *Work* (b) *Fracture strain*

Figure 3.19: *Results from the first two series of notched compression-tension tests.*

in tension after various compressive levels become more or less parallel. The transient Bauschinger effect is observed through the early re-yielding for the reversed load. Towards the end of the tensile phase, all the curves tend to become parallel including the specimens loaded in tension only. Circular and ductile cup-and-cone fracture surfaces were observed for all specimens. These fracture surfaces are investigated metallurgically in Section 5.7. The area A_f of the fracture surfaces increased with increasing compression, as clearly seen in Fig. 3.18.

Looking at the total "work per unit volume" carried out by the maximum principal stress σ_1 shown in Fig. 3.19(a), it is noted that the "work" increases for increasing compression as the total "distance" the force from the machine acts

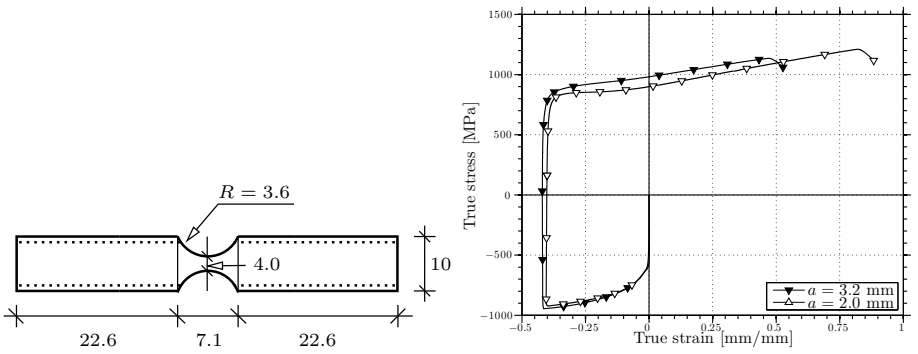

(a) *Specimen geometry in mm* (b) *Test restults*

Figure 3.20: *New specimen geometry (a) and comparison (b) between true stress-true strain relations for the current geometry and the one shown in Fig. 3.17(a).*

along is increased. The work done when σ_1 is positive[2] (which is thought to be a necessity for pores to initiate and grow), tends to decrease. This suggests that something happens during compression which appears to reduce the material's ductility. A decreasing "absolute" fracture strain as calculated by Eq. (3.13) also suggests ductility reduction. The "relative" fracture strain ε_r, obtained by using the cross-sectional area at load reversal A_r as reference rather than the initial area A_0, also exhibits a drop with increasing compression though not as steep. Both the absolute and relative fracture strains are plotted in Fig. 3.19(b).

As mentioned, the specimen geometry was modified to ameliorate the problems with necking in the threads after compression to 60% and beyond. The new geometry was compressed to 40% and then stretched to failure to have one test overlapping with the previous geometry. As the cross-sectional radius a was reduced from 3.2 mm to 2.0 mm as shown in Fig. 3.20(a), the maximum initial stress triaxiality will decrease by about 18% according to Eq. (3.6). Based on the results from Fig. 3.9(b), the fracture strain would be expected to increase somewhat, while the stress at fracture should be of the same order. A direct comparison of the true stress-true strain relations between the two geometries compressed to 40% and stretched to failure can be seen in Fig. 3.20(b), which confirms the argued expectations. The tests showed very good repeatability, and again the scatter between the two parallel series was low.

[2] A common notation is the Macaulay brackets, $\langle \sigma_1 \rangle = \max\{\sigma_1, 0\}$, and is adopted here.

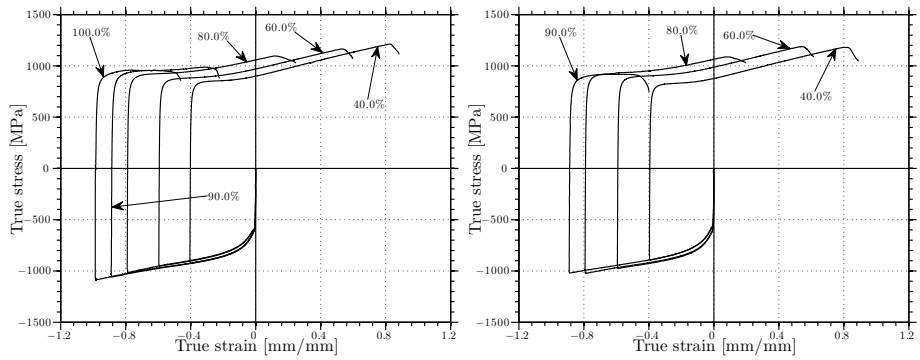

(a) *Series 1* (b) *Series 2*

Figure 3.21: *True stress-true strain curves for compression-tension tests on specimens with geometry as in Fig. 3.20(a).*

True stress-true strain curves from the latter tests are plotted in Fig. 3.21. Herein lies a very interesting feature: where tendencies to ductility reduction were observed in the previous tests, it is now even more evident. Compressing the specimen to 90% appears to decrease the ductility to a significant extent. The fracture mode was altered from a cup-and-cone fracture to a 45° shear fracture, which can be seen in Fig. 3.22. Again the surface area tends to increase with increasing compression as shown in Fig. 3.23, with the 90% and 100% specimens ((d) and (e) respectively) as exceptions since the fracture mode was a 45° shear fracture rather than a cup-and-cone fracture.

Compressing the specimen to 100% created a slight barrelling effect, causing the specimen to become widest at the centre. After stretching it to failure another 45° shear fracture was observed. As the specimen became widest in the middle, it seems that the shear fracture ran from above centre to below, i.e. between the two lowest cross-sectional areas. This should lead to a questioning of the results from the 90% specimen as a similar fracture surface was observed. There was however no such obvious barrelling effect when measuring the instantaneous diameter – the specimen seemingly kept its lowest diameter in the middle.

The total work carried out by σ_1 appears to saturate when compression is increased further (see Fig. 3.24(a)), and drops for the highest compression levels due to the significant drop in fracture strain caused by the change in fracture

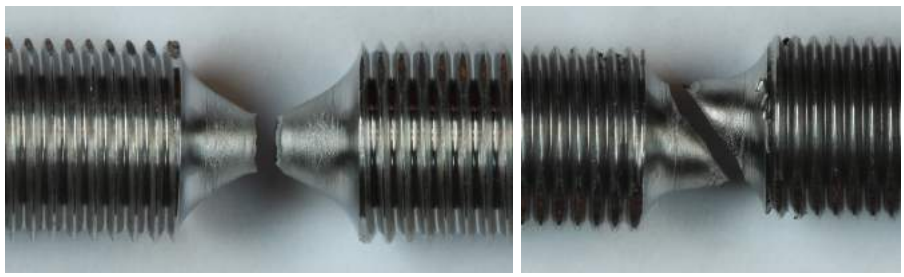

(a) *80%* (b) *90%*

Figure 3.22: *Altered fracture mode between 80% and 90% compression before tension.*



(a) *40%* (b) *60%* (c) *80%* (d) *90%* (e) *100%*

Figure 3.23: *Fracture surfaces of specimens shown in Fig. 3.20(a) after being exposed to different levels of compression before being stretched to failure.*

mode. Again, both the absolute and relative fracture strains show decreasing tendencies with increasing compression (Fig. 3.24(b)). It appears that compression before tension tends to reduce ductility.

Other specimens were exposed to compression only, including higher levels of compression (20%, 40%, 60% and 80%) for which the geometry in Fig. 3.17(a) was used. This series of four tests was carried out mainly to study the microstructure of the material at high compressive strains. Again, the laser based system described in Section 3.3 was used to constantly measure the change in diameter and keep track of its lowest magnitude. Compression to 80% caused the sample to get stuck in the threaded connection to the machine due to the high force level. For higher levels of compression (80%, 90% and 100%) the geometric shape in Fig. 3.20(a) was used. Results from the compression-only tests are presented in Chapter 5 as the potential change in the microstructure due to compression was the area of interest. Table 3.6 summarises the notched compression-tension tests.

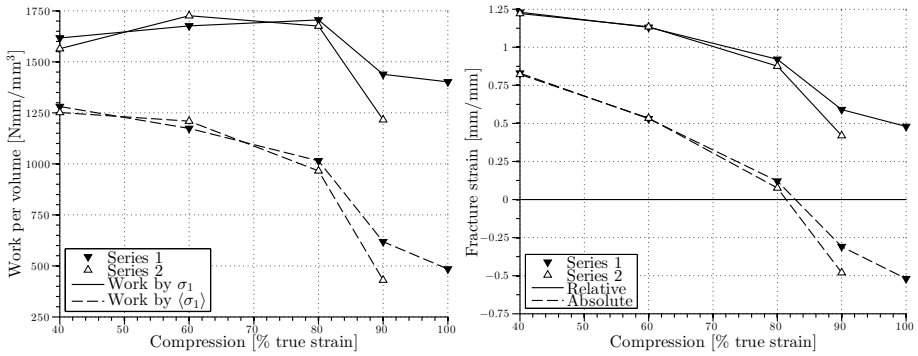

(a) *Work* (b) *Fracture strain*

Figure 3.24: *Results from notched compression-tension tests.*

3.7 Discussion

The quasi-static uniaxial tensile tests from different positions across the cross-section and from different directions (see Figs. 3.6 and 3.8) revealed clear indications of a homogeneous and isotropic material, whereas the longitudinally welded X65 steel pipes used in the study by Manes et al. [5] showed a clearly anisotropic behaviour. Circular fracture surfaces (shown in Fig. 3.7) and the perpendicularly measured diameter reduction during testing confirmed the assertion that the X65 material in the seamless pipes used herein is homogeneous and isotropic. Table 3.2 shows important data from the uniaxial tensile tests. Increasing the initial triaxiality by using notched tensile specimens led to a decrease in fracture strain which is quite typical of metals (see e.g. Ref. [62]). The stress at fracture also decreased somewhat, but not nearly as much – around 8-9% compared to over 50% for the fracture strain (see Table 3.3 for more details).

Split-Hopkinson tension bar tests showed a strain rate dependency in the material. Increasing strain rates led to an increased flow stress, a common property in many metals [63]. At 4% plastic strain and a strain rate of about 830 s^{-1}, the flow stress was 20% higher compared to the quasi-static case as shown in Fig. 3.12. The fracture strain, however, remained almost unscathed – showing a decrease of less than 3% and within the standard deviation from the quasi-static tests. The ductile fracture observed in the material tests heretofore occurs

Table 3.6: *Summary of notched compression-tension tests.*

Geo.	Comp.	ε_f	ε_r	σ^*_{init}	Work σ_1 [MPa]	Work $\langle\sigma_1\rangle$ [MPa]
Fig. 3.16(a)	0%	0.96	0.96	0.701	991	991
	10%	0.87	0.97	0.701	1053	976
	20%	0.75	0.95	0.701	1105	944
	30%	0.54	0.85	0.701	1107	849
	40%	0.43	0.84	0.701	1224	864
Fig. 3.17(a)	0%	0.96	0.96	0.701	949	949
	10%	0.89	0.99	0.701	1048	972
	20%	0.76	0.96	0.701	1110	947
	30%	0.57	0.87	0.701	1126	866
	40%	0.49	0.89	0.701	1156	901
Fig. 3.20(a)	40%	0.83	1.23	0.578	1618	1282
	40%	0.82	1.22	0.578	1565	1252
	60%	0.53	1.13	0.578	1675	1173
	60%	0.54	1.14	0.578	1726	1209
	80%	0.12	0.92	0.578	1708	1015
	80%	0.08	0.88	0.578	1676	966
	90%	−0.31	0.59	0.578	1439	618
	90%	−0.48	0.42	0.578	1216	430
	100%	−0.52	0.48	0.578	1402	485

through void nucleation, growth and coalescence and is extensively discussed in the litterature over the last decades (see e.g. the work by Rice and Tracey [64] or Tvergaard and Needleman [65]).

An element of kinematic hardening is also present in the material, according to the reversed loading tests, the results of which are plotted in Fig. 3.14. In these tests, there was no significant difference between loading in tension first compared to compression first. Effects of pre-strain in X65 steel was also investigated by Baek et al. [66], where large dog-bone specimens were loaded in tension to 1.5%, 5% and 10% strain. New axisymmetric specimens were then cut from the gauge area where the deformation was uniform, and subsequently loaded in tension perpendicular to the initial loading direction of the large specimen. This second batch of tests showed increasing yield stress and ultimate tensile strength with increasing pre-strain, while the area under the engineering stress-engineering strain curve decreased. Such an effect may very well be present in the current material, and may exert an influence on the behaviour in the component tests due to the complex stress and strain history encountered therein.

Compression-tension tests on the first series of notched specimens (see Fig. 3.16) showed a clear reduction in absolute fracture strain with increasing compression, while the relative fracture strain was less affected but still decreasing. Consequently, the "work" done when the major principal stress is positive, conditions thought to make pores grow and coalesce, decreases. This indicates an accelerated void nucleation [67]. Under compression, voids may extend perpendicularly to the load direction before growing along the load direction during tension [60]. Perpendicular void growth and/or more frequent void nucleation due to compression necessarily reduces the distance between voids, leading to earlier coalescence. Modifying the geometry of the notched specimens, seen in Fig. 3.20(a) along with the test results, allowed for compressive strains of 40%, 60%, 80%, 90% and even 100% to be attained. This made the reduction in both absolute and relative fracture strain even clearer. The fracture mode even changed for the 90% and 100% specimens (see Fig. 3.22), from a cup-and-cone type fracture to a shear dominated 45° angle fracture. More details around fracture and fracture mechanisms is provided later in Chapter 5, and in Ref. [29].

Chapter 4

Component tests

4.1 Introduction

This chapter contains descriptions of the experimental configurations, the tests themselves and the results emerging thereof.

First, an important study conducted prior to this one is discussed, namely the one by Manes et al. [5] mentioned earlier. An impact and hooking event against an offshore pipeline first causes a dent sustained by the impact before the pipeline is hooked and dragged out of position. Eventually the impacting object will release the pipeline, causing it to rebound and straighten the geometry. To investigate this load-cycle more closely, strips from a full scale, longitudinally welded X65 pipe were subjected to a quasi-static three-point bending test and subsequently stretched (see Fig. 4.1 for photographs of the setup). Load-diplacement curves were logged during the entire procedure. Afther this load sequence, the strips were investigated for cracks.

The hypothesis was that this load sequence would produce cracks which would reduce the subsequent axial capacity. Of all the tests carried out only one showed signs of cracking, and these were only superficial cracks (see Fig. 4.2) which did not seem to influence the force-displacement curve. The setup producing cracks was the one with the smallest indenter radius (10 mm) specified in the DNV

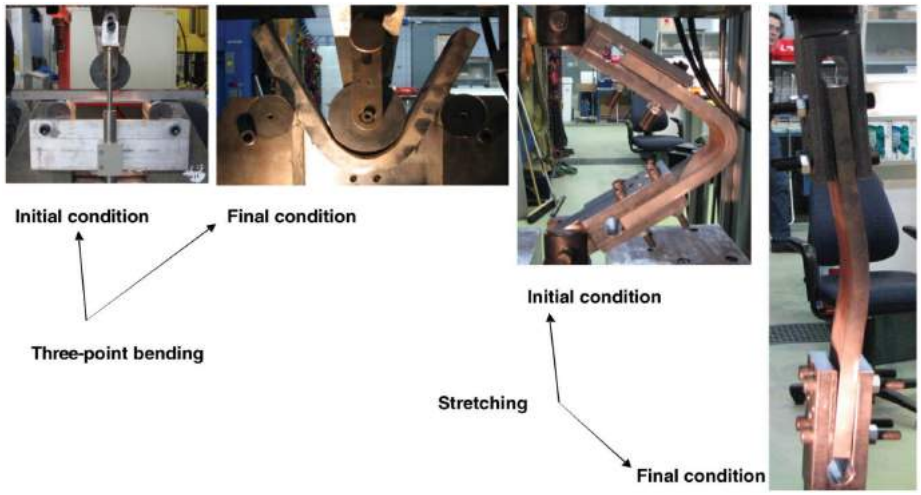

Figure 4.1: *Setup used by Manes et al. [5] for three-point bending and stretching.*



Figure 4.2: *Superficial cracks in test specimen used by Manes et al. [5].*

guidelines [22]. This result might change if a full pipe geometry is used, as plastic flow is more restrained. In addition, loading the pipe dynamically can also contribute to changing the outcome. Simulations of the procedure matched the experiments with reasonable accuracy.

In the present study, component tests have been set up to investigate a full pipe's behaviour during dynamic impact, as opposed to just strips loaded quasi-statically. Again the setup was created as a simplification of the actual event

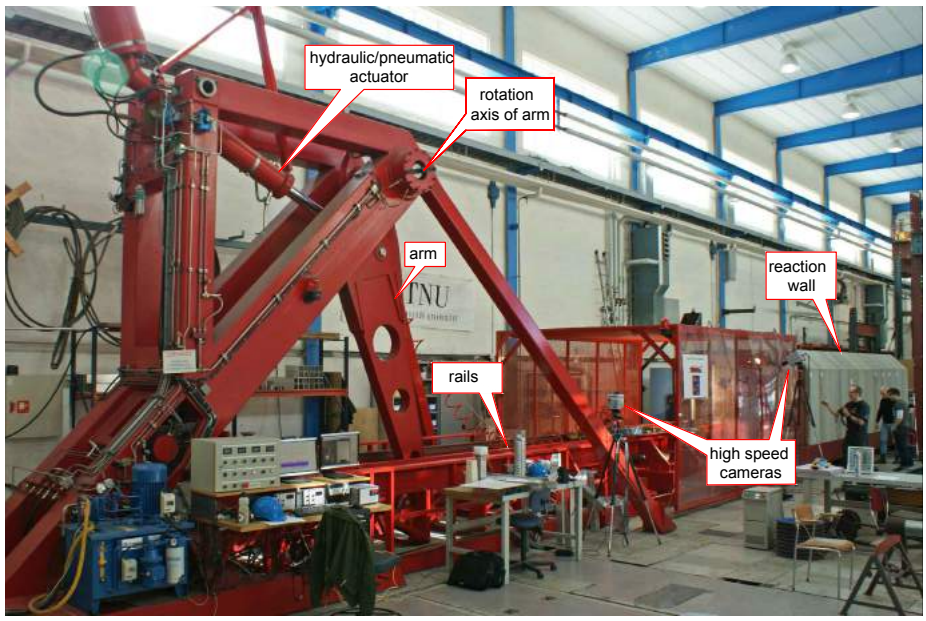

Figure 4.3: *The SIMLab "kicking machine" (pendulum accelerator).*

where a pipeline is struck, dragged out of position and released. The tests were performed in a pendulum accelerator – dubbed the "kicking machine" – shown in the photograph in Fig. 4.3 and described meticulously in the work by Hanssen et al. [68]. It basically consists of a frame with a rotational arm, which is actuated hydraulically. The arm accelerates a trolley with a given mass to a prescribed velocity, thereby generating a kinetic energy to be absorbed by the test component, making this a dynamic test setup.

Seamless X65 steel pipes used (and provided for this thesis) by the offshore industry were the test components in question. The pipes were subsequently stretched quasi-statically to simulate the effect of rebound and straightening of the pipeline after being hooked and released. The same setup was used to test open and closed water-filled pipes as well. Two cameras were used for the water-filled pipes, one to capture the global events and another to keep track to the top of pipe, where either a free surface of water or an end cap retaining the water would be located.

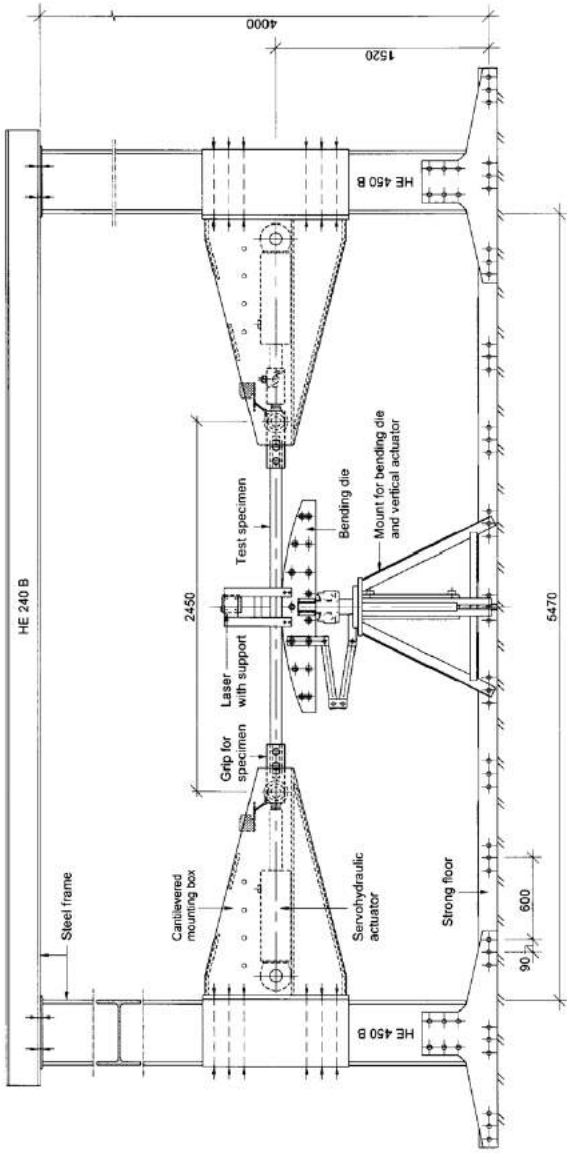

Figure 4.4: *Schematic overview of rig (measurements in mm) capable of applying axial and transverse load [69].*

Quasi-static three-point bending tests were conducted on pipes with the same geometry as used in the kicking machine. Two tests were performed to two different transverse displacements matching that obtained in the dynamic tests. This was done to investigate whether the load rate was of any significance. A comparison of absorbed energy dynamically vs. statically was also made.

Further tests were carried out in a rig (shown in Fig. 4.4) capable of applying axial and transverse loads simultaneously [69], modified to apply internal pressure to the pipe as well. The rig has three hydraulic actuators; two horizontal ones to apply axial load and one vertical for the transverse load. Two steel HE-450B columns (connected at the top by a HE-240B beam to make a frame) are bolted to the ground and have rather heavy dimensions. This is to keep the deformation of the rig itself during testing at a minimum. At each steel column, a height-adjustable connecting box is mounted to hold the horizontal actuators. The vertical actuator is simply bolted to the ground. These three actuators can be operated by deformation control or load control as the user sees fit. The intention of applying axial and transverse loads simultaneously is to come closer to the scenario where a pipeline is hooked and dragged out of position. As a pipeline is displaced, global axial forces arise resisting the movement. This rig can apply axial load as required, thereby creating a more realistic loading sequence. Internal pressure can be included to investigate how this may affect the results. These tests were quasi-static.

This chapter contains a lot of full-scale experiments, so a brief outline of the tests carried out is included here. Table 4.1 gives an overview of all the tests in alphabetical and numerical order. The chapter has been sectioned as following:

Section 4.2 This section describes the dynamic impact experiments conducted on empty pipes. In total six pipe samples labelled A-F were struck at various impact velocities, and subsequently pulled straight in a tension rig, during which fracture always seemed to present itself. Two additional pipes (K and L, high and medium impact velocity, respectively) were also tested without the succeeding stretching. This was done to see if any fracture would arise from impact only. These experiments have also been published in Ref. [29] along with some material tests and metallurgical examinations.

Section 4.3 Here, the exact same test setup as in the preceding section was used, with a slight modification. This time, open and closed water-filled pipes were impacted and stretched. For the open pipes a thick end plate

Table 4.1: *Experimental matrix for all component tests.*

Pipe	Section	Description
A	4.2	Dynamic impact followed by stretching
B	4.2	Dynamic impact followed by stretching
C	4.2	Dynamic impact followed by stretching
D	4.2	Dynamic impact followed by stretching
E	4.2	Dynamic impact followed by stretching
F	4.2	Dynamic impact followed by stretching
G	4.3	Dynamic impact on open, water-filed pipe followed by stretching
H	4.3	Dynamic impact on open, water-filed pipe followed by stretching
I	4.3	Dynamic impact on closed, water-filed pipe followed by stretching
J	4.3	Dynamic impact on closed, water-filed pipe followed by stretching
K	4.2	Dynamic impact, no stretching (for metallurgy)
L	4.2	Dynamic impact, no stretching (for metallurgy)
M	4.4	Quasi-static deformation (three-point bending)
N	4.4	Quasi-static deformation (three-point bending)
1	4.5	Quasi-static stretch-bending, no axial load, stretching (trial)
2	4.5	Quasi-static stretch-bending, constant axial load, stretching (trial)
3	4.5	Quasi-static stretch-bending, increasing axial load, stretching (trial)
4	4.5	Quasi-static stretch-bending, no axial load
5	4.5	Quasi-static stretch-bending, constant axial load
6	4.5	Quasi-static stretch-bending, increasing axial load
7	4.5	Quasi-static stretch-bending, no axial load, $p = 100$ Bar (trial)
8	4.5	Quasi-static stretch-bending, no axial load, $p = 100$ Bar
9	4.5	Quasi-static stretch-bending, constant axial load, $p = 100$ Bar
10	4.5	Quasi-static stretch-bending, increasing axial load, $p = 100$ Bar

was welded to the bottom of the vertically mounted pipes, while the closed pipes had one thick and one thin end plate, thereby limiting the end cap deformation to one end. Again, high and medium impact velocities were used for the two cases, making a total of four water-filled impact tests – pipe G, H, I and J. These four, along with pipes A and B, have been published in Ref. [30] which also includes numerical simulations with fluid-structure interaction.

Section 4.4 Continuing with the same boundary conditions, quasi-static tests equivalent to the impact tests at high velocity and medium velocity were carried out. Two pipes, M and N, were deformed in a testing rig to deformation levels registered from the dynamic tests for comparison.

Section 4.5 For these tests the rig capable of applying both axial and transverse loads was used. Three different axial load cases were considered – zero, constant and linearly increasing tensile axial load, together with deformation controlled transverse loading – with and without internal pressure. Four additional pipes (three initital trial tests, and one later to check the pressure system) were also used to test the rig and make sure things worked, leaving the number of pipes tested at ten in total.

Section 4.6 A brief summary and discussion is included in the final pages of this chapter.

4.2 Dynamic impact against empty pipes

4.2.1 Setup

This experimental setup is an attempt to recreate the loading scenario where a pipeline is hit by an impacting object and dragged out of position before being released and then straightened as a consequence of rebounding caused by the presence of global axial forces.

The experiments consisted of two main steps: A simply supported pipe was first struck by a trolley with a given mass and velocity in the pendulum accelerator mentioned above. Next, the pipe was straightened quasi-statically using displacement control in a standard 1200 kN Instron 8805 testing machine using bolts through the end sections (thicker pipe wall at the ends, explained later) of the pipe, leaving it free to rotate. The former part represents the impact and dragging, while the latter is thought to correspond to the rebound and straightening of the pipeline. These steps are of course a simplification of the actual load events, but will serve as indicators as to what may happen in a real case. These experiments are also described in Ref. [29].

Fig. 4.5 illustrates the difference between the actual impact scenario and the experiment, with the actual event divided in three stages. The first part is when the impactor hits and creates a local dent. Large global deformations are then caused by a continuation of the impact and hooking of the pipeline. These two steps occur simultaneously in the dynamic impact experiments in the laboratory. As the pipeline is displaced in the real case, axial forces (labelled N in Fig. 4.5) arise as a result of the displacements. These axial forces will not

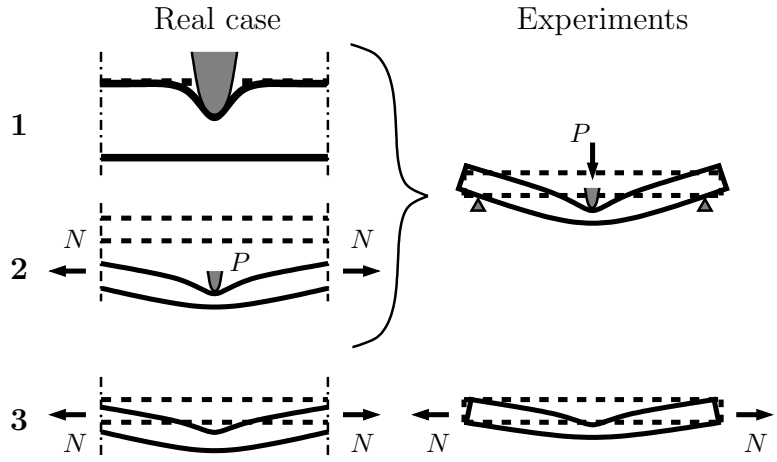

Figure 4.5: *Comparison of reality and experiments, respectively the left and right part of the figure. The dotted lines indicate the initial position, while the solid lines signify the displacements. Stage 1 is zoomed in for clarity, and the sketch is not to scale.*

be present in the tests due to the test pipes being simply supported, which is one simplification. When the pipeline is finally released in a real case, the axial forces move it towards its initial position. This corresponds to the stretch part of the experiments, which is conducted quasi-statically.

Although the actual case and the tests differ somewhat, the experiments should capture the main physics of the problem. Six pipes labelled A through F were tested in this setup: impact at different velocities followed by stretching. Two pipes, called K and L, were exposed to the impact part of the test only. This was done to make bent pipes available for a metallurgical study (see Chapter 5), and for comparison against quasi-static three-point bending tests on pipes M and N.

For reasons unbeknownst to the author, and much to his dismay, the load cell did not trigger when testing pipe L, thereby leaving the force-displacement curve unlogged. These four pipes (K, L, M, N) are discussed in Section 4.4 with respect to the differences between dynamic and quasi-static loading, while the two dynamic tests without stretching (K and L) are discussed in the latter part of the results section herein.

As indicated, an actual piece of a pipeline (albeit of decreased length to make

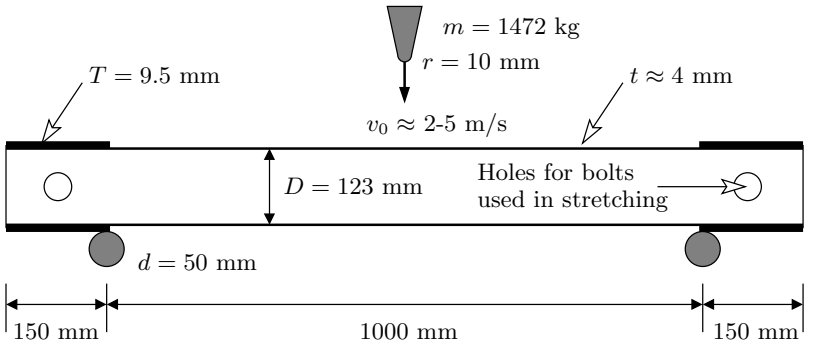

Figure 4.6: *Schematic sketch of the impact part the component test, which corresponds to stage 1 and 2 from Fig. 4.5.*

it fit in the test rig) was used as test component. Vital test parameters, like the free span of the pipeline, the trolley's mass and impact velocity, indenter shape and the pipe's thickness, were designed by means of numerical simulations and the guidelines given in DNV-RP-F111 [22]. A schematic sketch of the test setup is shown in Fig. 4.6. It has been noted, as one might expect, that a pointed indenter perforates the pipe more easily [70], thus the choice of the sharpest indenter in the guidelines ($r = 10$ mm).

A final test setup was decided on; the pipe was given a span of 1000 mm and a nominal thickness of 4 mm, resulting in a D/t ratio of about 30. This ratio is approximately the same as in many pipelines in use for oil and gas transportation [5] as well as in the tubes used in Ref. [15]. To achieve this thickness the pipes were lathed down from 9.5 mm to 4 mm, thus introducing a slightly uneven thickness across the cross-section. Note that the pipes were not polished after being lathed down. The pipes' thicknesses were measured by a portable ultrasound device and measurements were taken at multiple locations across each pipe, forming a consistent grid for direct comparison. A detailed account of the measurements can be found in Appendix C, while average thickness values for each pipe are listed in Table 4.2.

Now an estimate for the peak load is provided. The elastic section modulus w_e of a pipe cross-section is given by $w_e = \pi r_m^2 t$, where r_m is the middle diameter and t the thickness. This makes the elastic capacity of the cross-section $M_p = w_e \sigma_0$ with σ_0 being the yield stress. The maximum bending moment M_f of a simply supported beam of length ℓ loaded at midpoint by a load P_f, can be calculated

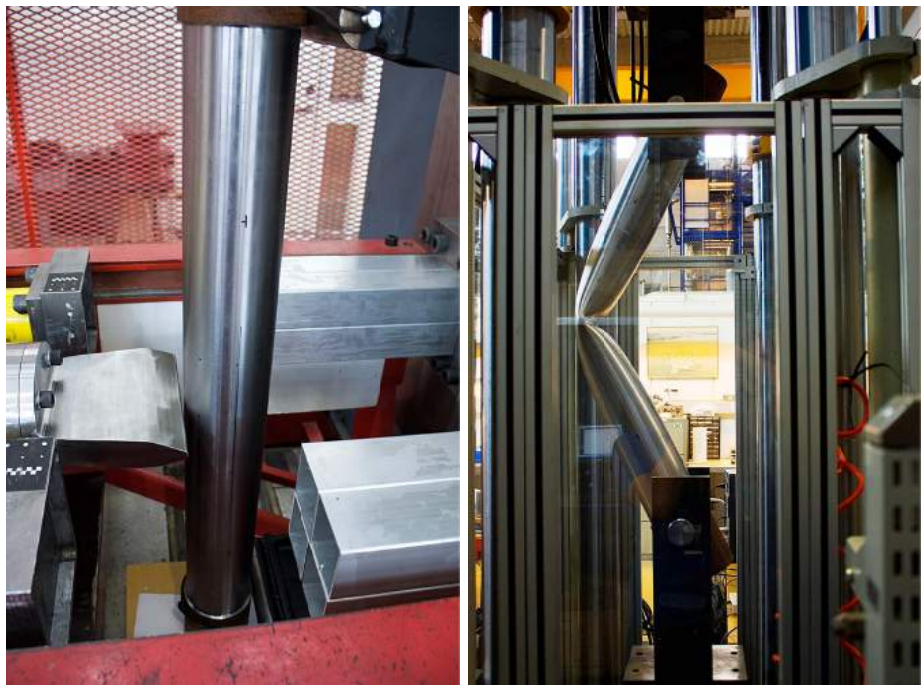

(a) *Impact testing* (b) *Stretching of pipes*

Figure 4.7: *The component tests' (a) impact phase, and (b) stretch phase.*

by $M_f = P_f \ell/4$. Rearranging these relations gives an expression for maximum load before plastification,

$$P_f = \frac{4\pi r_m^2 t}{\ell} \cdot \sigma_0 \approx 91 \text{ kN}$$

after inserting $r_m = 63.5$ mm, $t = 4$ mm, $\ell = 1000$ mm and $\sigma_0 = 450$ MPa as specified. This of course assumes small deformations and that each cross-section of the beam (pipe) is at 90° to the neutral axis.

The trolley was assigned a mass of 1472 kg and an initial velocity v_0 in the range of approximately 2 to 5 m/s, representing the velocity of a boat towing a mass [22]. Pictures of the test setup are shown in Fig. 4.7, where (a) shows

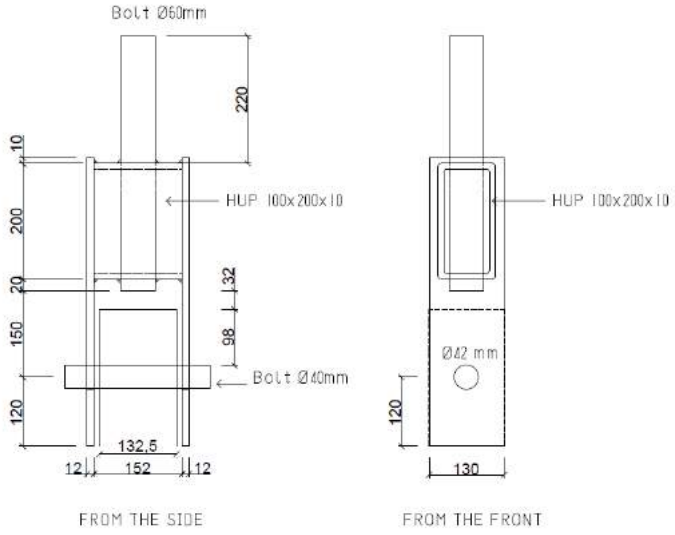

Figure 4.8: *Connection between the pipe and the tension machine used in the stretch part of the component test [33].*

the impact part of the experiments and (b) the stretching phase after the impact. If the global deformation of the pipe was too small after the impact, the tension step afterwards would require a very high axial load in order to see some straightening effect. For that reason, it was important to produce a global deformation sufficiently large (of the order of the pipe's radius).

The supports in the impact phase were massive steel cylinders with a diameter of 50 mm, while the nose of the trolley (the part making contact with the pipe) had a radius of 10 mm as described in [22]. To limit the maximum deformation, buffers were used to stop the trolley. The buffers can be seen in Fig. 4.7(a) as four square aluminium profiles on each side of the pipe. Each profile has a length of 320 mm, outer dimensions of 80 mm×80 mm, and a wall thickness of 3.5 mm. A load cell [71] was used to sample the contact force between the indenter and the pipe. In addition, the events were captured using a high-speed videocamera of type FASTCAM SA1.1 model 675 K-M1 operating at 5000 frames per second.

For the stretch test, custom made "forks" (see Fig. 4.8) were used as connection between the rig and the pipes. 42 mm holes were drilled in the unlathed end

sections of the pipes, and massive 40 mm bolts were used to connect the pipes to the forks through the holes. The connection was designed by Slåttedalen and Ørmen [33].

When carrying out the tension tests of the bent pipes, the stiffness of the tension machine might influence the results. To investigate whether this possible effect was of any significance, the machine stiffness in the tension rig was measured. To do this, a massive steel cylinder with diameter equal to the pipes' was placed in the machine and the load was applied. As the massive steel bolt acts almost rigidly and deformations therein are negligible, any deformation registered is therefore in the machine itself. Loading was applied to the same levels as registered in the stretch tests of the pipe (above 600 kN) and repeated four times. The first repetition showed a slightly softer behaviour as the rig was allowed to "settle", and was therefore excluded from the data set. The average of the registered deformation in the following three series (almost identical for the three) was then subtracted from the force-displacement curves logged from the pipe stretch tests. Effects are discussed in the results section directly below.

4.2.2 Results

Force-displacement curves for all pipes A through F during both impact and stretching are plotted in Fig. 4.9. The peak force in the impact tests (see

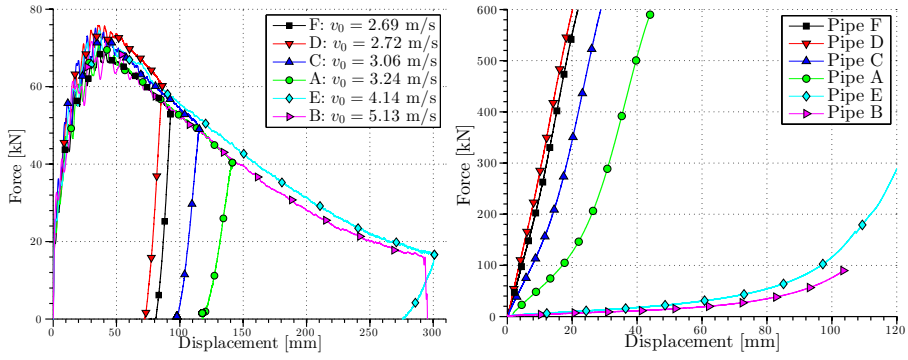

(a) *Impact data* (b) *Stretch data*

Figure 4.9: *Results from the (a) impact tests, and (b) stretch tests sorted by impact velocity.*

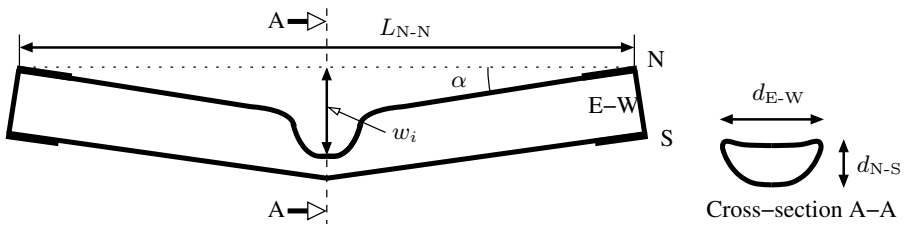

Figure 4.10: *Typical outline of deformation shape (not to scale) of pipes after dynamic impact load at midspan, along with explanation of measurements given in Table 4.2.*

Fig. 4.9(a)) averaged around 70 kN, with a slightly higher peak force corresponding to the pipes with slightly higher average thickness. This is a bit lower than the estimate of 91 kN, but still quite reasonable. The force increases in the beginning when the deformation is still local, and starts to decrease when a transition is made from local to global deformation, which suggests an explanation for the similar peak loads regardless of initial velocity. The remainder of the kinetic energy after the peak is mainly absorbed by global deformation, resulting in the rather large difference in deformation seen between the two pipes A and E – an increase from 3.24 m/s to 4.14 m/s (about 27%) and a relative increase in kinetic energy of more than 60%.

The deformation pattern observed corresponds well with the three modes of deformation identified by the quasi-static three-point bending tests conducted by Thomas et al. [15] and also identified by Soares and Søreide [18], which are crumpling, crumpling and bending, and finally structural collapse (see Fig. 1.2). Fig. 4.10 shows a typical outline of a deformed pipe. Photo series obtained by the highspeed camera can be seen in Fig. 4.11(a) and Fig. 4.11(b), which show pipes A and B respectively. The test setup showed very good repeatability.

From Fig. 4.9(b) it is very clear that higher initial velocity, and hence higher transverse deformation, produces a much lower force level during stretching. The trolley hit the buffers limiting the transverse deformation when impact testing pipes B and E, very clearly reflected in the force-displacement plot from the stretch phase (Fig. 4.9(b)). When the stretching phase initiates, the least deformed pipes can take the applied load as axial forces almost immediately, while the most deformed ones have to withstand a substantial bending moment first due to their large global deformation. As will be shown later, the most deformed pipes received a significant crack already after impact only.

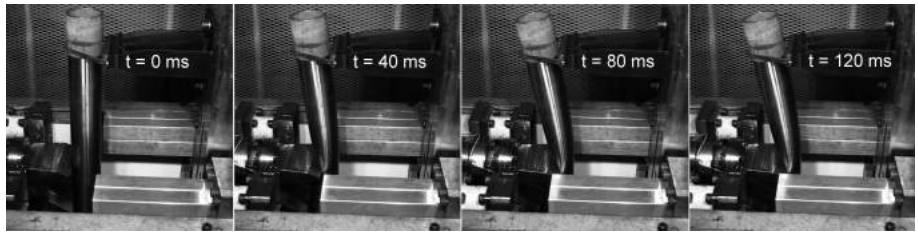

(a) *Pipe A, v_0 = 3.24 m/s*

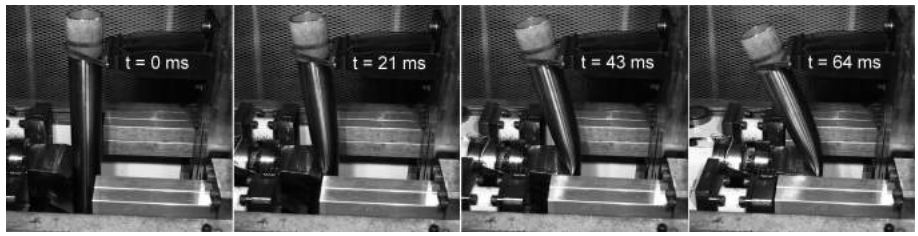

(b) *Pipe B, v_0 = 5.13 m/s*

Figure 4.11: *The impact phase of the component tests, examplified by (a) pipe A and (b) pipe B. Note that in this particular figure, t denotes time after initiation of impact measured in ms.*

In the impact phase, the pipe was aligned so that it was struck on the side labelled north, and all pipes deformed well into the plastic range. Fracture was observed by visual inspection in all pipes during the stretch phase, but at very different load levels, ranging from a maximum value of 274 kN to immediately after stretching (about 10 kN judged by visual inspection during stretching) for the most deformed pipe. Due to the large differences in deformation, different cross-head velocities were used in the stretch phase, but it was always kept in the quasi-static regime. During stretching, pipe B (v_0 = 5.13 m/s) ruptured through the entire thickness of the pipe wall (shown in Fig. 4.12(a) and (b)), while pipe A (v_0 = 3.24 m/s) seemed to suffer only superficial cracks and not through-thickness cracks (see Fig. 4.12(c)).

Table 4.2 lists several important parameters, with Fig. 4.10 serving as a legend for several measurements. Some of these numbers have been used in Chapter 2 for comparison against the methods described therein. It should be noted that one of the key parameters used which is the total displacement w_f, is *not* the

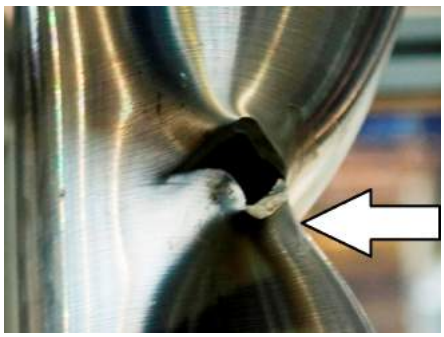

(a) *Overview of pipe B*



(b) *Through-thickness crack in pipe B*



(c) *Surface cracks in pipe A*

Figure 4.12: *Photographs of (a) impact zone on pipe B with an arrow signifying the impact direction and location, (b) close-up of through-thickness crack in pipe B and (c) surface cracks in pipe A. All images are taken after impact and stretching.*

same measurement as the w_i listed here. This is because w_i is measured post-impact from the top of the end sections to the bottom of the dent, which means that the rotation of the ends due to the deformation is included in w_i, thereby making it slightly larger than the w_f used in the equations in Chapter 2. The distance w_f is measured from the original position of the pipe's impact side, to

Table 4.2: *Experimental matrix for component tests A-F. See Fig. 4.10 for explanation of measurements.*

Pipe		**A**	**B**	**C**	**D**	**E**	**F**
Trolley mass	[kg]	1472	1472	1472	1472	1472	1472
Nose radius	[mm]	10	10	10	10	10	10
Avg. thickness	[mm]	3.89 ±0.36	3.86 ±0.34	4.04 ±0.18	4.26 ±0.38	4.19 ±0.32	4.09 ±0.30
				Impact test results			
Initial velocity	[m/s]	3.24	5.13	3.06	2.72	4.14	2.69
Kin. energy	[J]	7708	19356	6875	5435	12613	5316
Abs. energy*	[J]	7294	11736	6520	5096	12503	5083
Peak force	[kN]	70.7	72.7	75.1	75.8	74.6	69.7
w_i	[mm]	170	333	142	105	330	101
$L_{\text{N-N}}$	[mm]	1250	1104	1267	1286	1123	1288
$d_{\text{N-S}}$	[mm]	60	22	71	86	25	98
$d_{\text{E-W}}$	[mm]	180	199	172	162	195	159
α	[deg]	12	30	9	3	30	3
				Stretch test results			
Def. rate	$[\frac{\text{mm}}{\text{min}}]$	20	20	5	5	10	5
Max. force	[kN]	590	90	602	601	307	601
Fracture force†	[kN]	100	10	146	274	24	269

*Estimated by integrating the measured force-displacement curve.
†Determined by visual inspection during stretching.

the bottom of the dent in the deformed structure.

The aforementioned through-thickness crack has three distinct zones as indicated by the numbers on the picture in Fig. 4.12(b) and elaborated on below:

1. The impact side of the pipe
2. The side opposite to the impact side
3. The transition zone between the first two zones

The fracture surfaces of these zones will be examined more closely in the metallurgical study in Chapter 5. Looking at Fig. 4.12(c), traces of the pipe being milled down are visible and fracture appears to initiate at the bottom of these traces. An uneven surface may lead to stress and strain concentrations, thereby directing cracks towards specific locations, but as will be shown in Chapter 5, this is believed to be of minor importance for the fracture process itself.

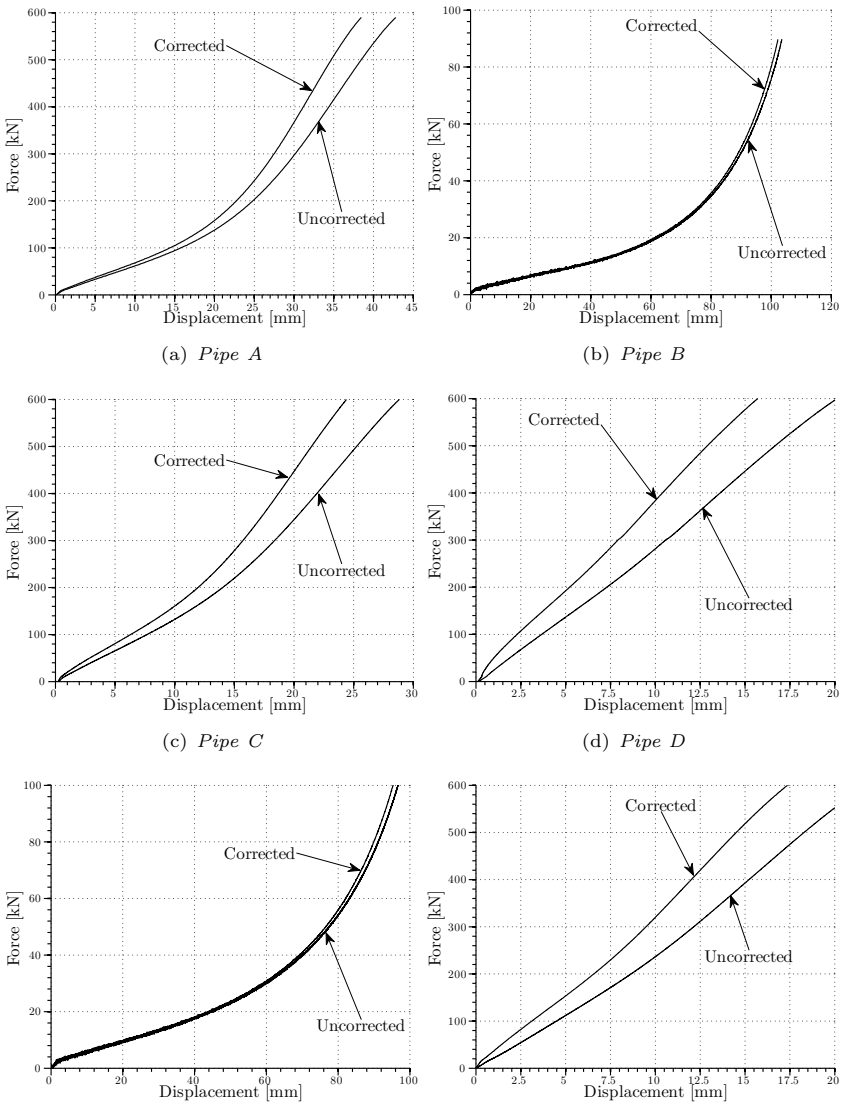

(a) *Pipe A* (b) *Pipe B*

(c) *Pipe C* (d) *Pipe D*

(e) *Pipe E* (f) *Pipe F*

Figure 4.13: *Corrected and uncorrected force-displacement curves from stretch tests. Note the different scales on each subfigure.*

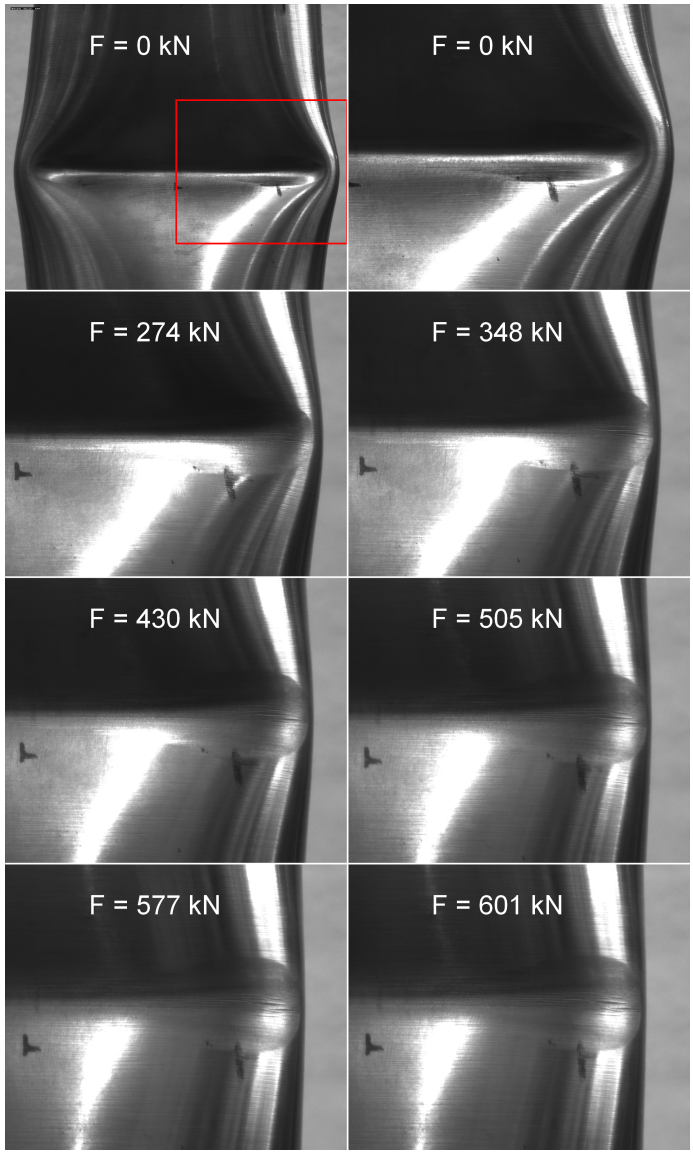

Figure 4.14: *Photo series of the stretch phase on pipe D, with fracture initiating at approximately 274 kN.*

In addition, the machine stiffness of the tension rig was measured. Corrected (machine deformations subtracted) and uncorrected (as registered) curves for pipes A to F are shown in Fig. 4.13. As seen in the figure, the deformation in the machine is proportional to the load applied. This means that the effect is less pronounced for the most deformed pipes as a lower force level is attained. For the least deformed pipes, the effect can be a significant fraction of the total deformation (see e.g. Fig. 4.13(f)). This can be important to remember when conducting numerical simulations. A photo series from stretching pipe D is shown in Fig. 4.14.



(a) *Dent in pipe K* (b) *Crack in pipe K*

Figure 4.15: *Dynamic impact against pipe K caused a clearly visible crack.*

Lastly, the impact experiments without stretching (pipes K and L) are discussed in brevity. The impact velocities were 5.18 m/s for pipe K and 3.26 m/s for L. This would make the deformation roughly equivalent to what was attained for pipes B (5.13 m/s) and A (3.24 m/s). These tests were carried out to have pipes subjected to impact only available for investigation in an optical light microscope and a scanning electron microscope (see Chapter 5). The most important observations are that the pipes behaved as their previously impacted relatives on a global scale, and that a significant crack emerged on pipe K. Fig. 4.15(a) shows the bent pipe, while part (b) shows that the crack is clearly visible to the naked eye. This adds another part to the explaination for the significantly lower force level registered for the most deformed pipes during stretching, and why the crack was visible so early on when stretching pipe B. Measurements of pipes K and L after impact, along with other relevant data, can be found in Table 4.4, where they are compared with quasi-static data.

A final note is made on Fig. 4.15(a), which shows pipe K with black and white spray paint on it. These spots are remnants from an attempt at using 3D Digital Image Correlation (DIC) [72] while testing dynamically. As the cameras were placed quite far away from the test specimens, and the lighting and geometry during deformation were far less than optimal, the results obtained were not particularly good and therefore not further discussed.

4.3 Dynamic impact against water-filled pipes

4.3.1 Setup

The general setup is as described in Section 4.2.1 including impact and stretching, but with a few modifications. These experiments have also been published in Ref. [30]. As seen in Fig. 4.7(a), the pipes are placed vertically in the pendulum accelerator rig and they are completely empty and open in both ends. To contain the water, a rigid steel plate was welded to the bottom end of four pipes – G, H, I and J – and then prepared for testing. Two of the pipes, I and J, were mounted with an end cap welded to the top as well for a complete seal. A 0.7 mm thick Docol 600DL steel plate was used at the top, as this material already is well characterised [62, 73]. Being only 0.7 mm thick, this membrane is more than one order of magnitude thinner than the bottom end cap, thus justifying the assertion that the deformation will take place at the top end cap only.



Figure 4.16: *Open, water-filled pipe.*

An open, water-filled pipe is shown in Fig. 4.16. The open pipes are easily filled to the brim. For the closed ones, one tap was mounted on both of the unlathed end sections of the pipes (see e.g. Fig. 4.23(b)) in an attempt to fill the pipes completely and leave no air inside. This is however a bit difficult to achieve in practice, so one has to consider the possibility that some air got trapped in the closed pipes. Although the setup is basically the same as in Fig. 4.6, a sketch with the modifications is presented in Fig. 4.17 for completeness. Note again that the thin end cap is used only for pipes I and J, while pipes G and H are left open at that end. For the water-filled pipes, two high-speed cameras were used. One camera was used to capture the global events, while another focussed

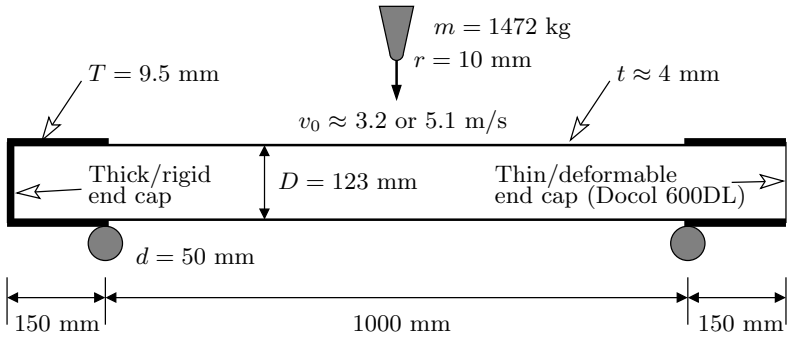

Figure 4.17: *Schematic sketch of impact test against water-filled pipes.*

on the top of the pipe where water presumably would flow out of the pipe or deform the membrane.

4.3.2 Results

Force-displacement curves for six component tests are presented in Fig. 4.18, with part (a) showing impact at about 3.2 m/s (pipes A, G, I) and (b) impact at about 5.1 m/s (pipes B, H, J). As seen, there is little difference between the empty pipes and the open pipes containing water. A slightly higher peak force is noted for the open water-filled pipes, but whether this is because of the added mass and inertia of the water, difference in thickness or local contact conditions is hard to tell. Most likely it is a combination, which can be difficult to quantify. Fig. 4.19 shows a typical outline of a deformed pipe, and serves as a legend for several measurements listed in Table 4.3.

Again, the force level during stretching is highly dependent on the deformation induced by the impact as seen in Fig. 4.20, first and foremost in the different scale between part (a) and (b), and also between each individual pipe. It is seen that the empty pipes (A and B) are the thinnest and thereby provide less resistance when stretching. For pipe B the deformation after impact was quite similar to the water-filled pipes impacted at the same velocity (H and J), but the force during stretching was still lower. Pipe A is both thinner and was deformed a bit more during impact, making the difference during stretching even more evident (see Fig. 4.20(a)). A correction for the machine stiffness during tension has been made for the water-filled pipes as well, with the plots shown

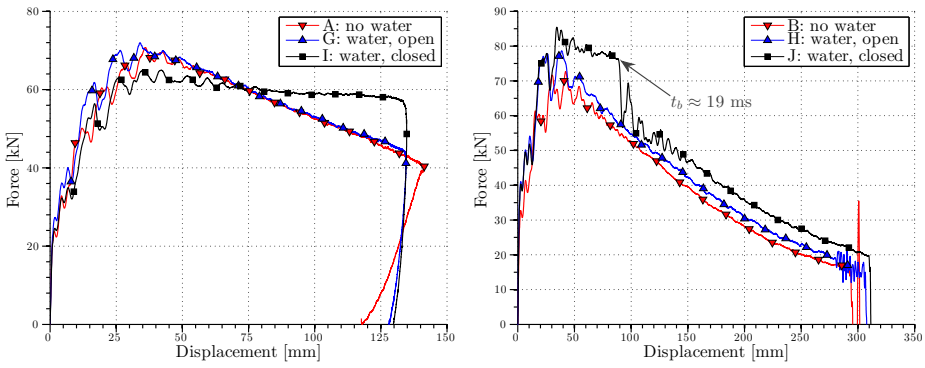

(a) *Impact at ≈ 3.2 m/s* (b) *Impact at ≈ 5.1 m/s*

Figure 4.18: *Data from impact against water-filled pipes.*

in Fig. 4.21. The trends are the same as in Fig. 4.13 with a more pronounced effect at higher loads, which is in accordance with expectations. Fracture was observed in all pipes during stretching, at very different load levels as before, the lowest being around 10 kN and the highest about 200 kN (see Table 4.3).

At 3.2 m/s (pipes G and I), the final global deformation was quite similar, with the empty pipe having a slightly larger deformation. This can be attributed to the lower pipe wall thickness of the empty pipe A (see Table 4.3), and the inertia of the water (or rather, lack thereof). Fig. 4.23 shows the course of deformation of pipes G and I during impact. The trolley hit the buffer in the rig when testing at 5.1 m/s (pipes H and J) as the pipes were unable to absorb all the kinetic energy alone – hence the matching total displacement of approximately

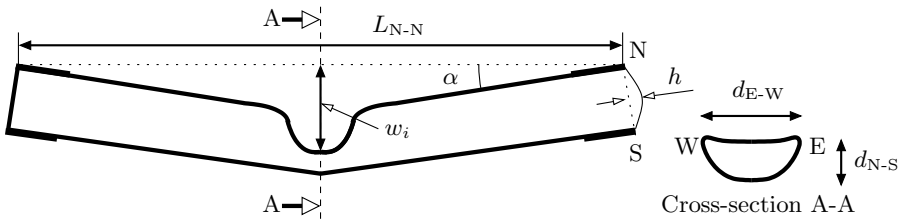

Figure 4.19: *Typical outline of deformation shape (not to scale) of pipes after dynamic impact load at midspan, along with explanation of measurements given in Table 4.3.*

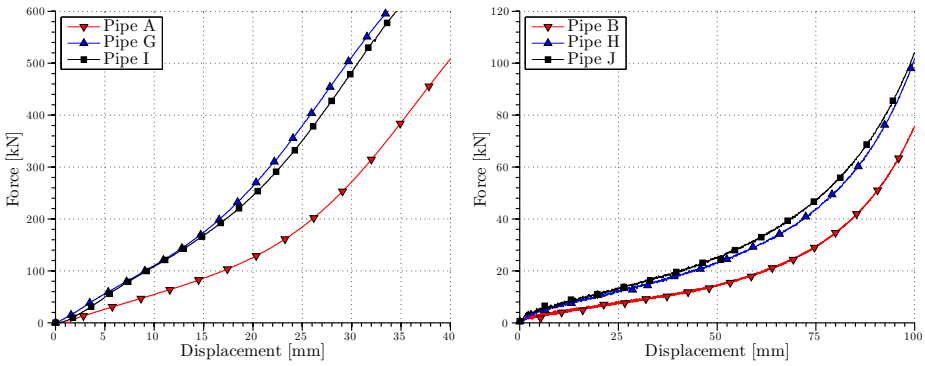

(a) *Stretching after impact at ≈ 3.2 m/s* (b) *Stretching after impact at ≈ 5.1 m/s*

Figure 4.20: *Data from stretching tests as logged (i.e. machine stiffness is not taken into account), note the different axis scales in (a) and (b).*

330 mm. Depicted in Fig. 4.24 is a photo series of pipes H and J taken from the high speed video of the global events.

For the closed water-filled pipes, the force-displacement curve during impact deviates strongly from the other two cases for both velocities. The force remained almost constant throughout the test. At the highest velocity, however, the thin end cap ruptured at the weld and the water was no longer confined to remaining within the volume of the pipe, thereby resulting in a sudden drop in the force – this is indicated by an arrow in Fig. 4.18(b). The rupture happened after approximately 19 ms, also shown in Fig. 4.22, after which the force-displacement curve attained a similar shape to those of the empty pipe and the open water-filled pipe (albeit with a slightly higher force level, most likely due to the water being funneled through a narrow orifice).

A certain pressure builds during the impact due to the change of volume in the closed pipes (pipes I and J). In turn, the thin end cap deforms accordingly. Based on the final deformation of the bulged end cap, it is possible to obtain an analytical estimate of the pressure which has caused said deformation. The procedure is based on Ref. [74], and is outlined in more detail in Appendix D. As seen in Fig. 4.22, the thin end cap ruptured at the weld in pipe J (5.04 m/s), thus relieving the pressure and rendering the measured end cap deformation useless. Pipe I (3.22 m/s), on the other hand, remained intact through the impact test

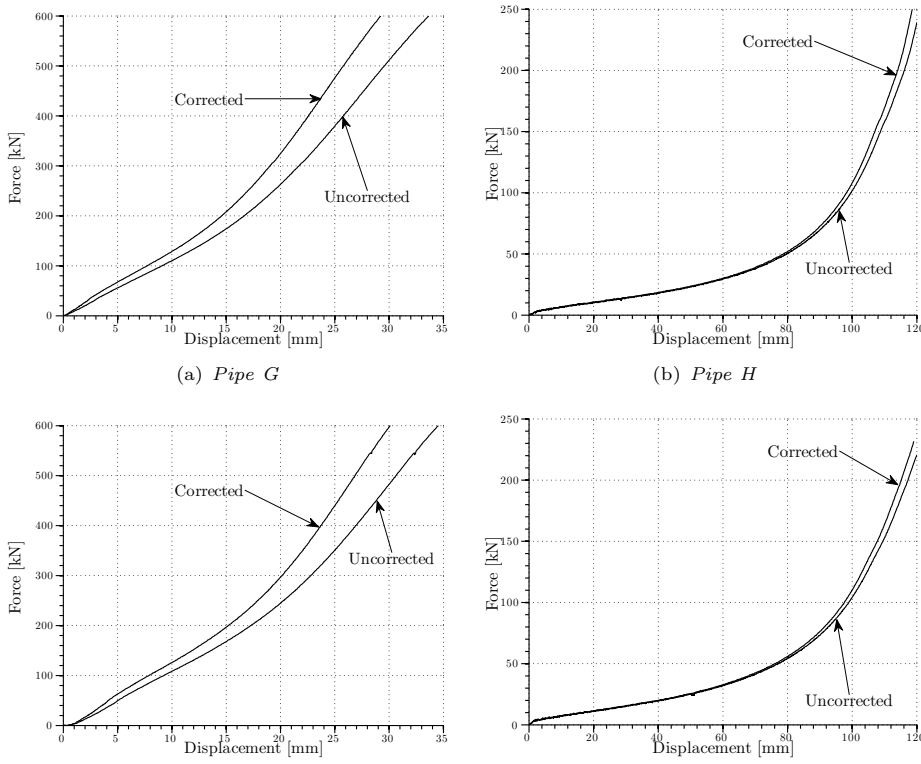

(a) *Pipe G* (b) *Pipe H*

(c) *Pipe I* (d) *Pipe J*

Figure 4.21: *Corrected and uncorrected force-displacement curves from stretch tests of pipes G-J. Note the different scales on each subfigure.*

letting the end cap form a nice dome arising from the pressure. The measured height was $h = 14$ mm, resulting in a pressure estimate of approximately 56 Bar. In hindsight, a pressure gauge should have been mounted on the pipes for more accurate data and for comparison with the numerical simulations carried out in Section 8.8. As mentioned, Table 4.3 contains various measurements recorded (like Table 4.2). The most notable feature is the high peak force for the closed, water-filled pipe (J) impacted at high velocity (5.04 m/s). This is explained by the water content and the pipe being closed, allowing pressure to build up during deformation.

Table 4.3: *Experimental matrix for component tests on water-filled pipes. See Fig. 4.19 for explanation of measurements.*

Pipe		**A**	**B**	**G**	**H**	**I**	**J**
Trolley mass	[kg]	1472	1472	1472	1472	1472	1472
Nose radius	[mm]	10	10	10	10	10	10
Avg. thickness	[mm]	3.89 ±0.36	3.86 ±0.34	4.08 ±0.21	4.06 ±0.32	4.02 ±0.23	4.16 ±0.27
Water?	-	No	No	Yes	Yes	Yes	Yes
Open/closed	-	Open	Open	Open	Open	Closed	Closed
				Impact test results			
Initial velocity	[m/s]	3.24	5.13	3.21	5.11	3.22	5.04
Kin. energy	[J]	7708	19356	7578	19245	7653	18713
Abs. energy*	[J]	7294	11736	7481	12908	7569	14731
Peak force	[kN]	70.7	72.7	71.9	78.6	65.0	85.4
w_i	[mm]	170	333	140	330	139	333
$L_{\text{N-N}}$	[mm]	1250	1104	1255	1095	1270	1103
$d_{\text{N-S}}$	[mm]	60	22	68	28	77	31
$d_{\text{E-W}}$	[mm]	180	199	174	198	168	198
h	[mm]	-	-	-	-	14	-
α	[deg]	12	30	8	26	9	32
				Stretch test results			
Def. rate	$[\frac{\text{mm}}{\text{min}}]$	20	20	5	10	5	10
Max. force	[kN]	590	90	674	316	601	232
Fracture force†	[kN]	100	10	150	10	200	14

*Estimated by integrating the measured force-displacement curve.

†Determined by visual inspection during stretching.

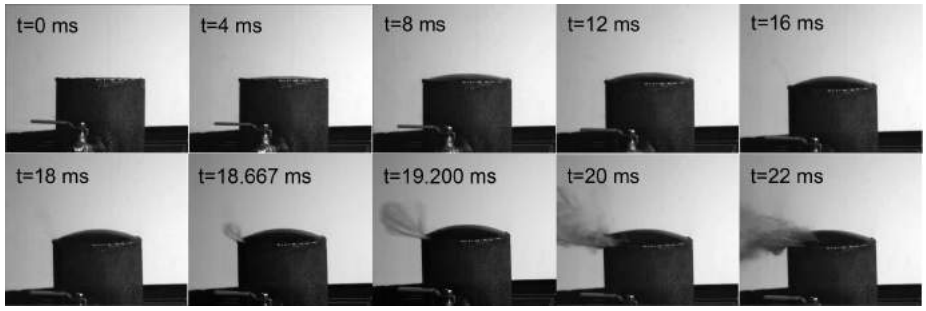

Figure 4.22: *Pictures of top membrane on pipe J, taken by the high-speed camera with t denoting time in ms in this figure.*

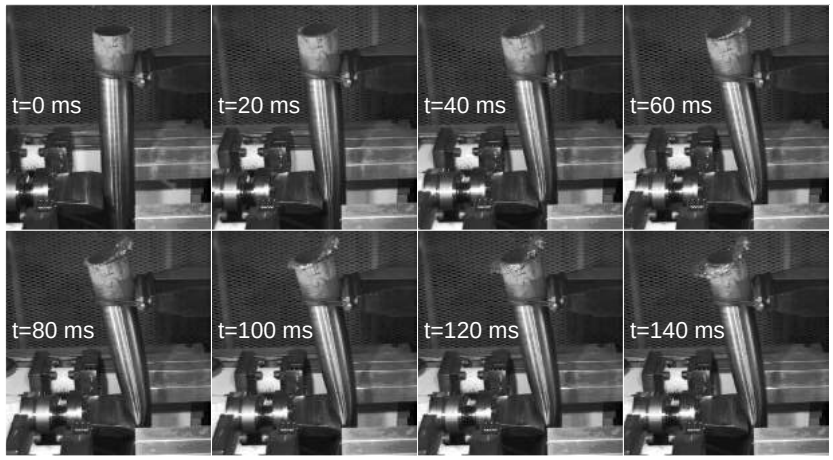

(a) *Pipe G, open, $v_0 = 3.21$ m/s, with time after impact specified in each frame*

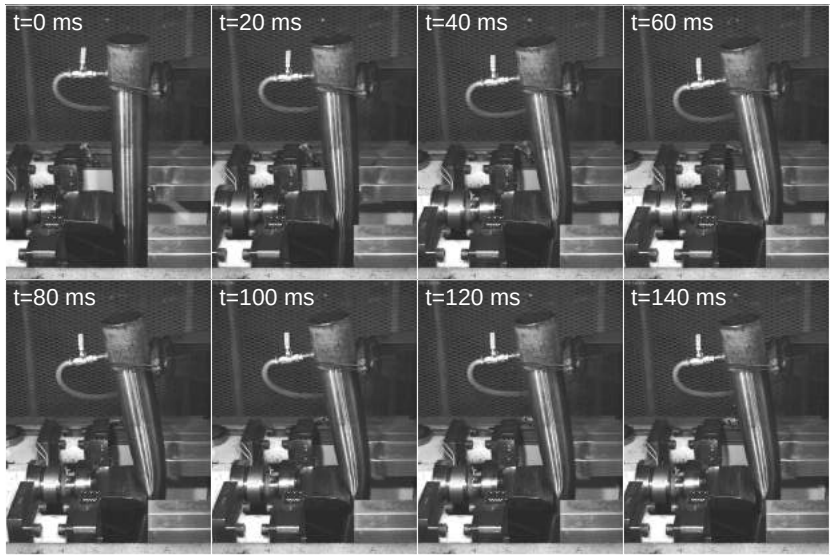

(b) *Pipe I, closed, $v_0 = 3.22$ m/s, with time after impact specified in each frame*

Figure 4.23: *Images from high speed video of impact against water filled pipes at 3.2 m/s.*

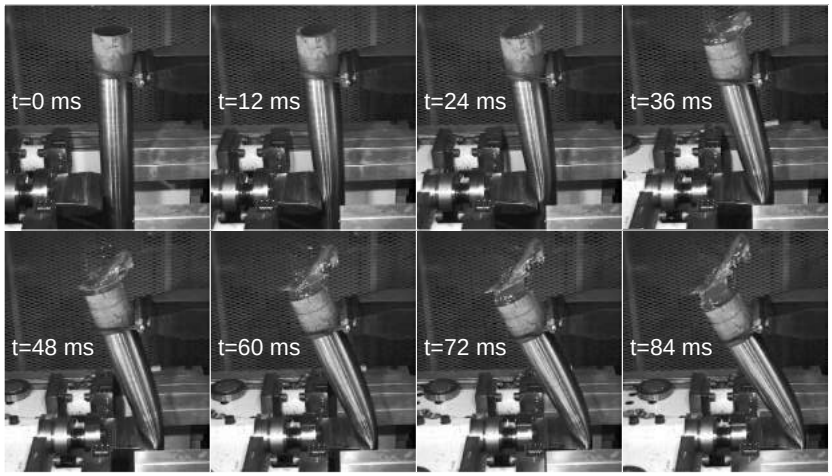

(a) *Pipe H, open, $v_0 = 5.11$ m/s, with time after impact specified in each frame*

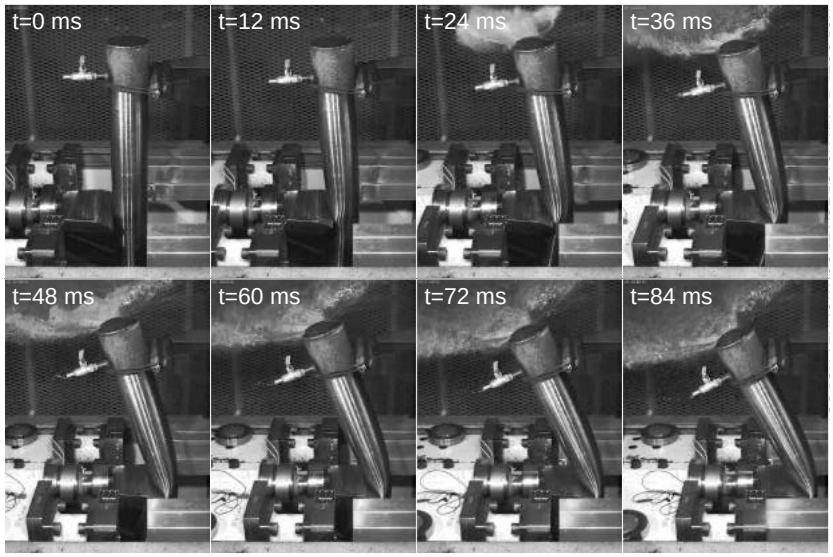

(b) *Pipe J, closed, $v_0 = 5.04$ m/s, with time after impact specified in each frame*

Figure 4.24: *Images from high speed video of impact against water filled pipes at 5.1 m/s.*

4.4 Quasi-static three-point bending

4.4.1 Setup

The setup is basically the same as for the dynamic impact tests against empty pipes, presented in Section 4.2.1. A picture of the setup can be seen in Fig. 4.25, and a sketch is shown in Fig. 4.26. The main difference lies of course in this test being quasi-static, which means that rather than delivering a certain amount of kinetic energy to the system, a prescribed deformation is attained by using a hydraulic actuator. Two tests were carried out, named pipe M and N, which received deformation equivalent to what was produced by an impact at approximately 5.1 m/s and 3.2 m/s, respectively. An Instron 1332 testing rig with 250 kN capacity has been used for the purpose, operated by deformation control in this case, and the very same indenter was taken from the trolley used in the impact experiments, and thereafter mounted in the current testing rig. The prescribed deformation was based on the results from the dynamic tests, with pipe M receiving a deformation corresponding to an impact velocity[1] of about 5.1 m/s, and N a deformation corresponding to an impact velocity of approximately 3.2 m/s. This means that pipes A, L and N are in the same batch for comparison, leaving B, K and M in the other batch.



Figure 4.25: *Picture of setup of quasi-static three-point bending tests.*

Unfortunately, the software for the rig stops logging after maximum deformation is attained, making the "rebound" during unloading unlogged. For that reason, 3D Digital Image Correlation (DIC) [72] with two cameras was used for both tests in an attempt to estimate the elastic deformation. Due to the rig's frame obscuring the view of the denting zone, the DIC cameras had to be placed quite

[1] By the same trolley (weighing 1472 kg) as used in the dynamic tests.

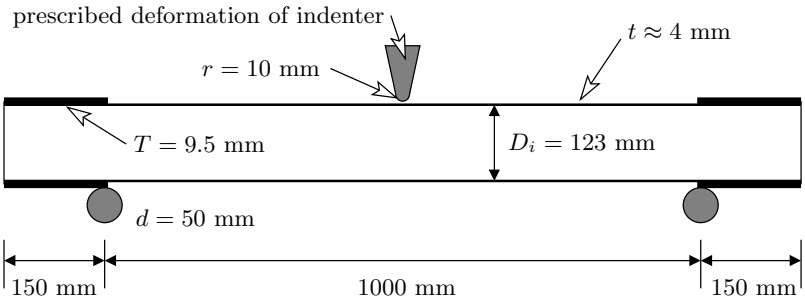

Figure 4.26: *Setup of quasi-static three-point bending tests.*

far away as seen in Fig. 4.27(a), thereby reducing the obtainable resolution and accuracy. Fig. 4.27(b) shows that a rather coarse speckled pattern for the DIC cameras was painted on the pipes due to both the distance from the specimen, and the magnitude of deformation which was to take place. The cameras have to see not only the pipe, but also the area into which they will deform.

As fracture was observed in both pipes subjected to impact only (K and L), discussed in Section 4.2.2 and 5.4, and shown in Fig. 4.15 among others, it was of great interest to see whether similar cracks would emerge while applying the same deformation quasi-statically and, if possible, assess how much influence the dynamics of the problem has on the results. The impact tests have a total time span of about 80 to 150 ms depending on the initial velocity. It is suspected that the rebound phase (only a fraction of the total time) during these tests causes the part of the pipe wall in contact with the indenter to experience a rapid reversal of the load from compression into tension, thereby initiating and propagating cracks. Naturally then, samples for investigation in microscopes were cut from both pipe M and N and investigated closely (see Chapter 5).

A quick summary of this study is listed below:

1. To use dynamic impact tests at medium and high velocity, i.e. at approximately 3.2 m/s (pipe A) and 5.1 m/s (pipe B) respectively, as basis for conducting quasi-static tests

2. To apply the dynamically obtained deformation quasi-statically with the same geometric boundary conditions

3. To check for differences in results

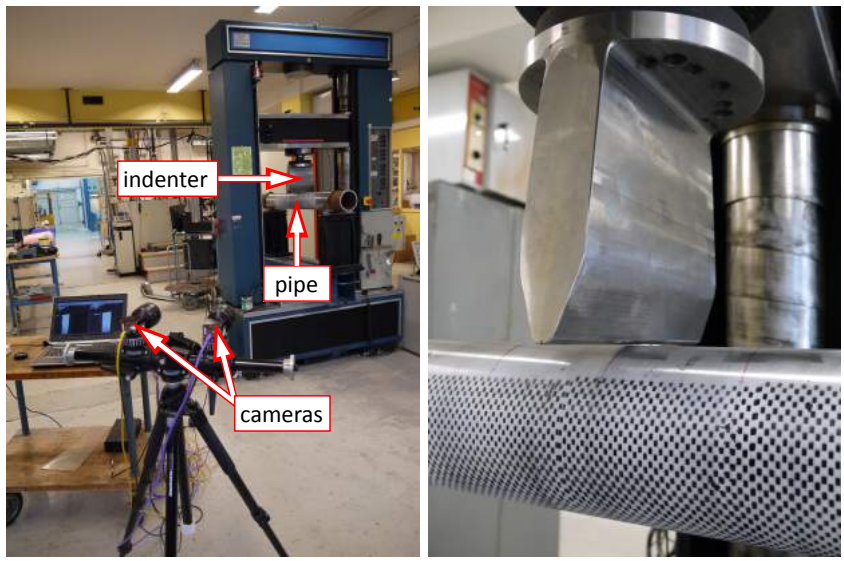

(a) *Camera position* (b) *Speckled pattern on pipe*

Figure 4.27: *DIC setup for quasi-static three-point bending tests.*

It became evident that it was not necessarily easy to obtain the exact same deformation quasi-statically as dynamically due to the fact that it was hard to estimate the amount of elastic deformation. Nevertheless, the deformation is still very similar and definitely within comparable magnitude (difference of the order of millimeters, see Table 4.4).

4.4.2 Results

Force-displacement curves are presented in Fig. 4.28, with (a) showing the "medium" deformation batch containing pipes A and N[2], and (b) the "high" deformation batch with pipe B, K and M. Firstly, it is noted that the dynamic tests generally have a higher force level throughout the test compared to their quasi-static counterparts. The peak force in test N was about 79% of the peak in test A, while test M had a peak force value 83% of the peak from test B,

[2] As previously mentioned, the load cell did not trigger when testing pipe L.

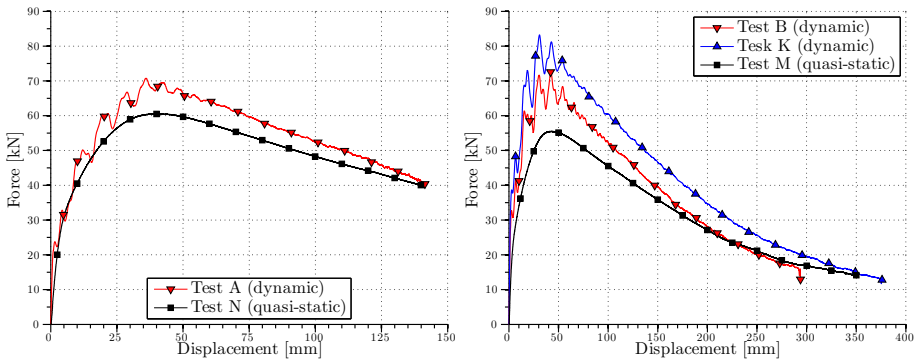

(a) *"Medium" velocity batch* (b) *"High" velocity batch*

Figure 4.28: *Force-displacement curves for dynamic vs. quasi-static tests.*

i.e. roughly 20% reduction of the peak force when going from dynamic to quasi-static. This is in accordance with expectations, as inertia forces and strain rate effects (see Section 3.4) announce their presence. In effect, this means that for a given deformation more energy is absorbed if the event is dynamic. Also, oscillations are clearly seen in the dynamic tests. As these tests take place over a small stretch of time, local contact conditions close to the load cell as well as stress waves and their possible reflections may influence the recorded force, as is evident here.

From Fig. 4.15, the fracture in pipe K is clearly visible after dynamic impact only. The framed area in Fig. 4.15(a) is zoomed in on in (b), showing the crack in plain sight. No such cracks were visible in pipe L, but internal cracks were discovered after investigating samples from the pipe in a light optical microscope (see Section 5.4 and Fig. 5.12). For that reason, it was of great interest to check pipes M and N (and M in particular due to the large deformation) for similar fracture.

To begin with, the magnitude between global and local deformation between pipes K and M was compared. These are very similar, as Figs. 4.29(a) and (b) can confirm (applicable to pipes L and N in (c) and (d) as well). The dynamically deformed pipes may have a slightly larger curvature locally, but this is difficult to quantify. More importantly, and despite similar deformation, no cracks were visible on the surface of the quasi-statically deformed pipe M. This is a very

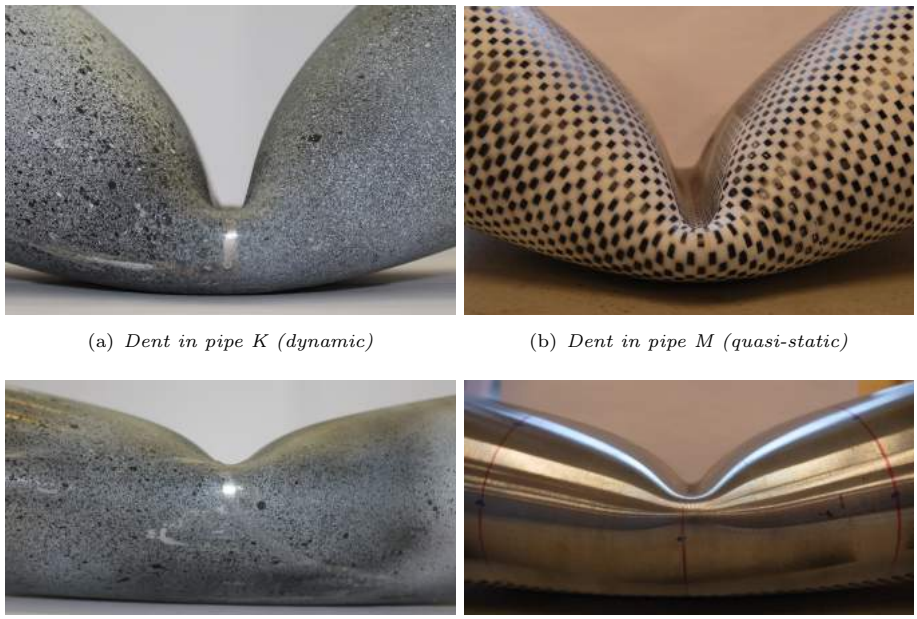

(a) *Dent in pipe K (dynamic)*

(b) *Dent in pipe M (quasi-static)*

(c) *Dent in pipe L (dynamic)*

(d) *Dent in pipe N (quasi-static)*

Figure 4.29: *Comparison of dent after (a) dynamic deformation and (b) static deformation.*

clear indication that the problem being dynamic is a crucial factor, completely in tune with established knowledge [75]. Cross-sections of pipe M and N from Fig. 4.29(b) and 4.29(d) can be seen in Fig. 4.30(a) and (b), respectively.

Doing quasi-static tests to replace dynamic tests may therefore be a directly dangerous way of conducting experiments. Also, obtaining an "equivalent static load" as a replacement for a dynamic load as suggested in NS-EN 1991-1-7 [42] and mentioned in Section 2.3, is not necessarily "equivalent" at all. So in order to obtain a meaningful equivalent static load, it must elicit the same response in the structure – which in this case appears to be, if not impossible, then very unlikely. Still, when doing simplified design calculations, one should use the energy delivered to a system as a design value rather than a static load.

The springback/rebound occuring after maximum deformation in the dynamic tests is a likely candidate to initiate the observed fracture. On the side of the



(a) *Pipe M* (b) *Pipe N*

Figure 4.30: *Cross-sections of pipe M (a) and pipe N (b).*

dent facing the indenter, the material suffers great compression during the course of deformation. In the dynamic tests, this compression is reversed into tension within a few milliseconds which is thought to be the moment when cracks are initiated. When doing this quasi-statically, this load reversal is slow and no rapid change of loading direction takes place, thereby gently unloading the pipe and hence reducing the likelyhood of fracture.

The DIC measurements were no better[3] than just measuring the final deformation after the entire test procedure, and comparing this with the maximum deformation value logged by the testing software. Regarding pipes L and N, neither showed any signs of fracture by a naked eye inspection. Pipe K is also the thicker of the lot, thereby attaining a higher peak force. Table 4.4 lists some key data from experiments on pipes A, B, K, L, M and N. Looking at the two quasi-static tests (M and N), which in principle are exactly equal to each other except the magnitude of deformation, it is observed that pipe N attains a higher peak force. This is mainly attributed to the higher average thickness, the only notable difference in initial conditions between the two tests. The statically and dynamically absorbed energies are somewhat more similar than expected. Some fraction of the initial kinetic energy in the dynamic tests necessarily contributes to accelerating the pipe, thereby increasing the force level registered by the load cell. Also, some kinetic energy is temporarily stored in the pipe during dynamic impact, and contributes to accelerating the trolley the other way after

[3]Due to the long distance to the specimen resolution was limited.

Table 4.4: *Experimental matrix for component tests for fracture investigation. See Fig. 4.10 for explanation of measurements.*

Pipe		**A**	**B**	**K**	**L**	**M**	**N**
Trolley mass	[kg]	1472	1472	1472	1472	-	-
Nose radius	[mm]	10	10	10	10	10	10
Avg. thickness	[mm]	3.89 ±0.36	3.86 ±0.34	4.12 ±0.26	4.17 ±0.36	3.74 ±0.25	3.90 ±0.26
				Test results			
Initial velocity	[m/s]	3.24	5.13	5.18	3.26	-	-
Def. rate	$[\frac{\text{mm}}{\text{min}}]$	-	-	-	-	10	10
Kin. energy	[J]	7708	19356	19750	7820	-	-
Abs. energy*	[J]	7294	11736	15167	-†	11251	6975
Peak force	[kN]	70.7	72.7	83.2	-†	55.5	60.6
w_i	[mm]	170	333	403	133	380	161
$L_{\text{N-N}}$	[mm]	1250	1104	1006	1263	1042	1249
$d_{\text{N-S}}$	[mm]	60	22	27	73	26	64
$d_{\text{E-W}}$	[mm]	180	199	202	171	202	178
α	[deg]	12	30	33	9	31	12

*Estimated by integrating the measured force-displacement curve.
†Load cell did not trigger during testing.

maximum deformation is attained. Hence, there is a discrepancy between the initial energy and the absorbed energy. A quick check shows that this difference is approximately the same as the kinetic energy of the trolley post impact. As mentioned, strain rate effects in the material can also contribute to an increased force level as indicated by the SHTB test results in Fig. 3.12.

4.5 Pipes subjected to stretching, bending and internal pressure

As this was a newfound use of a previously established rig, calibration of the sensors had to be done. This is included in Appendix E, except for two of the clinometers. In addition, a new load cell was procured for the vertical actuator. The rig was originally used for testing extruded aluminium profiles, and is thoroughly described by Clausen [69]. Nevertheless, a short description of the rig is included in the introduction to this chapter.

4.5.1 Modification of rig

To enable the rig to add an internal pressure to a pipe, some modifications were required. The mechanical modifications are described first. These mainly concern the connection between the pipe (test specimen) and horizontal actuators. Detailed drawings can be found in Appendix F.

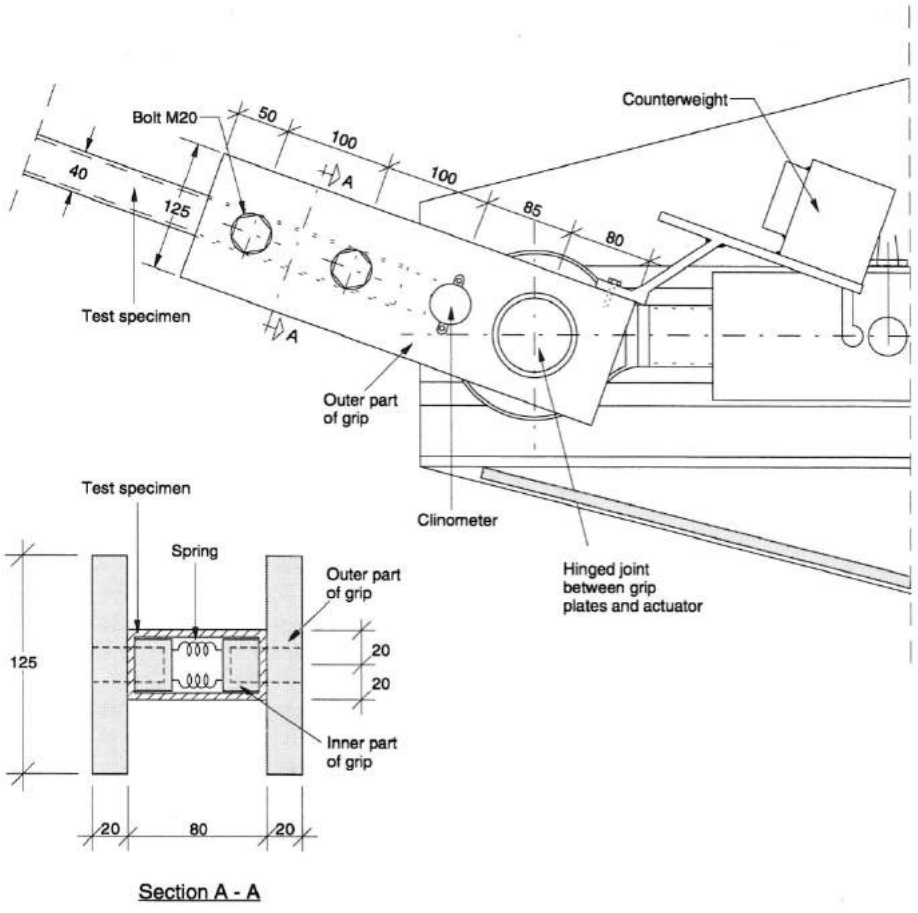

Figure 4.31: *Support for test specimen in the original setup [69], viewed from the side.*

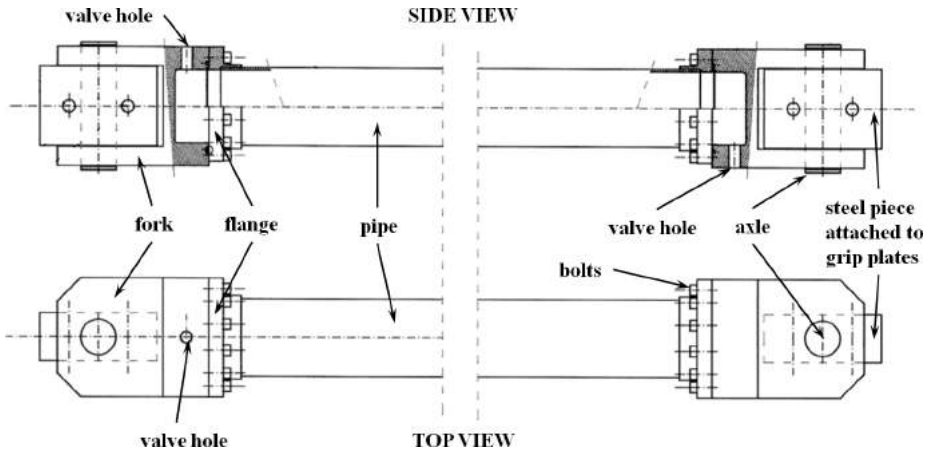

Figure 4.32: *Connection and pipe as mounted in the stretch-bending rig.*

Previously the test specimens had just been connected by bolts to grip plates attached to the actuators, able to rotate around the connection point (a hinged joint). These grip plates, referred to as "outer part of grip" in Fig. 4.31, are simply two parallel steel plates which do not make a good connection with a circular pipe. So, rather than connecting directly to the test specimen, specially designed transitions are used. These transitions are attached to the grip plates, like a test specimen would be attached in the rig's original area of application, with a massive steel piece (see Fig. F.6) fitting snugly between the grip plates.

This steel piece is in turn connected to a fork via an axle capable of rotating about the vertical axis. The forks (shown in Fig. F.5) help attach the circular geometry of a pipe to the rig, and contain threaded holes where valves for applying and controlling the pressure can be attached. Moreover, they have a large circular hole where the pipes are supposed to fit. They can not, however, be attached directly to the forks. A circular end flange, shown in Fig. F.4, is welded to each end of the pipe for a tight seal, and then bolted to the forks using 12 bolts in each end, securing another tight seal. The flanges are replaced with each pipe, while the forks remain the same for every test. An exception is made for the first series, where the pipes were delivered too long. Then the same set of flanges were used for the different pipes, which were cut shorter and welded to said flanges. Again it is referred to Appendix F for detailed drawings. An overview of the connection and the pipe is shown here in Fig. 4.32.

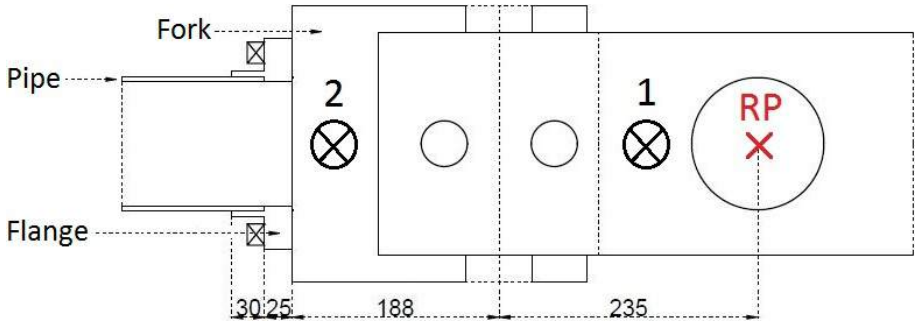

Figure 4.33: *Vertical cross-section sketch of connection between pipe and rig, including the position of the two clinometers labelled 1 (close to the rotation point) and 2 (on the forks).*

The additional connection parts are of course not rigid, other than by assumption. To gain some insight to how much, if anything, the connection itself bends when testing, two clinometers were used to measure the angles at different points. Number 1 was placed on the grip plates close to the rotation point (RP), while number 2 was located on the forks as shown in Fig. 4.33 A photograph of the fork and grip plates with the attached clinometers can be seen in Fig. 4.34. Any difference measured in angles between the two clinometers on each connection should provide some indication of the stiffness of the connection. For pipe 1, only the clinometer at the rotation point was in action, so comparative data is only available from pipe 2 and onwards.

Further, a system was designed to apply pressure to the pipes, and to keep the pressure constant throughout the test procedure. This system is shown in Fig. F.8 in Appendix F. It basically consists of a pump delivering pressure to the system at one end, and a reservoir into which displaced water can flow as the pipe's volume changes. When the desired pressure (100 Bar in this case) is attained by the pump a valve is closed, leaving the system at this pressure. As the pipe deforms, water flows into an accumulator acting as a reservoir with a water/gas mixture. The change of volume in the pipe is relatively small compared to the volume of the accumulator, thereby keeping the pressure approximately constant in the system as the volume change in the gas within the accumulator only causes a negligible increase in pressure. A pump can be mounted to the other end of the accumulator to supply additional pressure if it should drop.

This design is made to keep the pressure constant regardless of positive or neg-

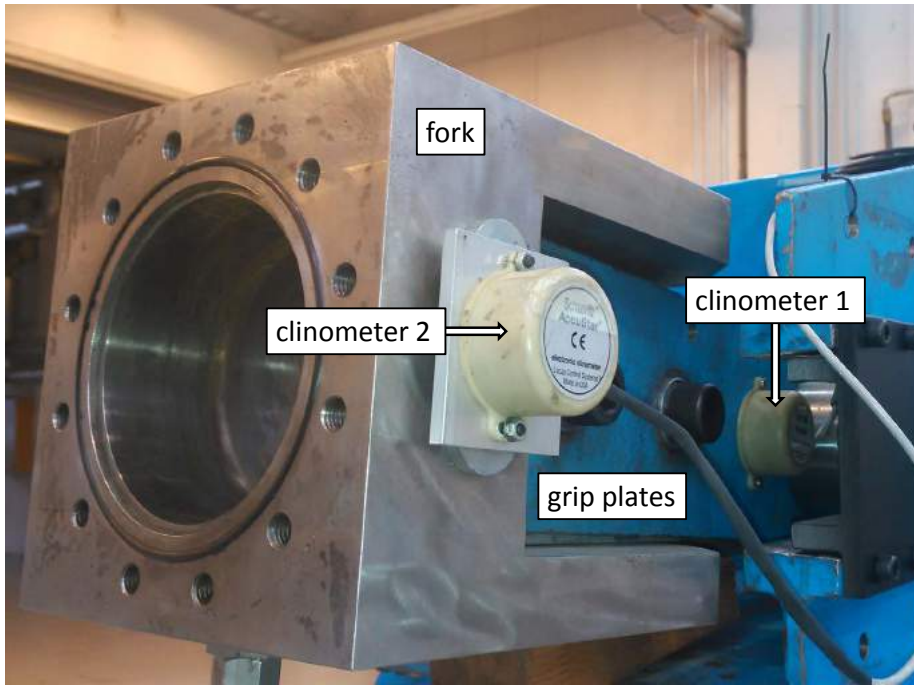

Figure 4.34: *Photograph of connection with clinometers attached. See Fig. 4.33 for a schematic sketch.*

ative volume change. In the present case, the volume change is purely negative and a simpler solution was opted for. The pump delivers the pressure as described above, but is left running during testing. At the other end, a pressure valve which opens automatically at approximately 100 Bar was mounted. With the pump constantly keeping 100 Bar, and the valve letting water out as the pressure rises, a good and simple system was derived to keep the pressure constant during testing. Fig. 4.35(a) shows the pump that was used (a Hydratron pump with a maximum capacity of 1000 Bar). The valve limiting the pressure to about 100 Bar is indicated by an arrow in Fig. 4.35(b). During testing, the pressure was constantly monitored by a pressure gauge. These tests had to be performed quasi-statically, as the dynamic tests' duration is about one tenth of a second. The change of volume in the pipe during this time is too large for the current pressure system to cope with, thereby resulting in an undesired pressure

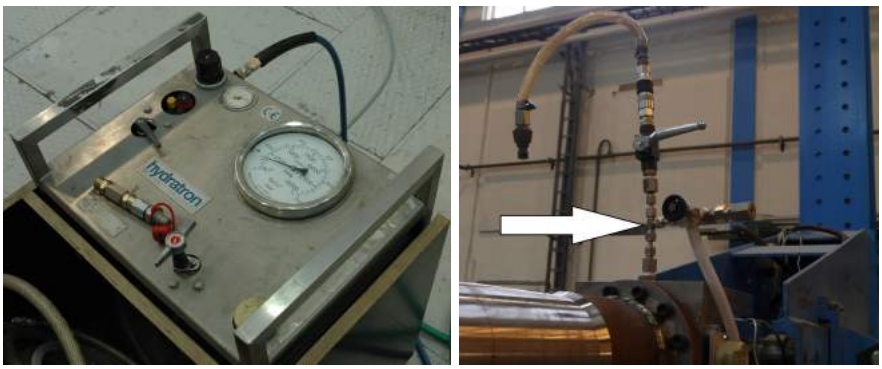

(a) *Pump* (b) *Valve*

Figure 4.35: *Pump and valve keeping the inner pressure constant.*

build-up if the tests were conducted dynamically. It is assumed that in a long offshore pipeline (tens to hundreds of kilometers), the volume change due to a dent only causes a negligible increase of pressure (if anything increase at all).

4.5.2 Experimental programme

Digital Image Correlation (DIC) has been used for all the tests. For the first series, four cameras were mounted on tripods and placed a little distance away from the rig and test specimen (see Fig. 4.36(a)). In the next two series, a custom made frame was attached to the bottom of the indenter, making two cameras follow the deformation and thereby acquire a better resolution. A picture of the setup can be seen in Fig. 4.36(b).

Series 1

Three main series of experiments were conducted in this rig, the first being a test series to uncover potential pitfalls or problems with the setup. Already when mounting the first pipe it was discovered that the three initial pipes were cut too long. This was ameliorated by cutting the excess length and welding the remainder of the pipe to the end pieces, which connect the pipes to the rig so this should not exert any significant influence on the test results.

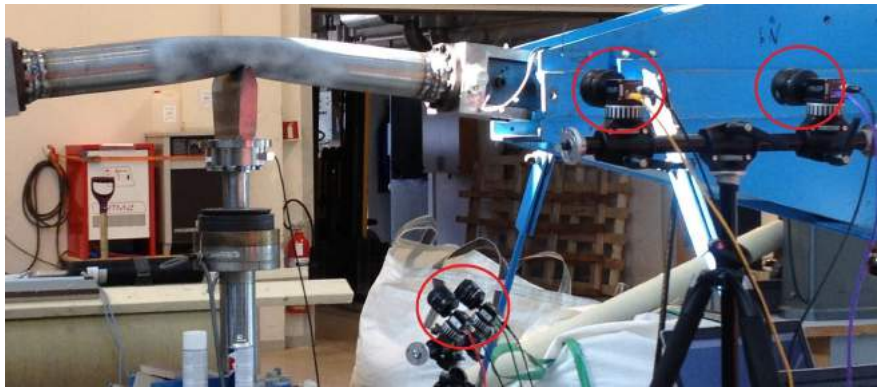

(a) *DIC for series 1*



(b) *DIC for series 2 and 3*

Figure 4.36: *Pictures of DIC setup used with stretch-bending rig.*

In any case, the first series of three unpressurised pipes, ingeniously labelled 1, 2 and 3, were tested with transverse deformation combined with various axial loads:

Pipe 1: Transverse displacement (300 mm at 25 mm/min) with no axial load applied by the horizontal actuators.

Pipe 2: Transverse displacement (200 mm at 25 mm/min) with constant axial load of 55 kN.



Figure 4.37: *Example of test component mounted in stretch-bending rig, with the arrows signifying the direction of the applied loads.*

Pipe 3: Transverse displacement (200 mm at 25 mm/min) with with linearly increasing axial load ($0 \rightarrow 55$ kN).

This setup was followed somewhat loosely, with modifications made underways. The rig with a test component mounted is shown in Fig. 4.37, along with arrows indicating the load directions. The value 55 kN was estimated from a finite element simulation[4] of a longer continuous pipeline using beam elements.

After transversely deforming the first pipe to 283 mm, it was deemed sufficient to limit the deformation to 200 mm for the rest of the pipes. A good amount of plastic deformation takes place at 200 mm, while the cross-section avoids getting completely crushed. All these pipes were stretched horizontally after removing the vertical indenter, making the test procedure as listed below:

1. Application of constant horizontal load (if relevant).
2. (a) Application of transverse displacement.
   (b) Application of linearly increasing horizontal load (if relevant).
3. (a) Locking of horizontal actuators.
   (b) Removal of vertical indenter.
   (c) Release of horizontal actuators.

[4]Simulation not discussed in detail.

4. Stretching of pipes.

Issues with the horizontal load cell resulted in an offset of magnitude 43.9 kN in the linearly increasing axial load, which will be discussed in the results section. Further, these pipes were cut and examined in a light optical microscope.

The first series was a sort of trial series, and very useful in terms of establishing a strict testing procedure.

Series 2

The next batch of tests – now with pipes of correct length and a properly calibrated and prepared rig – went rather smoothly, with a continuation of the labelling system derived above, extending it to pipes 4, 5 and 6, making this series as following:

Pipe 4: Transverse displacement (200 mm at 25 mm/min) with no axial load.

Pipe 5: Transverse displacement (200 mm at 25 mm/min) with constant axial load of 55 kN.

Pipe 6: Transverse displacement (200 mm at 25 mm/min) with with linearly increasing axial load ($0 \rightarrow 55$ kN).

None of these pipes were stretched afterwards and no pressure was applied, resulting in the following test procedure:

1. Application of constant horizontal load (if relevant).
2. (a) Application of transverse displacement.
   (b) Application of linearly increasing horizontal load (if relevant).
3. (a) Locking of horizontal actuators.
   (b) Removal of vertical indenter.
   (c) Release of horizontal actuators.

This setup was followed more strictly than for the first series, and the stretching was omitted so the pipes could be compared directly with the pressurised pipes discussed below.

Series 3

The third and final series is basically the same as series 2, with the exception of an additional pipe for testing the rig's pressure application system. This pipe was lathed incorrectly at the workshop, resulting in a thickness of approximately 3 mm rather than 4 mm, making it a perfect candidate for testing the rig with internal pressure applied to the pipe. Increasing the numbering sequence from above, the third series becomes

Pipe 7: Transverse displacement (200 mm at 25 mm/min) with no axial load and $p = 100$ Bar, reduced thickness of 3 mm.

Pipe 8: Transverse displacement (200 mm at 25 mm/min) with no axial load and $p = 100$ Bar.

Pipe 9: Transverse displacement (200 mm at 25 mm/min) with constant axial load of 55 kN and $p = 100$ Bar.

Pipe 10: Transverse displacement (200 mm at 25 mm/min) with with linearly increasing axial load ($0 \rightarrow 55$ kN) and $p = 100$ Bar.

The test process is also pretty much the same as series 2, with addition of inner pressure p of 100 Bar.

1. (a) Application of inner pressure.

   (b) Application of constant horizontal load (if relevant).

2. (a) Application of transverse displacement.

   (b) Application of linearly increasing horizontal load (if relevant).

3. (a) Locking of horizontal actuators.

   (b) Removal of vertical indenter.

   (c) Release of horizontal actuators.

Stretching is not conducted here either, making pipes subjected to the same load procedure with and without internal pressure available for direct comparison.

4.5.3 Results

Series 1

Results in terms of force, displacement, etc. are presented herein. Based on an intuitive engineering judgment, one would expect the resulting vertical force to be lowest when there is no axial load (pipe 1), highest when there is a constant axial load (pipe 2), and in between for the linearly increasing axial load (pipe 3). This is, however, not the case for these three tests due to an error in the horizontal load cell.

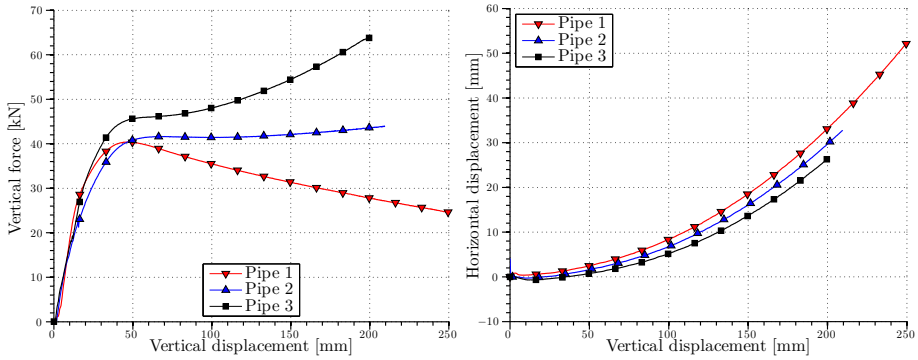

(a) *Vertical force* (b) *Horizontal displacement*

Figure 4.38: *Data (as function of vertical displacement) from the first series of pipes tested in stretch-bending rig.*

Fig. 4.38(a) clearly shows that pipe 3 experiences the highest vertical force, despite having a linearly increasing axial load. Pipe 3 also has the lowest horizontal displacement as seen in Fig. 4.38(b), indicating that it is somewhat held back to a larger extent than the other two. The vertical load cell was naturally displacement controlled, and from the calibration procedure its measurements were deemed accurate. Upon closer investigation of the horizontal actuators, it was discovered that in the beginning of the experiment on pipe 3, these actuators had made a sudden, discontinuous jump in the applied force due to an error in the load cell mounted. This jump was found to be approximately 43.9 kN and was added to the data initially registered in the log files from the test, making the force increase from 43.9 kN to 101.9 kN rather than the intended 0 kN

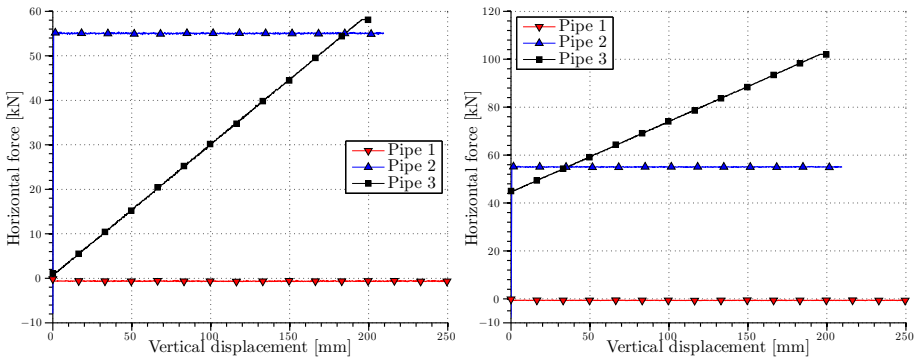

(a) *Intended* (b) *Actual*

Figure 4.39: *Horzontal force vs. vertical displacement from the first series of pipes tested in stretch-bending rig.*

to 55 kN. Fig. 4.39(a) shows the intended horizontal force as a function of the vertical displacement, taken directly from the log files; the corrected horizontal force for pipe 3 is plotted in (b). It should be noted that pipe 1 still has a marginal axial force which stems from the resistance from pulling the actuators out. This will also be present in subsequent tests with "zero" axial force.

Taking this into consideration, the vertical force as depicted in Fig. 4.38(a) makes more sense – a higher tensile axial force should stiffen the system and lead to a larger force in the vertical load cell for a given deformation. In this respect the tests can be said to have been a success as they uncovered a few problems with the equipment, but for comparing the effect of different axial loads they are not ideal. Nevertheless, some insight was gained. It is observed that without any axial force, the initial peak is the maximum force throughout the experiment. With a constant axial force, it tends to increase somewhat even after the initial peak despite having a slight "dip". This is expected for the case with linearly increasing load as well, perhaps with a more defined dip in the force level and an end point close to that of the case with constant axial load since the applied vertical displacement and horizontal load will be the same at the end of the step. It will of course not be exactly the same, as plastic deformation is path-dependent.

The angles at the forks and the rotation points were measured by the clinome-

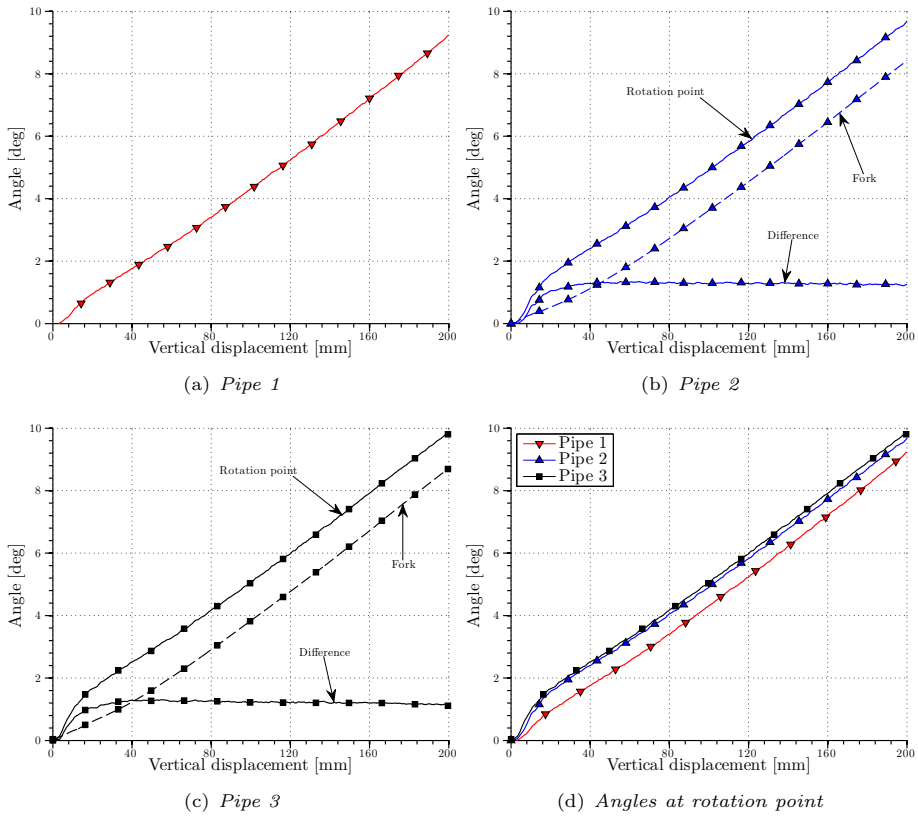

(a) *Pipe 1* (b) *Pipe 2*

(c) *Pipe 3* (d) *Angles at rotation point*

Figure 4.40: *Angles at the rotations points and at the forks during bending of test series 1, with the difference between the angles as well.*

ters. By using the fact that a simply supported beam under bending has zero rotation at midpoint and maximum rotation at the end points, it was expected that if any difference was present the largest value would be at the rotation points. This was also the case as seen in Fig. 4.40, which shows angle at the forks (dashed line) and at the rotation points as well as the difference between them. The plotted values are the average values between one side and the other. As seen, the difference is according to expectations and increases mostly during the initial denting phase of the experiments, and remains somewhat constant

(slightly decreasing) at about 1.3 degrees for pipe 2 and 1.2 degrees for pipe 3. This is not ideal, as the connection should be as rigid as possible. The inside surfaces of the grip plates were roughened in an attempt to create more friction for the subsequent tests, and thereby a stiffer connection.

For pipe 1, only the clinometers at the rotation points were active during testing, so any difference between angles in this test is not registered which is evident from Fig. 4.40(a). Nevertheless, the angles at the rotation points were compared between the three pipes in Fig. 4.40(d). Here, pipe 1 stands out in having an almost perfectly linear increase during testing (the linear increase continues beyond 200 mm vertical displacement).

Pipes 2 and 3 both have very similar development in the angle at the rotation points, with a steeper inclination of the curve in the beginning compared to pipe 1. This is probably due to the applied axial load for pipes 2 and 3, thus providing a stiffer system. When testing series 2 it will be interesting to see how a linearly increasing axial load affects this, as the load wil be small in the beginning of the test. Recall that an erroneous offset of 43.9 kN was applied to pipe 3 in series 1.

These three pipes were stretched as well. The horizontal actuators were locked upon reaching maximum vertical displacement, and the vertical indenter was then removed followed by unloading the axial force, allowing the stretch phase to commence. As the horizontal deformation differ between the three pipes after bending (see Fig. 4.38(b)), different force-displacement curves are expected. Larger axial forces applied during bending naturally means smaller initial horizontal displacement when stretching is applied, meaning that a direct comparison may not be entirely representative. When plotting the stretch step the force-displcement curves' initial point was located at the origin, and the results are in accordance with expectations as seen in Fig. 4.41(a).

Fig. 4.41(b) shows the angles at the rotation point, and they have quite different starting points due to the different transverse displacement during bending. For that reason, a direct comparison is not justified. As mentioned in Section 4.5.2 above, this series was used to establish a more rigorous testing procedure, so these results are not necessarily the best (or even good).

Samples from these three pipes were cut from the dented area and investigated in a light optical microscope, the results of which can be seen in Section 5.6. The strething part was omitted entirely for the subsequent series, as comparison of local deformation after combined stretching and bending only (with and without

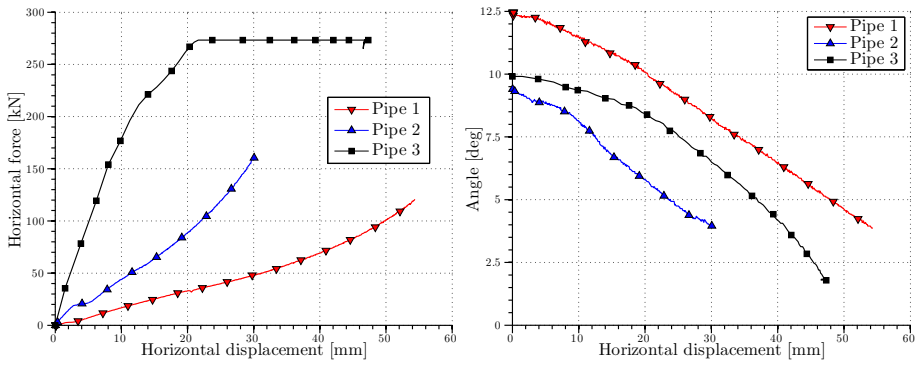

(a) *Horizontal force* (b) *Angles at rotation point*

Figure 4.41: *Horizontal force (a) and angle at rotation point (b) during stretching of test series 1.*

internal pressure) was of greatest interest. Some key parameters from the test are listed in Table 4.5 at the end of the section, along with data from series 2 and 3 for comparison.

Regarding the DIC measurements, the setup in Fig. 4.36(a) positioned the cameras too far away to obtain a reasonable accuracy. For that reason, none of the DIC data logged for this series is presented.

Series 2

For series 2 the same data has been registered, and the setup of the test progression was followed strictly. The malfunctioning load cell was now replaced, and the insides of the grip plates were roughened to increase friction.

Now the force-displacement curves (see Fig. 4.42(a)) are in accordance with the initial expectations, with the test with constant axial force being the stiffest (pipe 5). It is also observed that the test with linearly increasing axial load (pipe 6) ends on a point close to the end point of pipe 5's force-displacement curve. The horizontal force is now also as intended, and shown in Fig. 4.42(b).

Looking at the angles measured at the rotation points and the forks and the difference between them, all shown in Figs. 4.43(a)-(c), it is clear that the con-

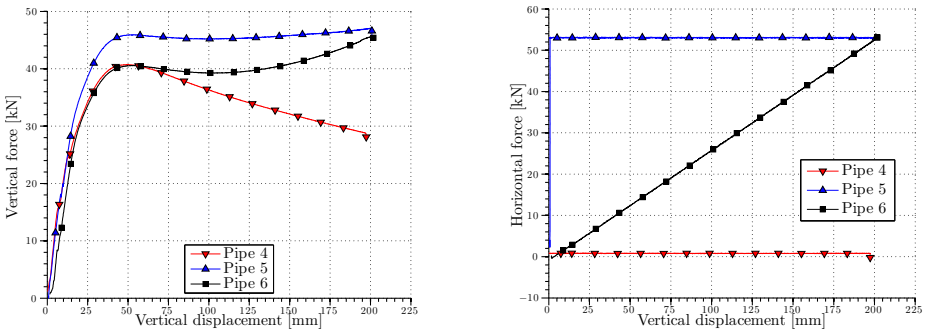

(a) *Vertical force* (b) *Horizontal force*

Figure 4.42: *Force-displacement curves from the second series of pipes tested in stretch-bending rig.*

nection behaves as desired, i.e. approximately rigidly. The dashed lines represent the rotation at the forks and the solid line the rotation close to the rotation points. There is only a marginal difference in rotation, a few tenths of a degree, which is within acceptable margins. Even when comparing the angles at the rotation point between the three tests there seems to be little or no difference as seen in Fig. 4.43(d). This means that the steeper inclination of the angle in pipes 2 and 3 in Fig. 4.40(d) compared to pipe 1 is not entirely attributable to the present axial force.

For series 2 some decent DIC measurements were obtained. Pipe 4 is the exception, but was a useful experience in terms of how to position and focus the cameras in subsequent tests. This is why pipe 5 and 6 both got decent data, as mentioned. Strain data is shown in Fig. 4.44, taken at five different steps during the course of deformation; at the beginning, after 50 mm vertical deformation, 100 mm, 150 mm and 200 mm. What can be seen is that the in-plane strain measurements are at most in the higher end of the 20%'s. The resolution acquired for pipe 6 was much better compared to pipe 5, and should provide more accurate results.

Both data sets for the strains are of the same order, which corresponds well with the physcial examination of the pipes after testing. Unfortunately, issues with the light, or more specifically, shadows, prohibited what would have been an almost perfect set of data from being obtained for pipe 6. Also, for small defor-

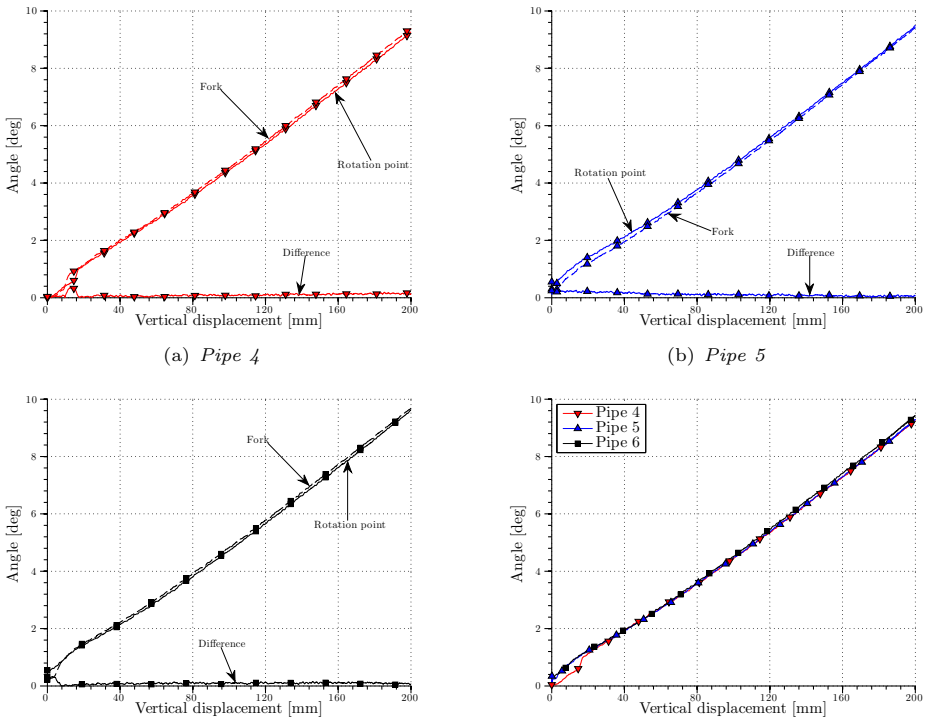

(a) *Pipe 4*

(b) *Pipe 5*

(c) *Pipe 6*

(d) *Rotation point*

Figure 4.43: *Angles at the rotations points and at the forks during bending of test series 2, with the difference between the angles as well.*

mations the noise can have a noticeable presence, as seen in the 50 mm frames. As this is still a technique under development, one should not pay too much attention to the specific numerical values obtained, but rather the general picture of the deformation and perhaps the values relative from test to test (given that the resolution and accuracy in the raw data are comparable). Data such as this can also be useful for comparison against numerically obtained results. Especially in explicit analyses where no equilibrium iterations are performed, some experimental data to verify the simulations' accuracy (at least within the same order of magnitude) can be essential at times. DIC will be discussed in more detail later (see section 4.6).

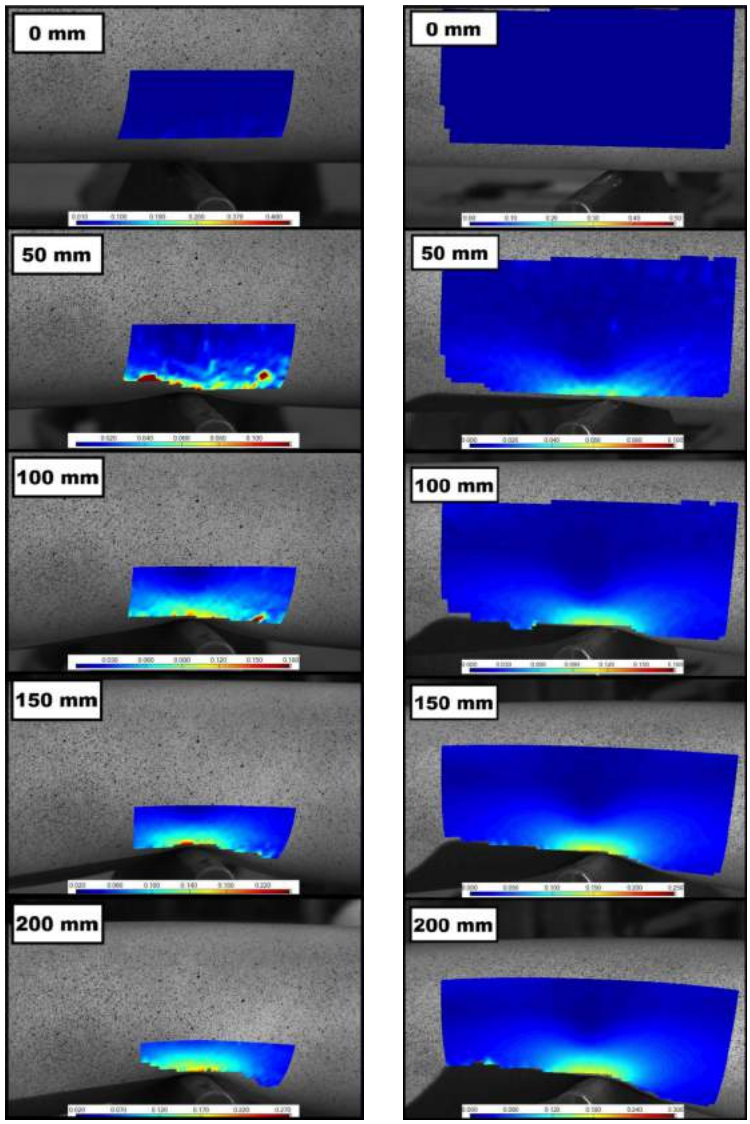

(a) *Pipe 5* (b) *Pipe 6*

Figure 4.44: *DIC measurements of pipes 5 and 6, showing the strain levels at the surface.*

Series 3

Pipe 7 was the first to be tested, as it was erroneously lathed down to 3 mm rather than 4 mm. It proved to be quite a useful exercise, as it revealed that the system with pressurised water was left completely closed, allowing pressure to build significantly during testing. The test was stopped and the pressure released. Next, the necessary changes were made and pipe 7 was tested further to check that the system funtioned properly, which it did.

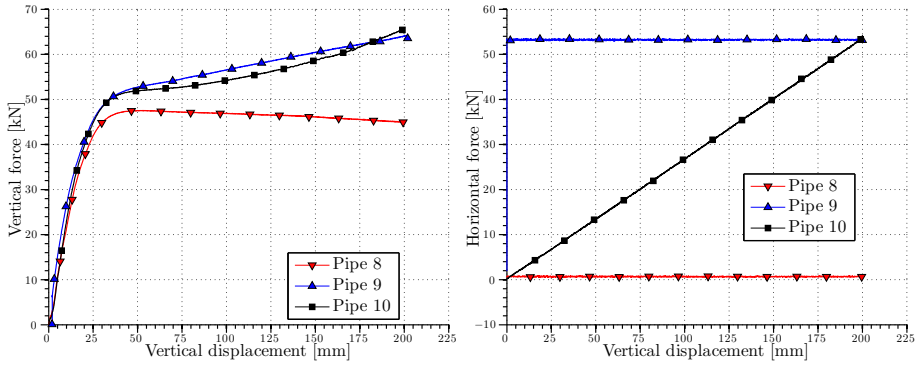

(a) *Vertical force* (b) *Horizontal force*

Figure 4.45: *Force-displacement curves from the third series of pipes tested in stretch-bending rig.*

Moving on, the results from pipes 8, 9 and 10 are largely in accordance with expectations. From Fig. 4.45(a) it is seen that pipe 10 has the largest force despite having a linearly increasing axial load. This time the load cell is correctly calibrated, and this difference can be traced to pipe 10 having a higher average thickness. Pipe 8 has the lowest general force level as no axial load was present, and it has the lowest pipe wall thickness as well. Fig. 4.45(b) shows that the horizontal forces are as prescribed. For pipe 8 the axial force is slightly above zero, which is the force required to pull the horizontal actuators out. Again the difference in angles between the rotation point and the fork is very small, and no plot is included to illustrate this point as it would be almost identical to Fig. 4.43.

Due to the addition of internal pressure of 100 Bar, the general force level is higher as the system is stiffened by said pressure. This is well illustrated in

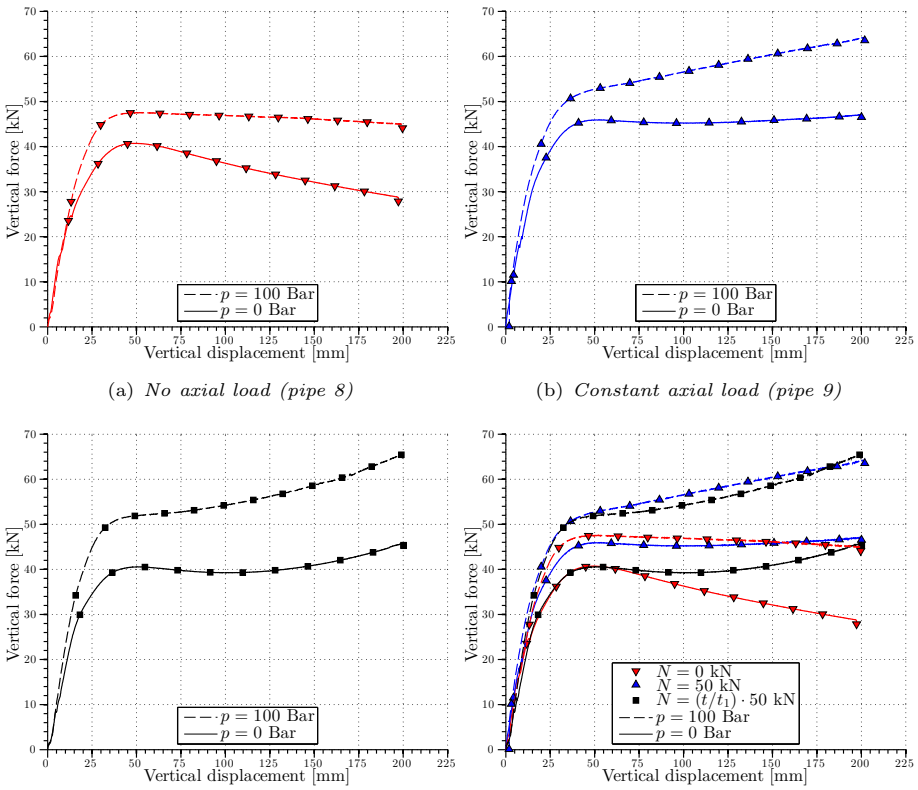

(a) *No axial load (pipe 8)*

(b) *Constant axial load (pipe 9)*

(c) *Linearly increasing axial load (pipe 10)*

(d) *Combined*

Figure 4.46: *Comparison of vertical force-displacement curves with and without inner pressure of 100 Bar, and with different axial loads.*

Fig. 4.46, where the force level in the pressurised tests are consistently above the corresponding tests without pressure. In practical terms this means that a given kinetic energy in form of an impact should produce less deformation when internal pressure is present. One should, however, be careful not to conclude too hastily, as dynamic effects may combine with pressure effects to create something unforeseen.

During and after the test procedure, the pipes' mode of deformation was disct-

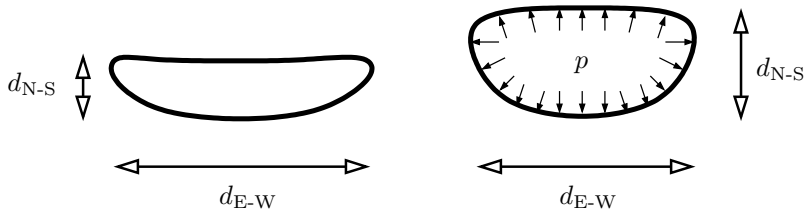

Figure 4.47: *Sketch of typical outline of deformed cross-section at midpoint for pipes without internal pressure (left) and with internal pressure (right), not to scale.*

inctly different with and without pressure. While no significant effect was found between the three axial boundary conditions, pressure has a most notable effect as sketched in Fig. 4.47. Without pressure, the cross-section at midpoint is much more compressed for the same level of global deformation. The internal pressure resists the cross-sectional deformation, in accordance with expectations and with previous experiments by Jones and Birch [13] as well as numerical simulations [32], some of which are presented in Chapter 7. Comparing $d_{\text{N-S}}$ and $d_{\text{E-W}}$ shows that the effect is relatively large. The same tendencies were observed in the closed water-filled pipes in Section 4.3. Unfortunately, the measurements for final deformation of pipe 9 is not accurate, once again due to a bug in the loading programme of the rig. After the test had run its course (and flawlessly at that), the horizontal actuators had a seizure and applied a compressive force oscillating around 100 kN thereby causing a deformation not directly comparable to the other tests. Upon investigating the pipe, a crack was discovered in the dent of this particular pipe. Some key results for all pipes 1-10 are listed in Table 4.5.

Also, the DIC measurements were quite good and a few words will be added on this and DIC in general. When carrying out the DIC analysis, the surface of the pipe is divided into a mesh of rectangular elements, in which the in-plane strains are calculated. Then by assuming constant volume during plastic deformation, the out-of-plane strain component is calculated. From this the equivalent strain, plotted in Figs. 4.48 and 4.49, is calculated.

Two different meshes have been used in the DIC software for pipe 5, shown in Fig. 4.44(a) and Fig. 4.48. A comparison of the magnitude of equivalent strain between loading with and without internal pressure is shown in the aforementioned figures. Fig. 4.48 gives a comparison between cases with constant



(a) *Legend for equivalent plastic strain*

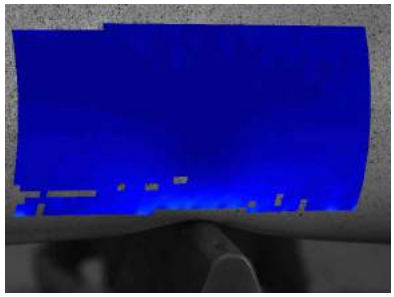

(b) *0 Bar, 67 mm (pipe 5)*

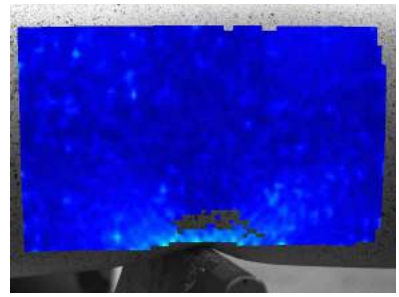

(c) *100 Bar, 67 mm (pipe 9)*

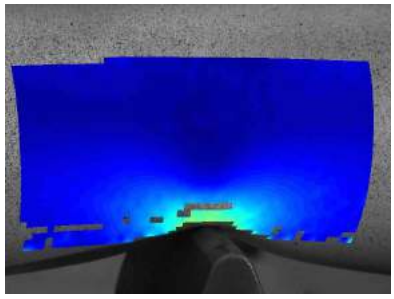

(d) *0 Bar, 134 mm (pipe 5)*

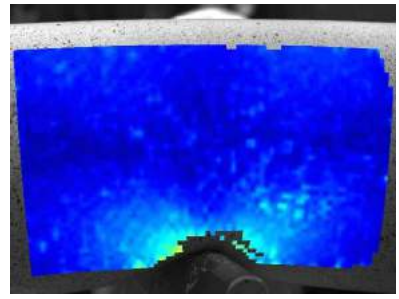

(e) *100 Bar, 134 mm (pipe 9)*

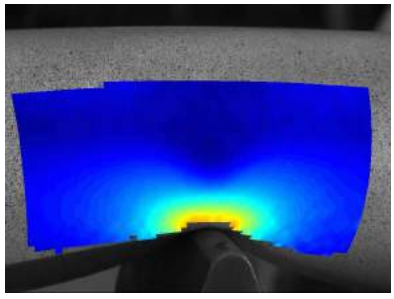

(f) *0 Bar, 200 mm (pipe 5)*

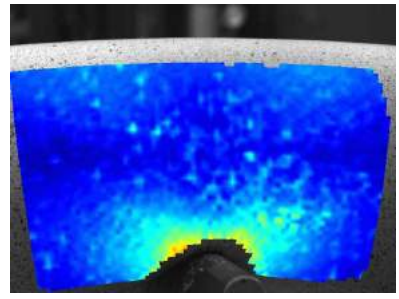

(g) *100 Bar, 200 mm (pipe 9)*

Figure 4.48: *Comparison of equivalent strain on the surface for various vertical displacements, without internal pressure (pipe5, left column) and with internal pressure (pipe 9, right column) for pipes with constant axial load.*



(a) *Legend for equivalent plastic strain*

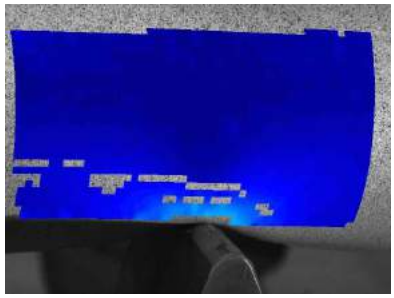

(b) *0 Bar, 67 mm (pipe 6)*

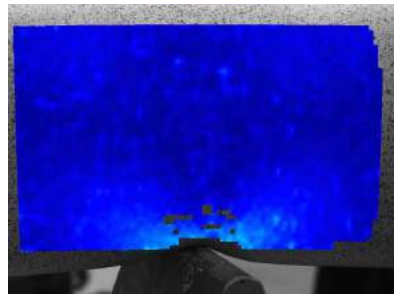

(c) *100 Bar, 67 mm (pipe 10)*

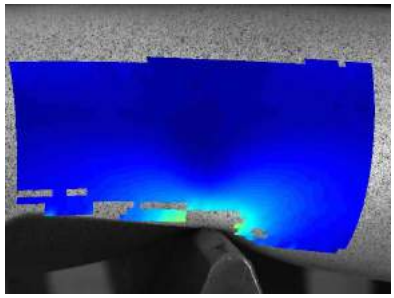

(d) *0 Bar, 134 mm (pipe 6)*

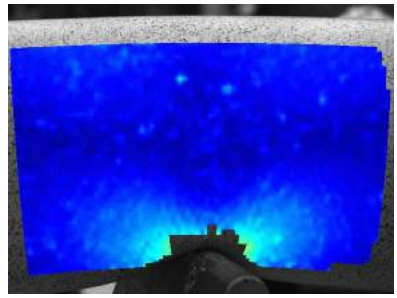

(e) *100 Bar, 134 mm (pipe 10)*

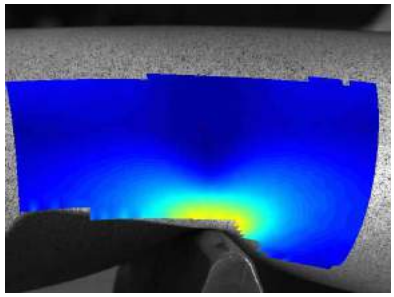

(f) *0 Bar, 200 mm (pipe 6)*

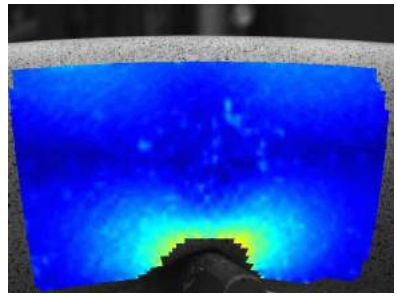

(g) *100 Bar, 200 mm (pipe 10)*

Figure 4.49: *Comparison of equivalent strain on the surface for various vertical displacements, without internal pressure (pipe 6, left column) and with internal pressure (pipe 10, right column) for pipes with linearly increasing axial load*

horizontal load (pipe 5 and 9), while Fig. 4.49 gives a comparison when the axial load is increasing linearly. Unfortunately the DIC results were not sufficiently accurate for the pipe 4 experiment due to the positioning of the cameras. Thus, comparison between unpressurised and pressurised pipes in the case of zero axial loading is omitted.

In any case, the differences in strain between $p = 0$ Bar and $p = 100$ Bar were not significant in any of the two cases. The margin of error is likely greater than any difference noted. That is not to say that the deformation is the same, which it is clearly not. This is shown more clearly later in Fig. 4.50. Based on this observation made directly after testing, some difference in strain was indeed expected. However, the most critical areas likely to contain differences are covered by the indenter, making data from these areas inaccessible by construction of the test setup. As indicated, absence of measured difference does not imply the absence of any difference. It is most likely down to the quality of the DIC analysis in this particular setup.

The process of correlating pictures to a strain measurement is highly sensitive to variations in light. As can be seen, a lot of noise is present in many of the pictures. Such noise can also lead to element distortion and miscalculation of the strains in the DIC software. Distorted elements have thus been deleted during the analysis. A shaded area is also present on the left hand side in two of the series (pipes 5 and 6), making it impossible to calculate the strain field in these areas.

4.6 Discussion

A wide array of full-scale tests have been performed on X65 steel pipes with a D/t-ratio of approximately 30. Dynamic impact followed by a quasi-static stretch step (pipes A-F) always produced fracture in the pipes as depicted in Fig. 4.12, but at very different load levels depending on the deformation (i.e. the impact velocity) from the impact step. In the study by Manes et al. [5] only one test displayed fracture, but these were quasi-static and conducted on strips of a pipe rather than a full cross-section. The peak force during impact was fairly constant regardless of impact velocity due to the shift of deformation mode from local to global, and the large mass ratio between the pipe and the trolley. Global deformation was naturally very dependent on the initial velocity since more kinetic energy has to be absorbed. So were the force-displacement curves

Table 4.5: *Test matrix of pipes subjected to combined quasi-static stretching and bending. See Figs. 4.10 and 4.47 for legends and illustrations.*

Pipe		**1**	**2**	**3**	**4**	**5**	**6**	**7**	**8**	**9**	**10**
Nose radius	[mm]	10	10	10	10	10	10	10	10	10	10
Transverse def.	[mm]	300	200	200	200	200	200	200	200	200	200
Thickness	[mm]	4.15	3.92	4.02	4.19	4.19	4.06	2.98	4.08	3.95	4.13
Nom. pressure	[Bar]	∼1	∼1	∼1	∼1	∼1	∼1	100	100	100	100
Axial load	[kN]	0	55 const.	0-55 linear	0	55 const.	0-55 linear	0	0	55 const.	0-55 linear
					Test results						
Transverse def.	[mm]	283	208	199	197	201	202	200	200	200	200
w_i	[mm]	-	-	-	120	120	122	-	117	159*	113
Horizontal def.	[mm]	68	33	26	31	24	25	-	32	27	26
$L_{\text{N-N}}$	[mm]	-	-	-	1200	1197	1198	-	1200	1168*	1200
Force at peak	[kN]	40.4	41.6	46.0	40.7	45.9	40.6	-	47.5	52.0	51.0
Max. vert. force	[kN]	40.4	44.0	63.8	40.7	47.0	45.7	-	47.5	64.1	65.4
Angle at RP	[deg]	13.7	10.2	9.9	8.7	8.5	8.7	-	9.6	11.6*	9.2
Angle at fork	[deg]	-	8.9	8.7	8.8	8.4	8.7	-	9.3	11.4*	8.9
Avg. pressure	[Bar]	∼1	∼1	∼1	∼1	∼1	∼1	100+†	103	103	101
$d_{\text{N-S}}$	[mm]	-	-	-	84	89	87	-	98	90*	97
$d_{\text{E-W}}$	[mm]	-	-	-	164	165	164	-	152	164*	152

* Post-test geometric measurements are inaccurate due to an erroneously applied compressive force.
† Increased from 100 Bar to about 130 Bar due to the system being completely closed.

from the subsequent stretching as well.

Cracks were discovered even after impact only – by the naked eye in pipe K after impact at about 5.1 m/s and later in the microscope in pipe L after impact at about 3.2 m/s (see Fig. 4.15 for pipe K and Fig. 5.12 in Section 5.4 for pipe L). The crack emerging in pipe K extended through 75% of the pipe's wall thickness. It was, as indicated, visible at the surface, but internal cracks of the same magnitude were also detected. At first the lower velocities did not seem to produce such fracture, but after a more thorough investigation in the microscope (see Section 5.4), cracks were indeed found without any visible signs on the surface. In the area where the cracks seem to initiate, the material appears to suffer compression to a great extent before the load is reversed, hence the motivation for the notched compression-tension tests. This is written in anticipation of Chapter 5, which discusses the topic in further detail.

Adding water to the pipes seemed to have a negligible effect, unless the pipe was closed (see Fig. 4.18). Closed water-filled pipes generally had a higher average force level during impact, and the post-impact deformation showed a more localised dent along the longitudinal direction of the pipe. This conforms with findings by Jones and Birch [13] and by Shah [26]. Unfortunately the weld attaching the end cap on pipe J ruptured during impact at 5.1 m/s, but the data up to that point should be accurate.

As mentioned, fracture was initiated in both pipe K and L after impact only. Next, deformation to the same level was applied quasi-statically to investigate the influence of dynamics. From a hands-on examination of the pipes tested quasi-statically, M and N, no fracture was visible on the surface. This supports the hypothesis that fracture initiates during the rapid springback after maximum deformation is attained in the dynamic tests. Fracture in pipes M and N is investigated in more detail in Section 5.4.

Further quasi-static tests were conducted, this time involving combined stretching and bending, with and without an internal pressure of 100 Bar. The pipes were deformed transversely to a prescribed value, while different axial loads were applied simultaneously. When a dent exceeds 5% of the outer diameter, the load bearing capacity reduces quickly [51]. In terms of final deformation, it was hard to distinguish between the three different tensile axial loads, whereas a compressive axial load can reduce the lateral collapse load significantly [76]. The transverse force-displacement curve was more affected by the axial load (see e.g. Fig. 4.42), which when increased lead to a stiffer response. The same applies to the effect of internal pressure; a stiffer response was registered. Now

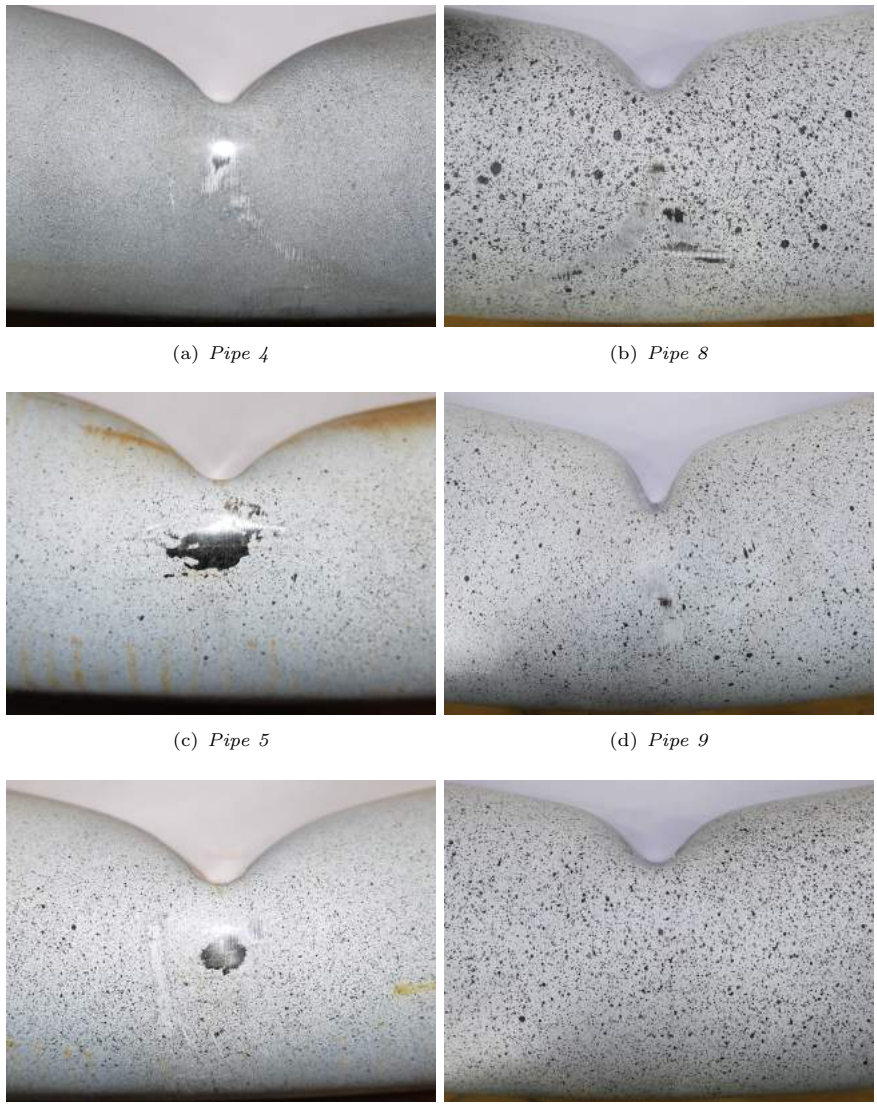

(a) *Pipe 4* (b) *Pipe 8*

(c) *Pipe 5* (d) *Pipe 9*

(e) *Pipe 6* (f) *Pipe 10*

Figure 4.50: *Local deformation in dent without pressure (left column) and with 100 Bar pressure (right column).*

a pronounced difference in cross-sectional deformation was noted as well, with the pressurised pipe having a much rounder final deformation as illustrated in Fig. 4.47, again in accordance with other works [13, 26, 77]. Pictures of this observation are shown in Fig. 4.50, where the left column shows the dent in the pipe after being deformed without pressure, and the right column with pressure. As observed, the "diameter" from top to bottom ($d_{\text{N-S}}$ from Fig. 4.47) is greater in magnitude when pressure is included. This may of course alter not only the magnitude of strains but also the strain path. Note that pipe 9, part (d) in Fig. 4.50, was compressed by an unintentional axial load after the test, resulting in a final deformation (even sharper dent) not representative for the described load sequence. For the quasi-static tests, it is important to remember that a certain deformation was prescribed, while in the dynamic tests a certain kinetic energy was delivered to the system.

Fracture in the pipes is discussed in substantial detail in Chapter 5 and in [29].

Chapter 5

Metallurgical investigation

After conducting the pipe impact experiments in Chapter 4, cracks always emerged during the stretch phase. Even the impact alone was enough to generate a crack clearly visible to the naked eye as seen in Fig. 4.15 and reported in Ref. [29]. Fracture surfaces from both component tests and some of the material tests from Chapter 3 have been investigated using a light optical microscope and a scanning electron microscope (SEM). The metallurgical study has been carried out in cooperation with Dr. Ida Westermann at SINTEF Materials and Chemistry.

5.1 Overview

As this chapter contains a lot of images from the microscopes, a succinct overview of the metallurgical work done is presented first.

To begin with, the material itself is investigated in its undeformed state. An energy-dispersive X-ray spectroscopy (EDS) analysis of the particles and matrix is also conducted. Secondly, pipes subjected to the entire load sequence of impact and stretching are examined under the microscope. They showed both ductile and brittle fracture surfaces. Next, two pipes that have been through the impact phase only are examined. A macroscopic crack through 75% of the

Table 5.1: *Overview of metallurgical investigations.*

Section	Description	Figure(s)
5.2	Investigation of undeformed material	3.3, 5.1-5.3
5.3	Pipes after impact and stretching	4.12, 5.4-5.8
5.4	Pipes after impact only	4.29, 5.9-5.12
5.5	Pipes after quasi-static bending	4.29, 5.13-5.14
5.6	Pipes after combined stretching and bending	5.15
5.7	Specimens after compression-tension	5.16-5.23
5.8	Specimens after compression only	5.25-5.27

wall thickness was found on the pipe impacted at the highest impact velocity. For the medium velocity, an internal crack not visible on the surface was discovered. Moving on, two pipes were deformed quasi-statically to the same levels of deformation attained with the higher and medium impact velocities to investigate whether similar fracture arised as in the dynamic impact tests. The material tests (notched compression-tension tests) from Section 3.6 are next under the microscope. All three specimen geometries from that section were used. Table 5.1 gives an overview of the metallurgical study.

5.2 Material

The material's mechanical properties are chartered in Chapter 3. Here, the microstructure, chemical composition and particle distribution are examined. As stated in Section 3.1, and also available in the material certificate in Appendix B, the matrix contains mainly Fe, with Mn and C as secondary constituents. The material has a ferritic grain structure, very similar in both the radial and longitudinal directions (see Fig. 3.3), with grain size ≤ 10 μm. Again it is referred to Appendix B for further details on the chemical composition of the material.

To reiterate, two main types of particles were identified; spherical particles and angular particles, examples of which are shown in Fig. 5.1. The spherical particles are quite numerous, and inhomogeneously distributed in the matrix. They also have two components, seen divided by a clearly visible line in Fig. 5.1(a), along with an indicating arrow. From the EDS analysis these particles are composed of Al_2O_3 (left part of particle in Fig. 5.1(a) and EDS in Fig. 5.3(b)) and CaS (right part of particle in Fig. 5.1(a) and EDS in Fig. 5.3(a)). Calcium is added to reduce aluminium oxide, thereby resulting in spherical particles. They

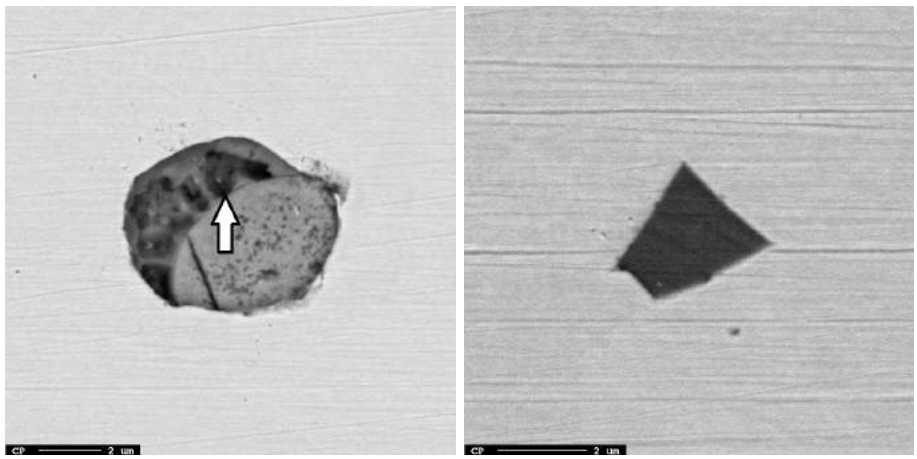

(a) *Spherical particle* (b) *Angular particle*

Figure 5.1: *Images of particles found in the material.*

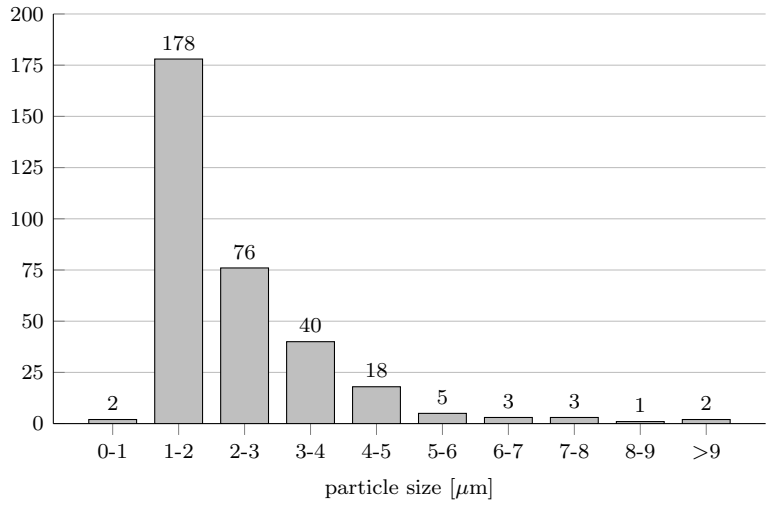

Figure 5.2: *Particle distribution of spherical particles based on 13 images, with the particle size in μm on the abscissa and the particle count on the ordinate.*

vary in size from around 1 μm to 10 μm and are bonded poorly with the matrix, thus serving as likely sites for nucleation of voids. Based on 13 different images of the material, these particles have been counted and lumped in different size groups. A total of 328 particles were noted, and the distribution is shown in Fig. 5.2. The area fraction of particles was estimated to approximately 0.05%.

The angular particles have a much stronger bonding with the matrix. Their size is typically 5 μm, and the EDS analysis (see Fig. 5.3(c)) shows that they contain mainly Ti, and C or N (inconclusive) second. These particles have not been found in relation to fracture and are less numerous, and are for that reason not further elaborated on.

5.3 Impact and stretching

Firstly, the fracture surfaces from the pipes[1] impacted and thereafter stretched were investigated to see what kind of fracture mechanisms that were present after the entire loading sequence described in Section 4.2. Visible fracture surfaces from the pipes were inspected, so the samples were taken from the pipes' most deformed area. Two main types of macroscopic cracks were present after impact and stretching; cracks on the pipe's surface (Fig. 5.4(a)) and through-thickness cracks (Fig. 5.4(b)). The through-thickness cracks have three different zones as mentioned earlier:

- Zone 1 is mainly exposed to large compressive strain before suffering tension, first during springback directly after the impact and then by stretching of the pipe.
- Zone 2 largely undergoes tension and shear in the impact and stretch phases.
- Zone 3 is the transition zone between the two aforementioned zones.

Fig. 5.5 shows the fracture surface of zone 1, exhibiting a classic textbook example of cleavage fracture [78]. These cracks were the first to appear during stretching of pipe B, almost immediately after applying the load. Although a cleavage fracture surface is called brittle, it may be preceded by large scale plasticity. As plastic flow is quite constricted in the dent of the pipe, this may

[1] Limited to pipes A and B as they had both main categories of cracks; surface cracks (pipe A) and through-thickness cracks (pipe B).

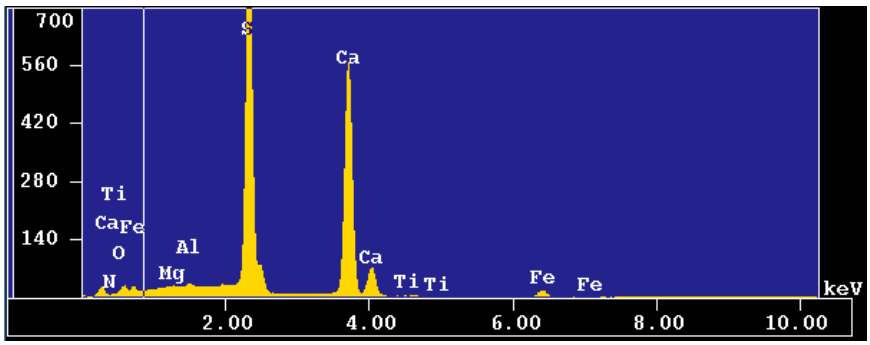

(a) *Left part of spherical particle*

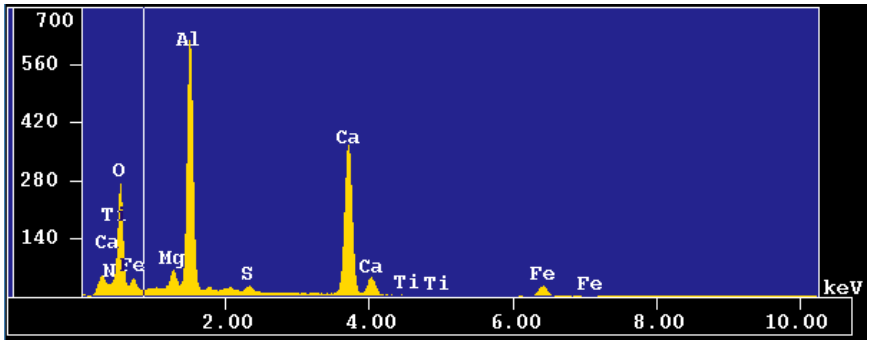

(b) *Right part of spherical particle*

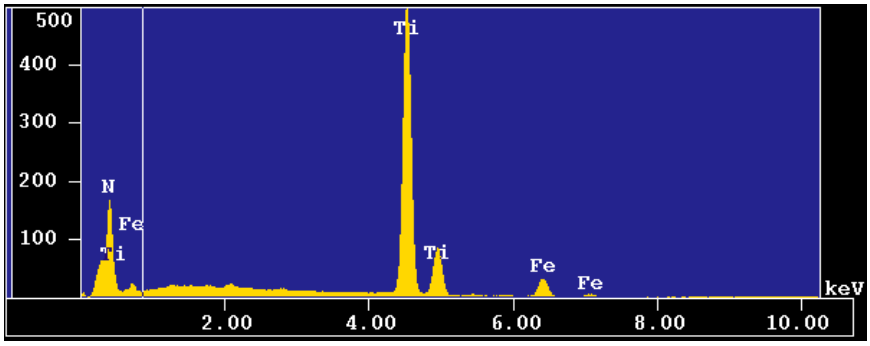

(c) *Angular particle*

Figure 5.3: *Energy-dispersive X-ray spectroscopy (EDS) of particles.*

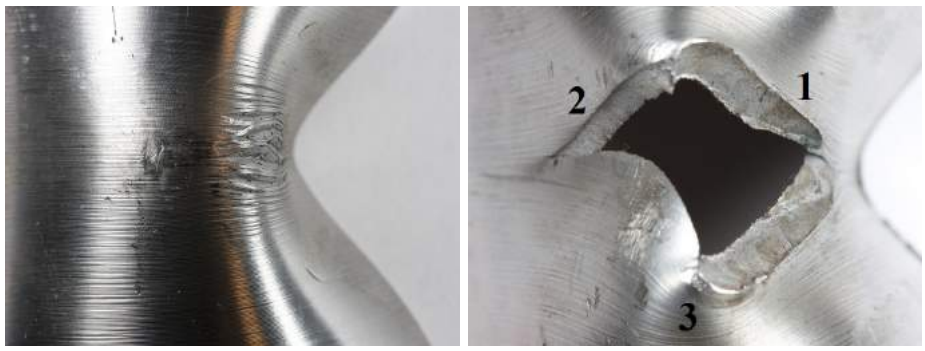

(a) *Pipe A, surface cracks* (b) *Pipe B, through-thickness cracks*

Figure 5.4: *Two main types of cracks arised in the pipes from the load sequence of impact and stretching, (a) surface cracks and (b) through-thickness cracks. Impact direction is from the right.*

contribute to a brittle behaviour when the load is reversed. Restrained plastic flow reduces the number of available slip system in the material, increasing the probability of cleavage fracture. Zone 2, seen in Fig. 5.6, has a fracture surface of a completely different character – a mixture of small and large dimples along with spherical particles (typically located at the bottom of the dimples) are observed, thus indicating a ductile fracture. This kind of fracture surface typically arises from nucleation, growth and coalescence of voids in the matrix of the material as discussed heavily in the literature (see e.g. [64, 65, 79–81]). This part of the crack propagated at a later stage of the stretch part of the experiments.

The final zone is a ductile "ridge" (framed by a black rectangle in Fig. 5.7(a)) in the transition from the ductile to the cleavage fracture surface. Large dimples with particles were observed along this edge, seen in Fig. 5.7(b). Cracked particles were also present, examplified by Fig. 5.7(c). A close up of one of the dimples with particles is offered in Fig. 5.7(d). It appears that voids initiate around the spherical particles (sometimes cracked), which bonded poorly with the matrix, thus providing conditions likely to produce fracture.

In addition to the through-thickness cracks, there were also surface cracks which were dominantly present in pipe A. These fracture surfaces' characteristics were very similar in nature to that of zone 2 from pipe B, i.e. ductile fracture as seen

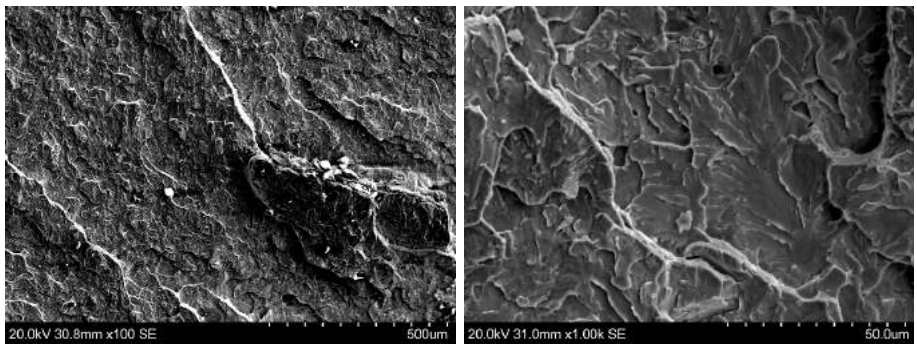

(a) $\times 100$ (b) $\times 1000$

Figure 5.5: *Cleavage fracture, typical of zone 1 from pipe B.*

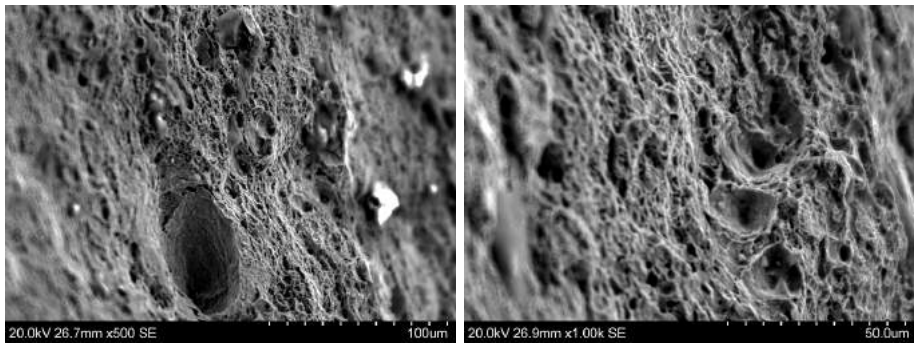

(a) $\times 500$ (b) $\times 1000$

Figure 5.6: *Ductile fracture, typical of zone 2 from pipe B.*

in Fig. 5.6. Further inspection in the SEM revealed areas with directional voids, typical of tearing. An overview is shown in Fig. 5.8(a), while Fig. 5.8(b) shows a close-up of a few directional pores. In pipe A, cracks became visible at the surface at a much higher load level compared to pipe B. This is expected as pipe B was more heavily deformed from the impact.

After seeing that cracks became visible almost immediately after initiating stretching in pipe B ($\leq$ 10 kN), and at a much later stage in pipe A (around

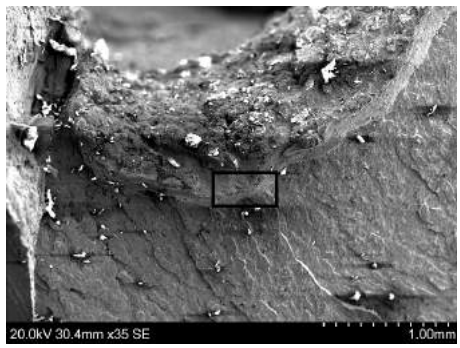

(a) *Ductile "ridge" (zone 3), ×35*

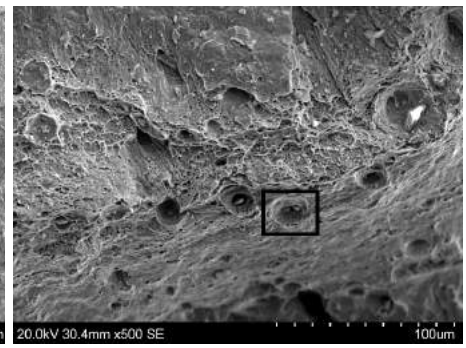

(b) *Large voids framed in (a), ×500*

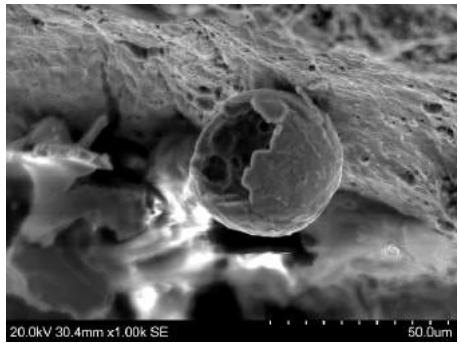

(c) *Cracked particle, ×1000*

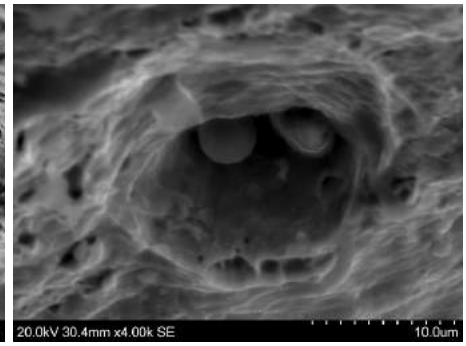

(d) *Void with particles framed in (b), ×4000*

Figure 5.7: *The transition between zones 1 and 2 in pipe B presents itself as a ductile "ridge" shown in (a), with large dimples including particles (see (b)). Some particles were observed to be cracked like in (c), and are important in nucleating voids as they are often seen at the bottom of such voids (d).*

100 kN), it was decided to investigate pipes subjected to the impact part only.

5.4 Impact only

Two additional pipes were subjected to impact, one in the upper end of the velocity spectrum (pipe K, 5.18 m/s) and one in the middle (pipe L, 3.26 m/s),

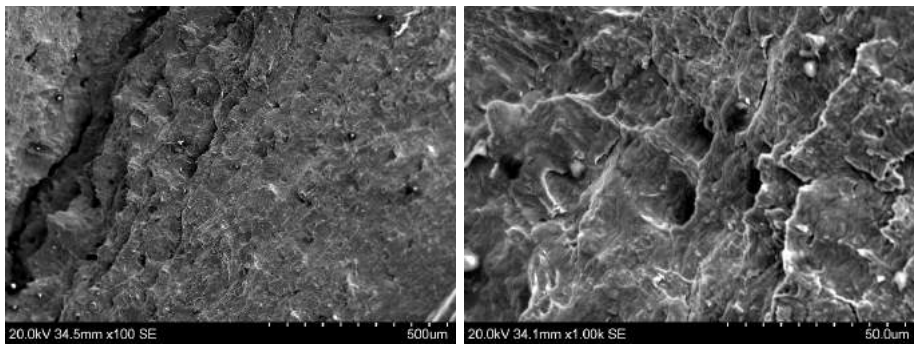

(a) *Fracture surface from A, ×100* (b) *Pores with directional tearing, ×500*

Figure 5.8: *Fracture surface from pipe A, ductile tearing with directional voids.*

corresponding to pipe B and A, respectively. These were not exposed to stretching, thus allowing investigation of potential damage after impact only. Samples were once again cut from the dent where the trolley hit the pipes, more specifically where cracks emerged during stretching.

Macroscopic inspections of pipe K revealed a clearly visible crack in the dent where the nose of the trolley hit. The crack ran through 75% of the pipe wall's thickness (pictured in Fig. 5.9(a)). This crack probably emerged during the springback after the impact. Investigation of the microstructure in the optical microscope disclosed a mixed fracture type (intercrystalline and transcrystalline) after large deformations (Fig. 5.9(c)). Further investigation showed that the grains were much less deformed at the end of the crack tip, which can be seen in Fig. 5.9(e). This indicates that the outer side of the pipe wall facing the impactor suffers more deformation compared to the inner side.

A cross-section of the pipe at the outer edge of the dent created by the trolley's nose, where the crack no longer was visible on the surface, was also investigated. Also this internal crack was found through 75% of the wall thickness, as seen in Fig. 5.9(b). This crack did not connect with any surface cracks, and may therefore be difficult to detect when inspecting a pipeline after an impact event. An intercrystalline fracture was found, with large deformation of the material's microstructure on the compressive side, shown in Fig. 5.9(d). Near the crack tip, however, the microstructure was once again much less deformed as seen in Fig. 5.9(f). This is due to the rather large difference in deformation between

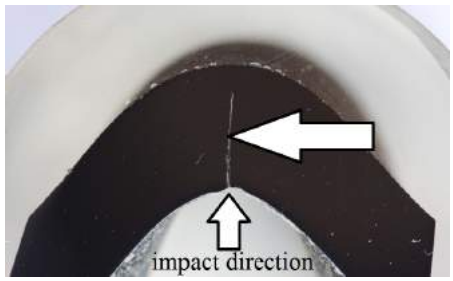

(a) *External crack*



(b) *Internal crack*

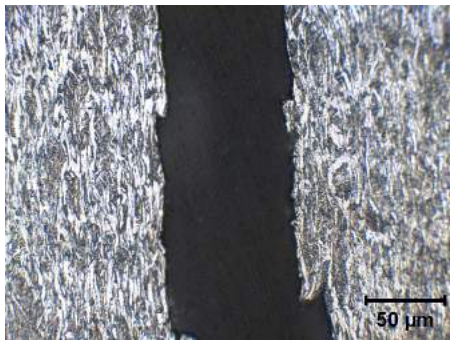

(c) *Fracture at ×50*

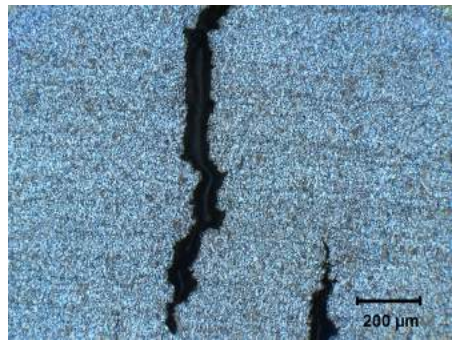

(d) *Internal fracture at ×10*

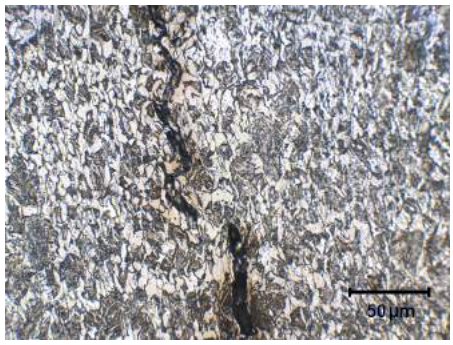

(e) *Crack tip at ×50*

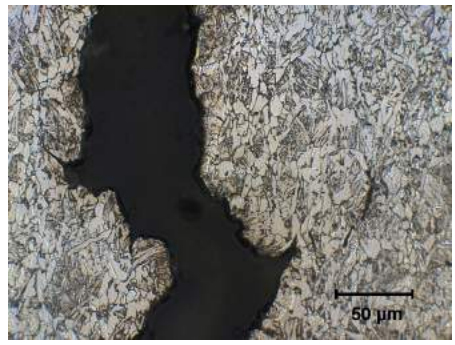

(f) *Microstructure around internal crack×50*

Figure 5.9: *Crack visible externally ((a), (c) and (e)) and internally ((b), (d) and (f)) found in pipe K subjected to impact at 5.18 m/s. SEM investigation of the fracture surface indicated by the horizontal arrow in (a) suggested a cleavage fracture (see Fig. 5.10).*

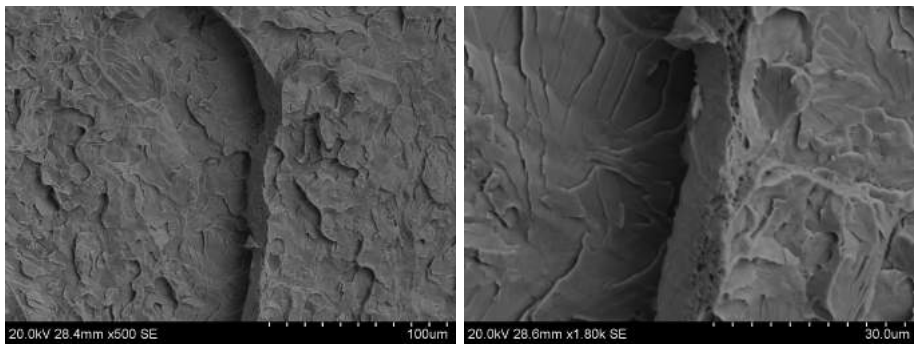

(a) $\times 500$ (b) $\times 1800$

Figure 5.10: *SEM images of fracture surface in pipe K, indicated by the horizontal arrow in Fig. 5.9(a).*

the inner and outer part of the pipe wall (the outer being most deformed). The fracture surfaces from this test (indicated by the horizontal arrow in Fig. 5.9(a)) were also investigated in the SEM, revealing a brittle cleavage fracture as seen in Fig. 5.10, very similar to Fig. 5.5. Small zones of ductile fracture are visible, an example of which is seen in Fig. 5.10(b), typically located at the transition area between two planes. As the crack did not run entirely through the pipe wall, some light bending of the specimens was necessary to separate the pieces and the make the fracture surfaces available for investigation. The small ductile zones mentioned are very likely caused by this light bending operation.

The pipe impacted at 3.26 m/s showed no immediate tendency to crack initiation, neither by visual inspection nor in the optical microscope. The surface was intact and no internal cracks were seen. Four samples were cut from the impacted area, all of which are shown in Fig. 5.11.

Sample 1 showed no signs of fracture at any magnification. Investigation of the second sample, shown in Fig. 5.12(a), revealed a latent crack approximately 300 μm long in the middle of the material thickness, where the traces from lathing the pipe exert little or no influence. This is one reason why these traces are thought to be of minor importance for fracture initiation. The crack was found around the grain and phase boundaries, and can be very hard to detect. Deformation of the microstructure appears to be relatively small (compare Fig. 5.12(a) to Fig. 3.3). Surface cracks of about 50 μm and below were

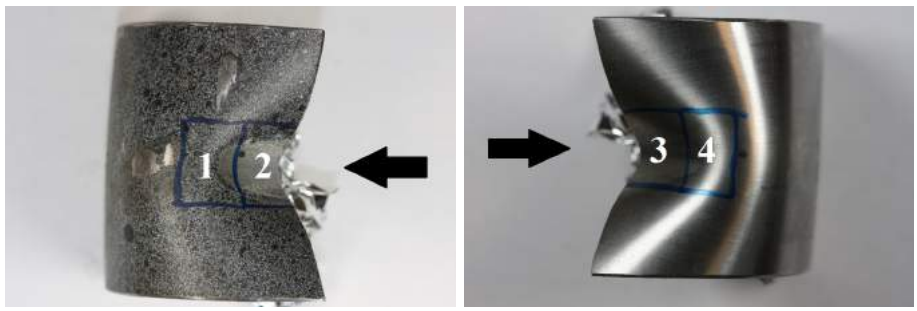

(a) *Overview of samples 1 and 2* (b) *Overview of samples 3 and 4*

Figure 5.11: *Overview of samples taken from pipe L subjected to impact at 3.26 m/s. The arrows point to the side of the sample which was inspected in the microscope.*

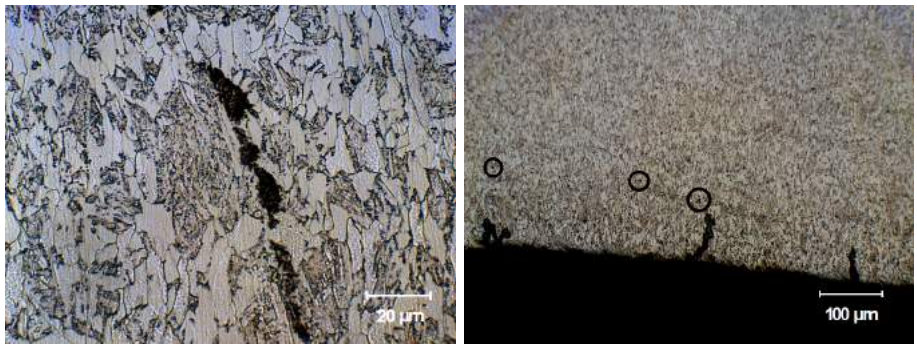

(a) *Crack from sample 2, ×100* (b) *Surface cracks in sample 3, ×20*

Figure 5.12: *Internal crack (a) and surface cracks (b) found in samples taken from pipe L subjected to impact at 3.26 m/s.*

observed at the impact side in sample 3, as shown in Fig. 5.12(b). These cracks may be initiated by the traces arising from the milling process, causing stress concentrations. Hard phases (examples are circled in Fig. 5.12(b)) can be seen near the surface in connection with the cracks, but as this investigation is conducted on a 2D plane, it is difficult to say with certainty whether or not such phases are significant with respect to crack initiation.

In sample 4 internal cracks were found along grain boundaries, with lengths

of approximately 20 μm. All the cracks were located towards the impact side of the pipe wall (but did not extend to the surface), where the magnitude of deformation is highest.

5.5 Quasi-static three-point bending

The cracks arising after impact only are thought to emerge mainly during the springback phase of the impact. To check this conjecture, quasi-static three point bending tests were carried out on the exact same setup as the dynamic tests from the kicking machine. Two pipes were tested, one corresponding to "high" impact velocity (pipe M) and the other to "medium" (pipe N), which means about 5.1 m/s and 3.2 m/s.

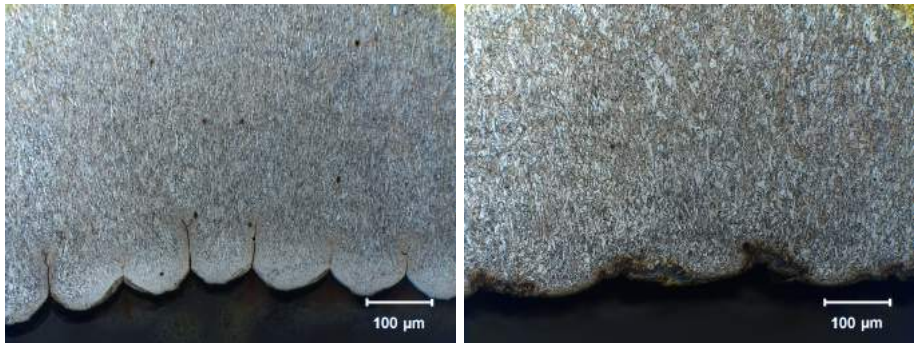

(a) *Pipe M* ×20 (b) *Pipe N* ×20

Figure 5.13: *Compressive side of pipe wall in the dent caused by quasi-static deformation.*

The pipes were loaded quasi-statically to the same deformation as attained in the dynamic tests. Section 4.4 offers a more detailed description of the experimental setup.

From a first-hand visual inspection, the pipes did not appear to suffer any cracks extending to the surface. This was confirmed by an examination using a light optical microscope. In the compressed zone of the dent some tendencies to crack initiation were observed in pipe M due to the lathing grooves on the pipe surface as seen in Fig. 5.13(a), where the microstructure is heavily compressed (applies

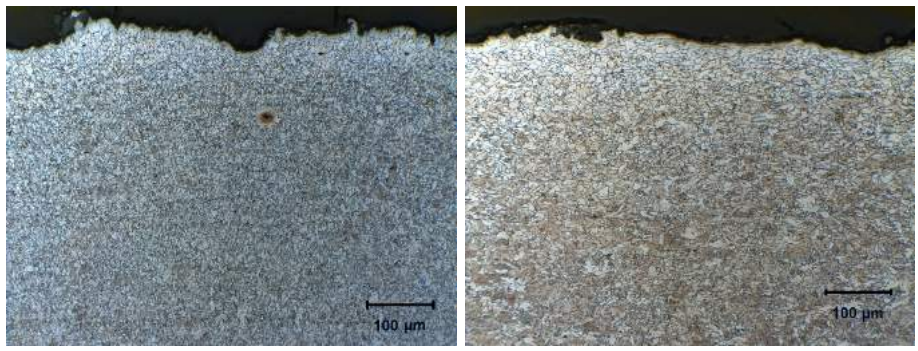

(a) *Pipe M* ×20 (b) *Pipe N* ×20

Figure 5.14: *Tension side of pipe wall in the dent caused by quasi-static deformation.*

to pipe N in Fig. 5.13(b) as well). These grooves may serve as crack initiators, and it is easy to imagine a load reversal may cause a crack to propagate quite far into the material, like seen in pipe K in Fig. 5.9.

On the tension side of the pipe wall in the dent, not much appears to have taken place. The microstructure is similar to the undeformed in Fig. 3.3. Based on this it is asserted that the problem being dynamic in nature is an important part.

Without the rapid load reversal, no cracks were visible to the naked eye and performing only quasi-static tests may produce erroneous or even dangerous results and conclusions. Dynamic tests should for that reason be an important part of an experimental matrix for these types of problems.

5.6 Combined transverse and axial load

This section contains an investigation of samples extracted from the pipes subjected to combined axial tension and transverse deformation as described in Section 4.5.

Samples from the pipes used to test the modified stretch-bending rig (pipes 1, 2 and 3) were examined in a light optical microscope. These were, in addition to being subjected to bending and stretching, also exposed to a stretch step

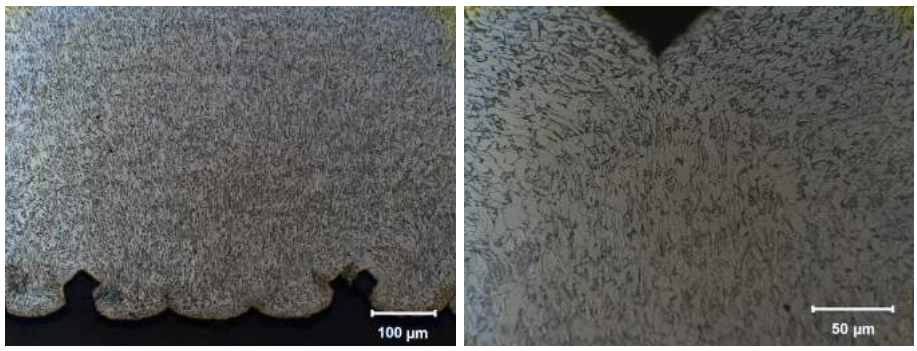

(a) *Pipe 1* ×20 (b) *Pipe 3* ×40

Figure 5.15: *Compressive side of pipe wall in the dent caused by quasi-static deformation.*

afterwards. During this step, cracks emerged on the pipes' surface as seen in the previous stretch tests (see Fig. 4.12). These cracks had a ductile fracture surface as observed earlier.

Nothing major was discovered in these pipes, and the deformed microstructure seen in Fig. 5.15 is similar to what is seen in the quasi-static three-point bending tests in Fig. 5.13, but to a lesser extent. The grains are quite compressed and aligned here, and a rapid reversal of the load might produce a significant crack. It seems that for a cleavage fracture surface to emerge, the stretch part has to be quick. As the load reversal was quasi-static, only ductile surface cracks were observed and no major crack propagation was present like for pipe B (see Fig. 4.12) or pipe K. For this reason, the pipes from series 2 and 3 in the stretch-bending rig were not cut into samples and investigated in the microscopes. These pipes were rather measured carefully and used to compare deformation with and without internal pressure (see Section 4.5 and Fig. 4.50).

5.7 Notched compression-tension tests

This section investigates the specimens deformed to large strain in compression, before the load is reversed into tension. The tests and their setup are explained and discussed in Section 3.6.

5.7.1 Initial geometry

In Section 3.6, material tests to large compressive strains have been carried out on notched specimens with geometries as shown in Figs. 3.16(a), 3.17(a) and 3.20(a). The compressed specimens were then stretched to failure in tension. The fracture surfaces of the notched compression-tension specimens were examined using scanning electron and optical light microscopes.

Fig. 5.16 shows overview images of the fracture surfaces from (a) tension only, to (e) 40% compression before tension, all taken in the SEM. These images are from the specimens with diameter 6.4 mm (Fig. 3.17(a)). A mixture of large and small dimples was found in the centre. Further, shear lips were present in

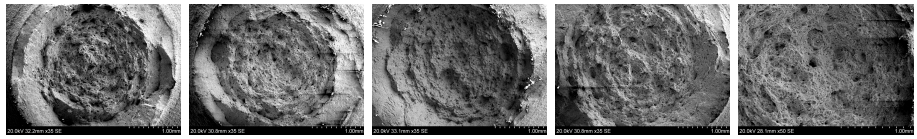

(a) *0%* (b) *10%* (c) *20%* (d) *30%* (e) *40%*

Figure 5.16: *Overview SEM images of fracture surfaces of notched specimens compressed to different levels of strain before being stretched to failure in tension. Dimpled surfaces are seen in the middle, while a more shear based fracture surface is observed along the edges.*

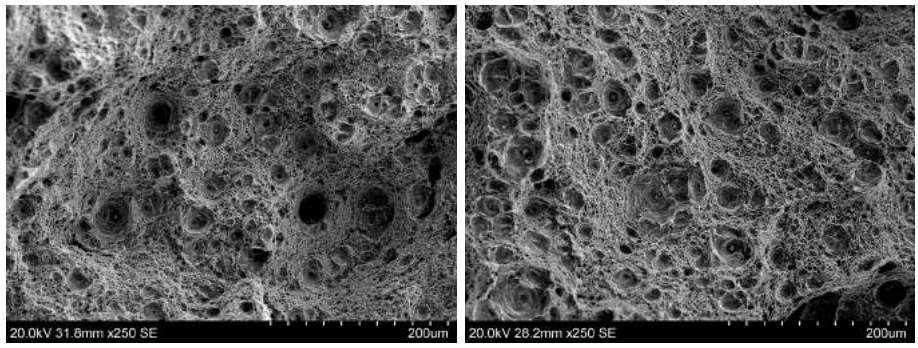

(a) *0% compression, deep dimples* (b) *40% compression, shallow dimples*

Figure 5.17: *SEM images of fracture surfaces of notched compression-tension specimens at* $\times$ *250 magnification.*

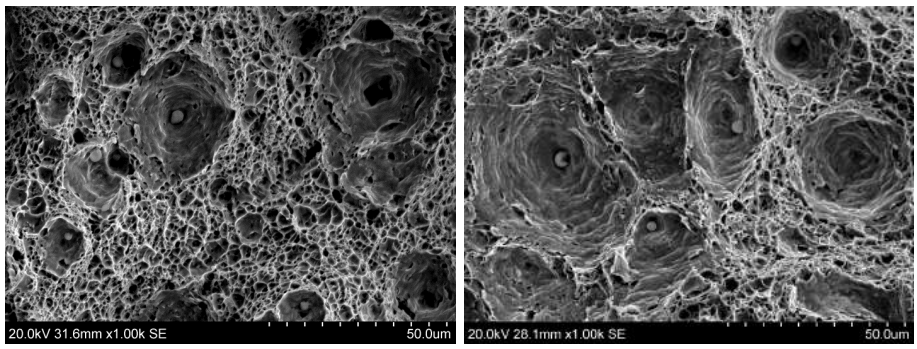

(a) *0 %* (b) *40 %*

Figure 5.18: *SEM images of fracture surfaces at ×1000.*

the region near the outer surface in accordance with the cup-and-cone fracture. The texture of the surface without any compression seems more uneven and rough compared with the 40% specimen, suggesting that the fracture occurs on a more well-defined plane in the latter. At 250 times magnification, the larger dimples appear to be deeper in the uncompressed specimen than those in the ones loaded in compression first (see Fig. 5.17), indicating that voids can grow to larger extents with less compression – a signal that ductility is being reduced with increased compression [82]. In specimens compressed to 20%, 30% and 40% the calcium aluminate particles are clearly seen in the large dimples, indicating once again that voids initiate around these particles in compression [67]. After compression, the stress level is considerably higher and the hardening similarly lower. This could lead to earlier void nucleation and accelerated void growth and coalescence by interligament necking at an early stage, partly confirmed by the unit cell analyses in Section 9.4.

In Fig. 5.18 the magnification is increased to 1000 times, revealing calcium aluminate particles in more or less all the large dimples. No specific quantifiable difference was found between the different magnitudes of compression at this magnification level. Nevertheless, the large dimples in the 0% specimen (Fig. 5.18(a)) appear to be spaced further apart than the large dimples in the 40% specimen (Fig. 5.18(b)). This could be an indication that more voids nucleate around particles under compression, and subsequently coalesce at lower strains from the following tensile load. Compression before tension is expected

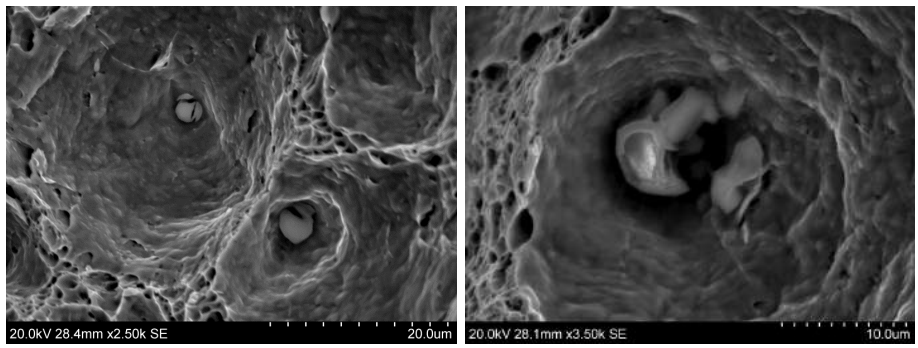

(a) $\times 2500$ (b) $\times 3500$

Figure 5.19: *SEM images of cracked particles in the specimen compressed to 40% at different magnification levels.*

to damage or fracture the spherical particles, and such a phenomenon is indeed observed here. This has been reported in the literature, e.g. by Cottrell [83]. By increasing the magnification to 2500 and 3500 times, cracked particles are clearly visible and even abundant, displayed in Fig. 5.19. This is easily comparable to what happens in the component test, where cracked particles are also observed (Fig. 5.7(c)).

A further examination was made using a light optical microscope; the sample compressed to 40% was investigated along with the reference 0% specimen. Both specimens were cut through the center along the longitudinal axis, making the fracture surface's profile and the specimen's inner surface available for inspection. Before they were placed in the microscope, they were ground and polished to 1 μm. Figs. 5.20(a) and (b) show that voids have formed in a zone near the fracture surface in both the 0% and 40% specimens. These voids become visible during tension but may initiate during compression.

Fig. 5.20(c), showing the 0% sample at 10 times magnification, displays a somewhat blurry edge compared to what is seen in Fig. 5.20(d), which shows the corresponding 40% sample at the same magnification. This suggests a less ductile fracture in the 40% specimen. Also, the voids in this specimen are more spherical and has an aspect ratio closer to unity compared to the more elongated voids of the 0% test. This indicates a more even pore growth when tension is preceded by compression.

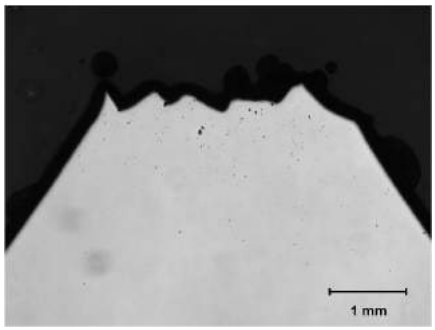

(a) *0%, ×5*

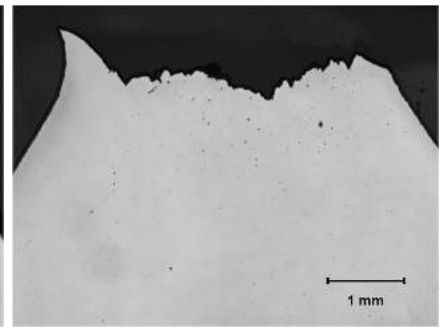

(b) *40%, ×5*

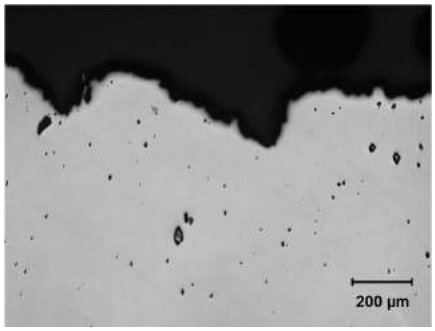

(c) *0%, ×10*

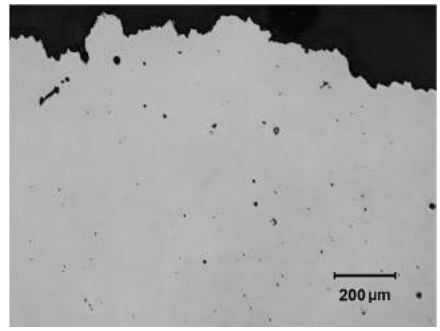

(d) *40%, ×10*

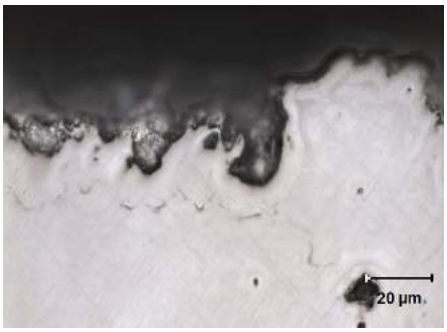

(e) *0%, ×100*

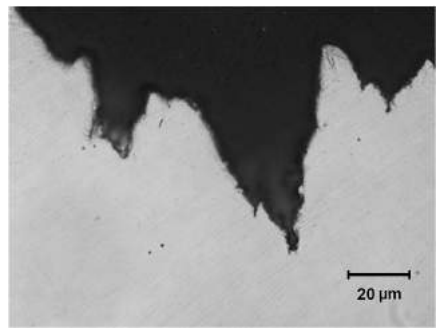

(f) *40%, ×100*

Figure 5.20: *Optical microscope images of longitudinal cross-section at different magnification levels. Both the 0% (left column) and 40% (right column) samples are shown.*

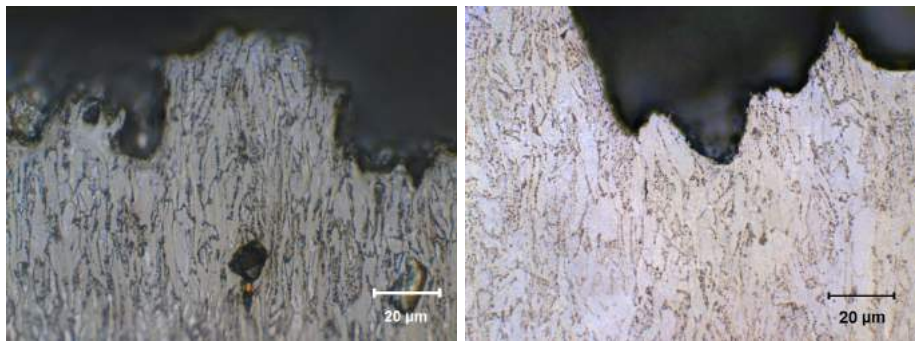

(a) *Microstructure, 0%* (b) *Microstructure, 40%*

Figure 5.21: *Optical microscope images of microstructure and defects in 0% specimen and 40% specimen at ×100 magnification.*

Additional voids may initiate around particles during compression and subsequent tension compared with tension only. They may then grow and coalesce more rapidly perpendicular to the load direction during tension. From Fig. 5.20(e) so-called ductile "fingers" are indentified in the 0% test. The 40% instance, on the other hand, does not have the same indications of ductility, made clear by the straight edges and high contrast of the fracture surface in Fig. 5.20(f).

When etched in nital, the microstructure also revealed another distinct difference between 0% and 40% compression. The grains are deformed and elongated to a much larger extent without the initial compression. Relative deformation is therefore decreased in the samples exposed to compression first, which is in agreement with the void shapes observed in Fig. 5.20(c) and (d).

Both samples' microstructures at failure are shown in Fig. 5.21, while the undeformed microstructure can be seen in Fig. 3.3. Defects of size 5-40 μm were observed in the specimen exposed to tension only, while the one compressed to 40% before tension showed such defects ranging from 5 to about 90 μm. Both cases are shown in Fig. 5.21, but be aware that this is a 2D representation of a 3D material, so the darker areas seen might as well be distorted areas in the vicinity of the calcium aluminate particles.

5.7.2 Modified geometry

Compression to 60% was attempted on the initial diabolo geometry, but barreling of the specimen and necking in the threads rather than in the gauge area prohibited valid test results from being obtained (see Section 3.6). Therefore a change was made in the specimen geometry; the cross-sectional diameter was reduced (shown in Fig. 3.20(a)) from 6.4 mm to 4.0 mm to postpone the onset of this barreling, which was incipient in the initial 40% specimens as well as the 60%. Two of each of the new specimens were compressed to true strain values of 40%, 60%, 80% and 90%, with 40% overlapping the initial test geometry for comparison. In addition one specimen was attempted compressed to 100% true strain before tension was applied.

In the new specimens compressed to 40%, 60% and 80%, the fracture surfaces typically had a mixture of small and large dimples in the center, while the edges showed tendencies to cleavage fracture with more compression leading to a larger portion of cleavage surface as well as more pronounced cleavage texture.

An overview of the fracture surfaces from the three cases 40%, 60% and 80% is shown in Fig. 5.22. Once again, cracked particles were observed in abundance. Compressing to 90% appears to decrease the ductility even further, and the fracture mode was altered to a 45° shear fracture which can be seen in Fig. 3.22.

Both the 60% and 80% specimens did show clear signs of cleavage fracture along the edges, examplified by Fig. 5.23(a) where a particle in a growing void is also shown, indicated by an arrow. This suggests that ductile behaviour and large scale plasticity may precede a cleavage fracture, as noted by Smith [84].

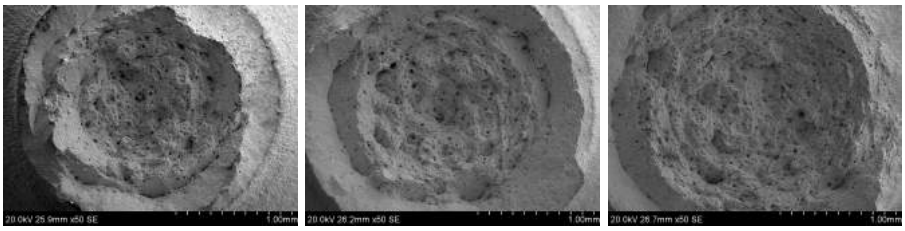

(a) *40%* (b) *60%* (c) *80%*

Figure 5.22: *Overview SEM images (×50 magnification) of fracture surfaces of modified notched specimens compressed to different levels of strain before being stretched to failure.*

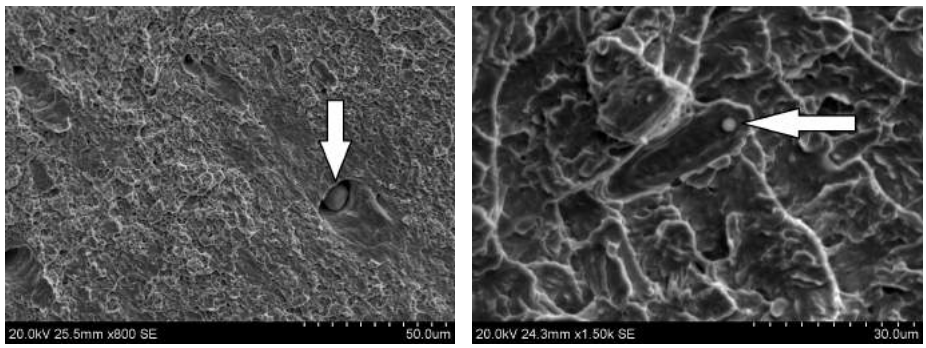

(a) *60%, ×800* (b) *90%, ×1500*

Figure 5.23: *SEM images showing indications of both cleavage fracture and ductile behaviour in specimens compressed to (a) 60% and (b) 90%.*

Similar results were found for the the 90% specimen, although with less presence of cleavage fracture areas. Fig. 5.23(b) shows the fracture surface of the 90% specimen, with a smaller particle in a growing void (again indicated by a lucid arrow).

Fig. 5.24 uses the 60% specimen as an example of the presence of both ductile and cleavage fracture, where (a) shows ductile fracture and (b) shows cleavage fracture. Part (c) displays the transition zone, while (d) indicates signs of cleavage in the 40% specimen. Similar observations were also made for the 80% specimen, while the 90% and 100% specimens had an altered fracture mode. As seen in Fig. 3.24(b) the fracture strain decreases, and along with the increasing level of cleavage fracture these are good indicators of the reduction in ductility with increasing compression.

Compressing the specimen to 100% created a slight barreling effect, causing the specimen to become widest at the centre. After stretching it to failure another 45° shear fracture was observed, although with much less indication of cleavage and an almost entirely ductile fracture. Being widest at the centre, fracture at the cross-section with lowest area or a shear fracture are more likely to occur. This leads to a questioning of the results from the 90% specimen as a similar fracture mode was observed.

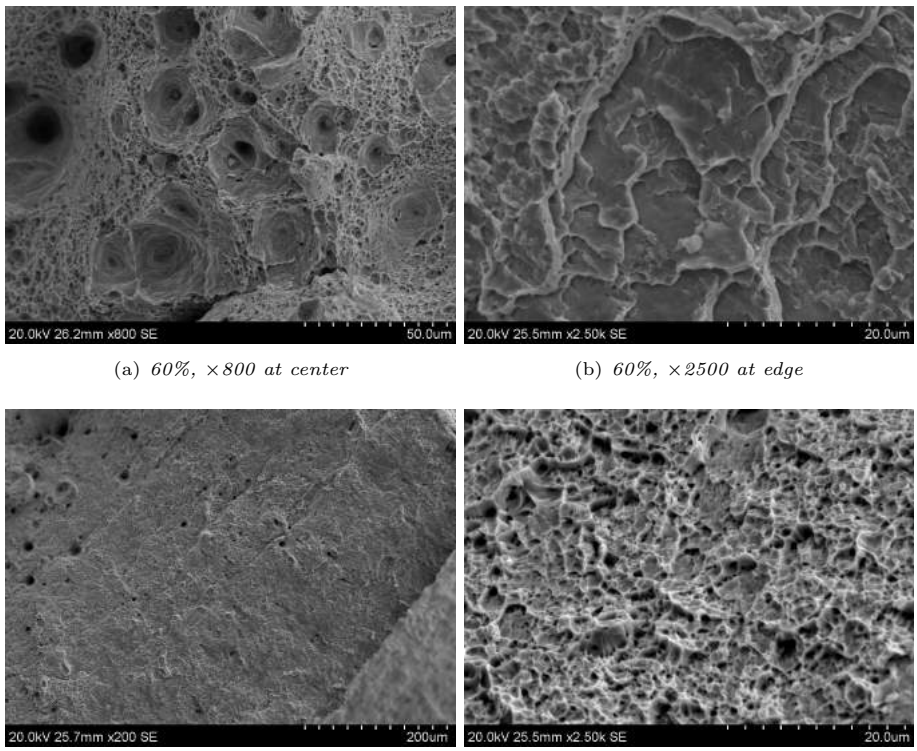

(a) *60%, ×800 at center*

(b) *60%, ×2500 at edge*

(c) *60%, ×200 transition*

(d) *40%, ×2500 at edge*

Figure 5.24: *Both ductile and cleavage fracture were present on the fracture surfaces of the 40%, 60% and 80% specimens; (a) shows a ductile fracture surface from the center of the specimen, and (b) portrays the cleavage fracture along the edges while (c) shows the transition from a dimpled surface (left) to a more brittle and clear-cut surface (right). Also included is (d), which displays the edge of the 40% specimen showing indications of cleavage fracture.*

5.8 Notched compression tests

These tests are identical to the ones discussed in the previous section, except for one large difference: the second step (tension) is omitted to investigate compression only. The specimens were then cut and examined in a light optical microscope.

5.8.1 Initial geometry

Specimens of the geometry in Fig. 3.17(a) were compressed to 20%, 40%, 60% and 80% (see Fig. 5.25) true plastic strain without being stretched in tension afterwards, and then investigated in a light optical microscope for comparison with the undeformed material. It is worth noting that the 80% sample of the initial notched geometry got stuck in the test machine due to a very high force when compressed, and had to be cut out of the machine (see Fig. 5.25(d)). From the compressed specimens it became evident that the machine was minorly askew, resulting in a slightly uneven deformation of the specimen.

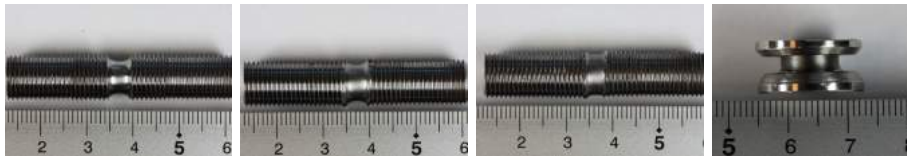

(a) *20%* (b) *40%* (c) *60%* (d) *80%*

Figure 5.25: *Notched specimens with initial diameter 6.4 mm compressed to various levels. Note that in (d) part of the equipment securing the specimen is included as the high compression force jammed the specimen. The numbers on the ruler show cm.*

Firstly, larger voids (150-200 μm) were found in all the compressed specimens in an area outside the notched zone, i.e. in the threaded area. No voids were found in the zone where they were observed in the notched compression-tension tests (examplified by Fig. 5.20), which indicates that voids mainly increase in volume during tension even though they may initiate during compression close to the spherical particles [67].

The angular particles did not appear to be affected by the deformation, while some irregularities were observed around the spherical particles. Between the different compression levels there did not seem to be any significant difference. Fig. 5.26 shows the microstructure. As the misalignment is much less pronounced for the lower compression levels, and no clear indicative difference is seen between the compression levels, it is asserted that the eccentricity is of minor importance.

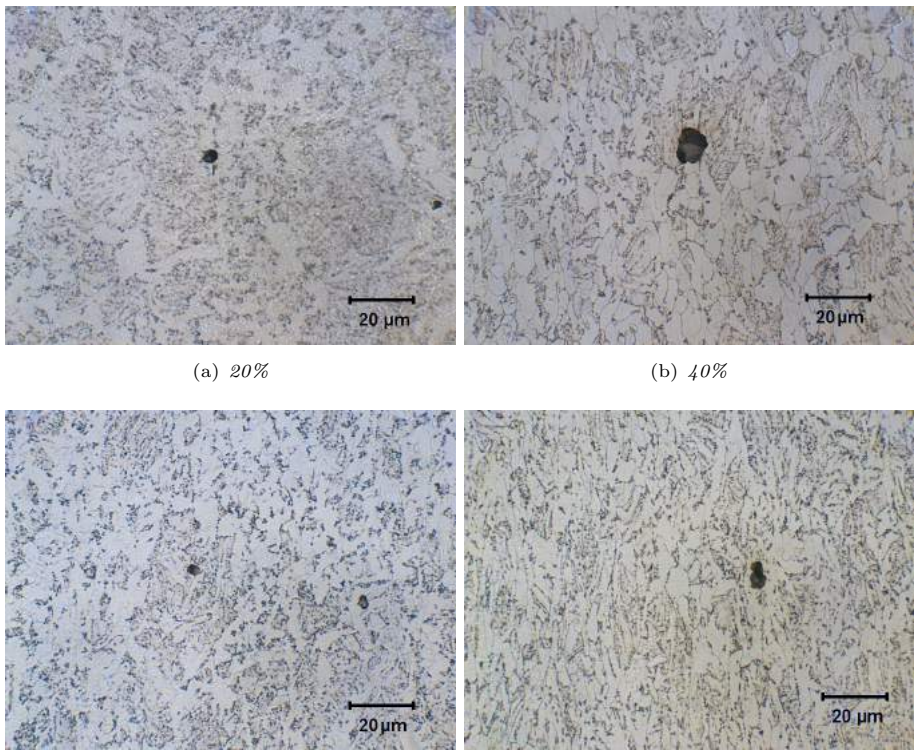

(a) *20%* (b) *40%*

(c) *60%* (d) *80%*

Figure 5.26: *Microstructure of notched specimens with initial diameter 6.4 mm compressed to various levels.*

5.8.2 Modified geometry

Compression to 80% for the geometry from Fig. 3.20(a) was also attained, as well as 90% and 100%. The microstructure and barrelling of the notched specimens compressed to 80%, 90% and 100%, are shown in Fig. 5.27.

Observation in the microscope showed that the profile of the specimens had a slight barrelling effect even at 80%, and more clearly so at 90% and 100%. The microstructure had deformed quite uniformly for the 80% and 90% specimens.

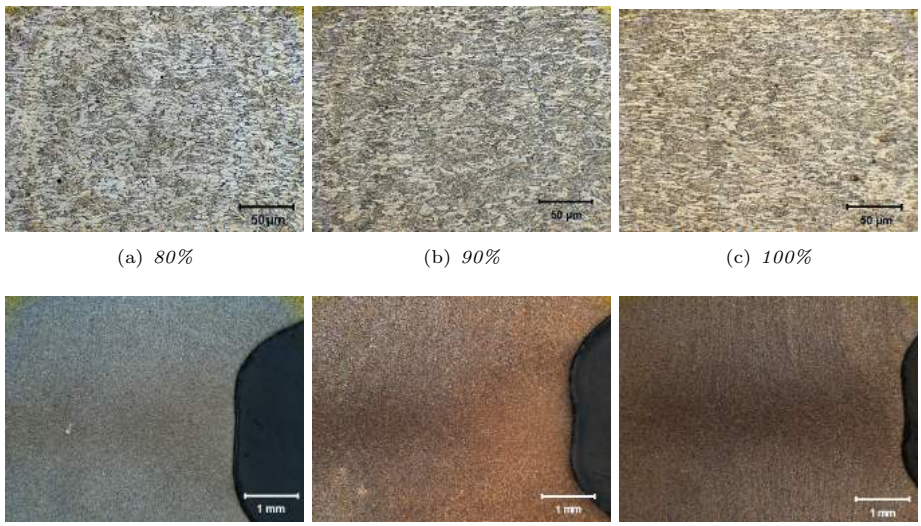

(a) *80%* (b) *90%* (c) *100%*

(d) *80%* (e) *90%* (f) *100%*

Figure 5.27: *Microstructure (top row) and barrelling (bottom row) of notched specimens with initial diameter 4.0 mm compressed to various levels of true plastic strain.*

These images displayed clearly visible shear bands in the microstructure of the 100% sample (see Fig. 5.27(c)), confirming the assertion that the fracture mode was altered due to the geometric conditions, and can thereby explain the more ductile fracture surface observed.

Such localised shear bands are fracture modes that most likely will not occur in impacted pipes. Thus, the reduced ductility seen in the 90% and 100% samples seems to be an effect of the deformed specimen geometries rather than a material property, and therefore not necessarily representative for the problem at hand.

5.9 Discussion

From the material tests it was clear that the material was quite ductile (true failure strain of about 1.6) so it was no surprise to see ductile fracture surfaces with void growth and coalescence, e.g. as in Fig. 5.6, in the pipes impacted

and subsequently stretched. Cracks were observed in all pipes subjected to the load sequence of impact and stretching, with the cracks emerging during the stretch phase. Very different load levels were needed to produce visible cracks during this phase, depending on the deformation from the impact. In the study by Manes et al. [5] on strips cut from an X65 steel pipe, only one of these quasi-static tests displayed fracture.

The ductile fracture observed in both the material and component tests occurs through void nucleation, growth and coalescence and is extensively discussed in the literature over the last decades [64, 65, 79–81]. Voids are often thought to initiate by particle-matrix decohesion or cracking of particles [85], confirmed here by the microscope images. As plastic deformation continues, voids grow in size and eventually coalesce.

More surprisingly, a textbook example of cleavage fracture (see Fig. 5.5) showed itself clearly in areas of the pipe exposed to large compressive strains which were subsequently reversed into tension. Even when omitting the stretch part of the component test fracture emerged quite clearly as shown in Fig. 5.9, leading to the hypothesis that fracture initiates during impact and, more specifically, during the springback. The highest impact velocity caused cracking through 75% of the pipe wall. The crack extended to the surface, but internal cracks of the same magnitude were also detected. At first the lower velocity did not seem to produce such fracture, but after a more thorough investigation in the microscope, cracks were indeed found within the pipe wall without any visible signs on the surface.

These observations of ductile-to-brittle transition and fracture after impact only in the dynamic component tests spawned an interest to examine which factors influence this behaviour as it is typically associated with low temperatures [19]. Almost any phenomena contributing to an increase in yield stress, such as high strain rates, constrained plastic flow, a triaxial stress state, low temperature, etc. can increase the susceptibility to cleavage fracture [78]. New component tests were conducted with exactly the same boundary conditions as the dynamic impact tests, with the exception that the pipes were deformed quasi-statically under displacement control to two different values. Deformation levels comparable to what was observed in the dynamic tests were attained, and the samples were cut from the pipes and checked for fracture with the naked eye and in the microscope. No fracture was found unlike in the dynamic tests, although a heavily deformed microstructure was observed. Grains were elongated perpendicularly to the compression direction (see Fig. 5.13), thereby creating aligned

grain boundaries which could serve as fracture planes which may, after a rapid load reversal during springback, emerge as cleavage fracture. Based on these observations, the problem being dynamic is deemed an important factor.

To investigate how large compressive strains influence succeeding tensile loading, diabolo shaped specimens were compressed to various levels of plastic strain (up to as much as 100% true plastic strain) before being stretched to failure in tension. Compression-tension tests on the first series of notched specimens (geometry in Fig. 3.17(a)) showed a clear reduction in absolute fracture strain[2] with increasing compression, while the relative fracture strain was less affected but still decreasing. This indicates an accelerated void nucleation [67]. Microscope images showed a less deformed microstructure and more shallow dimples (see Fig. 5.17), additional signs of earlier void coalescence [82]. Fig. 5.20 shows that voids were round and evenly shaped after compression-tension, as opposed to the rhombus shaped pores emerging from tension only. Under compression, voids may nucleate perpendicularly to the load direction before growing along the load direction during tension, thus creating a more even shape [60].

Cracked particles were observed as shown in Fig. 5.19, and may also contribute to earlier void coalescence as cracks formed in particles can propagate into the surrounding ferrite [86]. More frequent void nucleation along with cracking of particles, both due to compression, necessarily reduce the distance between voids, leading to earlier coalescence. The decreasing depth of pores with increasing compression is indicative of this. These forms of nucleation, illustrated by Sabih and Nemes [67] in Fig. 5.28 as mode (e) and (f), were observed in the compression-tension tests and the compression only tests. Notwithstanding the compression, the fracture surfaces in the specimens compressed up to 40% did not transform to brittle ones as seen in the component tests where the plastic flow is more restricted. Such restricted flow conditions may, as mentioned, increase the chances of cleavage fracture [78, 87].

Modifying the geometry of the notched specimens, seen in Fig. 3.20(a), allowed for compressive strains of 40%, 60%, 80%, 90% and even 100% to be attained. Tendencies to cleavage fracture were observed in the 60%, 80% and 90% specimens, depicted in Fig. 5.23, however less so in the 100% sample. McClintock [88] noted that cleavage planes initiated in adjacent grains rarely have a common intersection with the grain boundary, thus requiring additional deformation to cause void coalescence and thereby making fracture more of a process rather than an instantaneous event. This could explain the mixture of ductile and

[2]See Chapter 3 for more details.

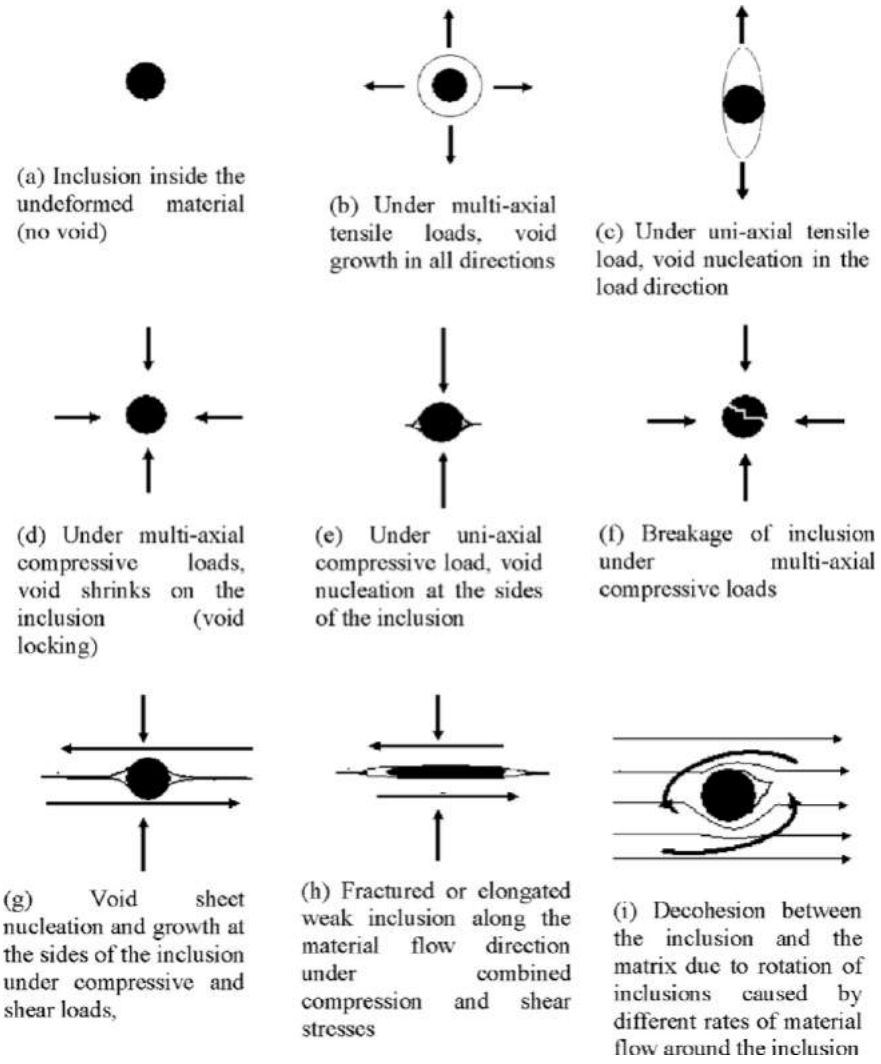

Figure 5.28: *Illustrations of the void and crack nucleation mechanisms around inclusions under different stress states [67].*

cleavage fracture surfaces seen in these specimens, confirming that these fracture modes are not mutually exclusive [84]. Hoagland et al. [89] found that brittle fracture could appear highly segmented, and attributed this to isolated regions difficult to cleave. They also noted that ligaments are the main source of resistance against cleavage crack propagation.

A high level of compression can further extend a void initiated at a cracked particle without necessarily increasing its volume, thereby requiring less tensile deformation to obtain void coalescence. Another account of the fracture could be that since the particles deform less than the matrix, stress concentrations arise around the particles. Locally the stress may be many times the yield stress, causing a ductile to brittle transition. Antretter and Fischer [90] found through numerical investigations that if a particle is already cracked, it increases the chance of a neighboring particle cracking due to stress concentrations, thereby initiating a cleavage fracture. A combination of decreased ligament size and increased local stress is entirely possible.

In the 80% and 90% specimens a slight barrelling effect was present, along with an apparent uniform deformation of the microstructure (see Fig. 5.27). At 90% and 100%, the fracture mode was altered to a 45° shear fracture (see Fig. 3.22) with significantly lower fracture strain. This might as well be an effect of the slight barrelling observed in the specimen, so one should be careful to conclude that this is a characteristic of the material. The 100% specimen exhibited barrelling and clearly visible shear bands, explaining the ductile fracture surface observed. Fixing the specimens with a slightly larger diameter might ameliorate the barrelling problem – an effort left for future work.

In summary it can be said that the problem being dynamic is important, and that the strain path is important. The combination of high compressive strain succeeded by rapid tensile loading seem to produce a cleavage fracture surface in the material not obtained by loading pipes to the same deformation quasi-statically. Areas of cleavage fracture were seen in quasi-static material tests, and this may have been observed in the pipes deformed quasi-statically as well, had they been stretched subsequent to the transverse deformation.

Chapter 6

Constitutive relations and fracture criteria

This chapter lays out the general framework for the constitutive relations and fracture criteria. Two different constitutive relations are described, and two different fracture criteria. In the numerical simulations presented later, the Johnson-Cook constitutive relation was used together with the Johnson-Cook fracture criterion as both are readily available in the standard version of the chosen finite element solver (ABAQUS/Explicit [91]). Kinematic hardening was later included with a Voce isotropic hardening rule (together with the JC fracture criterion) in an attempt to improve some parts of the initial results. Finally the combined isotropic/kinematic model was used with the Cockcroft-Latham fracture criterion in a user-defined subroutine. The calibration and adhering constants are presented in the final part of this chapter.

6.1 General formulation

As the elastic strains are small in metals and alloys, and plastic flow is assumed to be volume-preserving, the formulation is hypoelastic and limited to isochoric

plasticity, meaning that volumetric plastic strains are negligible. Plastic deformations and rotations may however be finite.

To obtain an invariant formulation for anisotropic materials, either initially anisotropic or deformation-induced (here induced by kinematic hardening), the corotational approach is adopted. The strain rate and stress measures applied in the formulation of the constitutive relations are then the corotational rate-of-deformation tensor $\hat{\mathbf{D}}$ and the corotational stress tensor $\hat{\boldsymbol{\sigma}}$. These tensors are defined as

$$\hat{\mathbf{D}} = \mathbf{R}^T \cdot \mathbf{D} \cdot \mathbf{R} \tag{6.1a}$$

$$\hat{\boldsymbol{\sigma}} = \mathbf{R}^T \cdot \boldsymbol{\sigma} \cdot \mathbf{R} \tag{6.1b}$$

in which $\mathbf{D}$ is the rate-of-deformation tensor, $\boldsymbol{\sigma}$ is the Cauchy stress tensor while $\mathbf{R}$ is a rotation tensor which takes local rigid-body rotation of the material element into account. $\mathbf{R}$ is acquired by a polar decomposition of the deformation gradient $\mathbf{F}$, that is $\mathbf{F} = \mathbf{R} \cdot \mathbf{U}$, where $\mathbf{U}$ is the right stretch tensor [92]. The tensors $\hat{\boldsymbol{\sigma}}$ and $\hat{\mathbf{D}}$ make up an energy conjugate pair, meaning that the deformation power per unit current volume ω_{def} can be defined by

$$\omega_{\text{def}} \equiv \boldsymbol{\sigma} : \mathbf{D} = \hat{\boldsymbol{\sigma}} : \hat{\mathbf{D}} \tag{6.2}$$

As the material time derivative of the corotational stress tensor $\dot{\hat{\boldsymbol{\sigma}}}$ is invariant, it is used to formulate the hypoelastic relation,

$$\dot{\hat{\boldsymbol{\sigma}}} = \hat{\mathbf{C}}_0^{\sigma} : \hat{\mathbf{D}}^e \tag{6.3}$$

in which $\hat{\mathbf{C}}_0^{\sigma}$ is the isotropic 4th order tensor of elastic moduli [93].

Further, the corotational rate-of-deformation tensor is decomposed into two parts, a (thermo)elastic part and a plastic part (temperature hereafter omitted)

$$\hat{\mathbf{D}} = \hat{\mathbf{D}}^e + \hat{\mathbf{D}}^p \tag{6.4}$$

with $\hat{\mathbf{D}}^e = \mathbf{R}^T \cdot \mathbf{D}^e \cdot \mathbf{R}$ being the elastic corotational rate-of-deformation tensor, and $\hat{\mathbf{D}}^p = \mathbf{R}^T \cdot \mathbf{D}^p \cdot \mathbf{R}$ the corresponding plastic tensor. This allows for a decomposition of ω_{def} as well,

$$\begin{aligned} \omega_{\text{def}} &= \omega_{\text{def}}^{e} + \omega_{\text{def}}^{p} \\ \omega_{\text{def}}^{e} &= \hat{\boldsymbol{\sigma}} : \hat{\mathbf{D}}^{e} \\ \omega_{\text{def}}^{p} &= \hat{\boldsymbol{\sigma}} : \hat{\mathbf{D}}^{p} \end{aligned} \tag{6.5}$$

Again, it is assumed that plastic deformation is isochoric, making the change in volume entirely elastic.

By integrating corotationally, a corotational deformation tensor $\hat{\boldsymbol{\varepsilon}}$ can be introduced as

$$\hat{\boldsymbol{\varepsilon}} = \int \dot{\hat{\boldsymbol{\varepsilon}}}\, \mathrm{d}t = \int \mathbf{R}^{T} \cdot \mathbf{D} \cdot \mathbf{R}\, \mathrm{d}t = \int \hat{\mathbf{D}}\, \mathrm{d}t \tag{6.6}$$

This can of course be done separately for the elastic and plastic parts of $\mathbf{D}$.

If the principal directions of the right stretch tensor $\mathbf{U}$ remain fixed during the deformation process, $\boldsymbol{\varepsilon}$ equals the logarithmic strain tensor, $\boldsymbol{\varepsilon}_L = \ln \mathbf{U}$, but not otherwise. Note that $\boldsymbol{\varepsilon}$ is sometimes used in finite element codes as an alternative to the logarithmic strain tensor $\boldsymbol{\varepsilon}_L$.

Moving on to the dynamic yield function f, this is given by

$$f\left(\hat{\boldsymbol{\sigma}} - \hat{\boldsymbol{\chi}}, R, H\right) = \sigma_{\text{eq}}\left(\hat{\boldsymbol{\sigma}} - \hat{\boldsymbol{\chi}}\right) - (\sigma_0 + R) \cdot H \tag{6.7}$$

where $\hat{\boldsymbol{\sigma}}$ is defined in Eq. (6.1b) and $\hat{\boldsymbol{\chi}}$ is the corotational backstress tensor, σ_0 is the yield stress and R is the isotropic hardening variable. Finally, H is multiplicatively included to account for the effect of strain rate. The scalar valued function σ_{eq} (the von Mises equivalent stress in this work) is given by

$$\sigma_{\text{eq}}\left(\hat{\boldsymbol{\sigma}} - \hat{\boldsymbol{\chi}}\right) = \sqrt{\frac{3}{2}\left(\hat{\boldsymbol{\sigma}}^{\text{dev}} - \hat{\boldsymbol{\chi}}^{\text{dev}}\right) : \left(\hat{\boldsymbol{\sigma}}^{\text{dev}} - \hat{\boldsymbol{\chi}}^{\text{dev}}\right)} \tag{6.8}$$

with the superscript "dev" denoting the deviatoric part (using the Caucy stress $\boldsymbol{\sigma}$ as an example),

$$\boldsymbol{\sigma}^{\text{dev}} = \boldsymbol{\sigma} - \frac{1}{3}\,\text{trace}\left(\boldsymbol{\sigma}\right) \cdot \mathbf{I} \tag{6.9}$$

where $\mathbf{I}$ is the second order identity tensor. The function $\sigma_{\mathrm{eq}}(\boldsymbol{\sigma}) \geq 0$ in Eq. (6.8) is assumed to be a positive homogeneous function of order one, meaning that $\sigma_{\mathrm{eq}}(k \cdot \boldsymbol{\sigma}) = k \cdot \sigma_{\mathrm{eq}}(\boldsymbol{\sigma})$ for any positive scalar k. The associated flow rule is adopted and ensures positive plastic dissipation

$$\hat{\mathbf{D}}^p = \dot{\lambda} \cdot \frac{\partial f}{\partial (\hat{\boldsymbol{\sigma}} - \hat{\boldsymbol{\chi}})} \tag{6.10}$$

where $\dot{\lambda} \geq 0$ is the plastic parameter, which is zero in the elastic domain and positive in the plastic domain. The equivalent strain rate $\dot{p}$ is defined to be energy conjugate to σ_{eq}, i.e.

$$(\hat{\boldsymbol{\sigma}} - \hat{\boldsymbol{\chi}}) : \hat{\mathbf{D}}^p = \sigma_{\mathrm{eq}} \dot{p} \tag{6.11}$$

Under the assumption that σ_{eq} is a positive homogeneous function of order one and using Euler's theorem for such functions, $\dot{p}$ is found to be equal to the plastic parameter from Eq. (6.10),

$$\dot{p} = \dot{\lambda} \tag{6.12}$$

This can then be integrated to find the equivalent plastic strain p,

$$p = \int_0^t \dot{p} \, \mathrm{d}t = \int_0^t \dot{\lambda} \, \mathrm{d}t \tag{6.13}$$

Finally, the loading/unloading conditions are expressed in Kuhn-Tucker form,

$$f \leq 0, \qquad \dot{\lambda} \geq 0, \qquad \dot{\lambda} f = 0 \tag{6.14}$$

So, in expressing the two different constitutive relations used herein, the framework presented above is used with various formulations of the backstress $\boldsymbol{\chi}$, the isotropic hardening R and the strain rate sensitivity H. A more general and eloquent formulation of this framework can be found in Ref. [93].

6.2 Constitutive relations

Two different constitutive models have been used in this study; the first is viscoplastic with isotropic hardening only [94], and the second is also viscoplastic but with combined isotropic and kinematic hardening [91]. Both models used are uncoupled with damage, and plastic flow is independent of direction (isotropic) and preserves volume (isochoric). The material tests in Section 3.3 show that the X65 material used herein is indeed isotropic. Elastic strains are as mentioned assumed small, while plastic deformation and rotation may be finite.

6.2.1 Isotropic hardening only (Johnson-Cook)

The X65 pipeline material has been modelled using the Johnson-Cook (JC) constitutive relation [94]. It accounts for isotropic hardening, strain rate sensitivity and thermal softening.

The JC flow stress σ_{JC} is expressed as [94]

$$\sigma_{\mathrm{JC}}\left(p, \dot{p}^*, T^*\right) = \left(A + Bp^n\right)\left(1 + C\ln\dot{p}^*\right)\left(1 - T^{*m}\right) \tag{6.15}$$

where p is the equivalent plastic strain, and A, B, n, C and m are material constants. The dimensionless equivalent strain rate is given by $\dot{p}^* = \dot{p}/\dot{p}_0$, with $\dot{p}_0$ being a user-defined reference strain rate. Strain rates below this threshold are treated as static.

The homologous temperature is defined as $T^* = (T - T_r)/(T_m - T_r)$, where T is the absolute temperature, T_r is the ambient temperature and T_m is the melting temperature of the material. This problem is assumed to be isothermal, thus omitting the temperature bracket of Eq. (6.15) and reducing the model to

$$\sigma_{\mathrm{JC}}\left(p, \dot{p}\right) = \left(A + Bp^n\right)\left(1 + C\ln\frac{\dot{p}}{\dot{p}_0}\right) \tag{6.16}$$

In terms of the framework laid out in Section 6.1, the yield stress σ_0 is equal to the constant A in Eq (6.16). The isotropic hardening R is described as

$$R\left(p\right) = Bp^n \tag{6.17}$$

while the viscoplastic effect H is described by

$$H\left(\dot{p}\right) = \left(1 + C \ln \frac{\dot{p}}{\dot{p}_0}\right) \tag{6.18}$$

and as kinematic is unaccounted for, $\boldsymbol{\chi}$ is simply set to zero,

$$\boldsymbol{\chi} = \mathbf{0} \tag{6.19}$$

Then these expression are inserted into Eq. (6.7) to obtain the final yield function.

6.2.2 Combined isotropic/kinematic model

This model combines both isotropic and kinematic hardening. As the material exhibited signs of kinematic hardening as seen in Section 3.5, this seems like a natural extension. Kinematic hardening $\boldsymbol{\chi}$ and the evolution thereof, is described as

$$\boldsymbol{\chi} = \sum_{i=1}^{N_\chi} \boldsymbol{\chi}_i \ , \qquad \dot{\boldsymbol{\chi}}_i = \frac{C_i}{\sigma^0} \left(\boldsymbol{\sigma} - \boldsymbol{\chi}\right) \dot{p} - \gamma_i \boldsymbol{\chi}_i \, \dot{p} \tag{6.20}$$

where C_i and γ_i are material constants, constituting an Armstrong-Fredericks type kinematic hardening. N_χ is the number of backstresses and σ^0 is the size of the yield surface,

$$\sigma^0\left(p\right) = \sigma_0 + \sum_{j=1}^{N_V} Q_j \left[1 - \exp\left(-b_j p\right)\right] \tag{6.21}$$

Eq. (6.21) is the Voce hardening law in which σ_0 is the yield surface at zero plastic strain, Q_j and b_j are material constants, and N_V the number of terms included. Strain rate dependency is as before included multiplicatively by the yield ratio denoted H

$$H\left(\dot{p}\right) = \left(1 + C \ln \frac{\dot{p}}{\dot{p}_0}\right) \tag{6.22}$$

where C is the same as in Eq. (6.16). The rate dependent data is entered as tabular data, with one curve for each strain rate and interpolated logarithmically between each rate [91]. In another case this has been implemented in a user-defined material model [93] with about the same results.

As above, the model is summarised with σ_0 being the initial yield stress. The backstress $\boldsymbol{\chi}$ is described by Eq. (6.20) and the isotropic hardening variable R becomes

$$R\left(p\right) = \sum_{j=1}^{N_V} Q_j \left[1 - \exp\left(-b_j p\right)\right]$$

Viscoplasticity is described by Eq. (6.22) which is exactly the same as Eq. (6.18). Again, these are inserted into Eq. (6.7) to obtain the final yield function.

6.3 Fracture criteria

6.3.1 Johnson-Cook

The Johnson-Cook fracture criterion has been used in several simulations herein. The JC fracture strain ε_f is given by [95]

$$\varepsilon_f = \left[D_1 + D_2 \exp\left(-D_3 \sigma^*\right)\right] \left(1 + D_4 \ln \dot{p}^*\right) \left(1 + D_5 T^*\right) \tag{6.23}$$

where σ^* is the stress triaxiality as defined in Eq. (3.5), D_1 to D_5 are material constants to be calibrated while $\dot{p}^*$ is the dimensionless plastic strain rate as before and T^* is the homologous temperature. Again due to the assumption of isothermal conditions, D_5 is equal to zero. The damage parameter ω_D is defined as [91]

$$\omega_D = \sum_{k=1}^{N_{\text{inc}}} \frac{\Delta p^{(k)}}{\varepsilon_f} \tag{6.24}$$

Here, $\Delta p^{(k)}$ is the change of equivalent plastic strain in increment k and the summation is, as indicated, performed over all the increments in the analysis. Failure is said to occur when the damage parameter becomes equal to unity.

6.3.2 Cockcroft-Latham

Most fracture criteria are based on void growth, while the fracture criterion suggested by Cockcroft and Latham [96] is based on what may be visualised as a kind of "plastic work". This model is used with a user-defined material model [93]. In simple terms, the criterion says that damage grows during plastic straining as long as the major principal stress σ_1 is positive, i.e. compression would not cause damage to accumulate. When the "plastic work" by $\sigma_1 > 0$ reaches a certain critical value W_{cr}, failure finally takes place[1].

It is expressed quite simply in mathematical terms as

$$\omega_D = \frac{1}{W_{\mathrm{cr}}} \cdot \int_0^p \langle \sigma_1 \rangle \, \mathrm{d}p \tag{6.25}$$

where ω_D is the damage parameter, which upon reaching unity signifies failure. The Macauley bracket notation used in Eq. (6.25) has the following definition,

$$\langle \sigma_1 \rangle = \begin{cases} \sigma_1 & \text{if } \sigma_1 \geq 0 \\ 0 & \text{if } \sigma_1 < 0 \end{cases} \tag{6.26}$$

In the applied user-defined material model, this has been implemented more generally in the form of the Extended Cockcroft-Latham (ECL) criterion [93, 97],

$$\dot{\omega}_D = \left\langle \frac{\phi \, \sigma_1 + (1 - \phi) \, (\sigma_1 - \sigma_3)}{W_{\mathrm{cr}}} \right\rangle^{s_0} \cdot \dot{p} \tag{6.27}$$

where $\sigma_1 > \sigma_2 > \sigma_3$ are the ordered eigenvalues of the Cauchy stress tensor. The parameters $\phi \in [0, 1]$ and $s_0 > 0$ are obtained by experiments. For $\phi = 1$

[1] W_{cr} is typically obtained from a smooth uniaxial tensile test (see Section 3.3).

and $s_0 = 1$, Eq. (6.27) reduces to the integrand of Eq. (6.25), which has been used in this thesis.

6.4 Identification of material constants

Finally, the various constants for the different constitutive relations and fracture criteria can be determined. This naturally requires experimental data in the form of material tests, all of which are expatiated in Chapter 3.

6.4.1 Constitutive relations

To determine the equivalent stress σ_{eq} from the measured major principal stress σ_1 after necking, Bridgman's analysis [55] was employed

$$\sigma_{\text{eq}} = \frac{\sigma_1}{\left(1 + \frac{2R}{a}\right) \cdot \ln\left(1 + \frac{a}{2R}\right)} \tag{6.28}$$

The relation between the radius of the specimen's cross-section at the root of the neck, a, and the radius of the neck profile, R, was estimated by the empirical relation proposed by Le Roy et al. [98]

$$\frac{a}{R} = 1.1 \cdot (p - \varepsilon_U) \tag{6.29}$$

valid for $p > \varepsilon_U$ where ε_U is the equivalent plastic strain at the onset of necking. Fig. 6.1 shows a uniaxial tensile tests along with the Bridgman corrected curve. When identifying the material constants, a least squares approximation [99] has been used to minimise the error. Another approach was attempted through inverse modelling using LS-OPT [100], which was employed by Aune and Hovdelien [35] without any significant improvement compared with the initially obtained values.

Johnson-Cook relation

Before necking, the strain rate is constant at the prescribed value. When necking commences and deformation localises, the strain rate increases somewhat

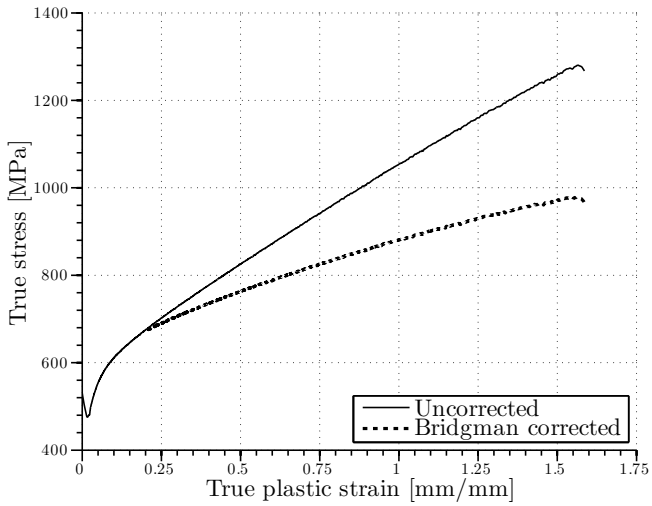

Figure 6.1: *Uncorrected and Bridgman corrected stress from uniaxial tensile tests.*

locally, resulting in more data points being logged before necking and thereby causing greater weight on the pre-necking data when calibrating. This can be ameliorated by extracting a fixed number of data points (say, 100) from the recorded values, equidistant in strain space causing equal weight throughout the whole strain range for the test.

The constants A, B and n were found through a least squares approximation to the test data from Figs. 3.6 and 3.8. Both the data set obtained directly and the data set equidistant in strain space were calibrated for, without any real significant difference in the simulation response. The constant C was determined through the average stress values at 4% plastic strain and the corresponding strain rates, all listed in Table 3.4. This calibration was also carried out in Ref. [33].

Fig. 6.2 shows the resulting true stress-true strain curves along with the experimental data. Here, three different tension test geometries are modelled with axisymmtric finite elements, and the results are quite satisfactory. The smooth test geometry was used for calibration, and the two notched to test the predictive capabilities.

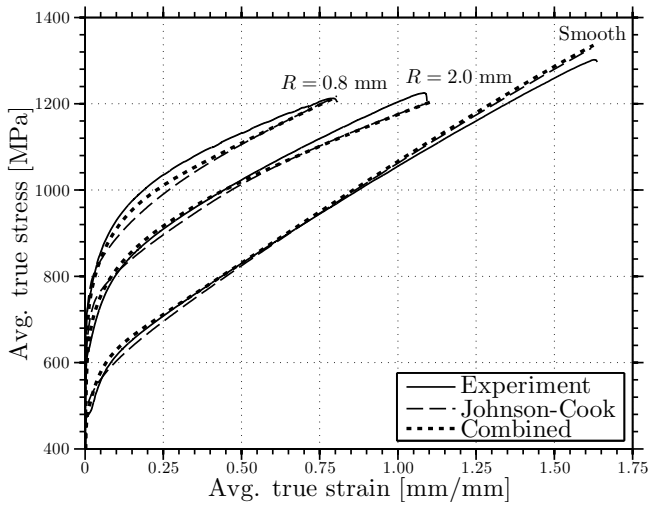

Figure 6.2: *Axisymmetric finite element simulations using the JC and combined material models, along with experimental data for three different tension test geometries. Data from the smooth test is used for calibration, while the two notched tests are included for illustrating the predictive capabilities of the models.*

Combined isotropic/kinematic hardening

Where isotropic hardening represents an expansion of the yield surface when plastic deformation occurs, kinematic hardening represents a translation of the yield surface (in the direction of the applied stress), meaning that the size of the elastic region remains constant. In a real material neither of these two extremes are true (although both can be used as good approximations in several cases), so a combination of the two seems like a natural way to progress as the material used herein showed clear signs of kinematic hardening as shown in Fig. 3.14. This model was calibrated with help from Fornes and Gabrielsen [34].

The fraction of isotropic versus kinematic hardening can be estimated by calculating the size of the elastic domain from the reversed loading material tests in Fig. 3.14. The elastic region is given by the "distance" between the point of unloading U and the point of re-yielding R as illustrated in Fig. 3.15. When determining point R, a unique Young's modulus E was used for each test[2],

[2]A slight decrease of E was found with increasing strain.

determined by the slope of the curve from the point of unloading U until zero stress as done in Ref. [59].

Table 3.5 lists the data used in this calibration, and a plot is shown with these data points along with the calibrated model in Fig. 6.3. Deviating from the remainder of the tests, the tension-compression test loaded to 0.4% in tension was excluded from the calibration. The measurement should not be considered invalid, but the shape of this upper yield point and plateu seen in the tests is difficult to reproduce with reasonably few terms of simple analytic expressions.

From 20% plastic strain and upwards until failure, data points from the initial smooth uniaxial tesile tests were used. This results in isotropic hardening dominating the upper part of the strain levels. Two terms were used in both the isotropic and kinematic hardening parts, and the material constants (listed in Table 6.1) were fitted in a least squares sense as indicated earlier. The material model was either entered as tabulated data or implemented as a user defined model using the listed constants. Results of axisymmetric simulations using the calibrated model can be seen in Fig. 6.2 and the fit is quite good for the two notched tensile tests in addition to the smooth tensile test.

6.4.2 Fracture criteria

The Cockcroft-Latham criterion is calibrated by integrating the measured true stress-true strain curve from the smooth uniaxial material tests as the only parameter required is the total plastic "work per volume" until failure. This has been done in Chapter 3, and the average value from the tests have been used. Since σ_1 will vary over the cross-section after necking, the measured value and hence the calculated area will be an approximation. The average value based on all smooth axisymmtric tension tests was $W_{\mathrm{cr}} = 1\,562$ MPa (also listed in Table 6.3 at the end of this section).

Moving on, the JC fracture criterion has been calibrated in two different manners. The first is directly from the smooth and notched tensile tests from Fig. 3.9, which provide different fracture strains derived from different initial stress triaxialities. The parameters in Eq. (6.23) are then calibrated to the data using the least squares approach as mentioned.

The second approach involves trying to make the JC criterion behave according to the fracture strains predicted by the CL criterion, as the latter was not initially available without using a user-defined model. For this batch of

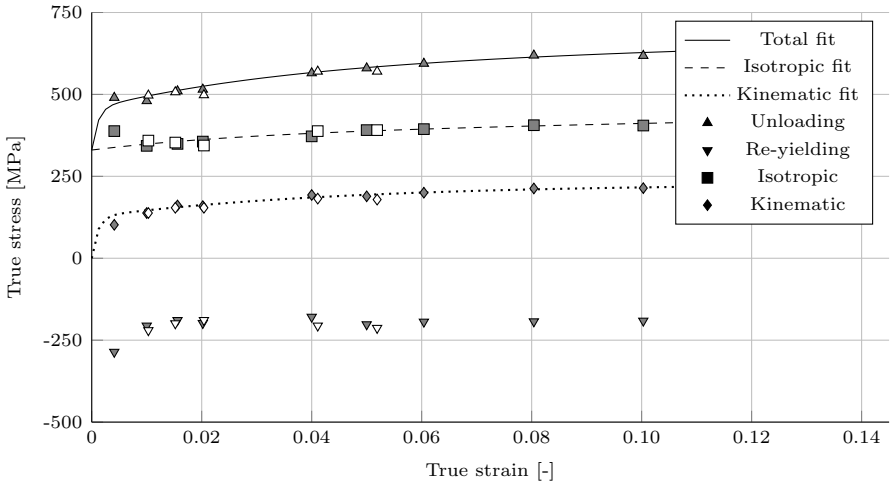

Figure 6.3: *Data used for calibration of combined material model. The gray hatched points are data from tension-compression tests while the white points are for compression first (multiplied by −1). The solid line shows the combined fitted curve, the dashed line the isotropic part and the dotted line the kinematic part.*

Table 6.1: *Constants for material models.*

Elasticity and density					
E [MPa]		ν [-]		ρ [kg/m^3]	
208 000		0.3		7 800	
Johnson-Cook model					
A [MPa]	B [MPa]	n [-]		C [-]	$\dot{p}_0$ [1/s]
465.5	410.8	0.4793		0.0104	$8.06 \cdot 10^{-4}$
Combined model					
Isotropic	σ_0 [MPa]	Q_1 [MPa]	b_1 [-]	Q_2 [MPa]	b_2 [-]
	330.3	703.6	0.47	50.5	34.7
Kinematic		C_1 [MPa]	γ_1 [-]	C_2 [MPa]	γ_2 [-]
		115 640	916	2 225	22
Strain rate				C [-]	$\dot{p}_0$ [1/s]
				0.0104	$8.06 \cdot 10^{-4}$

simulations, the JC constitutive relation was used (the combined model was introduced later). This approach can then be used to provide an estimate for the D_i constants in the JC fracture criterion, based on what fracture strain the CL criterion would provide.

Following the procedure by Dey [101] and assuming an axisymmetric state of stress, the maximum principal stress σ_1 can be expressed by the stress triaxiality σ^* and the equivalent stress σ_{eq} as

$$\sigma_1 = \left(\frac{2}{3} + \sigma^*\right) \sigma_{\text{eq}}$$

Inserting the JC equivalent stress from Eq. (6.16) into the above equation yields

$$\sigma_1 = \left(\frac{2}{3} + \sigma^*\right) (A + Bp^n) \left(1 + C \ln \frac{\dot{p}}{\dot{p}_0}\right) \tag{6.30}$$

This expression for σ_1 can then be used in the CL criterion in Eq. (6.25) and integrating to the fracture strain ε_f,

$$W_{\text{cr}} = \int_0^{\varepsilon_f} \left\langle \left(\frac{2}{3} + \sigma^*\right) (A + Bp^n) \left(1 + C \ln \frac{\dot{p}}{\dot{p}_0}\right) \right\rangle \mathrm{d}p \tag{6.31}$$

Under the assumption that the strain rate $\dot{p}$ is constant and equal to $\dot{p}_0$ during the tension test, Eq. (6.31) can be rewritten as a nonlinear equation for ε_f,

$$A\varepsilon_f + \frac{B}{n+1}\varepsilon_f^{n+1} - \frac{W_{\text{cr}}}{\frac{2}{3} + \sigma^*} = 0 \tag{6.32}$$

Table 6.2: *Fracture strain as calculated from the CL fracture criterion along with test data.*

Parameter		Values				
σ^*_{init} (Eq. (6.32))		0.33	0.65	0.89	1.39	1.90
ε_f (Eq. (6.32))		1.89	1.51	1.31	1.04	0.86
σ^*_{init}	(test)	0.33	0.66	1.00	-	-
ε_f	(test)	1.64	1.08	0.77	-	-

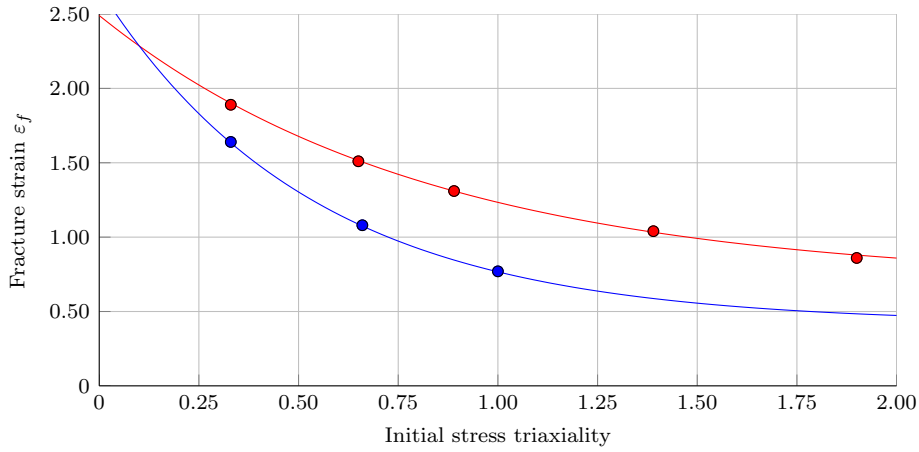

Figure 6.4: *The Cockcroft-Latham based adoptation of the Johnson-Cook fracture criterion (red line) with data points (red circles) along with the directly calibrated JC criterion (blue line) with test data (blue circles).*

Table 6.3: *Constants for fracture criteria.*

(Extended) Cockcroft-Latham					
W_{cr} [MPa]		ϕ [-]		s_0 [-]	
1 562		1		1	
Johnson-Cook					
CL-based	D_1	D_2	D_3	D_4	$\dot{p}_0$
	0.70	1.79	1.21	-0.00239	$8.06 \cdot 10^{-4}$
Test-based	D_1	D_2	D_3	D_4	$\dot{p}_0$
	0.42	2.25	1.87	-0.00239	$8.06 \cdot 10^{-4}$

which in turn provides estimates for ε_f for different σ^*. This was done in [33] for five different triaxialities and the results are provided in Table 6.2. There are now two sets of data for calibrating the JC fracture criterion; the set in Table 6.2 just obtained from the calculation and the experimental data from Section 3.3, also listed in Table 6.2. Fig. 6.4 shows the data points along with the curves fitted to Eq. (6.23). The two sets of data naturally gives rise to two sets of constants for the JC criterion, and both sets are listed in Table 6.3.

Intuitively, one would expect the fracture strain to be equal for the reference case, which is the smooth uniaxial tensile test. However, in the calculated values the stress triaxiality σ^* is tacitly assumed constant and equal to the initial one σ^*_{init} thoughout the test, thereby producing a higher fracture strain compared with the test data.

Chapter 7

Numerical simulations

7.1 Introduction

This chapter mainly concerns numerical simulations of selected component tests from Chapter 4. Experimental data logged in the physical tests are compared with equivalent data from the simulations, providing grounds for discussion and evaluation.

Simulations using standard methods available in a commercial finite element code are carried out with the intent to examine how well a commonly used software is able to handle a fairly complex problem involving several nonlinearities, e.g. large scale plasticity, contact, and even fracture. These analyses are mainly restricted to the impact of empty pipes (Section 4.2) and the subsequent stretching thereof. Pipes subjected to combined transverse and axial loading will also be simulated, with and without internal pressure.

Both the Johnson-Cook constitutive relation and the constitutive model including kinematic hardening are tested. Two different calibrations of the Johnson-Cook fracture criterion are tested as well. The impact phase is generally captured very well, while the force in the strech phase is somewhat overestimated. Fracture could not be accurately predicted. Finally, the submodelling feature in ABAQUS/Explicit was tested in an attempt to model the dented zone of the

pipe only. While it seemed like a resonable approach, the results were not as good as hoped for as the submodel approach is probably not intended for mesh refinement.

7.2 Impact and stretch simulations

This section contains simulations run with a comercially available finite element code, the choice of which has been ABAQUS/Explicit [91] as several Norwegian industrial actors utilise this software. Only standard techniques contained within this software were used in this chapter. The initial simulations were conducted to see what was possible to obtain with procedures already developed and readily available. Some of these results have been published in Ref. [31], and they were conducted with help from Slåttedalen and Ørmen [33], from Fornes and Gabrielsen [34], and from Digerud and Lofthaug [38].

7.2.1 Setup

These simulations are of the pipes subjected to the loading sequence described in Section 4.2, a loading sequence consisting of a dynamic impact part and a quasi-static stretch part. All analyses in this section are run explicitly, with both shell and volume elements. The general setup of the simulations is as depicted in Figs. 4.6 and 7.1, with the following orientation of the axes: The x-axis runs along the pipe's longitudinal direction, the y-axis is parallel to the initial velocity vector of the indenter, and the z-axis is normal to the plane spanned by the x- and y-axes.

Two planes of symmetry are exploited to reduce computational time, these planes are $x = 0$ and $z = 0$ as indicated by the hatched grey planes in Fig. 7.1. The support and the bolt are both modelled as rigid cylinders and obviously have the same diameters as in the experiments, which are 50 mm and 40 mm respectively.

The nose of the indenter has a radius of 10 mm, and is prescribed an initial velocity v_0 and a certain mass corresponding to the trolley in the experiments. In this case the mass is 1472/4 kg = 368 kg due to the two symmetry planes. The indenter is also modelled as rigid, and is restrained to moving in the y-direction only, which is equivalent to moving along a set of rails like the trolley

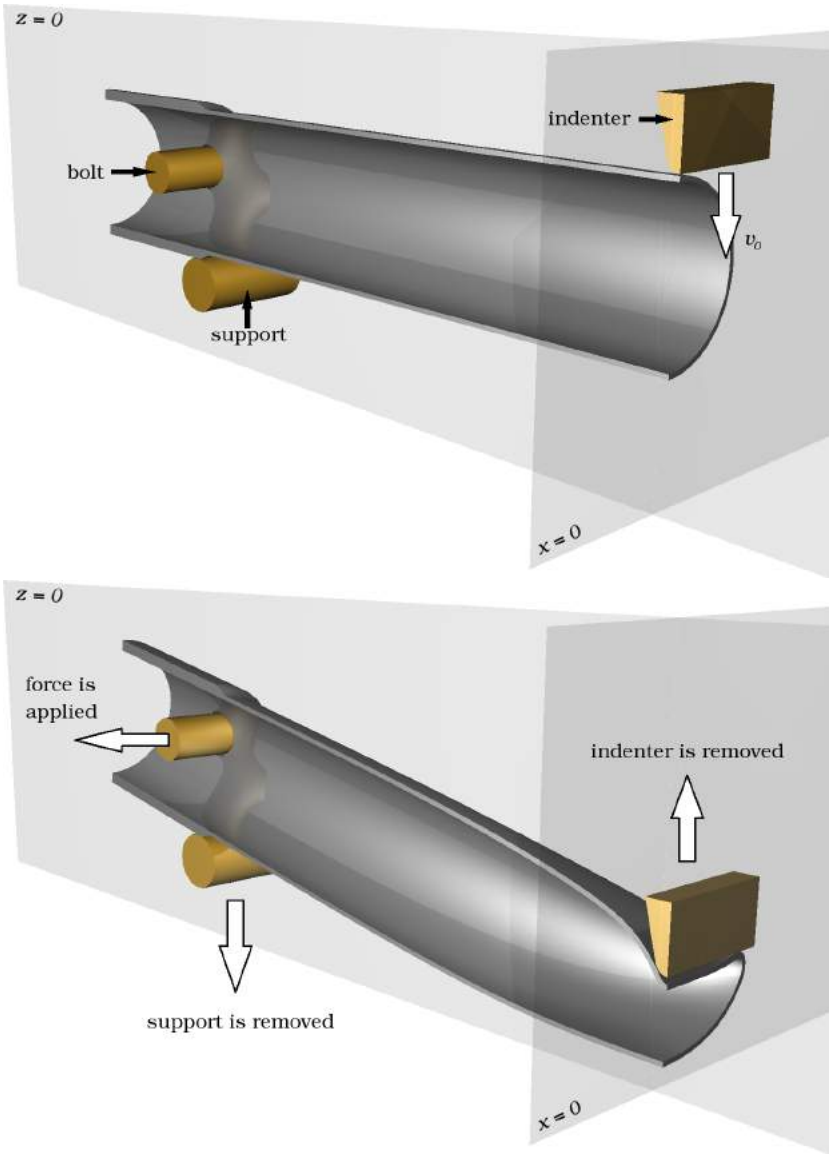

Figure 7.1: *Sketch of setup of initial numerical simulations conducted with comercially available tools, the top figure shows the impact step while the bottom shows the stretch step.*

in the test setup.

As each pipe had varying thicknesses in the experiments, this will be accounted for in the simulations by using the measured average thickness for each pipe. Also, the pipes have two different sections, the lathed area and the unlathed area. These two areas will of course be modelled with separate thicknesses. Details on the pipe geometries (i.e. the thickness measurements) can be found in Appendix C.

The main metric for evaluating the simulation results in this section is, naturally, the agreement between the experimentally obtained force-displacement curves (see Fig. 4.9) and the numerically obtained ones (which we will see several of on the coming pages). Chapter 6 describes the constitutive relations used, and the calibration thereof. In this section the ones used are the Johnson-Cook model and the combined model, described in Section 6.2.1 and 6.2.2, respectively. The fracture criterion used is the Johnson-Cook criterion [95] with the two different calibrations as shown in Fig. 6.4.

The final part of the model is the buffer, which is simply a rigid plate placed to stop the indenter at the same distance as in the experiments, meaning that it will not absorb any energy, just limit the deformation. This part differs from the physical experiments, in which the buffer consists of deformable aluminium profiles. Modelling these explicitly would require a more complex geometry, additional material parameters and more CPU resources. As most of the experiments went clear of the buffer, and the reasons stated above, this simplification seems adequately justified. Three contact pairs are present in the model, namely between the indenter and the pipe, between the support and the pipe, and finally between the indenter and the buffer. A penalty based surface-to-surface contact method [102] is utilised for all contact pairs.

As mentioned, the indenter is prescribed an initial velocity then just allowed to deform the pipe and energy is absorbed by plastic deformation of the pipe. This step lasts about 100-150 ms depending on the initial velocity, so a run time of 180 ms is typically used in the simulations. The stretch step, however, takes several minutes in real time as it is quasi-static, so time scaling has been utilised. A parametric study on time scaling was carried out, showing that the chosen bolt velocity (0.880 m/s) did not produce any undesired effects – both half and double this velocity generated more or less the exact same response (apart from some minor oscillations, which is to be expected).

Pipe thickness, impact velocity, element type and size, and choice of material

model are the main topics of interest for these simulations. Effects of these parameters will first be discussed for the shell models, as their running time is significantly lower. Experience and knowledge acquired from this endeavor will then be applied to the volume element models (although some things will be retested for these elements for verification) and some remarks will be noted towards the end.

7.2.2 Results

Dynamic, explicit simulations of pipes A to F were conducted with apt contributions from Slåttedalen and Ørmen [33], and from Fornes and Gabrielsen [34]. Not all results are shown, a selection showing the key results is presented. First, some simulation results using general purpose shells (called `S4R` in ABAQUS/Explicit [91], 4-node elements with reduced integration and 6 degrees of freedom per node) able to cope with being "thick" are presented. The general impression is that the results are quite good in global terms, and conforms with the three modes of deformation identified in Fig. 1.2. The numerical representation is shown in Fig. 7.2. As seen in Fig. 7.3, the numerical results complies well with the experimental data in the impact phase when using the average measured thickness for the pipe and a shell length of 2 mm.

Due to local variations in the thickness in the actual pipes used, one uniform thickness can misrepresent the pipe behaviour slightly. Thus, minor adjustments in the thickness (based on inverse modelling) is no blasphemous act and completely within reason. Lower thickness generally leads to a lower force level

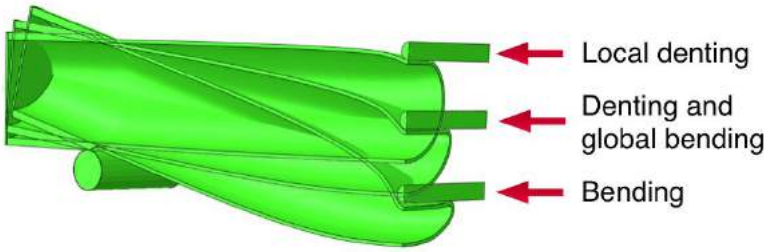

Figure 7.2: *The three modes of deformation are reproduced numerically.*

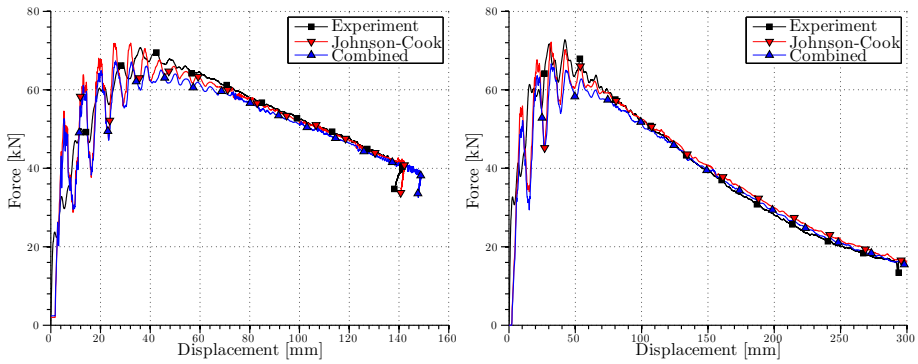

(a) *Pipe A, $t = 3.89$ mm, $v_0 = 3.24$ m/s* (b) *Pipe B, $t = 3.86$ mm, $v_0 = 5.13$ m/s*

Figure 7.3: *Experimental force-displacement data and numerical results from shell element simulations of impact test of pipe A (a) and pipe B (b).*

and higher end displacement[1]. There is very little difference in response between the two material models employed – the combined model has a slightly lower force level and produces a correspondingly higher displacement. Also, the impact velocity exerts the same influence as seen in the experiments, with the same consequences for the stretch step as well, into which the next paragraph now nicely transitions.

Where the impact phase was captured very accurately by the numerical tools employed, the stretch phase was not equally well represented as seen in Fig. 7.4. Also, some residual oscillations from the impact can be seen in the beginning of the force-displacement curves. It is worth noting that while testing pipe B, the the trolley hit the buffer in the rig. This was only included by limiting the maximum deformation in the analyses by a rigid plate the indenter could not traverse and hence did not absorb any energy. A simplification like this could of course be a source of error for the local deformation (and strain), to which the subsequent behaviour is quite sensitive. And because of the large impact velocity for pipe B, the force level during stretching is much lower as discussed in Chapter 4. Frames from the simulation of pipe B is shown in Fig. 7.5 along with corresponding frames from the high speed video, showing that the match is very good. The local denting is also captured quite well. Fig. 7.6 displays the

[1]Not explicitly shown until Fig. 8.20 to avoid increasing the already too large amount of graphs of this kind.

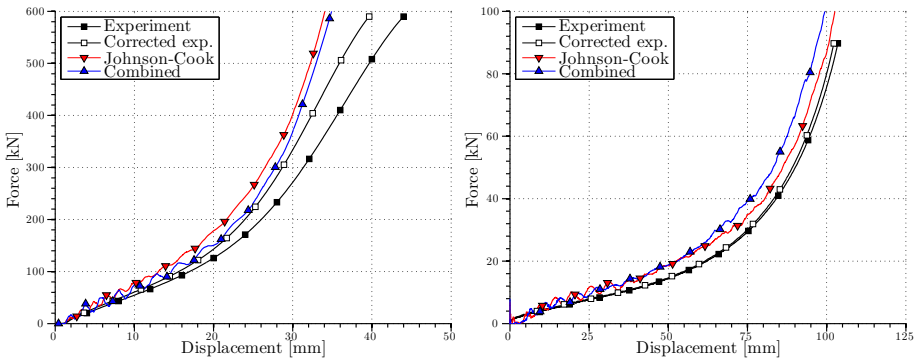

(a) *Pipe A, $t = 3.89$ mm* (b) *Pipe B, $t = 3.86$ mm*

Figure 7.4: *Experimental force-displacement data and numerical results from shell element simulations of stretch test of pipe A (a) and pipe B (b).*

numerical result of pipe B after stretching with a contour plot of the equivalent plastic strain, along with a picture of the physical specimen. The fracture itself, however, was not predicted accurately.

Of the two material models, one does not particularly out-perform the other for the stretch step either. At first the discrepancy was thought to arise from the machine stiffness in the rig being unaccounted for, but this only partly explains the gap. Additional clues can be found in the development of the damage parameter, plotted vs. equivalent plastic strain in Fig. 7.7 for the critical element in the model, i.e. the element which accumulates most plastic strain after the entire loading sequence. The maximum value it attains for pipe A (see Fig. 7.7(a)) during the load sequence is just below 0.8, where 1.0 signifies fracture. For pipe B in Fig. 7.7(b) the damage parameter eventually reaches 1.0, however much later compared with the experiment. In the experiments cracks emerged in all pipes during stretching, and this is not captured adequately here. When applied to burst testing of gouged pipes, a ductile failure approach with finite elements can produce good results [103].

Again no major difference was observed between the Johnson-Cook material model and the combined material model, except for pipe B when the test-based calibration of the Johnson-Cook fracture criterion was used (see Fig. 7.7(b)). In the end the damage parameter ends up at similar values but at somewhat

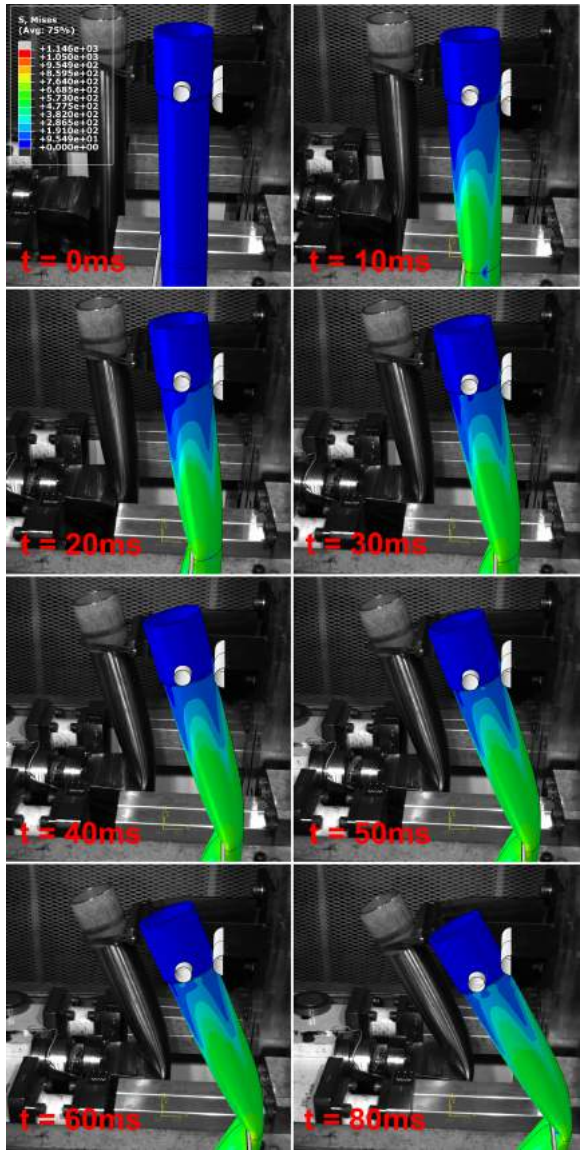

Figure 7.5: *Plot of finite element simulation of pipe B showing the von Mises equivalent stress using the Johnson-Cook material model, along with images from the high speed video from the experiment [33].*

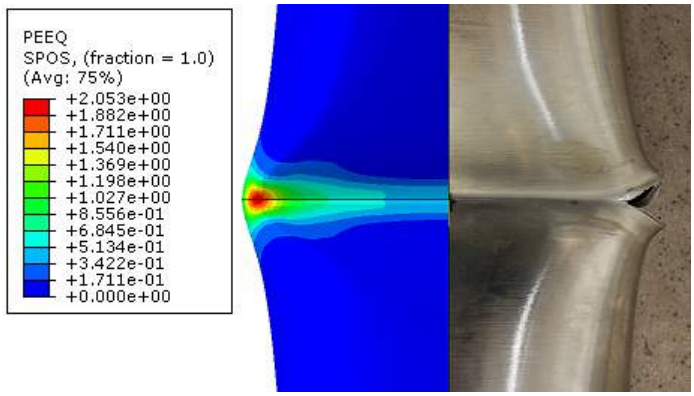

Figure 7.6: *Shell model of pipe B showing equivalent plastic strain after both impact and stretching with the Johnson-Cook material model, compared with an image of the corresponding full-scale test.*

different levels of plastic strain. The two techniques for calibrating the JC fracture criterion did produce some differences along the way to the final state, where they in the end were pretty close to each other. Still though, it is a bit too far from the test data to be called accurate. It is seen that the CL based calibration grows more rapidly during the impact step compared with the test based calibration. This is due to the triaxial state of stress in the element. During the impact, the triaxiality is much lower for large parts of the phase, and hence the damage grows more slowly (see Fig. 6.4). As has been noted in Chapter 5, fracture initiates before the stretch step commences and this fact is not adequately represented by the initial numerical simulations. The nonproportional loading herein is more difficult to predict fracture for, compared with, say, tensile tests like in Ref. [104].

The mesh for the volume element model initially had a uniform mesh with two elements across the thickness. 8-node linear brick elements with reduced integration and 3 degrees of freedom per node (called `C3D8R` in ABAQUS/Explicit) were used, and a lot of the same observations as for the shells are made. Naturally, the CPU time increased notably when utilising solid elements compared with shell elements. Specifically regarding the effect of wall thickness, the difference between material models, the accuracy of the impact step and the discrepancy in the stretch step are pretty much the same as for the shell models so plots are omitted for brevity.

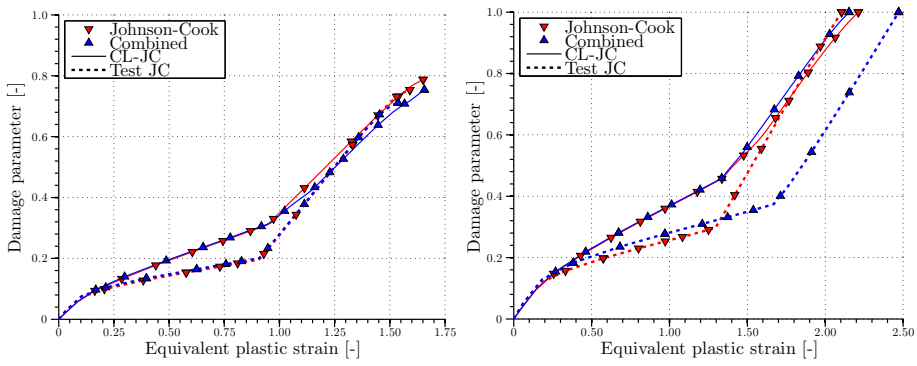

(a) *Pipe A* (b) *Pipe B*

Figure 7.7: *Development of the damage parameter in the critical element in shell models during the entire load sequence, where initiation of the stretch step occurs where there is a slight kink in the curves. Two calibrations of the JC fracture criterion are used, the Cockcroft-Latham (CL-JC) based calibration and the test based (Test JC).*

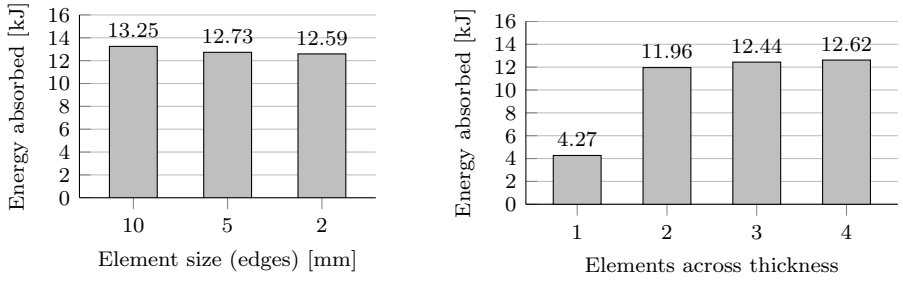

(a) *Shell element sensitivity* (b) *Solid element sensitivity*

Figure 7.8: *Mesh sensitivity study performed on a uniform mesh of pipe B in terms of absorbed energy (experimental value is approximately 11.74 kJ), with (a) showing the shell element analyses (b) showing volume elements.*

Regarding mesh sensitivity, the shell mesh was less susceptible to change. In terms of absorbed energy during impact, there was almost no difference between having edges with length 10 mm, 5 mm or 2 mm as shown in Fig. 7.8(a). This means that to estimate the global behaviour of the pipe during impact, an overly fine mesh is not needed as the force-displacement curves are very decent

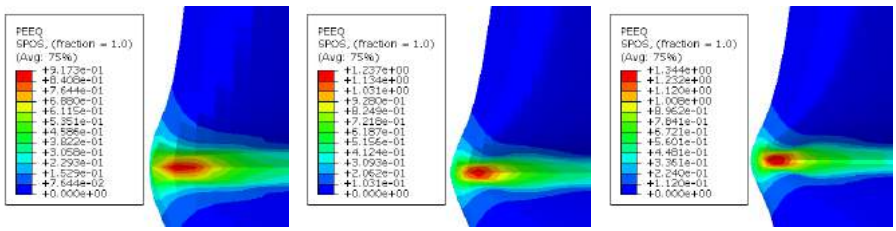

(a) *10 mm* (b) *5 mm* (c) *2 mm*

Figure 7.9: *Equivalent plastic strain after impact against pipe B, using various lengths for the shell elements (each with its own legend) [33].*

for a semi-coarse mesh. Halving the element size approximately quadruples the CPU time, and since shells are not particularly well suited for determining local strain (especially across the thickness), a relatively coarse mesh can be used to predict the global response. Locally though, the plastic strain increased with an increasing number of elements as more modes of deformation become available with more elements. A plot of the plastic strain after impact can be seen in Fig. 7.9. It is important to be careful though, as shell elements should not have a thickness much larger than the order of their lengths, which means that refining the mesh further than what is done here is not advisable. In order to predict fracture, which typically depends heavily on the plastic strain and triaxiality, it appears that using shells may not be the best approach due to the local strains (and thereby the fracture) being sensitive to the mesh grade even though the global response is not.

For the analyses using solid elements, a vast difference was seen when increasing from one to two elements across the thickness. Using only one element yielded rather atrocious results, as indicated in Fig. 7.8(b). With large displacements, rotations, and bending present, this is to be expected at linear solid elements in one row are generally not suited for bending problems [102]. Increasing to two elements improved the results drastically for the global response. Locally, more elements means higher plastic strain as for the shells (plot omitted). These simulations typically took 70 to 170 hours to complete. Refining the mesh even more would severely increase the CPU time so no further increase in number of elements was carried out.

As the indenter hits the buffer when analysing pipe B, thereby creating a disturbance which is not completely controlled, pipe D is used for further studies.

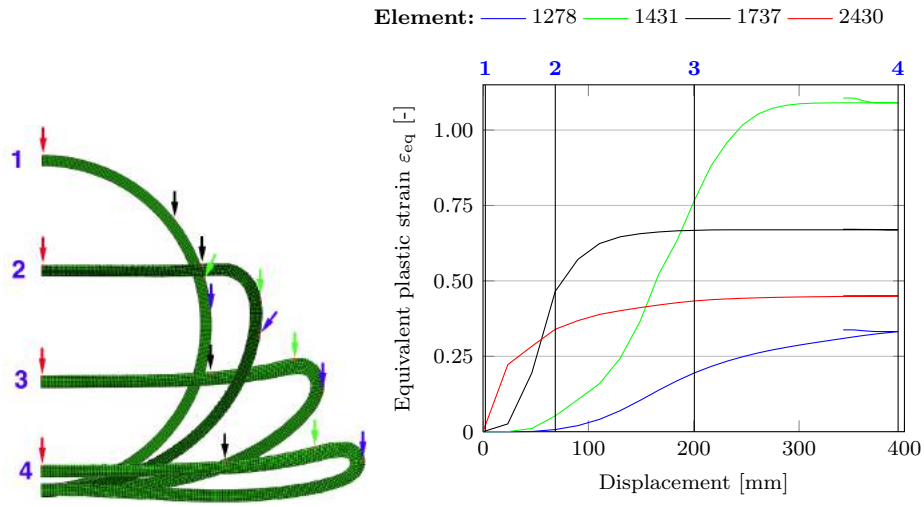

(a) *Stages of deformation* (b) *Equivalent plastic strain*

Figure 7.10: *Equivalent plastic strain at different locations and at different stages of deformation during the analysis.*

Using this analysis run with the JC constitutive relation and JC fracture criterion with the CL based calibration, some more detailed examinations of the results are made.

In the following discussion the focus is with the most critical element in the analysis. "Most critical" means the element where the equivalent plastic strain is largest after the full test procedure. A few words are well spent with this. The critical element at any given time is not necessarily the same as at any other time. To illustrate what is meant, Fig. 7.10 is used as an aid, with the most severely deformed pipe cross-section (pipe K in this instance, impacted at 5.18 m/s). In the beginning (from frame 1 to 2) element number 2430 (red line and arrow) directly under the indenter suffers the most, and then element 1737 (black) takes over as the plastic hinge passes through it (frame 2 to 3). Finally, element 1431 (green) is subjected to the highest plastic strain during the last stage (fram 3 to 4), while number 1278 on the outer edge just tags along the deformation. So in this case the most critical element for the simulation as a whole would be element 1431, and is thereby used to discuss the simulation and

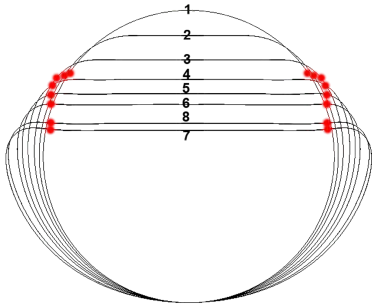

(a) *Cross-section during impact*

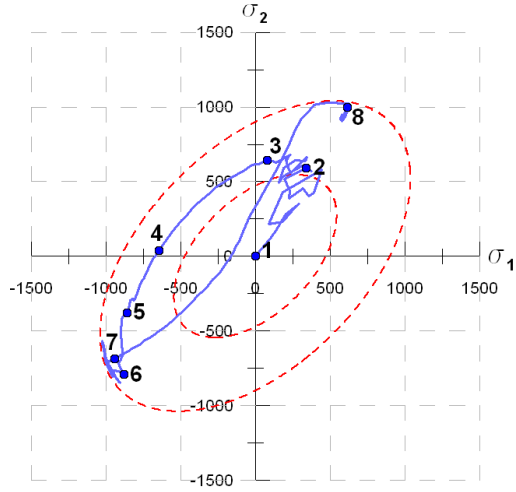

(b) *Principal stresses during impact*

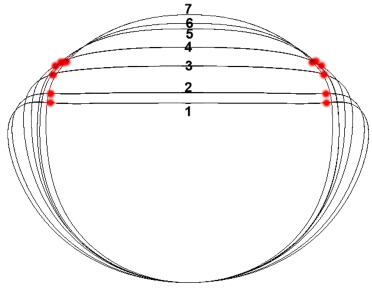

(c) *Cross-section during stretching*

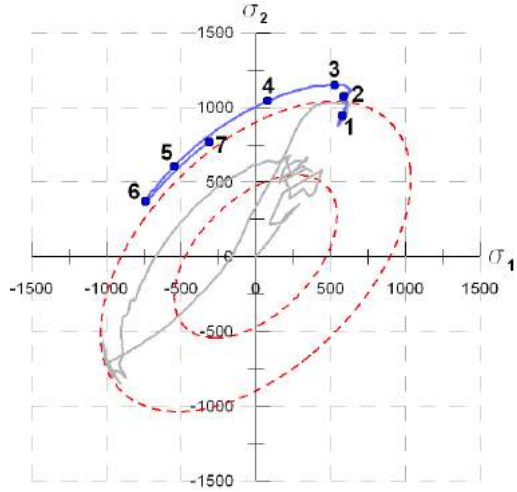

(d) *Principal stresses during stretching*

Figure 7.11: *Outline of cross-section and development of σ_1 and σ_2 during impact and stretch simulations of shell model of pipe D, with the smaller dashed oval shape represents the initial yield surface and the larger represents the yield surface after impact [33].*

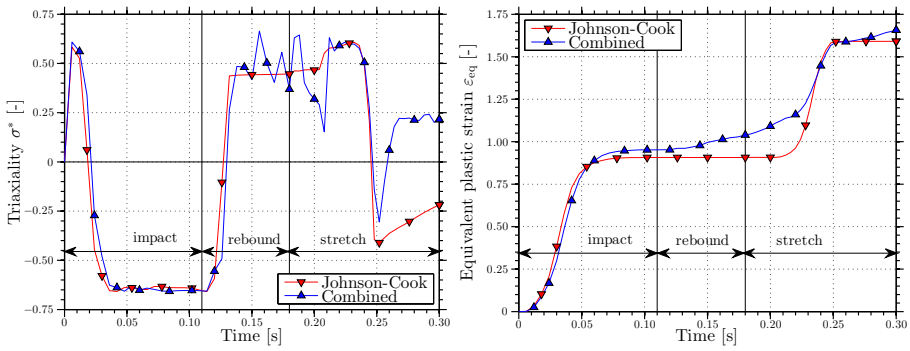

(a) *Triaxiality* (b) *Equivalent plastic strain*

Figure 7.12: *Triaxiality (a) and equivalent plastic strain (b) vs. time in critical element for shell analysis of pipe A ($v_0 = 3.24$ m/s).*

how damage evolves. This "most critical" definition is used in the discussion illuminated by Fig. 7.11.

The impact step is divided into 8 frames in Fig. 7.11 and the stretch step into 7, with (a) and (c) showing the outline of the cross-section during impact and stretching, respectively. The position of the most critical element is indicated by red dots in Fig. 7.11(a) and (c). Parts (b) and (d) contain the development of the two principal stresses σ_1 and σ_2 during impact and stretching, respectively, along with the initial yield surface and the yield surface after impact only.

From frame 1 to 2 during impact, deformation is largely elastic in the critical element and the stresses are positive. Progressing to frame 3 initiates plasticity and the stresses are still positive and the critical element is on the tension side of a bending deformation. This changes after the plastic hinge has passed through the critical element, and the load is largely compressive for the remainder of the impact. In such conditions the strain to fracture is large for the JC fracture criterion (see Fig. 6.4), and damage does not grow at all in the CL criterion when $\sigma_1 \leq 0$ (see Section 6.3.2).

Frame 8 shows that during the springback the stresses are once again tensile, and it is during this stage that the cleavage fracture surfaces seen in the experiments are thought to emerge. Large compressive strains before applying tension do appear to reduce the subsequent tensile strain to fracture according

to the experiments. As an example, the triaxiality and equivalent plastic strain during the course of the analysis have been plotted in Fig. 7.12 for pipe A. The triaxiality is negative during impact and turns positive during the rebound, and remains so during straightening of the pipe. During the latter part of the stretch phase the triaxiality is not necessarily positive as the cross-sectional profile itself retracts towards being a circle again, thereby causing a somewhat fluctuating stress state. Further, it is seen that the plastic strain does not grow particularly during rebound as this is mostly elastic (the combined model has lower re-yield stress and more plastic strain is induced). These are recurring trends in the analyses. From the experiments in Chapter 4 it has been shown that the rebound is the critical phase.

Moving on to the stretch step, it is noted that it starts off with tensile stress as expected. As the deformed cross-section transforms towards a circle again, some negative stresses are noted before it once again motions to a pure tensile stress state when the pipe straightens. From Fig. 7.7 it is clear that it is during this stage that the damage parameter grows most, and this is reflected through the state of stress. It is worth noting that the stresses become quite high in magnitude, almost three times the yield stress at most, which can be an agent for producing cleavage fracture. The same analysis has been conducted for pipe B, from which very similar results emerged and will for that reason not be plotted in detail. Apart from the obvious differences (larger deformation, larger plastic strain, etc.), the results were pretty much the same.

In Fig. 7.11 the yield surface expands with plastic deformation as the constitutive relation accounts for isotropic hardening only. If a purely kinematic hardening model had been used, the yield surface would merely have been translated rather than expanded, an illustration of which can be seen in Fig. 7.13, depicting the situation right after impact and before the springback. In turn this would result in a much lower yield stress and presumably lower force during stretching. This is what first spawned the idea of including kinematic hardening, but according to Fig. 7.4 the effect came out small, at least globally, when using the combined model. On the local level the values of the stresses naturally differed somewhat, but in terms of compression/tension the results were in agreement with each other.

From these intial simulations a few conclusion can be drawn. The impact phase is generally very well captured globally, but when fracture becomes important, i.e. during springback or further loading of the pipe, accuracy declines. That is not to say that the simulations are way off, but the residual capacity of the pipe

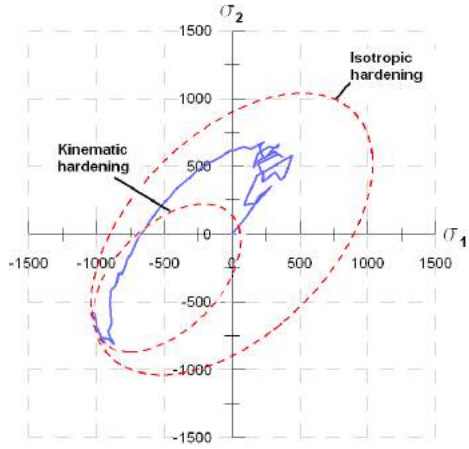

Figure 7.13: *The effect of a purely isotropic hardening material model and a purely kinematic [33].*

is overestimated but still in the same ballpark. When conducting such analyses one must be prudent.

Introducing a combined isotropic/kinematic hardening model appeared to exert litte influence on the results obtained. There were some minor differences, but on the whole results were very similar. Prediction of fracture locally proved difficult to achieve, but the fracture criterion employed may not be the best suited for this task.

In terms of mesh sensitivity, the shell mesh used was perhaps as fine as allowable, and all mesh grades using shells provided adequately accurate results in terms of global behaviour. So if the global response is the main topic of interest, shells seem to work well and have much lower CPU cost.

When local deformation becomes important, as it does in fracture, solid elements are the way to go as a more accurate strain field can be obtained by refining the mesh locally (in the thickness direction as well). For predicting the global response with solids, at least two elements are needed across the thickness to capture the bending modes induced on the pipe geometry.

In short, the global response is well represented during impact and the force is a bit overestimated in the stretch step, most likely due to fracture not being

captured adequately. The deformation is accurately described, but strains on a local level can be difficult to predict. In addition, these kinds of simulations make it possible to analyse the local deformation processes, e.g. as done in Fig. 7.11. This is, if not impossible, then very difficult, to quantify with the experiments alone. With dynamic transient experiments, as opposed to quasi-static tests, it can be hard to obtain accurate measurements on a local level as events take place over a very short time span.

7.3 Submodelling

7.3.1 Setup

Submodelling is a technique available in ABAQUS/Explicit in which a global simulation provides boundary conditions for a local simulation. In a step-wise bullet-point form the procedure looks like this:

1. Run global analysis.
2. Define area to be further investigated, which defines the geometry for the submodel.
3. Use global results as boundary conditions for the submodel.
4. Run analyses on submodel at less expense and evaluate results.

This approach seems like a good idea if the interesting things happening are confined to a rather small portion of the pipe. As the global deformations, and to a large extent the local deformations as well, are represented quite accurately by the solid elements in the preceding section, the boundary conditions for the submodel should be adequate.

Even if the displacements are accurate in the global simulations, this does not necessarily apply to the strains, which are obtained by the derivatives of the displacements, and hence less accurate. The idea is then to use the submodel with a refined mesh and thereby obtain a better description of the strain field. All models in this section are run with the combined material model and the CL fracture criterion, with apt contributions from Digerud and Lofthaug [38].

While trying out different sizes and widths of the submodel domain, some experiences have been gained. Though a lot simulations were run in order to obtain

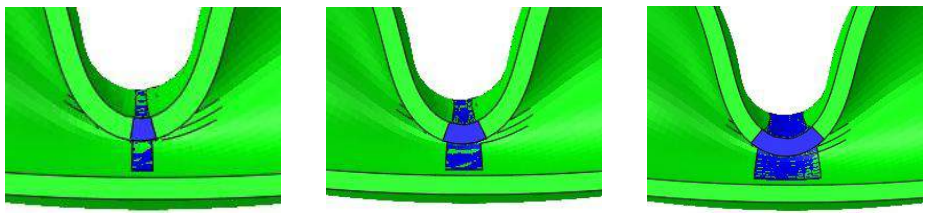

(a) *Width 4.1 mm, 312 els.* (b) *Width 8.2 mm, 624 els.* (c) *Width 16.4 mm, 1248 els.*

Figure 7.14: *Global model (green) with three elements across the thickness and submodel (blue) with various widths.*

this information, not all of them will be presented in detail. First it was deemed necessary to run a halved model rather than a quarter, i.e. the symmtry plane $x = 0$ in Fig. 7.1 is not utilised. The critical area is at midspan, so to obtain the best possible boundary conditions for the submodel this extension was used.

Further, the size of the submodel is important, and one has to balance between the critera "smaller for efficiency" and "larger for accuracy". Fig. 7.14 shows three different sizes of submodels, of which the middle was evaluated as the

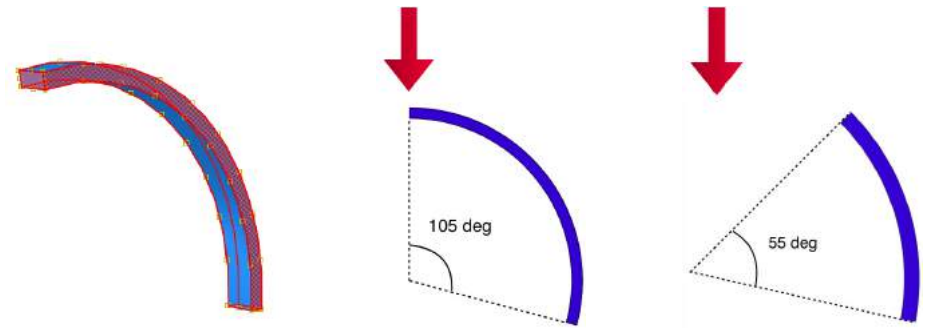

(a) *Surfaces where displacements are transferred from global model* (b) *105°* (c) *55°*

Figure 7.15: *Geometry and boundaries of the submodel domain, with the arrow indicating the indenter direction.*

better of the three in terms of accuracy and CPU time. Also, the plastic strain values of the models in Fig. 7.14(a), (b) and (c) were 0.807, 0.818 and 0.821, which are marginally different (the global model got 0.806).

As indicated in Fig. 7.14, the submodel does not extend around the entire circumference – only 105° (from the top) of the total 180° are modelled (55° was also tested). Fig. 7.15 displays the geometry of the submodel, and the surfaces on which displacements from the global model are applied.

7.3.2 Results

The three different submodels from Fig. 7.14 were run with the same element size, and the results from the submodel (blue) match the global result (green) exactly as expected, which makes for a promising start. To examine whether a mesh refinement of the submodel is a viable approach, a global model with nine elements across the thickness was run for comparison with a submodel refined from three to nine elements across the thickness with boundary conditions from the global model using three elements across the thickness.

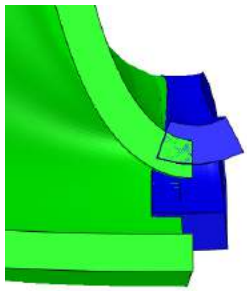

(a) *Global (green) and submodel (blue)*

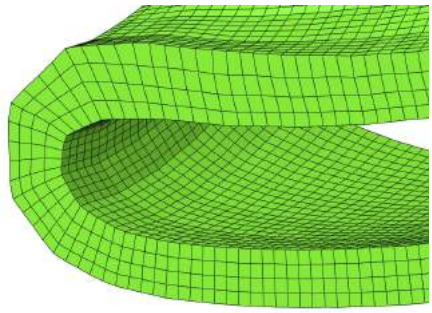

(b) *Submodel displacement transfer*

Figure 7.16: *Relations between global model and submodel for pipe K ($v_0 = 5.18$ m/s), with (a) showing a global model using nine elements across the thickness compared to submodel with nine elements across the thickness but with deformations from a global model with only three elements across the thickness. Part (b) shows how refining the mesh from a global model to a submodel introduces inaccuracies.*

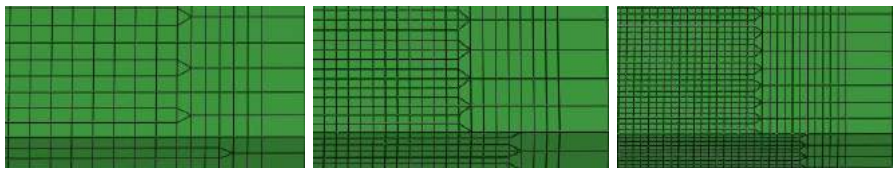

(a) *From two to three* (b) *From two to six* (c) *From three to nine*

Figure 7.17: *Various mesh transition zones, with the slightly darker shade at the bottom showing the variation across the pipe wall thickness.*

The results were, to exaggerate somewhat, deplorable. Fig. 7.16(a) shows the submodel with nine elements across the thickness (in blue, driven by the global model with three elements across the thickness) superposed with the global model with nine elements across the thickness (in green). As seen, the displacements do not match, which in practice just means that the global model with three elements across the thickness has not converged fully. Refining the submodel only can not ameliorate this.

Another thing is that the deformations are linearly interpolated where the mesh is refined, as depicted in Fig. 7.16(b). Here the transition is made from one element globally to four elements locally for illustrative purposes, and it is clear that the submodel suffers from the transfer of deformations. Although this particular example (one to four elements) is a bit misrepresenting and overstating the problem, the problem is still a real one as the linear brick elements only have C^0 continuity and no rotational degrees of freedom. It will of course be less influential for a finer global mesh, but this may force some artificial strains into the system.

Three submodels were run based on the global model with three elements across the thickness – one with three, one with six and one with nine elements across the thickness. In addition three global models with the same elements size were run for comparison as before, but not with e.g. nine elements along the entire pipe. The middle section of the pipe was refined with transition zones in the mesh generated by the open-source pre- and post-processor Salome [105], and the different mesh transitions are illustrated in Fig. 7.17.

Equivalent plastic strain in the most critical element has been plotted vs. the global displacement in Fig. 7.18. The global model and the submodel with three elements across the thickness naturally match quite well, but the hope that the

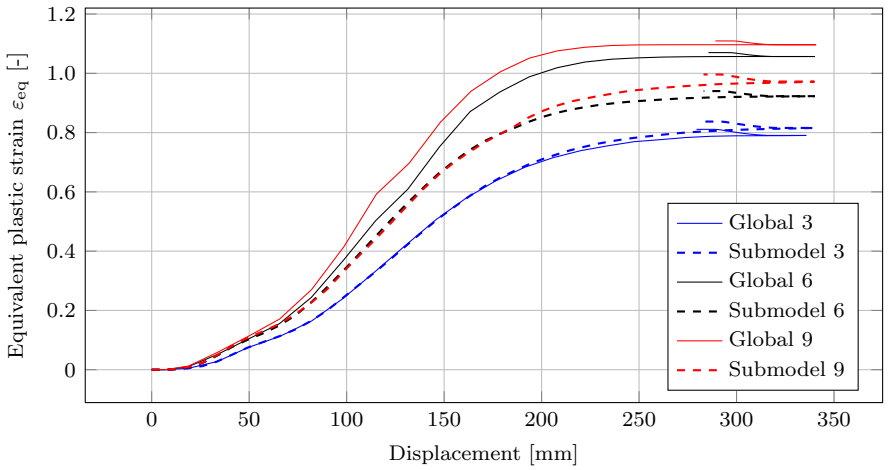

Figure 7.18: *Equivalent plastic strain vs. displacement for the critical element from the different global impact models of pipe K and corresponding submodels. Keep in mind that the submodels are driven by the global 3 model.*

refined submodels would provide a similar convergence as refining the global model deminishes here. In all models a small increase in plastic strain is seen during the springback phase.

During the course of these submodel investigations, it has become clear that using this feature with a mesh refinement is probably not its intended use. Sumodelling finds its niche when investigating a small component in a large global analysis, e.g. a crashbox in a car crash simulations. The point of the submodel is then to test different materials or conduct parameter studies at a severly reduced computational cost. Studies using submodelling is then left at that.

7.4 Simulations of stretch-bending experiments

Next the experiments from Section 4.5 are modelled numerically. This was done to see if the effect of adding a horizontal load in various forms was captured accurately and that the effect of internal pressure was adequately represented. Contributions regarding these simulations from Asheim and Mogstad

[36], from Jakobsen [37], and from Digerud and Lofthaug [38], are greatly appreciated.

7.4.1 Setup

This section contains simulations of the component tests conducted in Section 4.5, which imposed a displacement controlled transverse deformation while simultaneously applying an axial load in three different variations (no load, constant load, linearly increasing load). Both symmtry planes from Fig. 7.1 were used, and three parts were modelled: the pipe, the indenter and a rigid connection link to which the axial loads were applied. This was given a reference point corresponding to the point of rotation for the boundary condition in the actual rig. A sketch is drawn in Fig. 7.19, showing the three parts, and a typical pipe mesh is shown in Fig. 7.20.

The simulations were carried out in four steps analogous to the experiments:

1. Apply pressure and horizontal load (if they are to be included) using a smooth curve, duration 30 s.
2. Indenter displacement controlled to 200 mm with smooth acceleration to constant velocity and linear increase of axial load if included, duration 532 s.

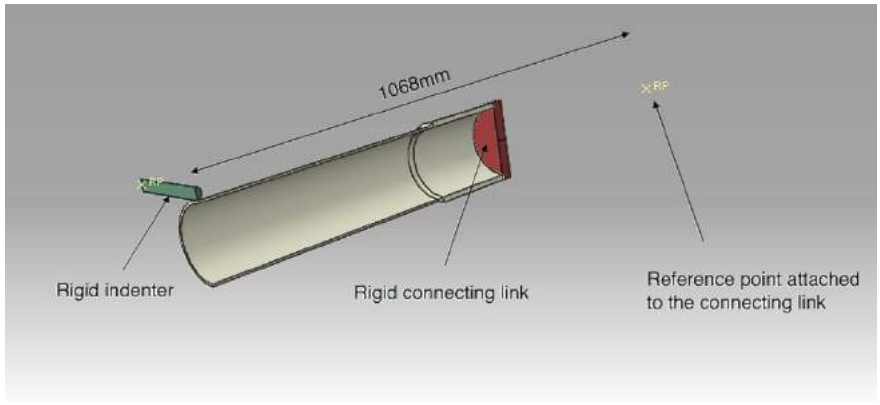

Figure 7.19: *Sketch of numerical setup for simulations of pipes tested in stretch-bending rig, using two planes of symmetry.*

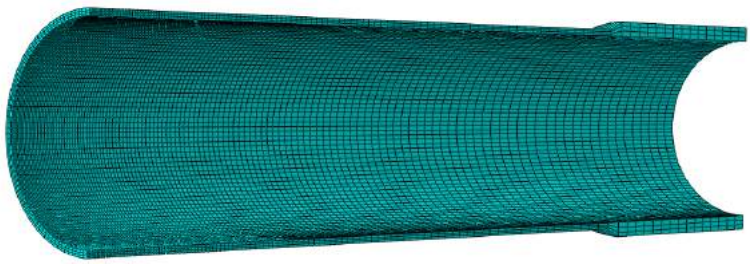

Figure 7.20: *Solid mesh used when simulating pipes with and without internal pressure.*

3. Fix reference point of rigid link while removing indenter, duration 25 s.
4. Release reference point of rigid link for unloading while interaction between indenter and pipe is deactivated.

The magnitude of the pressure and axial loads were as registered in the experiments. During the last step some oscillations were present in the model, without appearing to affect the results significantly. Further oscillations were noted as a consequence of mass scaling, a small study on which is performed in Fig. 7.21 and Table 7.1.

Here pipe 8 is used as an example with the mesh in Fig. 7.20 (three elements across the thickness), with different scale factors for the density. It is seen that scaling with 10^8 produces oscillations of an influential magnitude, while using a factor of 10^7 results in quite small oscillations by comparison. Still, the factor chosen to proceed with was 10^6 as it offered a good compromise between speed and stability of deformations as it is almost completely covered by the curve from the simulations using 10^5, presumably providing more accurate results.

Table 7.1: *Comparison between different magnitudes of mass scaling on the pipe with zero horizontal loading (pipe 8).*

Factor	CPU	Kin. energy	Rel. force	Ind. strain	End strain
10^8	1:00	0.9000%	−4.97%	0.501	0.726
10^7	3:10	0.0900%	−6.48%	0.474	0.709
10^6	9:09	0.0090%	−6.64%	0.461	0.740
10^5	30:06	0.0009%	−6.66%	0.459	0.795

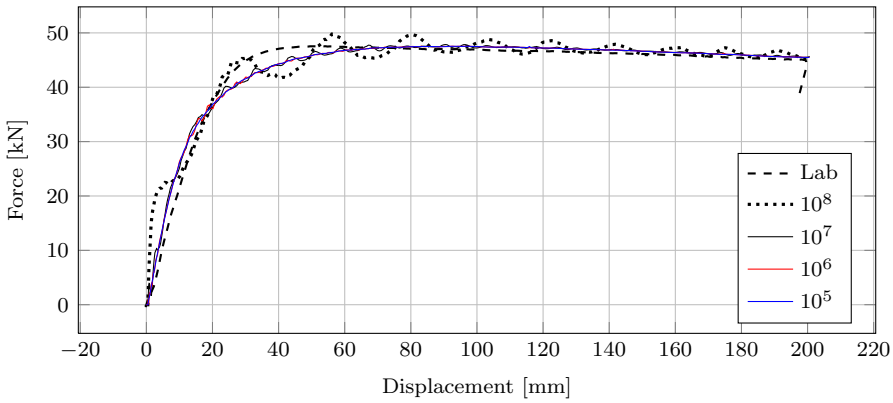

Figure 7.21: *Force-displacement plot for different mass scaling factors on the model with zero horizontal loading and 103 Bar pressure (pipe 8).*

Table 7.1 gives a summary with the scale factors in the left column, and the stated CPU times in [hours:minutes] are obtained when using 8 CPUs. When increasing the density with a factor 10, the CPU time decreases with a factor of about $\sqrt{10}$. The third column shows the kinetic energy relative to the total energy, while the relative force in the fourth column is the difference between the average indenter force in the simulations and in the experiments. The final two columns are the plastic strain right after maximum indentation depth is reached, and the maximum plastic strain after complete unloading, between which there is a significant difference.

A quick recapitulation of the what the different pipes are, is given here. Six pipes are simulated, and these are

Pipe 4 – No axial load, no internal pressure.

Pipe 5 – Constant axial load of 53 kN, no internal pressure.

Pipe 6 – Linearly increasing axial load from 0 kN to 53 kN, no internal pressure.

Pipe 8 – No axial load, 103 Bar internal pressure.

Pipe 9 – Constant axial load of 53 kN, 103 Bar internal pressure.

Pipe 10 – Linearly increasing axial load from 0 kN to 53 kN, 101 Bar internal pressure.

7.4.2 Results

Some results from shell element simulations of the stretch-bending process without pressure are plotted in Fig. 7.22. These simulations are conducted using shells with length 2 mm and the same contact formulation as used in the previous simulations. The results are quite satisfactory, and the effect of thickness is exactly as expected and shown earlier. Globally, the tensile axial load stiffens

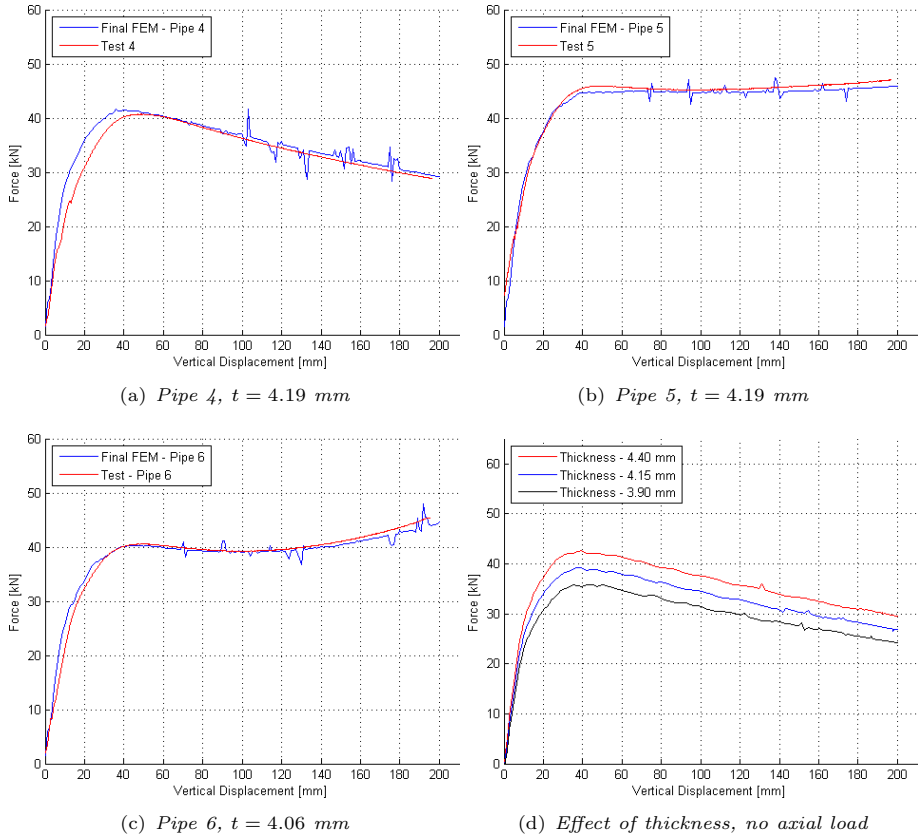

(a) *Pipe 4, $t = 4.19$ mm*

(b) *Pipe 5, $t = 4.19$ mm*

(c) *Pipe 6, $t = 4.06$ mm*

(d) *Effect of thickness, no axial load*

Figure 7.22: *Force-displacement curves from simulations (blue curves) of pipes 4, 5 and 6 ((a),(b) and (c), respectively) tested in stretch-bending rig along with experimental data (red curves), while part (d) shows the effect of altering the thickness [37].*

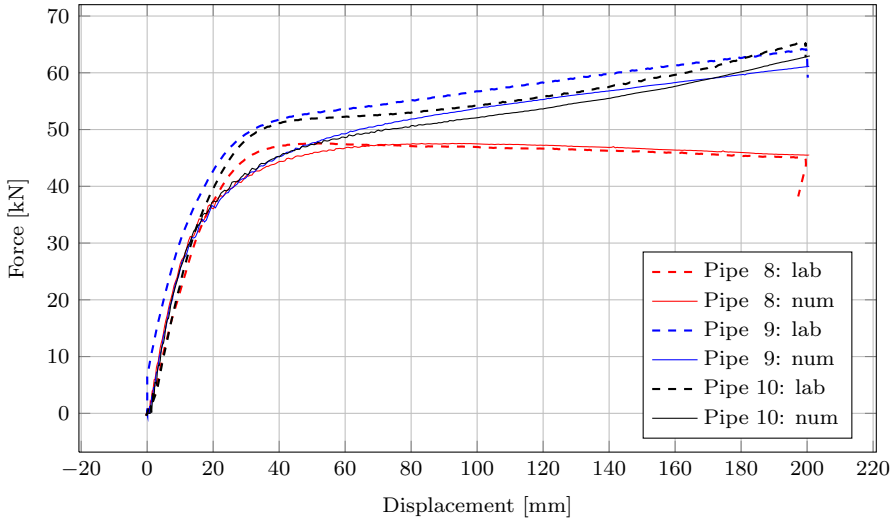

Figure 7.23: *Experimental (dashed curves) and numerical (solid curves) force-displacement curves for pipes 8, 9 and 10.*

the system as in the experiments. It is difficult to assess whether the axial force has any influence on the local strains (both experimentally and numerically). Further, the results are compared with DIC analyses of the same pipes. Only pipe 5 and 6 are included for DIC as the measurements for pipe 4 were of inadequate accuracy. The DIC results of the strain fields are shown in Fig. 4.44. The numerical results were quite similar in both distribution and magnitude, and will not be shown here for brevity. There is not a whole lot to learn other than recognising that the results are of the same magnitude and appear to represent the deformation well, so DIC results will not be further elaborated on here.

Moving on to the pipes with internal pressure, simulations are now performed with volume elements with three elements across the thickness. The mesh used is the same as in Fig. 7.20, and has a bias with higher element density towards the middle (1.4 mm at center, 10 mm at the end). In terms of force-displacement (see Fig. 7.23), the results are quite good with the simulations underestimating the force for deformations of about 20-60 mm. A better compliance with the experiments were obtained by Asheim and Mogstad [36] where only isotropic hardening was accounted for, meaning that the kinematic hardening part seems

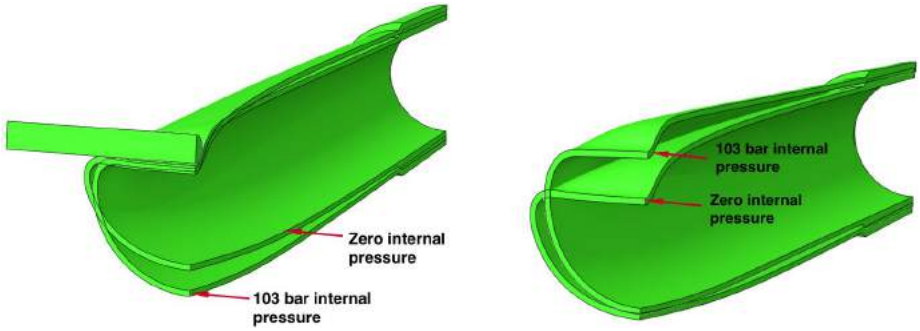

(a) *Right after max. indentation* (b) *After complete procedure*

Figure 7.24: *Comparison of deformation between loading with internal pressure (pipe 8) and without internal pressure (pipe 4), while no axial load is applied.*

to elicit a slightly too soft response in this case. Of course, local variations in wall thickness could also be important.

More interestingly, the deformation when including internal pressure was altered in accordance with the experiments, intuition and work by others (see e.g. Ref. [4]). The cross-sectional profile of the pipe appears much less squashed, and the internal pressure stiffens the response. Fig. 7.24 shows the deformed shapes of the pipes after maximum indenter displacement is attained (a), and after the full procedure (b). As seen, the deformation of the cross-section is as expected reduced when including pressure. Also, the magnitude of the maximum equivalent plastic strain at maximum indentation is decreased when adding internal pressure. This can be explained by the reduced curvature of the cross-sectional profile.

The cross-section at different stages can be seen in Fig. 7.25, along with equivalent plastic strain in the most critical element (marked in red) and the corresponding stress triaxiality. The figures on the left show the cross-section with the plastic hinge transversing it. First (stage 1-3) the element is bent with positive triaxiality before suffering a negative triaxiality during the following stages (3-6), during which plastic strain grows a lot. When unloading, the triaxiality becomes positive again. Differences between pressure and no pressure was greater than between the different axial loading conditions (no load, constant load and linearly increasing load) and was hard to quantify, hence no data is plotted to show this.

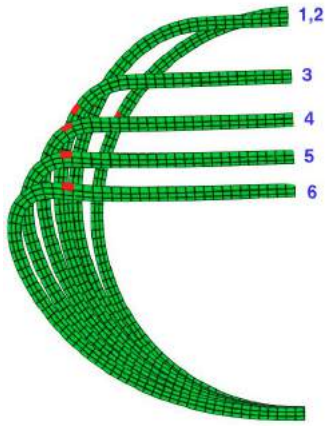

(a) *Stages of deformation, 0 bar*

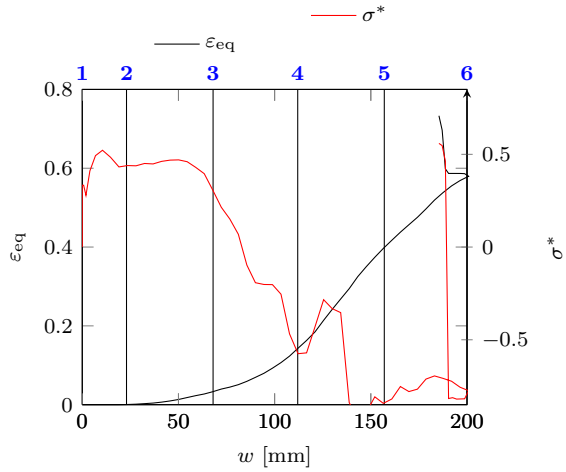

(b) *0 bar internal pressure*

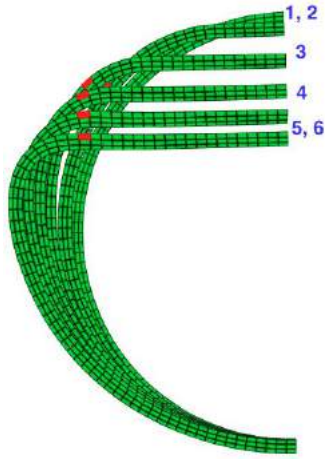

(c) *Stages of deformation, 100 bar*

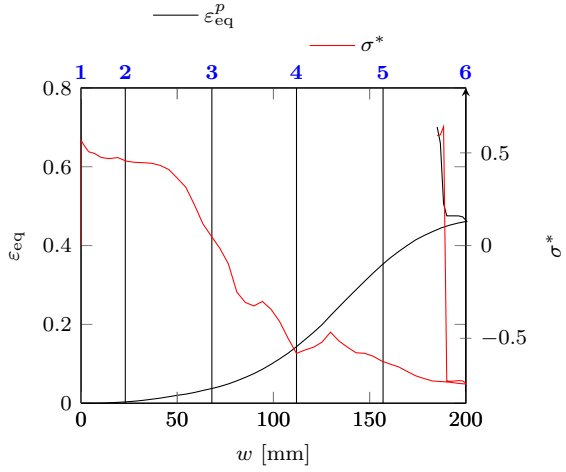

(d) *103 Bar internal pressure*

Figure 7.25: *Equivalent plastic strain, ε_{eq}, plotted against indenter deformation, w, along with the stress triaxiality, σ^*. Data is extracted from the element with the highest magnitude of equivalent plastic strain after loading and unloading (element marked in red).*

7.5 Discussion

In general the simulations are able to represent the impact phase with good accuracy, using both shell and volume elements. Employing a material model with isotropic hardening versus combined isotropic/kinematic hardening had little influence on the impact as both worked well, although some minor differences were detected during the stretch phase. The springback and stretching phase following the impact are not as well represented due to fracture taking place. Fracture initiates at scales much lower than the typical element size, which is one reason that it is very difficult to predict. Also, it seems that the pressure is well accounted for (at least on a global level) as the force-displacement curves are reproduced accurately.

Based on the many different approaches and simulations carried out in this thesis, an obvious continuation of this work would have been to rerun some of these models applying a fracture criterion accounting for brittle fracture. As the stress levels can become quite high (many times the yield stress), a stress based approach like in the work by Ritchie et al. [106] would make an excellent starting point. Also, from Fig. 3.9 it is seen that the stress at fracture is quite similar, which can serve as further justification for a stress based criterion. This is, however, left for further work.

Chapter 8

Fluid-structure interaction

8.1 Introduction

This chapter presents an outline of the idea behind the arbitrary Lagrangian-Eulerian formulation and of the treatment of fluid-structure interaction (FSI) in the Europlexus code, which is a state-of-the-art explicit finite element code made for fast transient dynamics involving FSI. Results from such simulations are also presented.

The notation and terminology used herein is similar to what is used in Ref. [107]. In Europlexus different discretisation techniques are available for the fluid domain; finite elements (FE), finite volumes (FV) and smoothed particle hydrodynamics (SPH).

For the FEs and FVs, the fluid-structure interface may be nodally *conforming* or *non-conforming*, or the structure may be *embedded* in the fluid mesh. Further, two different types of coupling between the fluid and the structure are available – a "weak" coupling and a "strong" coupling. An overview of the available FSI algorithms is available in Fig 8.1. Before going into detail on these terms, some more general topics are considered.

	Detection Strategy	Spatial Discretization		Enforcement Strategy	Name / command	Use with
FSI Algorithm 	**Basic** (no structural failure)	**Conforming** F-S meshes	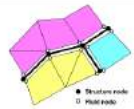	**Strong**	**FSA**	FE, NCFV
				Weak	Merge F-S nodes	CCFV
		Non-conforming F-S meshes		**Strong**	**FSA**	FE, NCFV
				Weak	Declare non-matching F-nodes	CCFV
	Embedded (structure can fail)	S-mesh is **Immersed** in the F-mesh	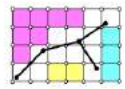	**Strong**	**FLSR**	FE, NCFV
				Weak	**FLSW**	CCFV

Figure 8.1: *A summary of fluid-structure interaction (FSI) algorithms in Europlexus [108], excluding SPH.*

8.2 The arbitrary Lagrangian-Eulerian formulation

In a *Lagrangian* formulation, each node of the computational domain corresponds to a specific material point throughout the calculation. This is the most widely used formulation in solid mechanics, as it nicely keeps track of how a structure deforms during loading [109]. If, say, a continuous flow of water was to be modelled, such an approach would require the modeler to keep track of each individual particle of water. To this end, the *Eulerian* formulation is superior, in which the nodes of the mesh are fixed in space and the water moves with respect to the grid, making the large displacements of the material points easier to handle [92].

The *arbitrary Lagrangian-Eulerian* (ALE) formulation seeks to utilise the advantages of both formulations, while, as far as possible, minimising the drawbacks. Using this method, the nodes may be moved along with the material in a Lagrangian sense, they may be kept in place to remain Eulerian, or, finally, the nodes can be moved arbitrarily to accomodate rezoning needs and avoid mesh entanglement. Fig. 8.2 illustrates the different descriptions in one dimension. In case of large motions/deformations of the (Lagrangian) structure in an FSI analysis involving ALE, the fluid mesh is allowed to follow these deformations in order to keep the mesh somewhat in order. Naturally, a clever way to describe

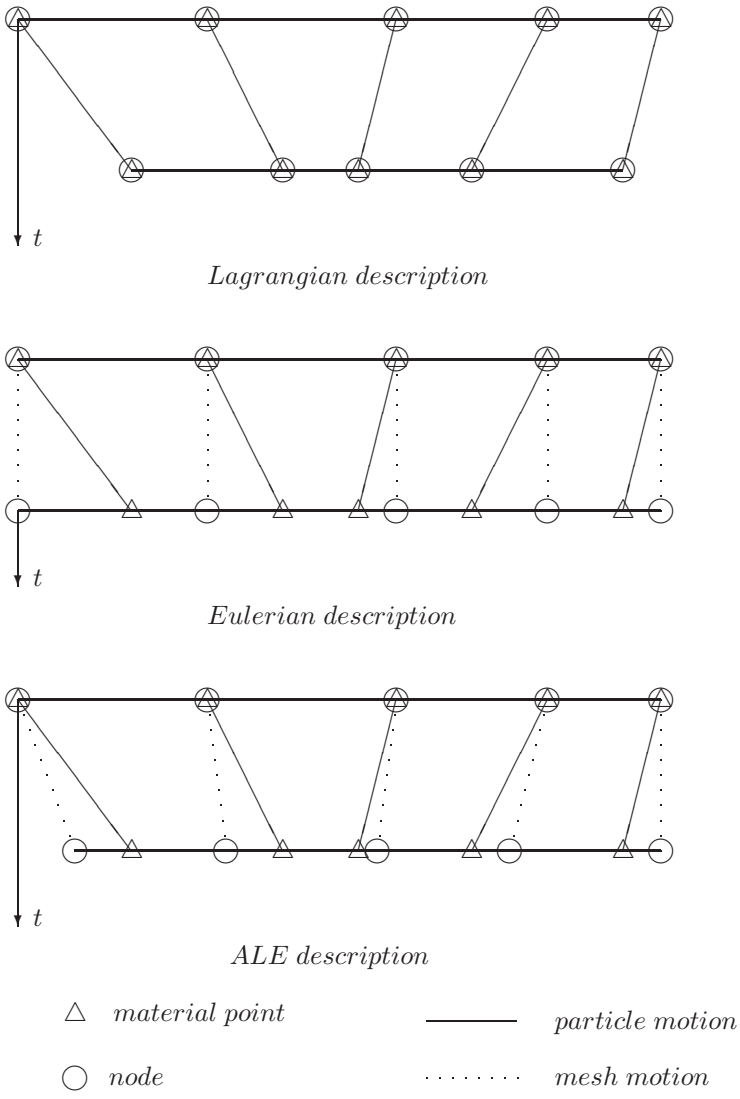

Figure 8.2: *1D example of Lagrangian, Eulerian and ALE mesh and particle motion [110].*

the motion of the fluid mesh is then needed, several of which are available in Europlexus. Some of them are explained herein, and all of them are described in the Europlexus manual [111]. It is worth noting that in an ALE calculation the motion of the nodes/mesh – which by definition can be arbitrary – do not necessarily bear any particular physical meaning. More details can be found in Ref. [112].

8.3 Governing equations

8.3.1 Structure

A Lagrangian formulation is consistently adopted for the structural subdomain, and the governing equation is that of dynamic equilibrium arising from the principle of virtual work. After discretizing the stucture using finite elements and generating the lumped (diagonal) mass matrix $\mathbf{M}$, the equation looks like

$$\mathbf{M}\mathbf{a} = \mathbf{F}^{\text{ext}} - \mathbf{F}^{\text{int}} \tag{8.1}$$

in which $\mathbf{a}$ is the vector of nodal accelerations, $\mathbf{F}^{\text{ext}}$ are the external forces and $\mathbf{F}^{\text{int}}$ are the internal forces. $\mathbf{F}^{\text{int}}$ is found by integrating the product of the matrix of shape function partial derivatives $\mathbf{B}$ and the Cauchy (true) stress $\boldsymbol{\sigma}$ over each element volume V_n, and subsequently assembling (Σ is the assembly operator in the following equation) the results for all elements from 1 to N_{els}

$$\mathbf{F}^{\text{int}} = \sum_{n=1}^{N_{\text{els}}} \int_{V_n} \mathbf{B}^{\mathrm{T}} \boldsymbol{\sigma} \mathrm{d}V \tag{8.2}$$

Eq. (8.1) is solved explicitly (lumped mass matrix) and directly integrated in time by finite differences. Details can be found in Refs. [108, 111, 113].

8.3.2 Fluid

Europlexus is an explicit solver, and the structure is always formulated as Lagrangian using finite elements of different kinds. The fluid generally uses a

Eulerian or ALE formulation (except when using SPH), and the coupling between the fluid and structure can be handled in different ways. By default, the fluid is modelled as *compressible* and *inviscid* using the well-known Euler conservation equations (see e.g. Ref. [114]),

$$\begin{aligned} \frac{\partial \rho}{\partial t} + \nabla \cdot (\rho \mathbf{v}) &= 0 \\ \frac{\partial \rho \mathbf{v}}{\partial t} + \nabla \cdot (\mathbf{v} \otimes (\rho \mathbf{v})) + \nabla p &= \mathbf{0} \\ \frac{\partial E_T}{\partial t} + \nabla \cdot (\mathbf{v} \, (E_T + p)) &= 0 \end{aligned} \tag{8.3}$$

where ρ is the fluid's mass density, p is the pressure and $\mathbf{v}$ is the fluid velocity vector with components v_1, v_2 and v_3 along each of the basis vectors in a cartesian coordinate system. The equations describe, in the order presented, conservation of mass, momentum and energy. E_T is the total energy per unit volume, given by

$$E_T = \rho e + \frac{1}{2} \rho \left(v_1^2 + v_2^2 + v_3^2 \right) \tag{8.4}$$

with e being the internal energy per unit mass for the fluid. Eqs. (8.3) are known as the Euler equations in *differential form*. In index notation, they can be expressed as

$$\begin{aligned} \frac{\partial \rho}{\partial t} + \frac{\partial \rho v_i}{\partial x_i} &= 0 \\ \frac{\partial \rho v_j}{\partial t} + \frac{\partial \left(\rho v_i v_j \right)}{\partial x_i} + \frac{\partial p}{\partial x_j} &= 0 \\ \frac{\partial E_T}{\partial t} + \frac{\partial \left(E_T + p \right) v_i}{\partial x_i} &= 0 \end{aligned} \tag{8.5}$$

Indices repeated twice in a term indicate summation over those indices. In vector form, the equations take on a rather consise form

$$\frac{\partial \mathbf{m}}{\partial t} + \frac{\partial \mathbf{f}_1}{\partial x_1} + \frac{\partial \mathbf{f}_2}{\partial x_2} + \frac{\partial \mathbf{f}_3}{\partial x_3} = \mathbf{0} \tag{8.6}$$

where

$$\mathbf{m} = \begin{bmatrix} \rho \\ \rho v_1 \\ \rho v_2 \\ \rho v_3 \\ E_T \end{bmatrix} \tag{8.7}$$

and

$$\mathbf{f}_1 = \begin{bmatrix} \rho v_1 \\ p + \rho v_1^2 \\ \rho v_1 v_2 \\ \rho v_1 v_3 \\ v_1 \left(E_T + p\right) \end{bmatrix}, \quad \mathbf{f}_2 = \begin{bmatrix} \rho v_2 \\ \rho v_2 v_1 \\ p + \rho v_2^2 \\ \rho v_2 v_3 \\ v_2 \left(E_T + p\right) \end{bmatrix}, \quad \mathbf{f}_3 = \begin{bmatrix} \rho v_3 \\ \rho v_3 v_1 \\ \rho v_3 v_2 \\ p + \rho v_3^2 \\ v_3 \left(E_T + p\right) \end{bmatrix} \tag{8.8}$$

indicating that $\mathbf{f}_i$ are numerical fluxes. Eq. (8.6) contains five conservation equations; conservation of mass, conservation of momentum in the three spatial dimensions and conservation of energy. There are, however, six unknowns in the set of equations making it indeterminate. A sixth equation is therefore required to close the system, and it is called an *equation of state* (EOS). A very commonly used EOS in fluid simulations is the ideal gas law, $p = \rho(\gamma - 1)e$, where γ is the adiabatic index, or ratio of heat capacities, given by $\gamma = C_p/C_V$ where C_p is the specific heat at constant pressure and C_V the specific heat at constant volume.

The Euler equations are governing the fluid in an ALE formulation as well, so the movement of the mesh has to be accounted for. The set of equations in Eq. (8.3) are formulated for a fixed control volume, and are therefore augmented by the mesh velocity $\mathbf{w}$ so they become

$$\begin{aligned} \frac{\partial \rho}{\partial t} + \nabla \cdot \left(\rho \left(\mathbf{v} - \mathbf{w}\right)\right) &= 0 \\ \frac{\partial \rho \left(\mathbf{v} - \mathbf{w}\right)}{\partial t} + \nabla \cdot \left(\left(\mathbf{v} - \mathbf{w}\right) \otimes \left(\rho \left(\mathbf{v} - \mathbf{w}\right)\right)\right) + \nabla p &= \mathbf{0} \\ \frac{\partial E_T}{\partial t} + \nabla \cdot \left(\left(\mathbf{v} - \mathbf{w}\right) \left(E_T + p\right)\right) &= 0 \end{aligned} \tag{8.9}$$

In a Lagrangian formulation, $\mathbf{w} = \mathbf{v}$, making some terms zero. See the work by Casadei [115] for additional details.

8.4 FSI algorithms using ALE in Europlexus

8.4.1 Introduction

The different ways of handling the fluid-structure interface can be divided into a so-called "strong" and "weak" formulation. When using the strong formulation, constraints are imposed on the particle velocity and the mesh velocity at the interface between the fluid and the structure. In a weak approach, the pressure from the fluid is applied as external forces on the structure. Traditionally, strong FSI algorithms are mostly used with finite elements (FE) and weak algorithms with finite volumes (FV). There is also the option of using SPH to represent the fluid [111].

Three different discretisation techniques are illustrated in Fig. 8.3. These are finite elements, node-centered finite volumes and cell-centered finite volumes. When using FE, the kinematic variables are discretised at the nodes while the state variables (e.g. the internal pressure) are discretised at Gauss points[1], conventionally located at the element's centre as in the left part of Fig. 8.3. In a node-centered finite volume approach, a virtual finite volume mesh centered at the fluid nodes is built up from the initial FE-like mesh provided in the input, thereby eliminating the need to provide different inputs for the different formulations. All variables are then discretised at the nodes. Finally, the cell-centered finite volume mesh has the same structure as the FE mesh, but all variables are discretised at the volume centre. In this latter case, a note should be made that the nodes themselves do not posess any physically relevant attributes. The nodes' positions are, however, needed to calculate the discrete volume contained within.

Another subdivision of FSI algorithms is connected to the extent of deformation/damage the structure can sustain. The basic formulations are able to handle large deformations, given a suitable mesh rezoning technique and that the structure *does not fail*. Contained in this class are the *conforming* and *non-conforming* discretisations mentioned above. Naturally, a class that can handle

[1] The number of Gauss points per element and their location, may, of course, vary depending on the exact element formulation. Usually, fluid FEs possess just one Gauss point each.

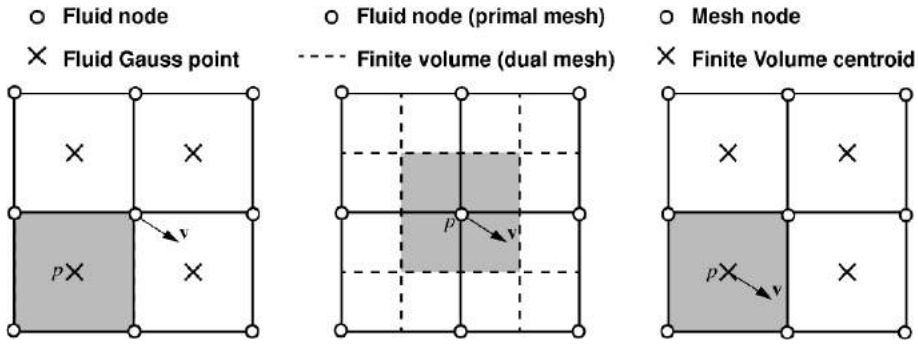

Figure 8.3: *Three different fluid domain discratisation techniques available in Europlexus; finite elements (left figure), node-centered finite volumes (centre) and cell-centered finite volumes (right) [107].*

structural failure also exists, and it is the *embedded* method. Smoothed particle hydrodynamics (SPH) is also capable of this feature.

8.4.2 Conforming FE discretisation

A *nodally* conforming finite element mesh means that for each node on the fluid-structure interface of the Lagrangian structure, there is a corresponding ALE fluid node and vice versa. They have the same coordinates, but are distinct nonetheless. Fig. 8.4(a) shows a continuous domain containing a structure S, and three fluids F_1, F_2 and F_3 and a junction J, while Fig. 8.4(b) shows its conforming FE dicretization. At each node there are two velocity vectors, one for the particles ($\mathbf{v}$) and one for the mesh ($\mathbf{w}$). The fluid-structure interaction is then enforced by constraining the particle velocities at the node pairs to have the same magnitude normal to the structure, i.e.

$$\mathbf{v}_F \cdot \mathbf{n} = \mathbf{v}_S \cdot \mathbf{n} \tag{8.10}$$

in which $\mathbf{n}$ is the unit normal to the discrete fluid-structure interface *at* the fluid node in question. Subscripts F and S indicate fluid and structure, respectively. An illustration of the constraint can be found in Fig. 8.5(a). In a general 3D case, computing $\mathbf{n}$ is by no means a trivial task, details of which can be found in the work by Casadei and Halleux [116], and by Casadei et al. [117].

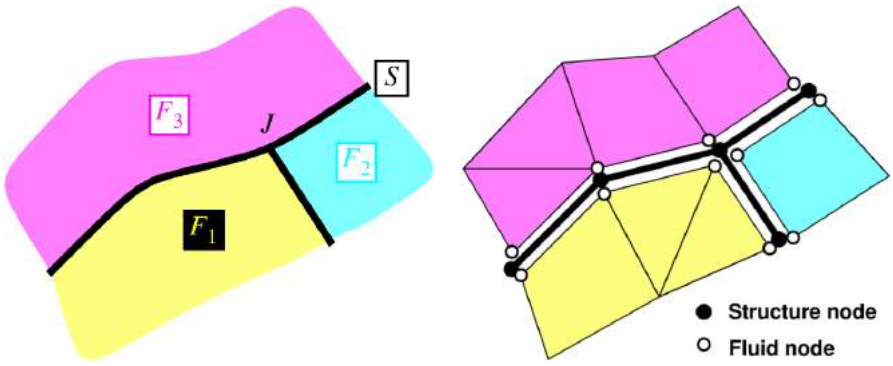

(a) *Continuous F-S domain* (b) *Conforming FE discretisation*

Figure 8.4: *Nodally conforming finite element discsretization of a generic FSI problem [107].*

This condition restrains the fluid from passing through *and* detaching from the structure, but allows it to move tangentially along the interface independent of the strucural velocity. This justifies keeping the fluid and the structural nodes separate, as a single node would not have a sufficient amount of degrees of freedom for two distinct tangential velocities.

Conditions such as the one in Eq. (8.10) are enforced exactly by the use of *Lagrange multipliers*, and the resulting system of equations is solved *implicitly*. This allows the FSI conditions to be coupled automatically with other essential conditions set forth by the user, e.g. restraints on movement, contact between bodies, symmetries, etc. As for the velocity $\mathbf{w}_F$ of the fluid mesh on the fluid-structure interface, which by definition is arbitrary in ALE, it is simply set to be equal to the velocity $\mathbf{w}_S$ of the structure's Lagrangian mesh,

$$\mathbf{w}_F = \mathbf{w}_S = \mathbf{v}_S \tag{8.11}$$

thus making sure that the fluid and the structure nodes at the interface remain superposed (see Fig. 8.5(b) for visual aid). The equality $\mathbf{w}_S = \mathbf{v}_S$, where $\mathbf{v}_S$ is the particle velocity in the structure, holds by virtue of the structure being Lagrangian. This completes the ALE description for the structure and for the fluid nodes attached to the structure. For the remainder of the fluid mesh, a certain movement needs to be specified, a topic treated in Section 8.5. A simple

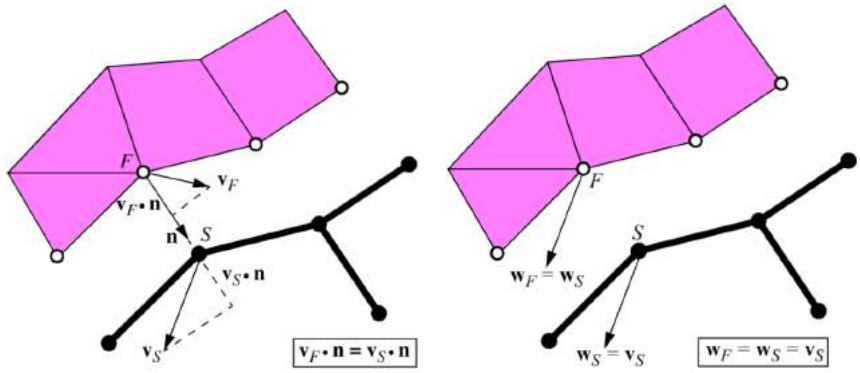

(a) *Constraints on particle velocities* (b) *Compatibility of mesh velocities*

Figure 8.5: *The strong approach for handling FSI problems using a conforming finite element mesh [107].*

example is the case of a purely Eulerian mesh, where $\mathbf{w}_F = \mathbf{0}$.

8.4.3 Non-conforming FE discretisation

In the case of a non-conforming finite element mesh, the nodes of the fluid and the nodes of the structure need not occupy the same position in space (although some of them will). More specifically, for each structural node there is a superposed fluid node but not the other way round. This case is then a generalisation of the conforming case [118], and a useful one as the fluid mesh generally needs to be finer than that of the structure (especially if shells are used) to acquire an accurate portrayal of the distribution of pressure forces [108]. Fig. 8.6 shows the generic FSI problem (a) and the non-conforming finite element discretisation (b).

As in the conforming case, the constraints in Eq. (8.10) and Eq. (8.11) still apply for each conforming node. Then for a fluid node corresponding only to a point S^* on the structure and not a node, the condition on particle velocities is completely analogous to Eq. (8.10),

$$\mathbf{v}_F \cdot \mathbf{n}_F = \mathbf{v}_{S^*} \cdot \mathbf{n}_F \tag{8.12}$$

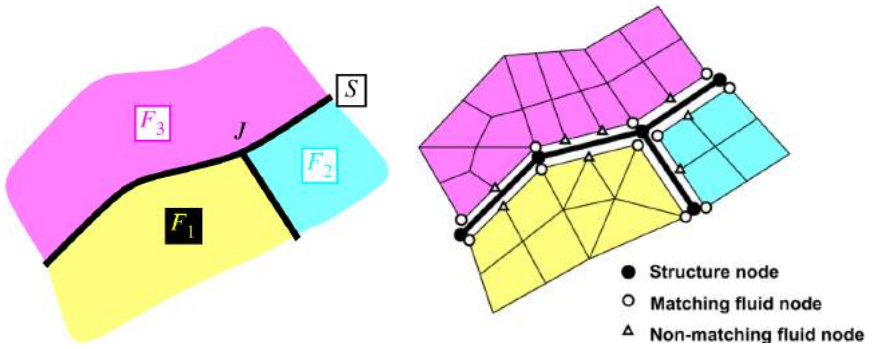

(a) *Continuous F-S domain* (b) *Non-conforming FE discretisation*

Figure 8.6: *Nodally non-conforming finite element discsretization of generic FSI problem [107].*

where $\mathbf{n}_F$ is the local normal unit vector, easily computed as the fluid domain is flat at non-conforming nodes [107]. Shape functions N_i from the structural elements are then used to interpolate for $\mathbf{v}_{S^*}$, which for the case in Fig. 8.7(a) becomes

$$\mathbf{v}_F \cdot \mathbf{n}_F = (N_1 \mathbf{v}_{S_1} + N_2 \mathbf{v}_{S_2}) \cdot \mathbf{n}_F \tag{8.13}$$

Equivalently, the velocity of the mesh is imposed as in Eq. (8.11)

$$\mathbf{w}_F = \mathbf{w}_{S^*} = \mathbf{v}_{S^*} = (N_1 \mathbf{w}_{S_1} + N_2 \mathbf{w}_{S_2}) \cdot \mathbf{n}_F \tag{8.14}$$

which is illustrated in Fig. 8.7(b).

8.4.4 Node-centered finite volumes (NCFV)

As the fluid nodes correspond to points on the boundary of the structure (conforming or non-conforming) a finite element approach is well suited since the particle velocities are discretised *at* the nodes. The constraints in Eqs. (8.10) and (8.12) are intuitive in the sense that the fluid is not allowed to pass *through* the structure, but is perfectly able to move *along* it.

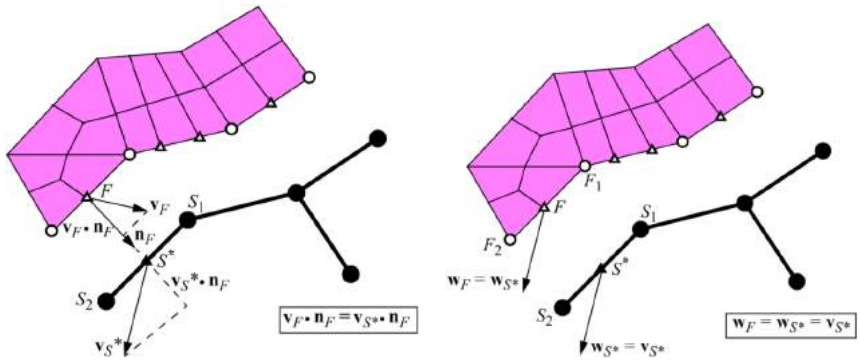

(a) *Constraints on particle velocities* (b) *Compatibility of mesh velocities*

Figure 8.7: *The strong approach for handling FSI problems with a non-conforming finite element mesh [107].*

The very same formulations can be utilised in a node-centered finite volume setting. In this setting the variables are discretised at the volume centre, meaning that the FV grid is offset such that its centres conincide with the nodes in the FE mesh (node-centered finite volumes, shown in the middle figure in Fig. 8.3). Again, the "strong" constraints from Eqs. (8.10) and (8.11) are enforced using Lagrange multipliers [119]. Since imposing Eq. (8.10) on the fluid velocity on the FV nodes ties the fluid in the entire finite volume to the structure, it is in a sense a "stronger" constraint compared to the FE case which just restrains the fraction at the local node. This comes from the fact that the velocity $\mathbf{v}_F$ is linearly[2] interpolated across the element, while in a finite volume it is uniform. More details on the coupling between the finite elements for the structure and the finite volumes for the fluid can be found in Ref. [113].

A "weak" coupling for the NCFV has also been implemented in Europlexus [120]. It works by considering the numerical fluxes[3] in the following way. Assume that NCFV number i, currently at pressure p_i, is contigous to a part of a structure along an edge of the finite volume. This edge has a length L (area in 3D) and unit normal $\mathbf{n}$, and the mass flux across this edge is set to zero. Momentum (force) and energy still have non-zero fluxes though, and they are given by $p_i L\mathbf{n}$

[2]This may of course depend on the element.

[3]These are fluxes in a fluid/finite volume terminology, and must be seen in conjunction with Eqs. (8.7) and (8.8).

and $p_i L\,(\mathbf{v}_i \cdot \mathbf{n})$, respectively, where $\mathbf{v}_i$ is the velocity of the fluid in volume i. Non-zero momentum flux across the edge comes from the fact that $\mathbf{v}_i$ represents the *average* velocity of the entire volume, and there is therefore no guarantee that $\mathbf{v}_i \cdot \mathbf{n} = 0$. Again it is referred to the work by Casadei and Leconte [113] for further details.

8.4.5 Conforming cell-centered finite volumes (C-CCFV)

This is another case of a "weak" FSI coupling, where pressure forces transmitted to the structure are used rather than constraints on the velocities. Forces generated from the fluid are assembled with other external forces (if any) and subsequently used to calculate the dynamic equilibrium in Eq. (8.1). The motion of the ALE nodes (i.e. the mesh) at the fluid-structure interface are restricted to follow the same motion as that of the structure, meaning that Eq. (8.11) is used to compute the mesh velocity. This results in the structure acting on the fluid's state, thus providing a feedback loop.

For the conforming case of cell-centered finite volumes (right in Fig. 8.3), the easiest strategy is to merge each fluid and structure node along the boundary as shown in Fig. 8.8. An approach like this makes the pressure forces from the finite volume act directly upon the structure using the normal force assembly procedure. Computing these forces is achieved through a simple pressure $\times$ length (area in 3D) calculation, illustrated in Fig.8.8(a). For each volume with a pressure p a force $\mathbf{f}_p$ is computed,

$$\mathbf{f}_p = pL\mathbf{n}_S \tag{8.15}$$

acting along a length L with a unit normal $\mathbf{n}_S$. Each of the structural nodes on L (belonging to both the fluid and structure) receives its appropriate share of the load, thus affecting the motion of the structure. It is worth noting that it is possible to handle structural failure with the weak formulation due to the nodes being merged at the interface. In Fig. 8.8(b), a structure has one fluid on each side with a pressure p_a and q_a on each side. Failure in the structure can be treated by eroding the structural element, simply allowing the fluid to flow freely between the finite volumes where the flux was previously blocked. This option has not been put to use in this thesis, and will for that reason not be elaborated on. See [107] for more details.

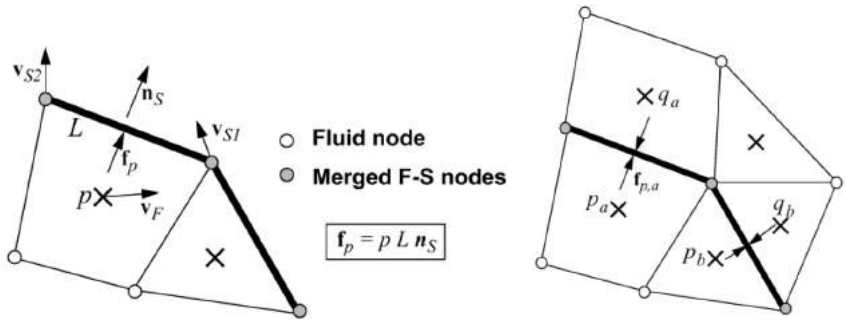

(a) *Single fluid domain* (b) *Two fluid domains*

Figure 8.8: *Conforming CCFV mesh using a weak algorithm for FSI [107].*

8.4.6 Non-conforming cell-centered finite volumes (NC-CCFV)

Fig. 8.9(a) shows a non-conforming CCFV mesh. Like in Section 8.4.3, there are now some nodes that are mathcing while others do not – mathcing nodes can then be merged as in the case above. The residual nodes can not be merged to the structure, so the code is set up in a way that whether or not one chooses to merge the matching nodes the solution remains unchanged [107]. In Fig. 8.9(a) the nodes are kept distinct.

Distribution of pressure forces is a rather straight forward process in the case of a conforming mesh, since each FE has a corresponding FV. Now each FE has multiple FVs, necessitating some adjustments. Observing Fig. 8.9(b), the ith finite volume exerts a pressure p_i over a length L_i (area in 3D) giving rise to the pressure *force* $\mathbf{f}_{p,i}$ acting on point C_i (located at the centre of the FV) along the structural element's unit normal $\mathbf{n}_S$ (no summation rule applied),

$$\mathbf{f}_{p,i} = p_i L_i \mathbf{n}_S \tag{8.16}$$

There is, however, no structural node at point C_i to apply the force to. The force is then distributed as follows. Let L_{Ai} and L_{Bi} be the lengths of the structural elements on each side of C_i such that $L_S = L_{Ai} + L_{Bi}$. A natural

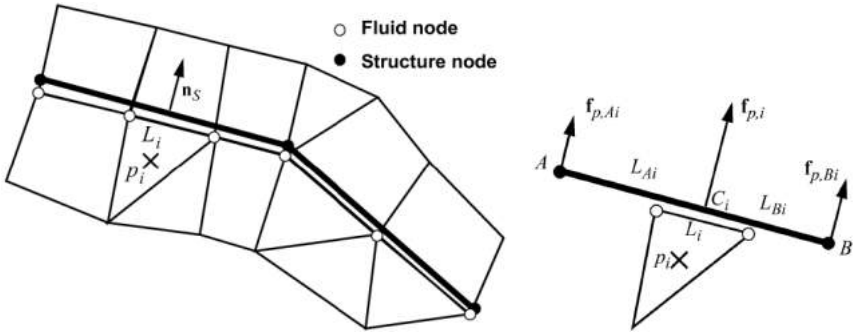

(a) *Hierarchic mesh, two fluids* (b) *Distribution of pressure forces*

Figure 8.9: *Non-conforming CCFV mesh using a weak algorithm for FSI [107].*

distribution is to use the fraction of the lengths, i.e.

$$\mathbf{f}_{p,Ai} = \frac{L_{Bi}}{L_S} \cdot \mathbf{f}_{p,i} \tag{8.17a}$$

$$\mathbf{f}_{p,Bi} = \frac{L_{Ai}}{L_S} \cdot \mathbf{f}_{p,i} \tag{8.17b}$$

This concludes the non-conforming CCFV formulation.

8.5 Rezoning algorithms

8.5.1 Description

`MEAN`

The `MEAN` rezoning algorithm is very simple and offers a way to (try to) keep the mesh regular. It calculates one node's position based on the position of the neighbouring nodes: The mean position of the surrounding nodes becomes (approximately) the position of the node in question. This has the advantage of being cost effective on the CPU, but handles a circular mesh particularly badly. Fig. 8.10 illustrates a part of a circular mesh, with nodes labelled 1 to 9. When calculating the position of node 5, three of the four neighbouring nodes (nodes

2, 4, 6 and 8 in Fig. 8.10) will always have a lower y-value, thus forcing node 5 towards the centre. This was also observed in the simulations presented briefly in Section 8.5.2 and illustrated in Fig. 8.11, and as the nodes retracted inwards the element size eventually diminished, causing failure in the simulations. The `MEAN` technique has therefore not been used extensively.

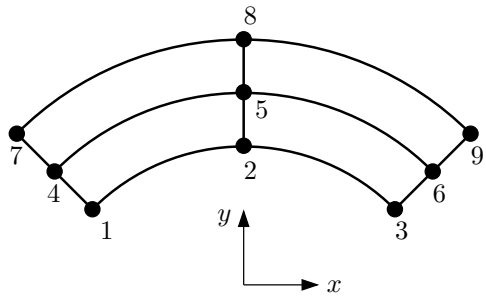

Figure 8.10: *Part of circular mesh.*

`AUTO`

This is the default rezoning technique in Europlexus. It is an implementation of Giuliani's algorithm [121], and serves as a good first approach if no prior knowledge to how the mesh will most likely deform is available. As this approach tries to keep the elements regular, it mostly carries through the entire simulation except in cases of severe distortions. By attempting to keep the aspect ratio of the elements' faces close to unity, a regular mesh is maintained. This algorithm is the one mainly used in the FSI-simulations discussed later.

`ELAS`

In this case, a ficticious elastic material is tied to the fluid mesh. It makes the fluid mesh respond to the deformations caused by the Lagrangian structure in an elastic manner, thus attempting to keep it from undergoing severe distortions. In terms of CPU cost, it is relatively expensive, but does a good job in keeping the mesh regular, espacially if large rotations are involved. The difficulty within this method is choosing a suitable stiffness for the ficticious material. When testing this method, too large local deformations caused the time step in the calculations to decrease below the critical threshold (10^{-13} s) and the analyses crashed.

`MANU`

It is also possible to set up an input file where one specifies the movement of the nodes manually. This can be a very powerful method if one knows the main physics of the problem and how it behaves. Unfortunately, it requires a convoluted input which can be difficult for the average user to set up. This method is mentioned here to show that other alternatives are available in the code. Here it has only been tried for a few very simple test cases.

8.5.2 Simulation attempts

Different rezoning algorithms were tested on simulations involving water-filled pipes, thereby necessitating a circular mesh. The simulations (discussed in more detail in Section 8.8) basically have the same setup as the component tests in Section 4.3. Three of the different algorithms listed have been tested on the pipe impact simulations, and the effects can be seen in Fig. 8.11. Both the `MEAN` and `AUTO` look quite similar, but only `AUTO` managed to carry the simulations to the end and was for that reason the main rezoning algorithm used. `MEAN` contracted the elements too much, while local deformations cause the ELAS to fail.

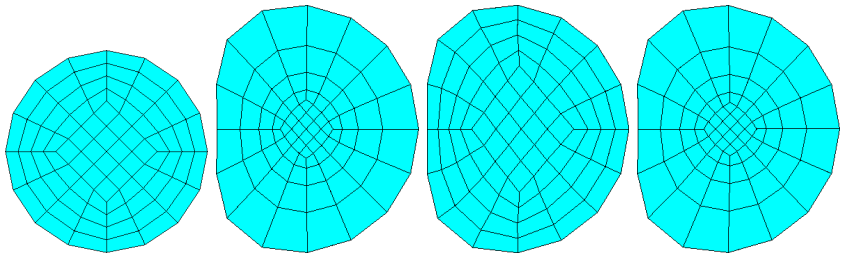

(a) *Initial mesh* (b) *MEAN* (c) *ELAS* (d) *AUTO*

Figure 8.11: *Effect of various rezoning techniques 10 ms after impact at a cross-section in the middle of the pipe (where the impactor struck.*

8.6 Embedded FSI algorithms

Up to this point, the algorithms treated have been based on an ALE formulation where the structure is Lagrangian and the fluid ALE. The fluid nodes

on the fluid-structure interface have been forced to follow the movement of the structure, while the rest of the fluid mesh have been controlled by the various rezoning techniques described in Section 8.5. This provides a rather exquisite solution to a complex problem, but suffers nevertheless from two shortcomings reducing the applicability:

- The rezoning algorithms are not able to retain a suitable form on the mesh if the deformations are too severe, especially if rotations are involved.
- If the structure fails (elements are eroded or replaced by flying debris) it is very difficult to connect the two fluid domains initially separated by the failed structure since the fluid nodes on each side are usually kept separate.

An exception from the second problem is the CCFV with weak coupling (see Section 8.4.5 and [107]), but the first is still largely prevalent. The *embedded* approach is an attempt to circumvent these problems, but it comes with a price of reduced accuracy. Fig. 8.12 illustrates the main idea, which is to surround (embed) the structure in a fixed (Eulerian) fluid mesh, and then work out the fluid-structure interaction for the FEs/FVs in the vicinity of the structure.

This means that the work related to meshing is significantly reduced – one no longer has to make sure that nodes conform, or merge relevant nodes and so on. The structural (Lagrangian) mesh is generated as usual and embedded

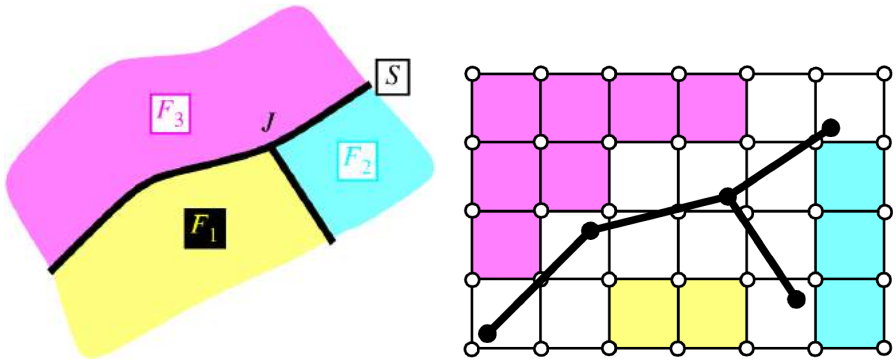

(a) *Continuous F-S domain* (b) *Embedded FSI approach*

Figure 8.12: *Embedded discsretization of a generic FSI problem [107].*

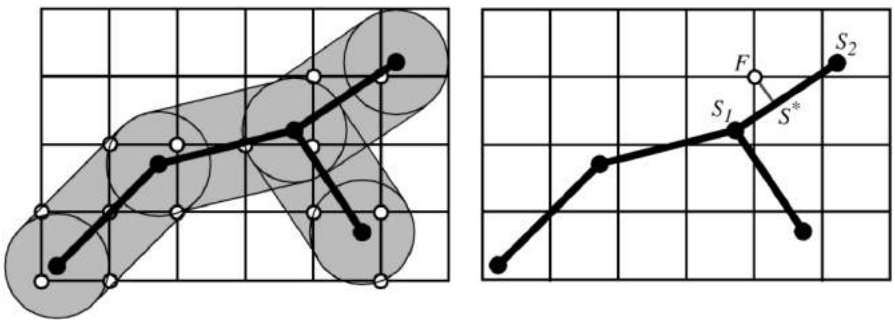

(a) *Influence domain* (b) *Embedded F-S coupling*

Figure 8.13: *Strong coupling in embedded FSI approach [107].*

in a completely independent (and even completely regular if desired) Eulerian fluid mesh, thus removing any possibily of the fluid mesh becoming distorted. A consequence of this approach is that the quite elegant ALE formulation becomes redundant.

In order to establish the FSI, information about which nodes are close enough to the structure is needed. These coupled fluid nodes are said to lie within the structure's *influence domain*, portrayed as the shaded area in Fig. 8.13(a). Since the structure deforms, it is necessary to generate the influence domain for each time step, warranting a fast search algorithm[4].

A circle (sphere in 3D) with a given radius specified by the user based on the local mesh density is centered on every structural node. Quadrangles (cones, prisms and hexahedra in 3D) then connect the spheres, forming an area (volume in 3D) which then constitutes the influence domain. Fluid nodes falling herein become coupled nodes (marked with circles in Fig. 8.13 (a)).

The choice of circle radii is not a trivial matter; a too small influence domain will produce leakage of fluid across the structure. If the domain is too big, too much fluid will be connected to the motion of the structure thereby causing an unphysical load to the structure. Fluid mesh size is of course a critical factor when determining the radius for the domain.

[4]A bucket sort algorithm is implemented.

8.6.1 Strong coupling in the embedded FSI algorithm

Application to FE

The embedded FSI algorithm on strong form is called the *FLSR algorithm*, which is suitable for use with both FE [122] and NCFV [113] as the fluid velocities are discretized at the nodes (see Fig. 8.1 for an overview). Let F in Fig. 8.13(b) be a fluid node within the influence domain, and S^* the point on the structure closest to F[5]. A fitting constraint is then imposed on the particle velocities on these two points. One way of doing this is similar to Eq. (8.13),

$$\mathbf{v}_F \cdot \mathbf{n}_S = \mathbf{v}_{S^*} \cdot \mathbf{n}_S = (N_1 \mathbf{v}_{S_1} + N_2 \mathbf{v}_{S_2}) \cdot \mathbf{n}_S \tag{8.18}$$

The fluid does not have a defined normal $\mathbf{n}_F$, forcing the use of the structure's normal $\mathbf{n}_S$ instead. Like in the FSA algorithm, the fluid is left to slide along the wall but not through. There are however numerical examples of spurious passage of fluid through the structural barrier [107].

A second alternative exists for the strong coupling, and this ties the fluid to the structure in all directions, i.e.

$$\mathbf{v}_F = \mathbf{v}_{S^*} = N_1 \mathbf{v}_{S_1} + N_2 \mathbf{v}_{S_2} \tag{8.19}$$

which can be interpreted as a "stronger" condition than Eq. (8.18). This prevents fluid from leaking across the structure, but one caveat is that it may cause an unphysical load to the structure.

Application to NCFV

The FLSR algorithm works well when FEs are used for the fluid [122]. Unfortunately some fluid leakage is detected when using NCFV, regardless of the radius used for the influence domain. This is an effect of how the transport of mass and energy is evaluated. In an FE formulation, it depends on the relative difference in velocity between the mesh and material. On the structure this difference is zero by virtue of the structure being Lagrangian. Fluid nodes tied

[5] This point is generally not a node.

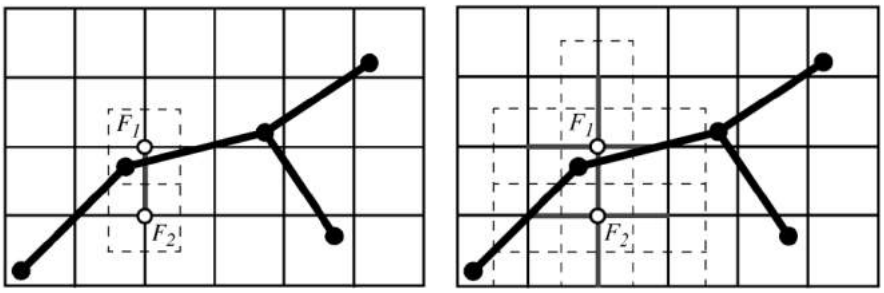

(a) *Both nodes in influence domain* (b) *One node in influence domain*

Figure 8.14: *Blocked fluxes in embedded FSI algorithm with NCFV using the strong approach [107].*

to the structure by Eq. (8.19) also have zero relative velocity, ensuring that no mass and energy is tranferred through the structure.

When using FVs, transport terms are represented by numerical fluxes (touched briefly upon in Section 8.4.4). Calculating these fluxes is more complex when using FVs compared to FEs, and depends on the space order (1st or 2nd) and the chosen Riemann solver [107]. What this eventually boils down to is that zero relative velocity between the mesh and the particles at a given node does not guarantee zero mass and energy transport. Further, the flux is *not* calculated at the nodes, but on the interface between cells using an interpolated value of the velocity.

One should expect to solve the problem by blocking another row of fluid cells as the interpolated velocity between these rows would be zero. But alas, numerical examples show that fluid may still leak despite choosing a large influence domain [107]. The solution lies in explicitly blocking the numerical fluxes of mass and energy "close" to the structure. Two approaches have been implemented; the first blocks the fluxes between two NCFVs if *both* fluid nodes representing the volume are coupled with the structure (see Fig. 8.14(a)). The second blocks the fluxes between two cells if at least one of the nodes representing them are coupled with the structure, causing more fluxes to be blocked than in the first case as shown in Fig. 8.14(b).

8.6.2 Weak coupling in the embedded FSI algorithm

The weak version of the embedded method is fit for use with CCFV, and it is dubbed the *FLSW algorithm* in Europlexus (see Fig. 8.1 for an overview). An influence domain is needed in this case as well, and it is constructed in the exact same manner as for FLSR. Rather than searching for nodes in the domain, it is practical to search for *faces* directly. The face centers are marked with squares in Fig. 8.15(a), and it is here that the numerical fluxes are computed. Remember that velocities are discretized in the volume centers when using CCFV.

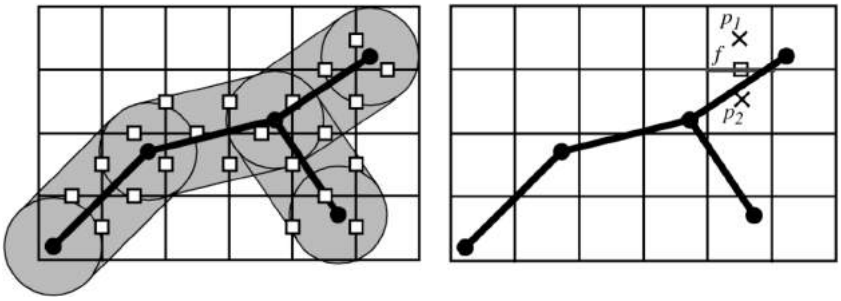

(a) *Faces in influence domain* (b) *Pressure drop force calculation*

Figure 8.15: *Embedded FSI algorithm with CCFV using the weak approach [107].*

In the weak approach forces are transmitted to the structure rather than imposing certain conditions on the particle velocities. Considering Fig. 8.15(b), the coupled face labelled f separates the two volumes V_1 and V_2 currently at pressures p_1 and p_2, respectively. The pressure drop force $\mathbf{f}_{\Delta p}$ is then computed by the following equation;

$$\mathbf{f}_{\Delta p} = (p_1 - p_2)\, L_S \mathbf{n}_f \tag{8.20}$$

where L_S is the length (area in 3D) of the face f, and $\mathbf{n}_f$ its unit normal. The force in then "applied" to the point on the structure closest to the face center, namely S^* (see Fig. 8.16(a)). "Applied" meaning that it is distributed to the nodes like in Eqs. (8.17a) and (8.17b) where $L_S = L_A + L_B$,

$$\mathbf{f}_{\Delta p,A} = \frac{L_B}{L_S} \cdot \mathbf{f}_{\Delta p} \tag{8.21a}$$

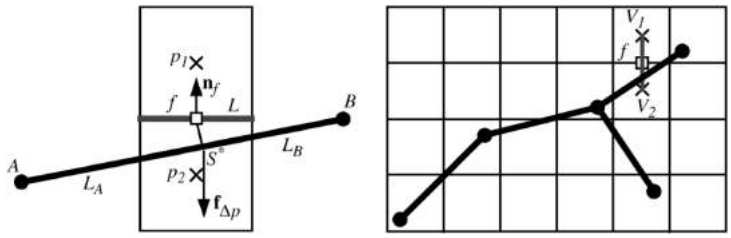

(a) *F-S coupling force* (b) *Blocking of fluxes in CCFV*

Figure 8.16: *Forces and blockages in FLSW algorithm with CCFV [107].*

$$\mathbf{f}_{\Delta p,B} = \frac{L_A}{L_S} \cdot \mathbf{f}_{\Delta p} \tag{8.21b}$$

Just like in the NCFV case in Section 8.6.1, it is needed to set specific fluxes to zero to avoid spurious leakage of fluid, as indicated by the shaded line in Fig. 8.16(b). This is done by one of the two means discussed earlier, depicted in Fig. 8.14.

It should be noted that Eq. (8.20) is the weak equivalent of Eq. (8.19), coupling the fluid and the structure in all directions. To obtain the weak equivalent of Eq. (8.18), one can project the force along the unit normal of the structure, $\mathbf{n}_S$, assuming this can be calculated. Unfortunately fluid leakage will still be an issue, as in the strong case.

A classification of the FSI algorithms discussed until now is listed in Table 8.1.

8.7 Smoothed particle hydrodynamics (SPH)

8.7.1 Introduction

The smoothed particle hydrodynamics (SPH) method was developed in the 70's by Gingold and Monaghan [123] and by Lucy [124]. A typical example of its application was the numerical simulation of the fission of a rotating star [125]. Today this method has a wide variety of applications, including offshore related problems [126]. In SPH the continuum is discretised by a set of points, at which certain quantities are known (e.g. the velocity or pressure). These points are

Table 8.1: *A classification of FSI algorithms [108].*

FSI algorithm	FSI detection	Basic	No structural failure, moderate rotations
		Embedded	Structure can fail, arbitrary rotations
	FSI enforcement	Strong	Constraints on fluid and structure *velocities* are imposed, e.g. by Lagrange multipliers
		Weak	Pressure forces are transmitted from the fluid (slave) to the structure (master) and structure motion provides weak feedback on the fluid

also assigned a radius and a mass (hence the term *particles*). The particles are, as touched upon earlier, Lagrangian, but do not constitute a "mesh" in the traditional finite element sense. Elements in a Lagrangian mesh would have a fixed connectivity, but in SPH connectivity is recalculated at each time step, thus avoiding a warped and largely deformed mesh. This is however a costly procedure, and material laws can be more difficult to treat. SPH can be effectively coupled with standard finite elements to model e.g. impact phenomena [108].

8.7.2 SPH formulation

Starting from the conservation equations, the general SPH formulation is as follows [108]:

1. Take one of the terms from the dynamic conservation equation at point $\mathbf{r}$
2. Multiply by a kernel $W(\mathbf{r}, h)$ with certain properties
3. Integrate over fluid domain (with special attention to boundaries)
4. Approximate integrals by discrete sums
5. Term of SPH equation at point $\mathbf{r}$ is obtained
6. Repeat for remaining terms of conservation equation

How this is done in detail will now be presented briefly, using the density as an example in the end.

Establishing the motion of a particle during a time step requires constructing the forces a piece of fluid would be subjected to. This is done based on the data contained within the particles (pressure, density, etc.) for each term in the equations. To this end a kernel is used to "smooth" a particle's data, say its mass, to a certain distribution within the particle's neighborhood. So for a position $\mathbf{r}$ in the fluid, the pressure (for example) is determined by the sum of each individual particle's influence at that point. The magnitude of a particle's influence at $\mathbf{r}$ is depending on the chosen kernel[6] and the characteristic length h.

Before doing any discretisation of any kind, consider any vector- or scalar-valued field $A(\mathbf{r})$ in the domain $\mathbf{r} \in \Omega$. The identity

$$A(\mathbf{r}) = \int_{\Omega} A(\mathbf{r}') \, \delta(\mathbf{r} - \mathbf{r}') \, \mathrm{d}\mathbf{r}', \tag{8.22}$$

where $\delta(\mathbf{b})$ is the Dirac δ-function and $\mathrm{d}\mathbf{r}'$ a differential volume element, is the starting point. Here, $\mathbf{b}$ is just a dummy vector. An approximation $\bar{A}(\mathbf{r})$ by an integral interpolant to the exact field $A(\mathbf{r})$ is given by

$$A(\mathbf{r}) \approx \bar{A}(\mathbf{r}) = \int_{\Omega} A(\mathbf{r}') \, W(\mathbf{r} - \mathbf{r}', h) \, \mathrm{d}\mathbf{r}' \tag{8.23}$$

in which $W(\mathbf{b}, h)$ is an interpolating kernel. The kernel must be normalised, i.e.

$$\int W(\mathbf{b}, h) \, \mathrm{d}\mathbf{b} = 1 \tag{8.24}$$

and it must tend to $\delta(\mathbf{b})$ in the limit where $h \to 0$,

$$\lim_{h \to 0} W(\mathbf{b}, h) = \delta(\mathbf{b}) \tag{8.25}$$

This makes sure that $\bar{A}$ is close to A [127].

[6] There are infinitely many possible kernels [125].

In Europlexus, the cubic spline called M_4 is utilised to construct the kernel [108], and it has the following form in one dimension with $q = |x|/h$, x being the distance from the particle's centre,

$$M_4(x) = \begin{cases} \frac{1}{6}\left[(2-q)^3 - 4(1-q)^3\right] & \text{for } 0 \le q \le 1 \\ \frac{1}{6}(2-q)^3 & \text{for } 1 \le q \le 2 \\ 0 & \text{for } q > 2 \end{cases} \tag{8.26}$$

Fig. 8.17 illustrates Eq. (8.26) as a funtion of q. The kernel in one dimension is then $M_4(x)/h$. In 3D the coefficient for normalising the integral in Eq. (8.24) is $1/(4\pi)$ rather than $1/6$ as in Eq. (8.26) for the 1D case. Also, the kernel becomes $M_4(\mathbf{r})/h^3$ when extended to 3D. This makes sense as the kernel is integrated over a length in 1D and a volume in 3D[7], thus maintaining correct physical units,

$$W_4(\mathbf{r}) = \frac{M_4(\mathbf{r})}{h^3} \tag{8.27}$$

Returning to the approximation in Eq. (8.23) while assuming a fluid with density $\rho(\mathbf{r})$ occupies Ω, the fluid is discretised into a certain number of mass elements $i \in \{1, \ldots, N_p\}$, each with mass m_i, density ρ_i, field quantity A_i and location $\mathbf{r}_i$ in Ω. From Eq. (8.23), $\bar{A}(\mathbf{r})$ can be rewritten as

$$\bar{A}(\mathbf{r}) = \int_\Omega \frac{A(\mathbf{r}')}{\rho(\mathbf{r}')} W(\mathbf{r} - \mathbf{r}', h)\, \rho(\mathbf{r}')\, \mathrm{d}\mathbf{r}' \tag{8.28}$$

in which a mass element would be $\rho(\mathbf{r}')\mathrm{d}\mathbf{r}'$. Following the discretisation mentioned above, this integral can be approximated by a sum over all the particles

$$\tilde{A}(\mathbf{r}) = \sum_{i=1}^{N_p} m_i \frac{A_i}{\rho_i} W(\mathbf{r} - \mathbf{r}_i, h) \tag{8.29}$$

[7] And of course a surface in 2D.

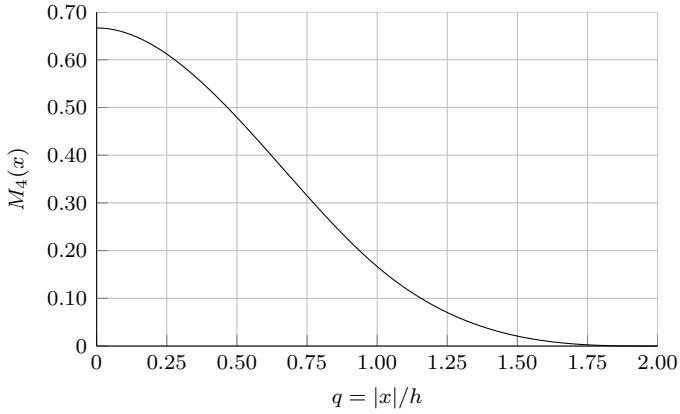

Figure 8.17: *The M_4 kernel used with SPH in Europlexus.*

If A is the density, the sum in Eq. (8.29) provides the following sum for the estimated density $\tilde{\rho}$ at point $\mathbf{r}$,

$$\tilde{\rho}\left(\mathbf{r}\right) = \sum_{i=1}^{N_p} m_i W\left(\mathbf{r} - \mathbf{r}_i, h\right) \tag{8.30}$$

The particles' masses are thereby smoothed out from a set of discrete masses to form a "continuous" density.

Technically one does not always sum over *all* the particles all the time as tacitly assumed in Eqs. (8.29) and (8.30), this depends on the kernel and the characteristic length h. If a Gaussian kernel is used, two particles at any finite distance always exert some influence on each other although the effect diminishes with increasing distance. In Europlexus the kernel of choice is Eq. (8.27), which means that particles further apart than $2h$ do not influence each other. When the kernel becomes zero at a finite distance, it is said to have compact support (which is usually the choice in SPH).

Now that a general approach[8] has been established for the approximation of integrals over the fluid domain (examplified by the density in Eq. (8.30)), this recipe can be applied for each term in the conservation equations.

[8]Some modifications are required for derivatives, see [128].

8.8 Simulations using fluid-structure interaction

8.8.1 Introduction

Contained herein are simulations of the open and closed water-filled pipes from Section 4.3 using the various techniques for fluid-structure interaction described in Chapter 8, available in Europlexus [111]. Purely Lagrangian simulations of an empty pipe are carried out as well. Some of the results obtained in this section are presented in Refs. [30, 32]. A great many thanks to Folco Casadei for his highly qualified contributions to these simulations. In terms of numerical simulations, many earlier studies regarding pipes and fluid-structure interaction treat waterhammer effects [129]. An analytical model for an impulse load against a pipe with a flowing medium has also been proposed [130]. However, none of these studies are directly relevant for the problem at hand.

Europlexus is an explicit finite element code, developed jointly by Joint Research Centre (JRC) in Ispra, Italy, and by the French Commissariat à l'Energie Atomique (CEA) for fast transient dynamics involving fluid-structure interaction (FSI). Typical examples of usage is blast loading of structures, or high velocity impact (see e.g. Ref. [107]).

8.8.2 Numerical modelling

For these simulations, no symmetry planes are used. Potential pitfalls with reflections, diffusion, etc. are thereby avoided albeit at the cost of increased CPU time. The fluid domain is, as mentioned, modelled by the Euler equations, assuming compressible inviscid behaviour [115]. Finite Elements (FE), cell-centred Finite Volumes (FV) or Smoothed Particle Hydrodynamics (SPH) were employed here for the fluid discretisation in space. Yet another fluid formulation based on node-centred Finite Volumes is available in the code, but was not used in the present study. Europlexus offers a rich variety of FSI models, as described in Chapter 8 and Ref. [107]. Conforming, non-conforming or embedded (immersed) meshes can be employed. The enforcement of FSI conditions can be achieved either in a strong manner (typical of FE) by means of Lagrange multipliers to impose velocity constraints, or in a weak manner (typical of cell-centred FV), by transmitting pressure forces. The general setup of the numerical simulations is as in the experiments, presented in Fig. 4.17.

Structure model

An appropriate Lagrangian finite element discretisation of the pipe was obtained in [32], where $24 \times 78 = 1\,872$ shell elements were used (24 along the circumference and 78 along the length as shown in Fig. 8.18), making the element edges about 16 mm long. The elements[9] are 4-node shells with 6 degrees of freedom per node, and 20 Gauss points (5 across the thickness). In addition, 180 such elements were used to model each end cap. This structural mesh is referred to as "medium" and used as a basis mesh for the pipe in the simulations. Shell elements were chosen as they are faster than solids, and generally capture the global deformation well as seen in Section 7.2. Other mesh grades than medium were also used, coarse (16×52), fine (32×104) and extra fine (40×130). The constitutive relation used for the structure in the FSI simulations is the Johnson-Cook model, described in Section 6.2.1, as it was readily available in Europlexus. Its implementation into Europlexus is described in Ref. [131].

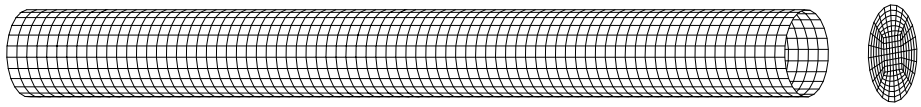

Figure 8.18: *Medium mesh for pipe (*24×78 *elements) and end caps (180 elements).*

Both the supports and the indenter were represented by 40 material points (rigid spheres) each, thereby approximating a cylinder. The pinball contact algorithm, originally proposed by Belytschko and co-workers for impact and penetration problems with erosion (see Belytschko and Neal [132]), was used to enforce the contact conditions. The method does not account for friction, and works by embedding a rigid sphere (pinball) in each element candidate for contact. Then, contact detection reduces to checking interpenetration of two spheres, a trivial and geometrically robust operation which by construction avoids the pitfalls of other detection algorithms, e.g. based on master nodes penetrating into slave surfaces.

The supports were assigned pinballs of radius 25 mm, and the indenter's pinball radius was set to 10 mm (see Fig. 4.17). Indeed, these components are represented quite accurately by spherical pinballs. However, as concerns the pipe, quadrilateral shell elements would be only poorly represented by spheres (especially for long shell edges), so two alternative strategies were tested. In

[9] These shell elements are called `Q4GS` in Europlexus [111].

some cases, node-based (rather than element-based) pinballs with a diameter equal to the shell thickness were assigned to all shell nodes of the pipe in the impact zones. Here one runs the risk of spacing the pinballs too far apart if the shell mesh is coarse (an example will be shown later). Alternatively, a "hierarchic" pinball technique (also initially proposed by Belytschko and co-workers, see Ref. [132] and references therein) was used in the pipe, which starts with a pinball size approximately equal to the shell's length and is subsequently reduced to the order of the shell thickness as contact progresses. The difference in behaviour between the two contact formulations will be shown in Fig. 8.19. The supports are fixed in all spatial directions while the indenter is only allowed to move in the impact direction, thus representing the nose of the trolley which in the experiments is limited to travelling along the rails in the pendulum accelerator.

Fluid model and fluid-structure interaction schemes employed

The fluid inside the pipe in experiments G, H, I and J is discretised in various different manners, and the FSI technique varies accordingly. These techniques are described in detail in Chapter 8, and a brief explanation is given here to bring the differences to mind. Three main variations of representing the fluid are employed in the present work: *i*) by an arbitrary Lagrangian-Eulerian (ALE) mesh of either FE or FV; *ii*) by a completely Eulerian mesh of either FE or FV; *iii*) by smoothed-particle hydrodynamics (SPH). As in the experiments, all fluids' initial pressure is atmospheric (approximately 10^5 Pa).

ALE approach In the first case, the end cap mesh seen in Fig. 8.18 is extruded along the pipe's longitudinal axis to create linear 8-node volume elements containing one Gauss point located at the centre. For a conforming fluid mesh – i.e. a mesh with one corresponding fluid node for each structural node on the fluid-structure interface and vice versa – this results in $180 \times 78 = 14\,040$ elements for the medium structural mesh. A finer fluid discretisation would give a non-conforming fluid mesh, with one corresponding fluid node for each structural node on the F-S interface albeit not the other way round. Making the fluid coarser than the structure is not advisable. The simulations herein are run with a conforming fluid mesh.

Euler-Lagrange approach In the second case, the structure and fluid meshes are built independently. The Lagrangian structure mesh is then "embed-

ded" or "immersed" in a regular, parallelepiped Eulerian fluid mesh which represents the fluid domain both inside (water) and outside (air) the pipe. In the present calculations, a block of $60 \times 36 \times 180 = 388\,800$ fluid bricks was used, measuring $500 \times 300 \times 1\,500$ mm. Absorbing boundaries are specified along the entire envelope of the fluid domain in order to avoid spurious reflections of pressure waves along the mesh boundaries.

While the ALE approach only requires a standard single component material model, although it can be extended to a multi-phase multi-component material model, the Euler-Lagrange approach requires the latter for the fluid domain, able to represent an arbitrary mixture of liquid water and air. Such models are more complex and less accurate than single-component models. The tracking of interfaces between the phases is less precise and subject to numerical diffusion. However, as a counterpart, all difficulties related to mesh rezoning are avoided by construction since the fluid mesh is Eulerian (fixed). For FE in the fluid, coupling between the fluid and the structure is achieved by the so-called FLSR algorithm, explained in Section 8.6.1. See Refs. [107, 122] for further details.

In the present Euler-Lagrange simulations the impactor has been left out of the FSI scheme for simplicity, since it only serves as a means for delivering the kinetic energy to the pipe.

SPH approach In the third and final case, the fluid is modelled by classical SPH particles, all of the same size and initially arranged in a densely packed (hexagonal close-packed) configuration, only approximately filling the pipe. The fluid description is Lagrangian in this case, and it lends itself well to the treatment of impacts. There is no additional difficulty to model a partially filled pipe and the fragmentation or jetting of the water is naturally described. The SPH method is briefly explained in Section 8.7, and an introduction including derivation of the SPH equations can be found in Ref. [125].

In the present calculations a radius of the SPH particles of 2.5 mm is chosen. To fill the entire pipe 169 971 particles are needed, albeit with some slight gaps near the pipe wall. Fluid-structure interaction in this case reduces to Lagrangian contact between the SPH particles and the shell elements of the pipe.

8.8.3 Numerical results

This section summarises the results of the numerical simulations performed with the various models. The main focus has been with pipes A and I from Chapter 4, as they showed a distinctly different behaviour in the experiments (in terms of force-displacement response) and there was no failure of the material (which was the case for pipe J). The results emerging from the simulations have been sorted according to the numerical technique used, and not necessarily according to the pipe experiments. First, some purely Lagrangian simulations have been run for validation purposes before fluid-structure interaction is introduced.

Empty pipe simulations (Lagrangian)

Despite having an appropriate mesh density from previous work [32], a few simulations with different mesh grades were run. The coarse mesh did not perform satisfactorily, and a converging tendency was observed for increasing number of elements, as seen in Fig. 8.19. More elements also tended to generate a softer behaviour, which is natural as more degrees of freedom are available and the system is less "restrained". As mentioned, only shell elements have been used for the structure in the fluid-structure simulations.

Different shell thicknesses were tried out numerically for the pipe due to the mid section being lathed down in the experiments, which resulted in a slightly uneven thickness and a slightly different average thickness for each pipe. A higher thickness lead to a higher force level and correspondingly lower deformation, illustrated in Fig. 8.20. This also conforms with expectations, as higher thickness should provide a stiffer response as already noted in the prior section, but not shown explicitly in terms of force-displacement curves.

No significant difference between nodal and hierarchic pinballs was observed, except for the case with the coarse mesh where the nodal pinballs simply were too far apart to ensure sufficient contact conditions (see Fig. 8.19). For pipe B, the final deformation is equal for all analyses as the trolley hit the buffer in the experiment. This buffer was also included in the analyses as a rigid barrier the indentor could not pass, hence the clutter of data points at the end of the analyses. The impact was well captured, and in accordance with the results from Section 7.2 as well as previous work [31], both using ABAQUS/Explicit to perform the numerical simulations of empty pipes.

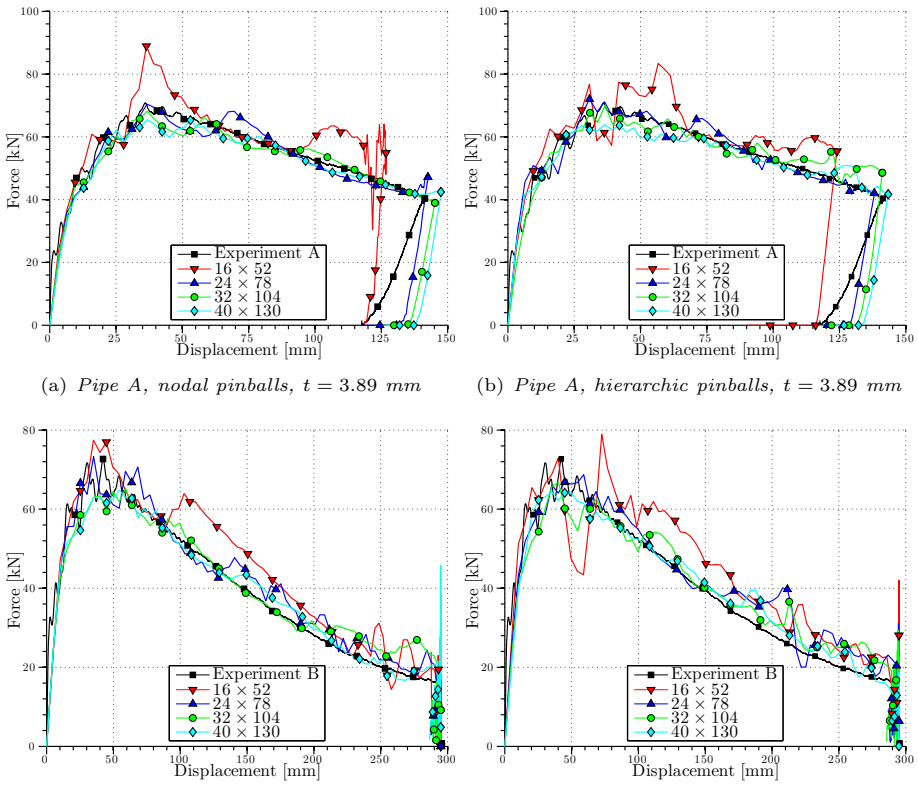

(a) *Pipe A, nodal pinballs, $t = 3.89$ mm*

(b) *Pipe A, hierarchic pinballs, $t = 3.89$ mm*

(c) *Pipe B, nodal pinballs, $t = 3.86$ mm*

(d) *Pipe B, hierarchic pinballs, $t = 3.86$ mm*

Figure 8.19: *Mesh and contact model sensitivity study on empty pipes.*

Conforming ALE simulations of filled pipe

A conforming mesh for the fluid was constructed within the pipe, and a simulation was set up for comparison with experiment I. All initial simulations (using the different discretisations) with a pipe completely filled with water showed that the response was much too stiff (see e.g. Fig. 8.21). Therefore, it was suspected that in the nominally filled-closed tests (I, J) some air could have remained trapped at the tube top, since the filling tap was not at the highest point (see Figs. 4.23(b) and 4.24(b)).

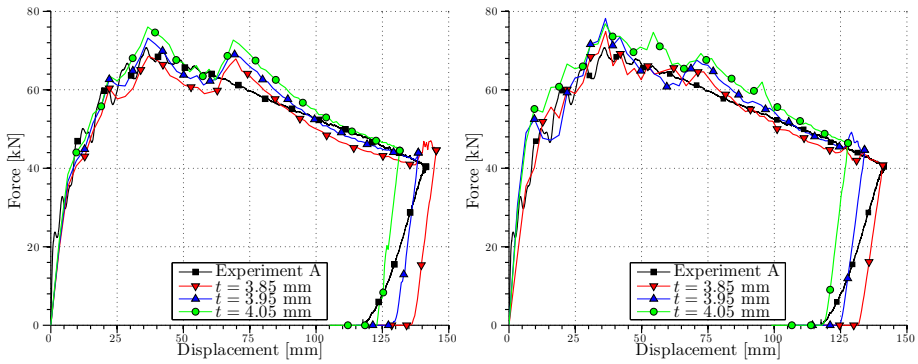

(a) *Pipe A, nodal pinballs*

(b) *Pipe A, hierarchic pinballs*

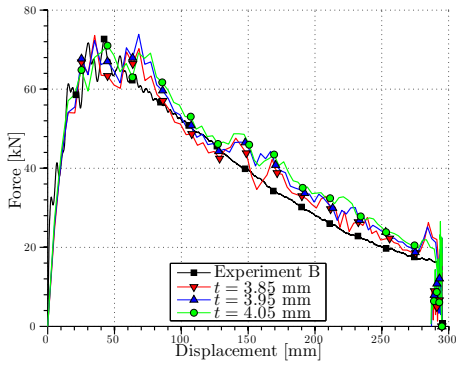

(c) *Pipe B, nodal pinballs*

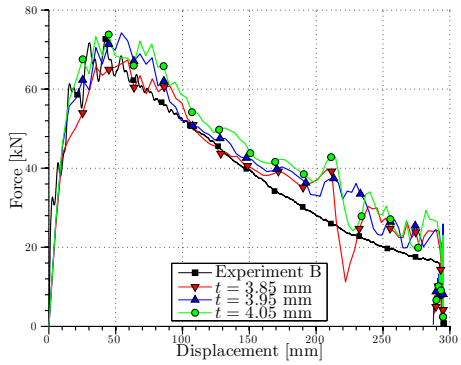

(d) *Pipe B, hierarchic pinballs*

Figure 8.20: *Thickness and contact model sensitivity study on empty pipes, medium mesh density* (24×78)*. For large deformation (*> 200 *mm) the hierarchic pinballs can cause some oscillations.*

To check this conjecture, the effect of increasing the air content in the pipe was investigated by using a multi-phase multi-component material model allowing for a mixture of air and water. For each mesh density, the top layer of elements was modelled as air. Increasing the air content successively to two and three rows of elements showed that higher air content changed the behaviour towards that of an open water-filled or empty pipe, which is what one would expect in practice as well. This is the case for all mesh densities, and one row of

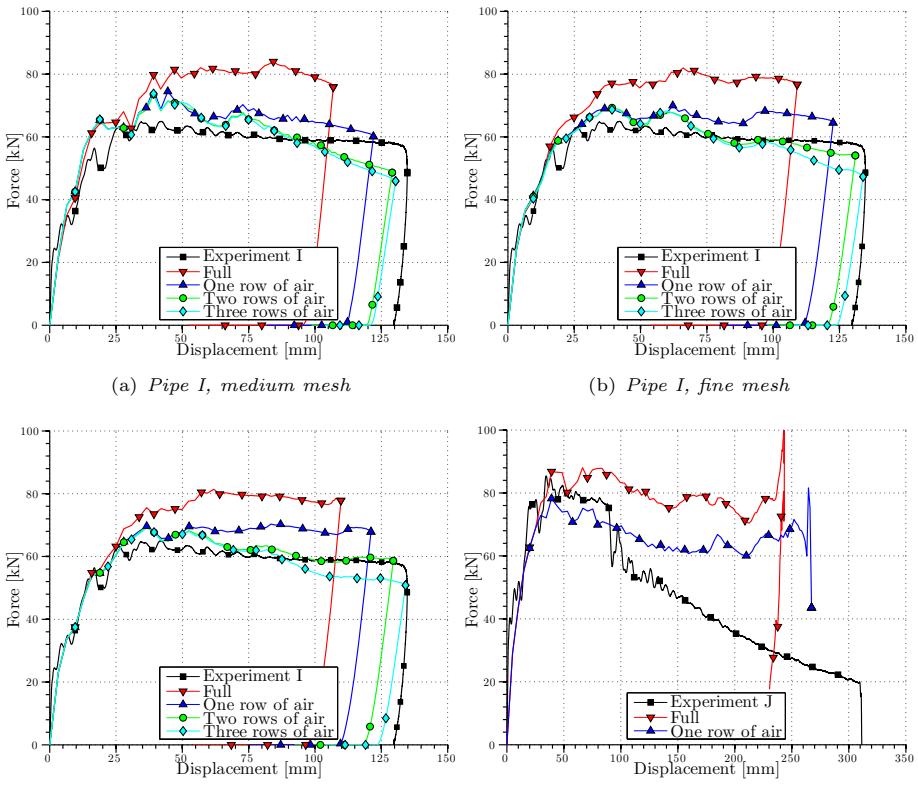

(a) *Pipe I, medium mesh*

(b) *Pipe I, fine mesh*

(c) *Pipe I, extra fine mesh*

(d) *Pipe J, medium mesh*

Figure 8.21: *Simulations of closed, water-filled pipes (experiments I and J).*

elements with air has a greater influence on the medium mesh (Fig. 8.21(a)) compared to, say, the extra fine mesh (Fig. 8.21(c)). One row in the medium mesh is approximately 19.2 mm, while in the extra fine mesh one row is about 11.5 mm. So it seems that to obtain a flatter force-displacement curve as seen in the experiments, it is crucial to have the correct fraction of air trapped in the pipe so that pressure builds up accordingly. After this consideration, a rather good match with the experimental data is acquired. It is worth noting that the stiffness of the test, i.e. the initial tangent of the force-displacement curves, is well captured in all simulations as this part takes place before any significant

rise of pressure (the change of volume is still small at this point).

The same setup with a medium mesh was applied to pipe J, the closed water-filled pipe impacted at 5.1 m/s. In the experimental case the weld attaching the end cap failed after about 19 ms (and deformation of approximately 90 mm, as seen in Fig. 4.18(b)), and since fracture is unaccounted for in the present study, results beyond this point would be inaccurate at best. From Fig. 8.21(d), it can be seen that results are quite decent until the point of failure. The simulation with a completely full pipe has a higher peak force and force level throughout the analysis compared to the experiment and the simulation with one row of air at the top. This second simulation has a force-displacement curve slightly below the experimental, suggesting that the air content is somewhat less than one row of elements in this case.

A refined mesh should be tested with the same setup for pipe J, but this was not explored in more detail as a proof of concept for this approach is shown for pipe I. Besides, no fracture criterion is employed at the moment, rendering further analyses somewhat redundant. Despite smooth-looking curves, the simulations of pipe J did have some instabilities due to excessive distortion of the cross-section, and Giuliani's rezoning algorithm [121] succeeded in keeping the mesh in the impact zone from becoming warped. The analyses ran almost to the point of maximum deformation, but failed due to excessive distortion of the mesh. Nevertheless, the impact is captured and results are available for comment. Some oscillations are noted in Fig. 8.21(d) towards the end of the impact, which is explained by the pipe "wrapping" around the impactor.

Fig. 8.21 shows simulations with FE in the fluid. Equivalent tests with cell-centred FV were conducted and gave very similar results, but these are not shown here for brevity. Also, simulations including a gravity field were conducted to no avail – the results remained indistinguishable.

Embedded simulations of filled pipe

Simulations with a Eulerian mesh of either FE or FV for the fluid (now including also the air external to the pipe) combined with a Lagrangian mesh for the structure took longer time since the model has a lot more elements. The search and update of the influence domain can also be costly, but all trouble with building the mesh and mesh update algorithms is effectively eliminated. The fluid mesh consists of $60 \times 36 \times 180$ elements, spanning $500 \times 300 \times 1\,500$ mm,



(a) *FSCP=0* (b) *FSCP=1* (c) *FSCP=0, Vofire* (d) *FSCP=1, Vofire*

Figure 8.22: *Diffusion in embedded calculations of pipe I after 85 ms (in a vertical cross-section of the dented zone), with the plots showing fluid density in kg/m^3. Colors indicate fluid density, red is highest and blue is lowest.*

and the medium structural mesh (24×78) was initially used for the pipe.

Alternatively, a finer pipe mesh (32×104) was also tested with the following refinement of the fluid mesh: while using the same number of fluid elements ($60 \times 36 \times 180$) it was possible to reduce the dimensions of the fluid box without the boundaries disturbing the FSI conditions, so the updated mesh is $350 \times 220 \times 1\,400$ mm. This makes the longest fluid edge about 7.8 mm while the structural shells are 12.5 mm, thus maintaining a finer discretisation of the fluid mesh compared to the structure.

The initial simulation with FE in the fluid and FLSR for the coupling showed that the response was closer to an open than to a closed pipe. This can be due to diffusion which is undoubtedly present as expected (see Fig. 8.22(a)). This may be ameliorated by coupling the fluid in all spatial directions (FSCP = 1) rather than just along the structure's normal. Obviously, diffusion is still present as seen in Fig. 8.22(b).

The anti-diffusion algorithm called "Vofire" [133] was successfully employed to reduce diffusion (see Figs. 8.22(c) and 8.22(d)). From the force-displacement curves in Fig. 8.23(a), internal pressure is not rising sufficiently to keep the force-level flat throughout the impact, possibly indicating the need for a finer discretisation. As Vofire worked quite well, this option is kept on for the remainder of the embedded calculations.

By using the slightly finer mesh, a flatter force-displacement curve is obtained (see Fig. 8.23(b)) similar to the full pipes from Fig. 8.21. Increasing the air contents at the top has the same effect here, although less pronounced, as this fluid mesh is Eulerian and some diffusion will remain even with Vofire. Fig. 8.23(b) also shows that the flat part of the force-displacement curve is harder to predict. This may be due to the fact that in an embedded calculation, there is no

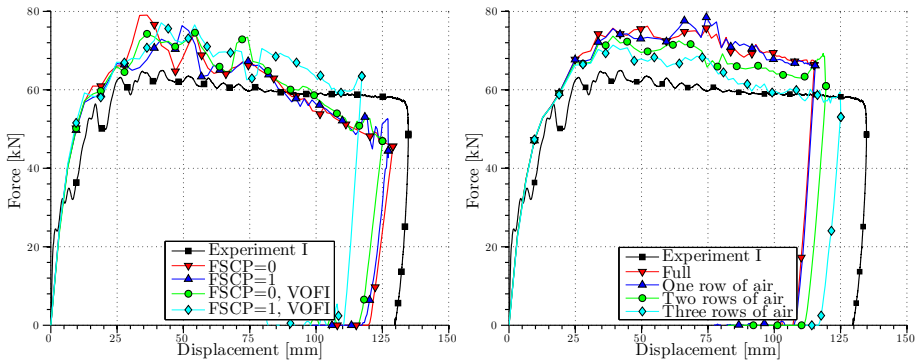

(a) *Medium mesh* (b) *Fine mesh, FSCP=1, Vofire*

Figure 8.23: *Force-displacement curves from embedded simulations of pipe I.*

well-defined fluid-structure border, unlike in classical ALE, thereby losing some accuracy. For a confined reservoir, an ALE approach (as far as this can work) seems to provide better results. If a submerged structure with surrounding fluid was to be modelled, an embedded technique is the natural choice as the Eulerian part of the embedded mesh is easily extended to account for surrounding water as done in [32].

Like in the case of conforming ALE simulations with FSA, equivalent tests to those of Fig. 8.23 were conducted with cell-centred FV in the fluid and FLSW coupling. Results were very similar to those obtained with FE/FLSR, and are omitted for brevity.

Embedded simulations of submerged pipe

Even though no experiments were conducted on this particular setup, simulations of a pipe submerged in water were also carried out. To this end, the embedded FSI technique was employed as it is easily modified for such simulations.

The exact same setup as above was used, except that in the fluid "box" the air outside the pipe was replaced with water and the end caps were removed to prevent any potential pressure build-up inside the pipe. This was done to isolate the effect of submerging the pipe in water. The simulations were run

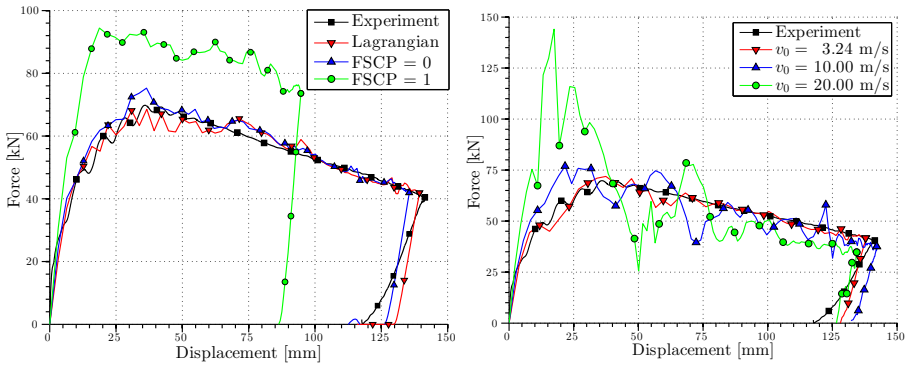

(a) *Different FSI techniques* (b) *Effect of velocity*

Figure 8.24: *Effect of submerging the pipe in water, medium structural mesh is used with thickness 3.89 mm.*

with Vofire, and the fluid-structure coupling parameter equal to both zero and one.

Fig. 8.24(a) shows the resulting force-displacement curves. As seen, the effect of including surrounding water is minimal when FSCP=0, and the simulation result is very close to the Lagrangian solution and the experimental data, which is pipe A (no water) in this case. Coupling the fluid to the structure in all spatial directions probably ties too much mass to the pipe, and thereby alters the force-displacement response radically, suggesting an unphysical loading of the pipe [32].

As the force arising from fluid flow around a circular cylidinder is proportional to the square of the magnitude of the flow velocity [134], extra simulations were run where the impactor's velocity was increased to 10 m/s and 20 m/s. To retain the kinetic energy delivered to the system, the mass was increased correspondingly and the results are presented in Fig. 8.24(b). Increasing the velocity to 10 m/s does not appear change much in terms of force-displacement. At 20 m/s, an effect emerges showing a higher peak force and larger oscillations.

This is, however, a severly exaggerated velocity for a water-travelling vessel and this velocity was chosen mainly to provoke an effect in the simulations. It can be said that at these velocities, submerging an experiment like pipe A in water seems to have a negligible effect. It remains to show this experimentally.

SPH simulations of filled pipe

Finally, simulations performed by the SPH method are presented. A first simulation was conducted for the case of an open water-filled pipe (test G), for which a Lagrangian description such as SPH lends itself particularly well. As shown in Fig. 8.25, SPH is able to represent water overflow at the pipe top in a natural way, without having to use multi-phase material and to discretise an initially empty space, like it would be with FE/FV fluid models. The results in terms of force-displacement curves are also very good, as shown in Fig. 8.26(a).

Next, a simulation assuming a nominally filled closed pipe (pipe I) is shown in Fig. 8.27. The pipe was discretised by a uniform mesh of 32×104 shells. Fig. 8.27(a) shows the initial SPH mesh near the impacted zone, using particles with a uniform radius of 2.5 mm, while Fig. 8.27(b) shows the deformed mesh at the instant of maximum deflection (at about 90 ms). Fig. 8.26(b) shows the contact force vs. displacement of the impactor.

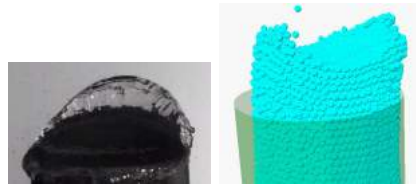

(a) *Test G* (b) *SPH result*

Figure 8.25: *Experiment and SPH simulation of open-filled pipe (G).*

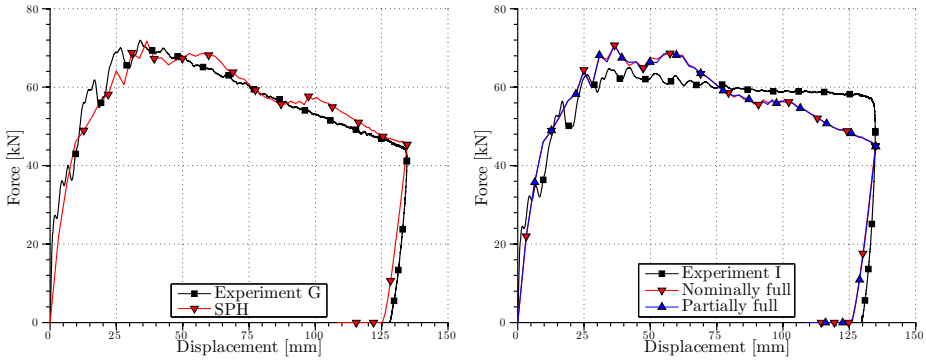

(a) *Pipe G (open)* (b) *Pipe I (closed)*

Figure 8.26: *Force-displacement curves from SPH simulations with experimental data.*

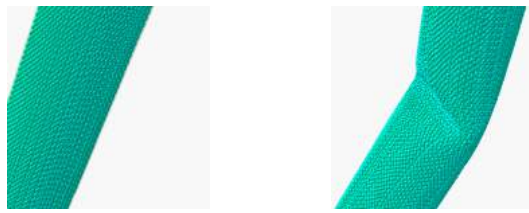

(a) *Initial SPH mesh* (b) *Mesh at 90 ms*

Figure 8.27: *SPH for nominally filled and closed pipe (I).*

The agreement with the experiment is quite good, with the exception perhaps of the latter part of the curve (for displacements larger than 100 mm). No gross overestimate of the contact force is observed, unlike other simulations with a filled pipe. This is due to the fact that with the standard SPH model available in the computer code it is impossible, in practice, to fill in a pipe perfectly, even in the initial configuration, because all particles are supposed to have the same diameter. Despite the use of an hexagonal close-packed array of (equally-sized) particles some gaps always remain between the particles and the cylinder. The total mass of the particles was 15.02 kg (for a water density of $\rho = 1\,000$ kg/m^3), while the nominal mass of the water is $M_w = \pi R^2 L \rho = \pi(63.31 \times 10^{-3})^2 \times 1.3 \times 1\,000 = 16.37$ kg, with R the inner tube radius and L the total tube length, including the extensions.

To confirm the above conjecture, a second calculation with particles only partially filling the pipe and leaving an empty zone of 25 mm in the upper part of the tube was run. As a matter of fact, this simulation gave very similar results, as seen in Fig. 8.26(b). Fig. 8.28 shows the initial SPH mesh for a partially filled pipe, and the mesh after 90 ms. The SPH particles flow nicely to fill the gap after impact.

Another shortcoming of the SPH method in the closed-filled pipe case is that the residual internal pressure in the tube is not correctly predicted (unlike with FE or FV-based models), again due to inaccurate representation of liquid volume near the walls and consequent lack of precision in representing the pressure field along the boundaries of the fluid domain, in contact with the structure. Such drawbacks of the classical SPH method are known from the literature and are due basically to incomplete neighbourhood of the particles near the boundaries. These aspects are of course much less important in classical SPH applications



(a) *Initial mesh* (b) *Mesh at 90 ms*

Figure 8.28: *SPH simulation of partially filled pipe, showing the top of the pipe.*

such as high-speed impact of projectiles, and also in the present case if one considers an open-filled pipe, where very little (if any) internal pressure is built up in the fluid, anyway.

It may be concluded that SPH is a very powerful and versatile method to treat FSI problems: there is no difficulty in representing partially filled vessels and one could easily add the treatment of structural failure, formation of water jets, etc., if needed. However, a drawback of the method in its standard form is the inability to accurately represent a perfectly filled reservoir, whenever this may be of importance. These simulations took about 3 days of CPU time each. A simulation with twice coarser SPH mesh (particle radius of 5 mm, thus 8 times less particles) was attempted to reduce the computer time, but results were not accurate enough. This was expected, since it is well known that SPH methods require a very fine mesh.

Summary of FSI simulations

Some selected simulations are compared with experimental data in Table 8.2, including the estimated pressure from the experiments. The reported CPU times were measured on a normal desktop computer running the sequential (non-parallelised) version of the code. To summarise, Fig. 8.29 gives a visual comparison of the various numerical simulation approaches investigated in the present work: (a) the Lagrangian approach used for the empty pipe (test A); (b) the SPH formulation used for the open-filled pipe (test G); (c) the ALE formulation with FSA coupling and (d) the Euler-Lagrange formulation with embedded coupling, used for the closed-filled pipe (test I). Only half of the model, cut vertically through the center, is shown to highlight the internal of the tube. In the right part of Fig. 8.29(c) the inner ALE fluid mesh around the

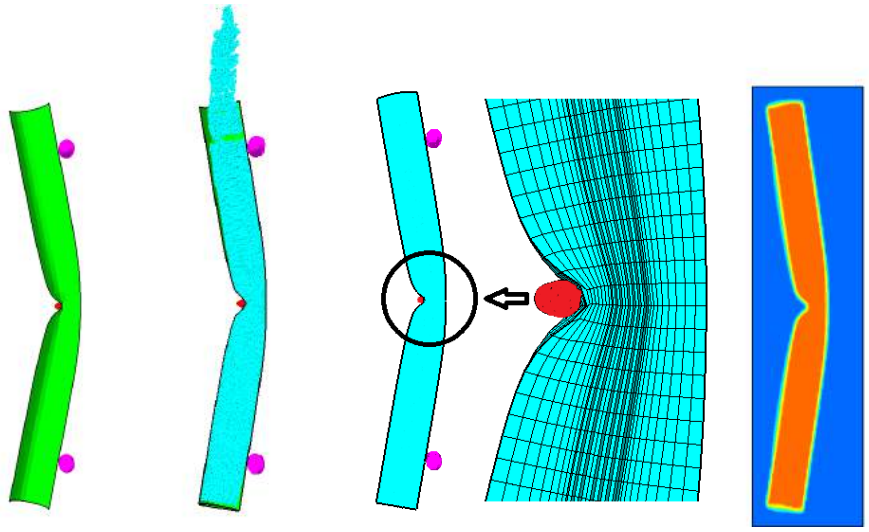

(a) *Empty pipe* (b) *Open-filled, SPH* (c) *Closed-filled, ALE* (d) *Closed-filled, embedded*

Figure 8.29: *A visual comparison of all the FSI approaches used in the numerical simulations for the various cases of the pipe experiments, using the same Lagrangian mesh for the structure in all cases.*

Table 8.2: *Selected numerical results compared with experiments (see Fig. 4.10 for legend).*

	Pipe A		**Pipe G**		**Pipe I**		
	Exp.	LAGR	Exp.	SPH	Exp.	FSA	FLSR*
Stru. mesh	-	32×104	-	32×104	-	32×104	32×104
Fluid els.	-	-	-	169 971	-	33 280	388 800
Rows air	-	-	-	0	-	2	3
d_i [mm]	170	169	140	140	139	132	129
$d_{\text{N-S}}$ [mm]	60	60	68	67	77	72	71
$L_{\text{N-N}}$ [mm]	1250	1246	1255	1252	1270	1255	1257
h [mm]	-	-	-	-	14	11	6
F_{peak} [kN]	71	70	72	72	65	69	71
p [MPa]	-	-	-	-	5.6†	2.4	2.0
CPU [days]	-	0.09	-	3.01	-	1.03	25.78
Fig. no.	4.18(a)	8.19(b)	4.18(a)	8.26(a)	4.18(a)	8.21(b)	8.23(b)

*FLSR calculation is with Vofire and FSCP=1.
†Based on analytical estimate from the method laid out in Appendix D.

impacted zone is visible, showing the importance of a robust rezoning algorithm. Fig. 8.29(d) shows the embedding fluid mesh only, with an isoplot of the density as in Fig. 8.22. The water (red) is nicely retained within the confines of the pipe, while the air (blue) remains outside the pipe. All in all the results were satisfying.

Chapter 9

Unit cell modelling

9.1 Introduction

This chapter contains unit cell analyses based on the compression-tension tests carried out in Section 3.6. The main topic of interest is to see how large scale compressive strains affect subsequent stretching of the material. Effects of material models, particle volume fraction and so on will also be investigated using axisymmetric unit cell analyses. Damage under compression, especially in a unit cell containing a particle, is heretofore studied to a very small extent in the literature. Zheng et al. [135] conducted compression-torsion experiments without investigating the damage mechanisms in too much detail, while Bao and Wierzbicki [136] compressed aluminium cylinders with various ratios of height to diameter and concluded that the secondary tensile stresses in the circumferential direction developing due to barrelling caused fracture in the equatorial region.

Further tests were carried out by Bao and Wierzbicki [136] on diabolo shaped specimens to avoid barrelling and the problem with friction. Also, fracture initiated in the middle of the gauge area for similar reasons. It has also been discussed theoretically in Refs. [137–139], while Tvergaard [140, 141] demonstrated that damage occurs in the negative stress triaxiality regime, given that a shear deformation component exists. Kweon [142] attempted to model the

phenomenon through a crystal plasticity framework, where damage arised from tensile hydrostatic stresses in grains caused by grain-to-grain action which followed from the shear deformation component.

Here unit cell simulations with constant triaxiality will be conducted in the following sections to investigate any potential damage mechanisms under compression (among other things).

9.2 Description of unit cell

Computational cell models have been around for over four decades now, and have proved useful in developing ductile fracture models. Such analyses typically consist of a characteristic volume element of a given material, including a single particle or void. Work of this kind dates back to the study by Needleman [143], and also by Tvergaard [144] for a square array of cylindrical voids. The influence of spherical voids was further studied by Tvergaard [145], and by Koplik and Needleman [146]. A spherical particle initially bonded to a ductile matrix, rather than just modelling an empty void, was introduced by Needleman [147]. Further discussion of models of this kind can be found in Ref. [148], limited to tension only.

Fig. 9.1 shows the main concepts of the axisymmetric model with periodicity. By being circular, the hexagonal stacked array is not exactly represented by an axisymmetric model but a good approximation is obtained. The unit cell analyses herein will be limited to axisymmetric models with a spherical particle inside a ductile matrix. This means that if Σ_{33} is the global stress over the entire cell along the axis of symmetry, then $\Sigma_{22} = \Sigma_{11}$ as indicated in Fig. 9.1.

If warranted, a cohesive bond between the particle and matrix can be accounted for. Since the spherical particles in the current X65 material bonded poorly with the matrix (see Section 5.2 and Ref. [29]), no cohesion between the particle and matrix was modelled, as has been done in previous work (see e.g. the study by Steglich and Brocks [150]). Further, the hard particle was simply modelled as linear elastic with Young's modulus $E = 208\,000$ MPa and Poisson ratio $\nu = 0.3$. The matrix was modelled using two different elasto-plastic material models; one with isotropic hardening only (Johnson-Cook, see Section 6.2.1), and one with combined isotropic/kinematic hardening (see Section 6.2.2) to investigate the effect of including kinematic hardening. The material tests are quasi-static, so

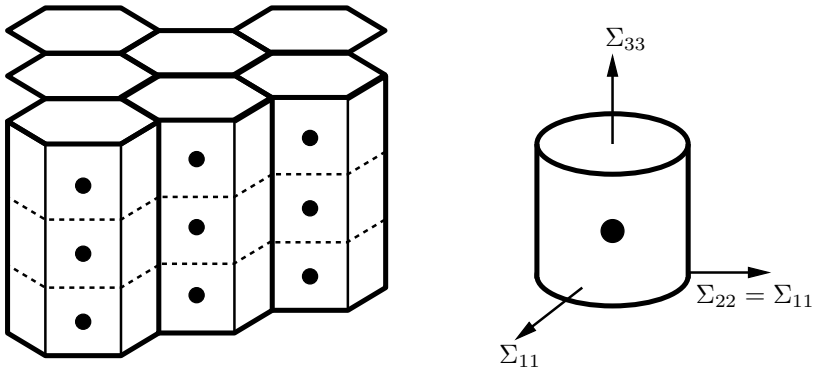

Figure 9.1: *Axisymmetric model for doubly periodic array of spherical voids or particles [149].*

no strain rate sensitivity will be accounted for.

Other parameters of interest are the particle volume fraction, the stress triaxiality, the friction between the particle and the matrix and of course the level of compression before tension. Most studies have focussed on the coalescence of voids at different stress triaxialities in tension with varieties of void size and shape among other things, but here compression (at different triaxialities) in sequence with tension (also at different triaxialities) will be examined in more detail.

Being axisymmetric, $\Sigma_{11} = \Sigma_{22}$ as stated in Fig. 9.1. This means that the von Mises effective stress Σ_e is given by the absolute value of the difference between the net axial stress Σ_{33} and the net lateral stress Σ_{11} as laid out in Ref. [148]

$$\Sigma_e = |\Sigma_{33} - \Sigma_{11}| \tag{9.1}$$

The hydrostatic stress Σ_h is

$$\Sigma_h = \frac{1}{3}\left(\Sigma_{33} + 2\Sigma_{11}\right) \tag{9.2}$$

which in turn makes the stress triaxiality ratio Σ^* equal to

$$\Sigma^* = \frac{\Sigma_h}{\Sigma_e} = \text{sign}\left(\Sigma_{33}\right) \cdot \frac{2\rho_c + 1}{3\left|1 - \rho_c\right|} \tag{9.3}$$

where ρ_c is the ratio of stresses, i.e. $\rho_c = \Sigma_{11}/\Sigma_{33}$, a ratio remaining constant throughout the analysis as the Riks algorithm [151] (arc-length method) is used with a global load proportionality factor λ. The effective stress Σ_e and the effective strain E_e can be said to represent the macroscopic response of the unit cell, with Σ_e defined in Eq. (9.1) and with E_e given by

$$E_e = \frac{2}{3}\left|E_{33} - E_{11}\right| \tag{9.4}$$

The strains E_{33} and E_{11} are defined as functions of the current height H and current radius R of the unit cell, respectively,

$$E_{33} = \ln\left(\frac{H}{H_0}\right) \tag{9.5a}$$

$$E_{11} = \ln\left(\frac{R}{R_0}\right) \tag{9.5b}$$

The constants H_0 and R_0 are the initial values of the height and radius, respectively, as indicated in Fig. 9.2(a). Further, the vertical outer edge is restrained to remaining vertical while the upper horizontal edge is restrained to remaining horizontal. In the analyses conducted here in, the values of Σ_{33} will be used to measure the response of the cell rather than Σ_e as the sign is important when visualising the results. Due to the constant triaxiality, Σ_{33} is easily converted to Σ_e and vice versa. Further, an initial particle volume fraction ω_0 is given for each analysis. As the analyses progress and the particle and matrix separate, the total volume fraction of the particle and the resulting void are defined together as ω, and will naturally change during the course of the analyses.

9.3 Setup of analyses

ABAQUS [91] with Python [152] scripting has been used to create the cell models in this section. By running some initial test simulations, a good mesh

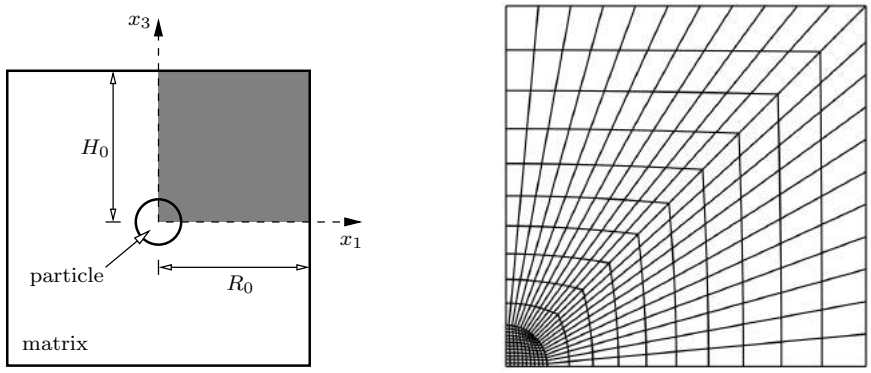

(a) *Unit cell quadrant* (b) *Finite element mesh*

Figure 9.2: *One quadrant (hatched area) of unit cell (a) and a typical finite element mesh with particle and matrix (b).*

was obtained, both in terms of accuracy and speed. Due to the sheer number of analyses planned, a fast yet good performing mesh was essential. The mesh used is shown in Fig. 9.2(b) – with 220 elements for the matrix and 119 for the particle – is made up of four-node axisymmetric elements with reduced integration and hourglass control (`CAX4R` in ABAQUS [91]).

To make the cell model as close to the experimental data as possible, axisymmetric models of the material tests themselves were set up with both material models. By utilising symmetries, only one quadrant of the geometry was modelled, and this was done for the following geometries:

- Smooth axisymmetric specimen in Fig. 3.5.
- Two notched (profile radius of notch at the root $R = 0.8$ mm and $R = 2.0$ mm) axisymmetric specimens in Fig. 3.9(a).
- Diabolo shaped specimen (radius at minimum cross-section $a = 3.2$) in Fig. 3.17(a), hereafter referred to as "D1".
- Diabolo shaped specimen (radius at minimum cross-section $a = 2.0$) in Fig. 3.20(a), hereafter referred to as "D2".

Fig. 9.3 illustrates the general procedure developed and employed. The global models were run with different mesh grades to ensure convergence. In total five

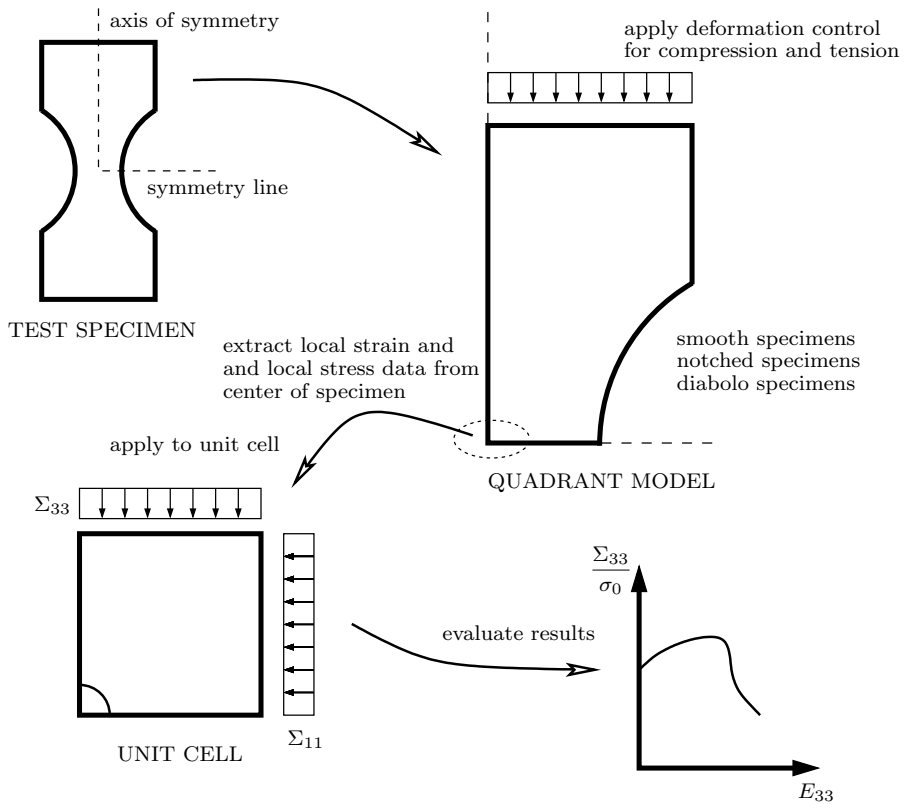

Figure 9.3: *Procedure for creating boundary conditions for unit cell analyses based on global analyses of test specimens.*

different grades were tested, with 5, 10, 20, 50 and 100 elements over the radius. As convergence was obtained at 20 elements, and to avoid having an element size close to the unit cell size, this mesh density was the one chosen to progress with as basis for the cell models.

Then, from the global analyses the stress triaxiality σ^* and the strain in the axial direction ε_{33} (i.e. along the axis of symmetry) were used to drive the unit cell models. Triaxiality values were picked from the center of the global model, where the values are highest and fracture initiates [153]. For the specimens loaded in tension only, various triaxialities were tested on the unit cells, including a mean

triaxiality, a lower and an upper triaxiality in addition to various other values tested for verification purposes.

To make sure the correct triaxiality is applied, a unit stress Σ_{33} is applied in the axial direction, along with a connected stress Σ_{11} calculated from Eq. (9.3) with $\rho_c = \Sigma_{11}/\Sigma_{33}$. Then the load proportionality factor λ in the Riks algorithm drives the analysis forward until void colescence is reached for the tension only samples. When doing compression before tension, λ is increased until a certain deformation H of the cell is reached, calculated from the strain in the global model ε_{33},

$$H = H_0 \cdot \exp\left(\varepsilon_{33}\right) \tag{9.6}$$

This is done for different triaxialities (and hence, different values of ρ_c) and for different levels of compressive strain. After the given compressive strain is attained, a second step with the tensile triaxiality is applied until void coalescence to see how compression affects this. Compressive and tensile triaxiality data from global simulations of material tests were used, in addition to broader ranging triaxiality values as the values from the material tests were fairly close to each other. Both H_0 and R_0 were set to unity.

9.4 Results

9.4.1 Tension only

Like indicated, the tension only cases will be examined first to check that the model is able to capture and recreate results obtained by previous studies on unit cell models, an apt summary of which can be found in work by Benzerga and Leblond [148]. First off, it is observed from Fig. 9.4(a) that the global models of the material tests capture the behaviour of the three types of axisymmetric specimens (smooth, notched $R = 2.0$ mm, notched $R = 0.8$ mm) loaded in tension quite well, and should thereby provide decent local results as convergence appears to be reached. These are shown in Fig. 9.4(b), which consists of the stress triaxiality σ^* plotted versus the strain in the axial/longitudinal direction, ε_{33}, both taken from the center of the specimen. This data will be used to determine the load ratio ρ_c for the edges in the unit cell.

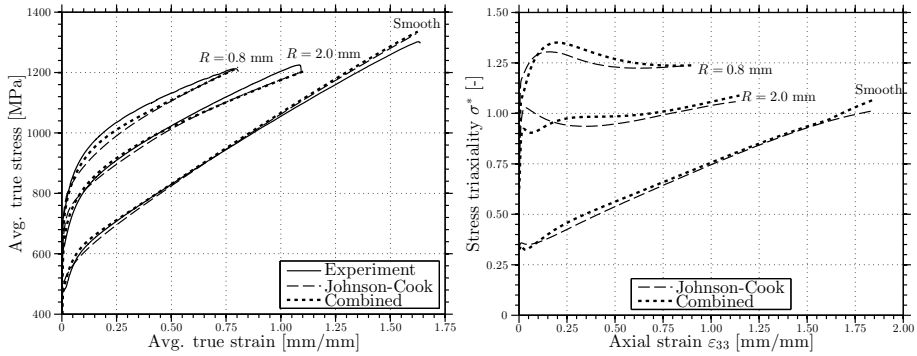

(a) *Global analyses and experiments* (b) *Local data from global analyses*

Figure 9.4: *Analyses of tension tests with different geometries, with (a) showing the global response in terms of true stress and true strain compared with experimental data, and (b) displaying local stress triaxiality σ^* and longitudinal strain ε_{33} at the center of the specimen.*

As the triaxiality in the center of the specimen varies a lot during the course of deformation, and a Riks algorithm with a global load proportionality factor is used (i.e. constant ρ_c), three different triaxialities from the global analyses are used: a lower (typically the initial) triaxiality ($\div$), a maximum triaxiality ($+$) and a mean triaxiality (M), all of which are shown in Tables 9.1 and 9.2. The former contains the load ratios ρ_c while the latter contains the triaxiality values Σ^*. Other triaxialities were also tested and compared with results from other studies, see e.g. [148] and references therein. In the case of both the notched specimens, the triaxiality does not vary as much as the case of the smooth specimen, so a constant triaxiality should therefore be a fair approximation for the notched specimens. Since the smooth specimen develops a neck, the triaxiality is bound to vary more. It starts out at 1/3 and increases to above 1, thereby constituting a much larger span of variation.

Another crucial parameter is the initial particle volume fraction ω_0. Making the particle larger should lead to earlier ligament necking and thereafter fracture. The six different ω_0 tested are (in ascending order): 0.0001, 0.0002, 0.0005, 0.0010, 0.0020 and 0.0050, with 0.0005 being the experimentally obtained value (see Section 5.2). Even though it is suspected to be of minor importance, different coefficients of friction were tested for the contact between the particle and matrix. This parameter might be of importance when compression is included,

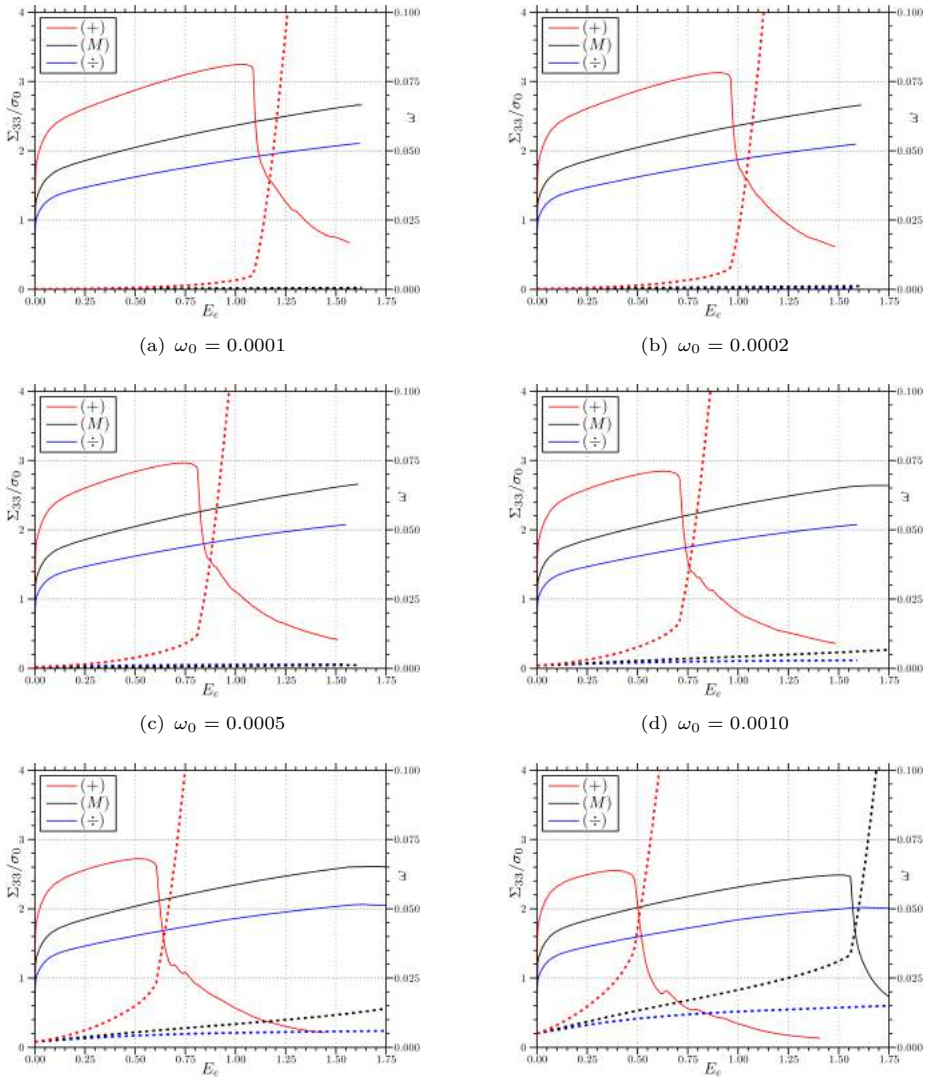

(a) $\omega_0 = 0.0001$

(b) $\omega_0 = 0.0002$

(c) $\omega_0 = 0.0005$

(d) $\omega_0 = 0.0010$

(e) $\omega_0 = 0.0020$

(f) $\omega_0 = 0.0050$

Figure 9.5: *Relative axial stress Σ_{33}/σ_0 (solid line) and particle/void volume fraction ω (dotted line) vs. effective strain E_e for various Σ^* ((+), (M) and (÷) from smooth specimens) and ω_0, using the combined material model and a coefficient of friction $\mu = 0.6$.*

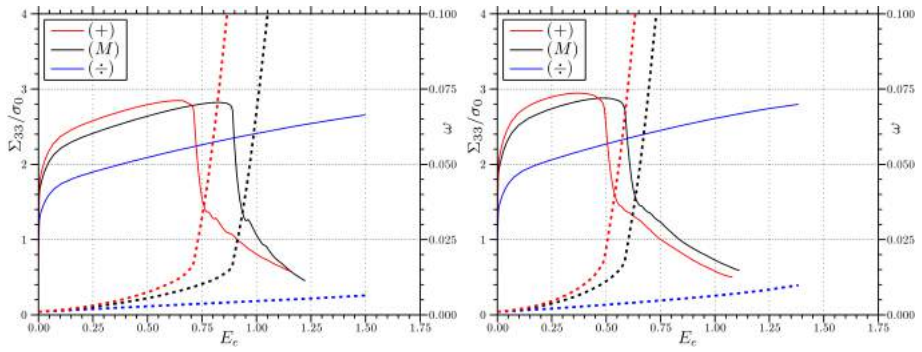

(a) $R = 2.0$ *mm* (b) $R = 0.8$ *mm*

Figure 9.6: *Relative effective stress* Σ_{33}/σ_0 *(solid line) and particle/void volume fraction* ω *(dotted line) vs. effective strain* E_e *for various* Σ^* *((+), (M) and (÷) from notched specimens) and* $\omega_0 = 0.0010$*, using the combined material model and a coefficient of friction* $\mu = 0.6$*. See Table 9.2 for specific values of the stress triaxialities.*

as contact is more prominent.

From Fig. 9.5, showing data using triaxialities from analyses of the smooth specimen with a combined material model, it is seen that higher triaxiality values lead to earlier coalescence of voids as thoroughly documented in the literature [146, 148]. The same applies to the initial particle volume fraction ω_0. For the lowest triaxiality (denoted (÷) in Fig. 9.5 and throughout the chapter), void coalescence did not occur for any of the ω_0 used. The middle triaxiality value (M) obtained coalescence for the highest ω_0, while the highest triaxiality (+) always produced coalescence (albeit at different effective strain levels E_e varying with ω_0). This is completely in line with both intuition and previous work [154]. Results for the Johnson-Cook isotropic hardening model were very similar to Fig. 9.5, and omitted here for brevity. Also, between the different coefficients of friction there did not seem to be any difference.

The results from the notched specimens, with $R = 2.0$ mm and $R = 0.8$ mm in Fig. 9.6(a) and (b) respectively, show the same trends. A sharper notch produces higher values of triaxiality as seen in Table 9.2, and hence an earlier coalescence of voids and is shown for $\omega_0 = 0.0010$. An attempt to predict the fracture strain was also made, with $\omega_0 = 0.0005$ and the average triaxialities from the three different test geometries. As the two notched geometries have fairly constant

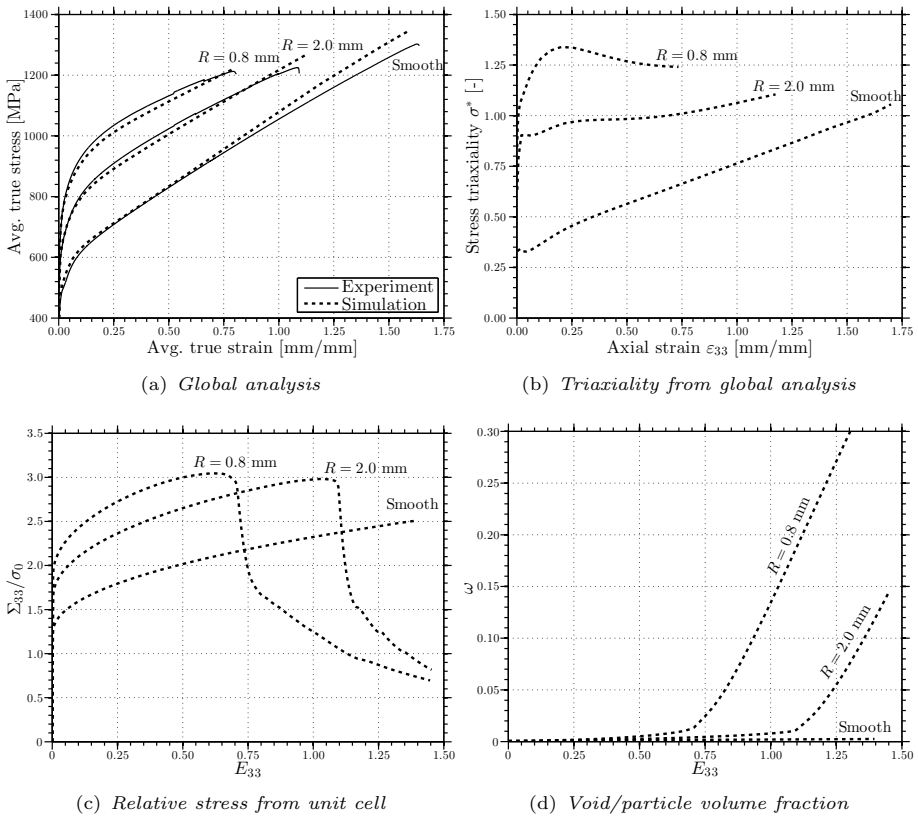

(a) *Global analysis*

(b) *Triaxiality from global analysis*

(c) *Relative stress from unit cell*

(d) *Void/particle volume fraction*

Figure 9.7: *The global analyses in (a) and (b) provide boundary conditions for the unit cell analyses, the results of which are shown in (c) and (d). Comparing (a) and (c) reveals that the unit cell does a decent job in predicting the global fracture strain.*

triaxialities, decent results are expected of these, whereas the smooth specimen has too much variation in the triaxiality to make any reasonable prediction. If anything, the average triaxiality should overestimate the fracture strain. For simplicity, and as the results were quite similar, data is shown only for the combined material model.

First, the results from the global analysis of the test specimens are shown along with the experimental data in Fig. 9.7(a) and, as before, this is used to generate

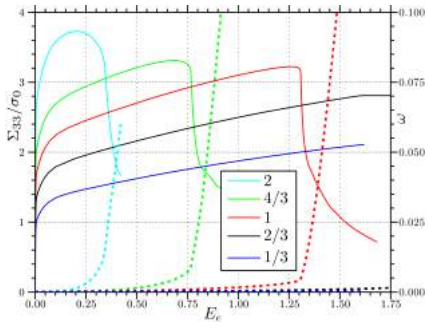

(a) $\omega_0 = 0.0001$

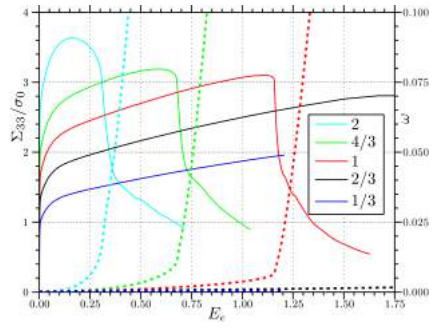

(b) $\omega_0 = 0.0002$

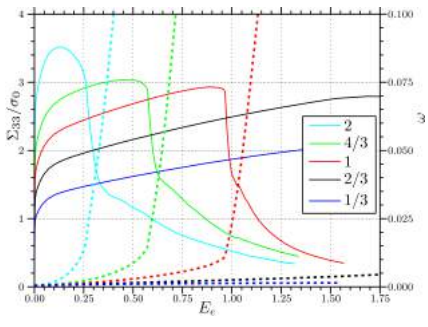

(c) $\omega_0 = 0.0005$

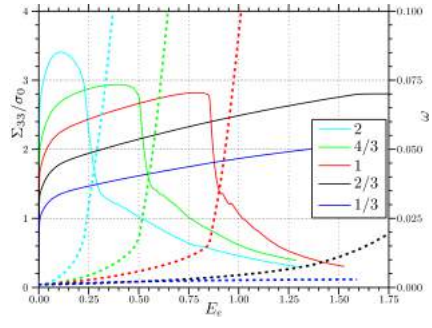

(d) $\omega_0 = 0.0010$

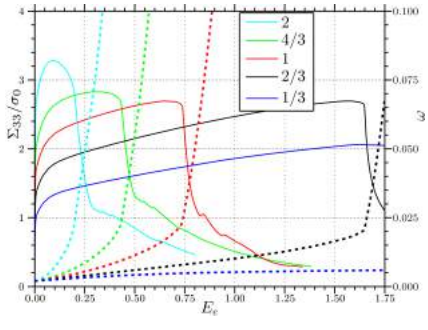

(e) $\omega_0 = 0.0020$

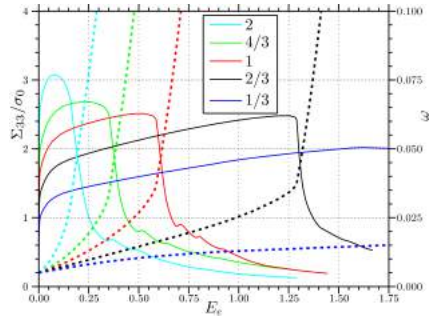

(f) $\omega_0 = 0.0050$

Figure 9.8: *Relative effective stress Σ_{33}/σ_0 (solid line) and particle/void volume fraction ω (dotted line) vs. effective strain E_e for various Σ^* (1/3, 2/3, 1, 4/3 and 2) and ω_0, using the combined material model and a coefficient of friction $\mu = 0.6$.*

a (mean) triaxiality for the cell model. The triaxialities as they progressed through the global analyses are shown in Fig. 9.7(b). Further, parts (c) and (d) show the unit cell results, with (c) containing the relative axial stress Σ_{33}/σ_0 versus the axial strain E_{33} for comparison against the global strain ε_{33}, and (d) showing the void/particle volume fraction ω versus the axial strain E_{33}. As seen, the unit cell obtains coalescence for about the same strain as the material tests for the two notched specimens, while the triaxiality/initial particle volume fraction combination fails to produce coalescence at all for the smooth specimen. In any case, where the triaxiality is roughly constant the unit cell model gives good predictions of the fracture strain; around 0.75 for the sharpest notch and about 1.10 for the other notch, which is promising for further analyses.

In addition, "typical" triaxiality values as used in the literature were tested on the unit cell model as opposed to using values from the global FE analyses of the material tests. The chosen values were 1/3, 2/3, 1, 4/3 and 2, and these were run for the same values of ω_0 as before. Once again the conclusions are the same. Fig. 9.8 shows plots of the relative axial stress Σ_{33}/σ_0 and void/particle volume fraction ω versus effective strain E_e. The very same trends emerge in Fig. 9.8 as in Fig. 9.5, so these comments are not reiterated.

9.4.2 Compression-tension from material tests

Again global analyses of the test specimens were used to derive triaxiality data for the unit cell, as illustrated in Fig. 9.3. Now the triaxialities were applied to the unit cell in two steps, one representing the compression step (negative) and the other the subsequent tension (positive). Three different triaxiality values were used for each step and in combination, all listed in Table 9.2, making a total of nine different triaxiality combinations. In addition, the influence of particle volume fraction and friction coefficients were investigated in all possible different combinations. This amounts to a vast number of analyses; five different compression levels for two different geometries, nine triaxial sequences, six initial particle volume fractions and five friction coefficients make up a total of $2 \times 5 \times 9 \times 6 \times 5 = 2700$ different analyses. Then double this number to account for the two different material models. Needless to say, not all of the results will be presented here, but rather the trends emerging from the data. It was essential to script this procedure to make it viable at all. Post-processing was also somewhat of a challenge.

As before, global analyses of the test specimens (geometry shown in Fig. 3.17(a))

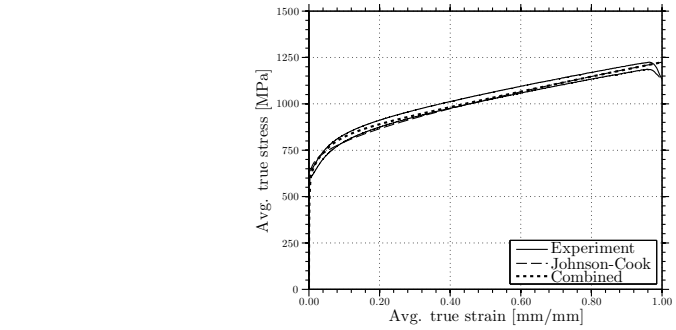

(a) *0%*

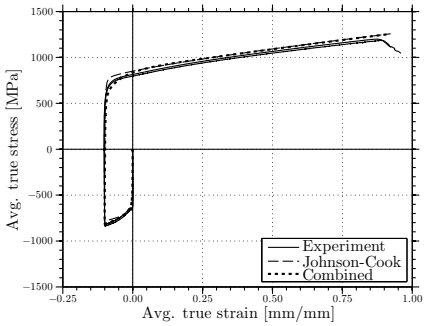

(b) *10%*

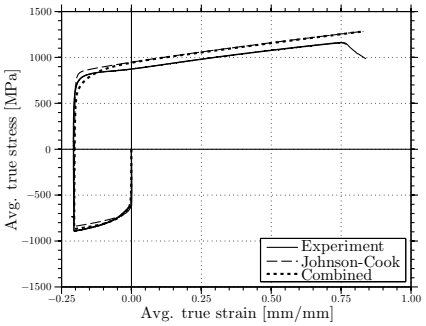

(c) *20%*

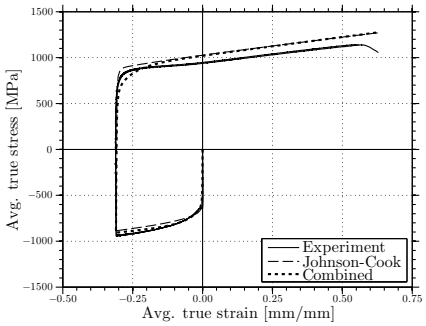

(d) *30%*

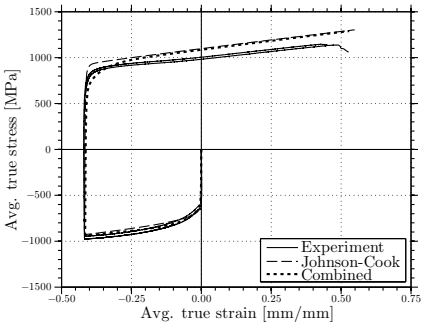

(e) *40%*

Figure 9.9: *True stress-true strain curves from simulations of notched compression-tension tests (diameter 6.4 mm dubbed D1), along with two experimental curves for each.*

were conducted and compared with the experimental results. These are the specimens with the label D1 as introduced earlier. From Fig. 9.9 it is observed that the global simulations match the experiments quite well, with the exception perhaps of the latter part of the curve after reversing the load. The difference between the combined and JC model presents itself most prominently during the re-yielding phase. As expected, the isotropic hardening has a sharper curvature and predicts a higher stress at re-yielding while the combined model has a more round shape at re-yielding. For larger tensile strains, the curves for the two models appear to converge.

The triaxialities extracted from the global analyses are shown Fig. 9.10, making it evident that the variation in triaxiality is not particularly big but variation is still there. In compression it is quite stable around -1, with the JC model having a value of $\sigma^* < -1$ in the beginning and then moving towards $\sigma^* > -1$ while the combined model exhibits a reversed behaviour, making the average values of both approximately -1 (see Table 9.2). When the load is reversed into tension, re-yielding occurs at a triaxiality just below 1 (with the combined model slightly lower than the JC model) and then steadily increases.

With the immense amount of data, some selected simulations showing the trends are included. From the D1 batch, the specimen compressed to 40% plastic strain is chosen to proceed with[1], meaning that Fig. 9.10(e) contains the triaxiality data that will be applied as boundary conditions for the unit cell; three compressive values each with three succeeding tensile values, making a total of nine.

The results are presented in Fig. 9.11, which has two subfigures showing the response of the cell, with the left showing the axial stress Σ_{33} relative to the yield stress σ_0 as a function of the axial strain E_{33}, and the right shows the void/particle volume fraction, also as a function of the axial strain E_{33}. As the compressive triaxiality was quite constant (see Fig. 9.10), only the mean has been included, which is $\Sigma^*_{\text{comp}} = -1.0098$. The initial particle volume fraction is $\omega_0 = 0.0005$ as in the material, and the coefficient of friction is $\mu = 0.4$ (no significant difference was observed between the various coefficients of friction).

Comparing the experimentally obtained fracture strain from Fig. 9.9(e) with the predicted strain to coalescence in the cell, it looks quite decent for the two highest triaxialities, (M) and $(+)$ which are close in magnitude (1.0001 and 1.1641 respectively, confer with Table 9.2 for other values). Experimental values in the range of 0.40 to 0.50 are definitely of the same magnitude as the values

[1] The effect of compressing to different levels before stretching is discussed later.

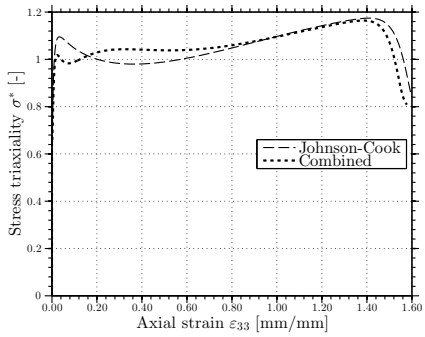

(a) *0%*

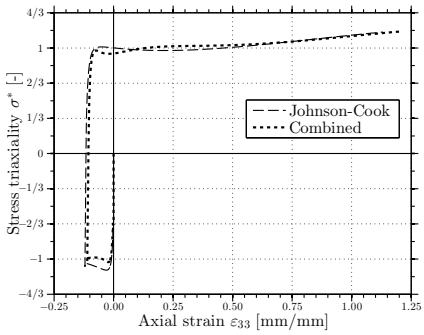

(b) *10%*

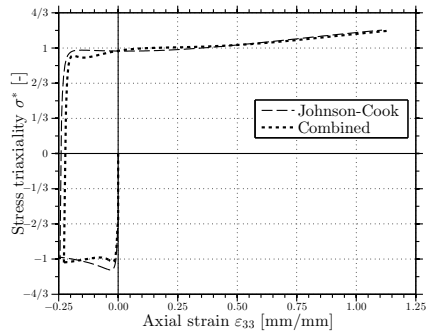

(c) *20%*

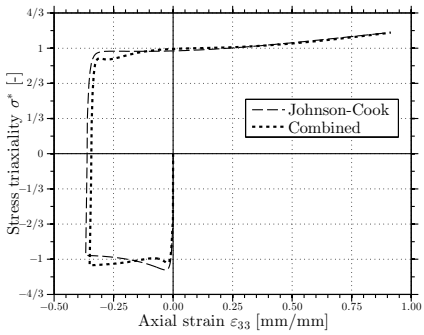

(d) *30%*

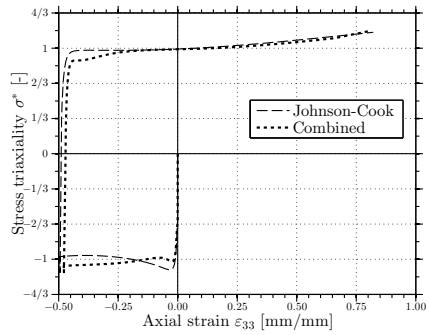

(e) *40%*

Figure 9.10: *Stress triaxiality σ^* vs. axial strain ε_{33} in the center of the notched specimens (diameter 6.4 mm dubbed D1), taken from the global axisymmetric analyses.*

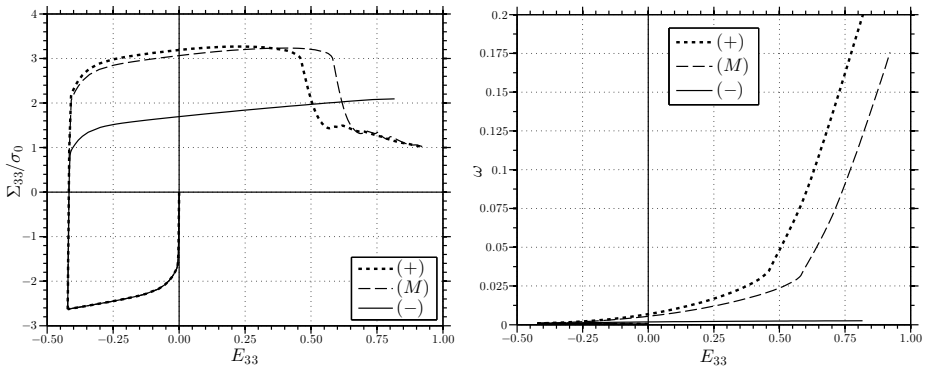

(a) *Relative axial stress* (b) *Void volume fraction*

Figure 9.11: *Unit cell results with boundary condition from a D1 specimen compressed to 40% plastic strain with* $\Sigma^*_{\text{comp}} = -1.0098$*, and subsequently stretched with three different triaxialities.*

obtained by the cell models in Fig. 9.11. For the notched tensile specimens the average triaxiality gave the best results, here the maximum tensile triaxiality was most accurate. This might be an indication that there are some mechanisms during the compressive phase which are not not properly represented by the cell model, thereby requiring higher triaxiality to induce coalescence at the right strain magnitude. A higher relative axial stress is observed for higher absolute values of triaxiality, which is a general observation for more or less all cell simulations. The effect of variation in compressive triaxiality preceding tension will be explored numerically later.

The same procedure has been repeated for the D2 specimens, whose geometry is drawn in Fig. 3.20(a). Again the global simulations match the experimental data quite well as plotted in Fig. 9.12, excluding the latter part of the curve during the tensile load. An explanation for this can be that when compressing to such high levels of plastic strain, dislocations pile up at obstacles and provide large resistance to further straining, and when the load is reversed these dislocations are much less restrained thereby creating the plateu seen after re-yielding. This is hard to capture numerically, and the combined material model is calibrated for smaller strains.

Further, the triaxiality values, plotted in Fig. 9.13, vary more for the D2 sim-

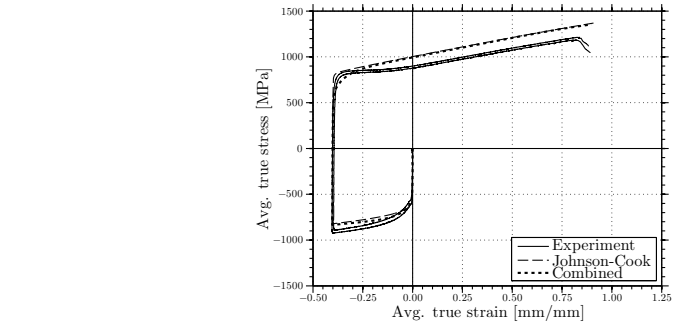

(a) *40%*

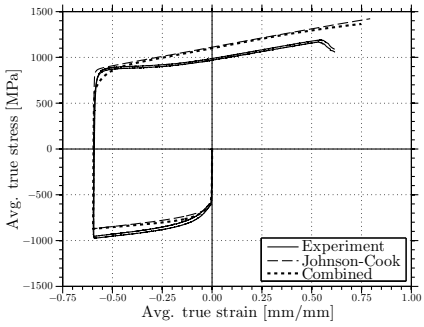

(b) *60%*

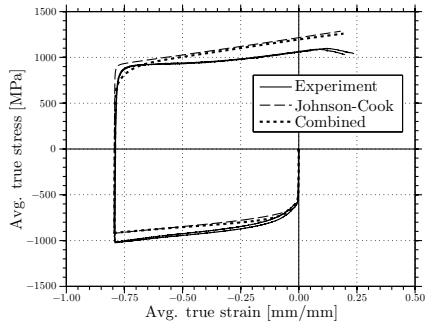

(c) *80%*

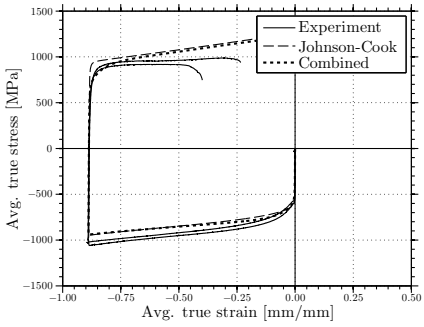

(d) *90%*

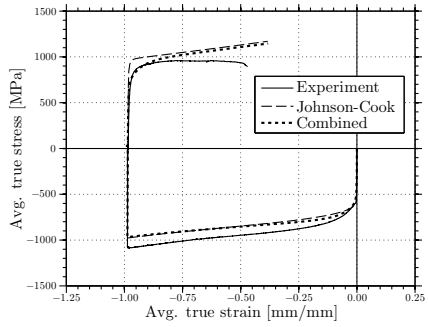

(e) *100%*

Figure 9.12: *True stress-true strain curves from simulations of notched compression-tension tests (diameter 4.0 mm called D2), along with two experimental curves for each compression level (one for 100%).*

ulations compared with the D1 simulations. Due to the difference in geometry, the relative deformation of the specimen is much larger, hence giving rise to the somewhat larger variation of triaxiality during each test, particularly during the re-yielding phase (again, see Tables 9.1 and 9.2 for specific values). For this reason the fracture strains predicted by the unit cell model are not expected to be outstandingly accurate. Still, the model should be able to at least capture the the fracture strain within its magnitude, meaning that among the ranges of triaxialities and initial particle void volume fractions tested, the values closest to the actual values should not be too far off and the fringe values should produce bounds including the measured fracture strain.

As before, a subset of the total data is chosen to represent the trends observed. This time it is the D2 specimen compressed to 80% plastic strain, which means that Fig. 9.13(c) provides the triaxiality data. Fig. 9.14 has two subfigures showing the response of the cell in terms of (a) and (b) void volume fraction. with the same structure as Fig. 9.11. In all subfigures the initial particle volume fraction is $\omega_0 = 0.0005$ as in the material, and the coefficient of friction is $\mu = 0.4$.

The cell model appears to estimate the fracture strain with decent accuracy even when compression precedes tension, and again the prediction was best for the highest tensile triaxiality (+). In general, the pure tensile cell model predicted the fracture strain with good accuracy (given that the triaxiality was fairly constant in the experiment) when using the mean triaxiality value from the global analysis. There is a greater variation in triaxiality in these D2 diabolo specimens (due to larger relative deformation of the specimens) which can partly explain this, but at the highest triaxiality the strain to coalescence should not be larger than what is seen in the tests. This could indicate that some mechanism is not captured adequately by the analyses as suggested earlier. Between the three compressive triaxialities used for the D2 compressed to 80% little difference is observed. The lower triaxiality appears to lead to a slightly earlier onset of coalescence as noted for the D1 simulations, although this will be explored later.

The accuracy of the global models may of course be a bottleneck for the cell models, but even with this consideration in mind the results are uplifting. Using triaxiality data from a larger simulation (in scale) to provide boundary conditions for a unit cell model might prove a fruitful endeavor, given, as mentioned, that the triaxiality remains approximately constant. Using the JC model compared to the combined model did not reveal any significant differences; minor adjustments in triaxiality values (see Table 9.2) and almost overlapping

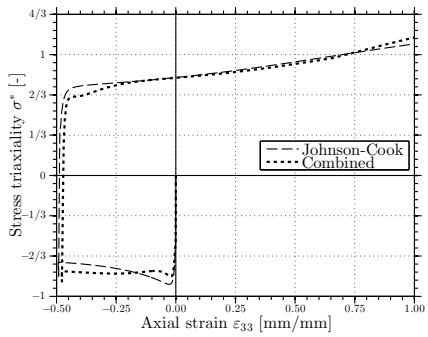

(a) *40%*

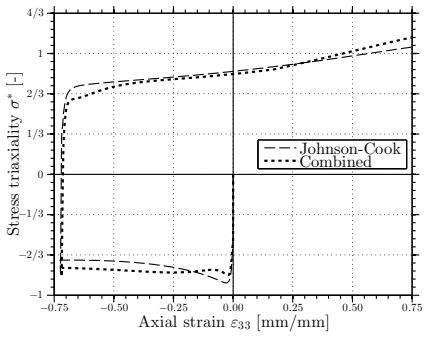

(b) *60%*

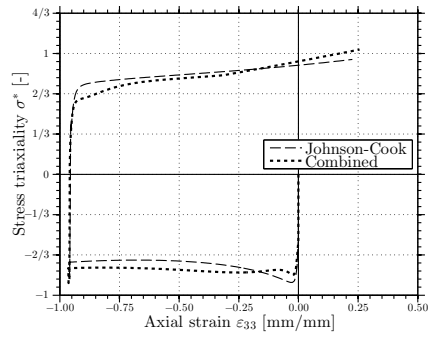

(c) *80%*

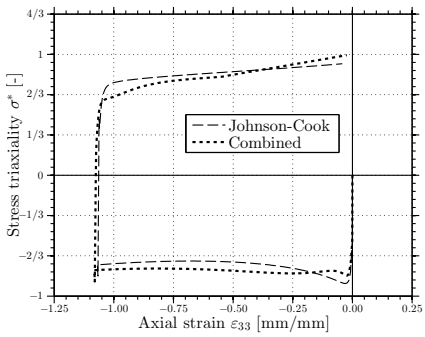

(d) *90%*

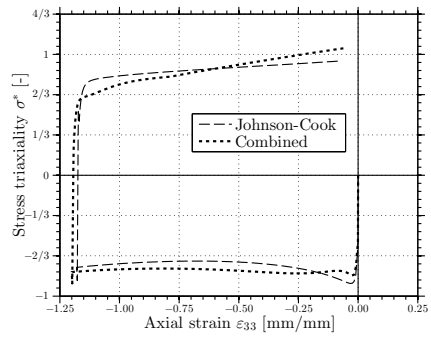

(e) *100%*

Figure 9.13: *Stress triaxiality σ^* vs. axial strain ε_{33} in the center of the notched specimens (diameter 4.0 mm called D2), taken from the global axisymmetric analyses.*

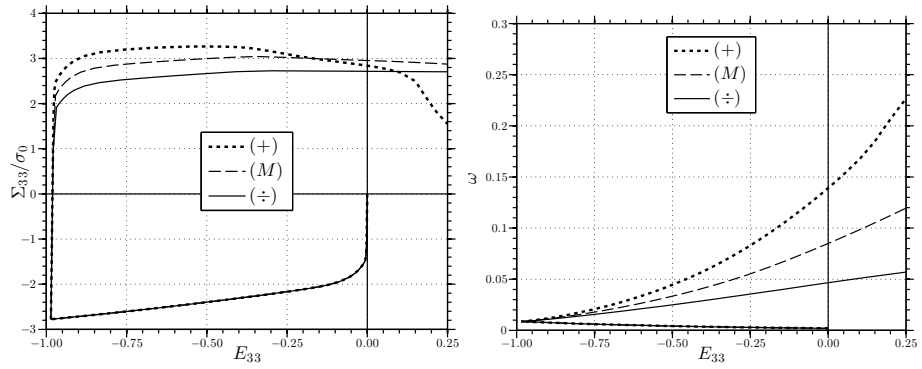

(a) *Relative axial stress* (b) *Void volume fraction*

Figure 9.14: *Unit cell results with boundary condition from a D2 specimen compressed to 80% plastic strain with* $\Sigma^*_{\text{comp}} = -0.8308$ *and subsequently stretched.*

curves (rather than actually overlapping curves) were the only ones directly attributable to this. The effect of varying the coefficient of friction was even less, if anything. Still, an important quastion remains unanswered; how does increasing the compression affect subsequent tensile behaviour? This will be explored in the following section, along with the influence of the magnitude of the compressive triaxiality.

9.4.3 Compression-tension with user-specified triaxiality values

As the compressive triaxialities from the material tests were all somewhat similar in magnitude, analyses with user-specified values ($-1/3$,$-2/3$,-1,$-4/3$ and -2) were run in addition. Compression of the unit cell was also run to 20%, 40%, 60%, 80% and 100%, and a triaxiality value of 1 was chosen for the tensile step to limit the horrendous amount of data already not in print. The effect of the tensile triaxiality on the strain to coalescence is already well established, so a value known to produce coalescence was chosen. The value is also close to what is extracted from the global simulations. Finally, the experimental particle volume fraction was chosen, $\omega_0 = 0.0005$.

It is worth noting that despite a displacement-based termination criterion in

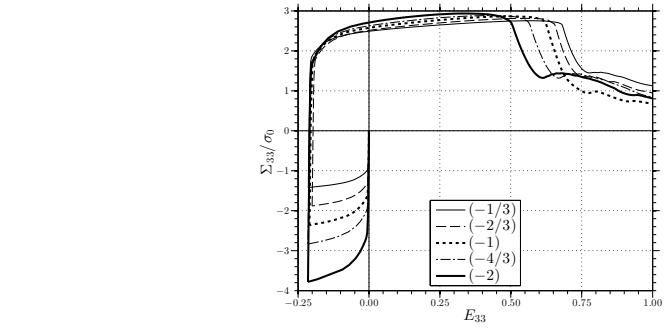

(a) *20%*

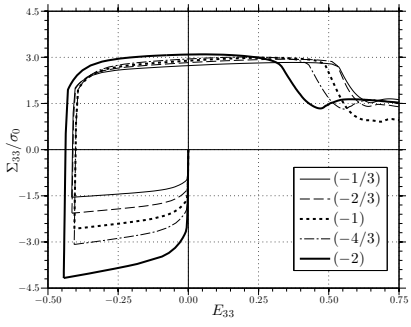

(b) *40%*

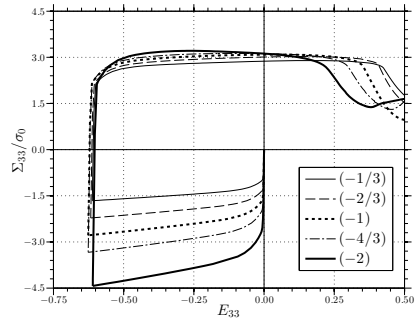

(c) *60%*

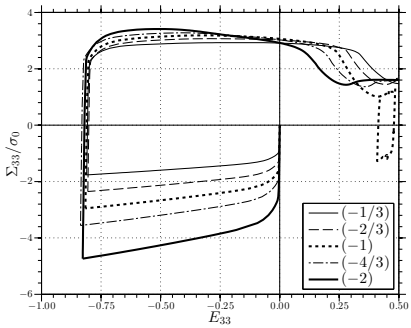

(d) *80%*

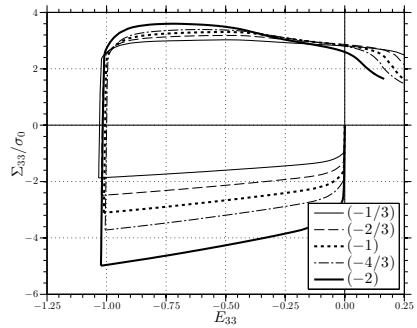

(e) *100%*

Figure 9.15: *Compression-tension of unit cell to different levels of strain with various compressive triaxialities using the same tensile triaxiality* Σ^*_{tens} *for each simulation. Plots show development of relative axial stress* Σ_{33}/σ_0 *vs. axial strain* E_{33} *for* $\omega_0 = 0.0005$.

the Riks algorithm, the compressive phase stops at somewhat different levels of strain (best seen in Fig. 9.15(b)) for the various compressive triaxialities. The cause of this is the automatic incrementation of said Riks algorithm; the compressive phase stops once a certain (user-specified) displacement is attained. This displacement is eventually exceeded by an arc length increment which may be long or short (or in between for that matter) depending on the analysis progression up to that point. In turn, this will cause a variation of the amount the termination criterion is exceeded by. Any further considerations of this effect are not made, as it is not of any vital importance[2].

Again it is seen that an increasing absolute value of compressive triaxiality leads to an increase in the axial stress level in the cell, clearly evident in Fig. 9.15. An increased stress level increases the likelyhood of microcracks forming in the material [78, 155], and should therefore decrease the strain to failure. Figs. 9.15 and 9.16 show that the strain to fracture does indeed decrease with the negative triaxiality.

Moving on to the development of the void/particle volume fraction, a slight increase is detected during the compressive phase (see Fig. 9.16) contrary to common assertions [142]. The lowest triaxiality (-2) has the lowest increase in volume, if any increase at all.

Sabih and Nemes [67] discussed perpendicular void initiation and growth under compression (see illustration in Fig. 5.28), and this is to some degree confirmed by the analyses herein. Fig. 9.17 shows the unit cell compressed to 80%, using two different compressive triaxialities, and it is clearly shown the lowest triaxiality (-2) keeps the matrix more or less completely in contact with the particle whereas the highest value $-1/3$ leaves a small gap between the particle and the matrix.

For the lower compression levels (20% and 40%), a rather clear, steep and defined change of increase in the void growth rate is detected (see Fig. 9.16(a) and (b)), commonly used to identify the onset of void coalescence and interligament necking [148]. This clear change of rate becomes somewhat blurred out for increasing compression as shown in Fig. 9.16(e), Nevertheless, the results are quite clear in indicating that lower negative stress triaxiality decreases the tensile strain to fracture after compression.

[2]This effect can be minimised by specifying a maximum allowable arc length. That would, however, increase the CPU time of the analyses significantly. Not necessarily very much for a single analysis but for the entire sequence of analyses in the script it can have a profound effect.

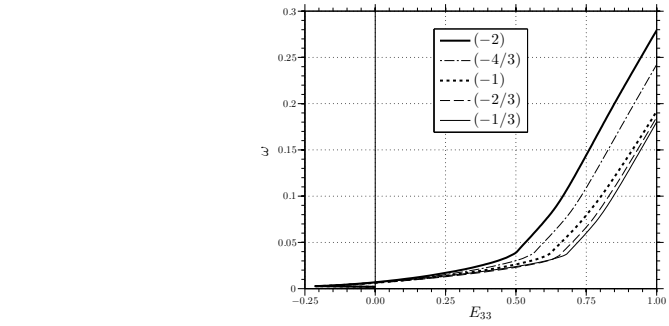

(a) *20%*

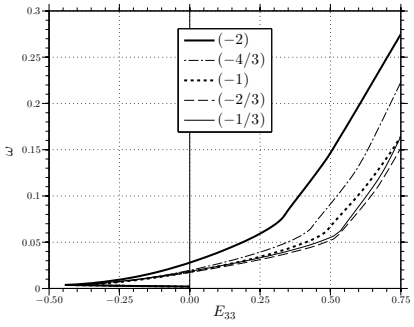

(b) *40%*

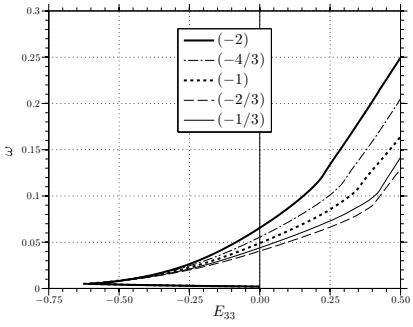

(c) *60%*

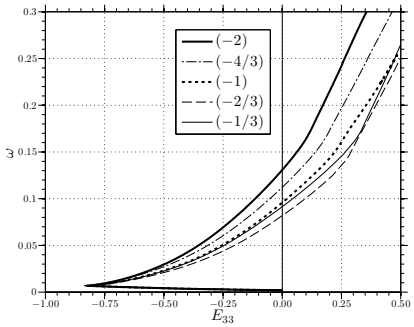

(d) *80%*

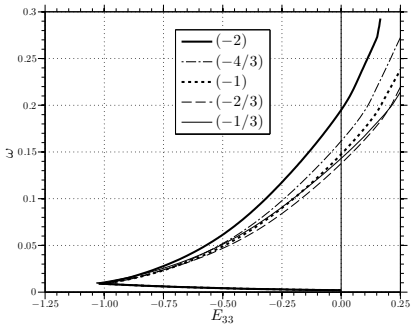

(e) *100%*

Figure 9.16: *Compression-tension of unit cell to different levels of strain with various compressive triaxialities using the same tensile triaxiality* $\Sigma^*_{\text{tens}} = 1$ *for each simulation. Plots show development of void/particle volume fraction* ω *vs. axial strain* E_{33} *for* $\omega_0 = 0.0005$.

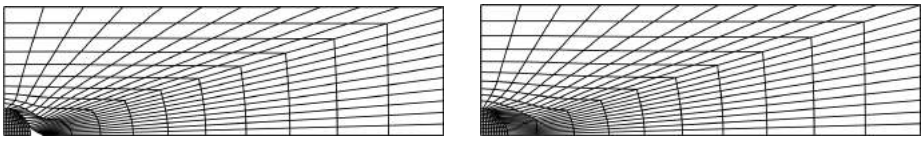

(a) $\Sigma^*_{\text{comp}} = -1/3$ (b) $\Sigma^*_{\text{comp}} = -2$

Figure 9.17: *Unit cell compressed to 80% with* $\omega_0 = 0.0005$ *and* $\mu = 0.6$*. Note the difference in deformation close to the particle.*

Also, increasing the compression seems to speed up the void growth when the load is reversed. This is also seen in the SEM images from the metallurgical investigations in Chapter 5 (compare the images in Fig. 5.17(a) and (b)) where pores tend to be more shallow for increasing compression, and in some cases even cleavage fracture is seen.

Results of cell models with compressive and tensile triaxialities of magnitude equal to unity are plotted in Fig. 9.18, in which an additional cell model with pure tension (i.e. 0% compression, shown in red) was run for comparison. All other parameters (material, friction, etc.) were left the same. In parts (c) and (d) the tensile step with different preceding compression has been plotted from the same point of origin. Here an interesting feature emerges; despite an accelerated void growth with increasing compression, the relative strain increment to coalescence appears to increase. The strain increment to maximum load, however, seems to decrease. This point on each curve is indicated by a gray dot in Fig. 9.18(c).

The normalised stress Σ_{33}/σ_0 also increases for the increasing compression, and keeping in mind that this increases the chances of cleavage fracture [78] a stress based fracture criteria could account for this effect. In Fig. 9.19 the maximum principal stress (relative to the yield stress) locally in the unit cell after load reversal has been plotted vs. the compressive triaxiality. This local stress has been picked after a tensile strain increment of $\Delta E_{33} = 0.50$ has been applied, and this has been done for all compression levels (0%, 20%, 40%, 60%, 80% and 100%). Here it is evident that increasing the compression level and increasing the absolute value of the compressive triaxiality, both clearly contribute to increasing the local maximum principal stress.

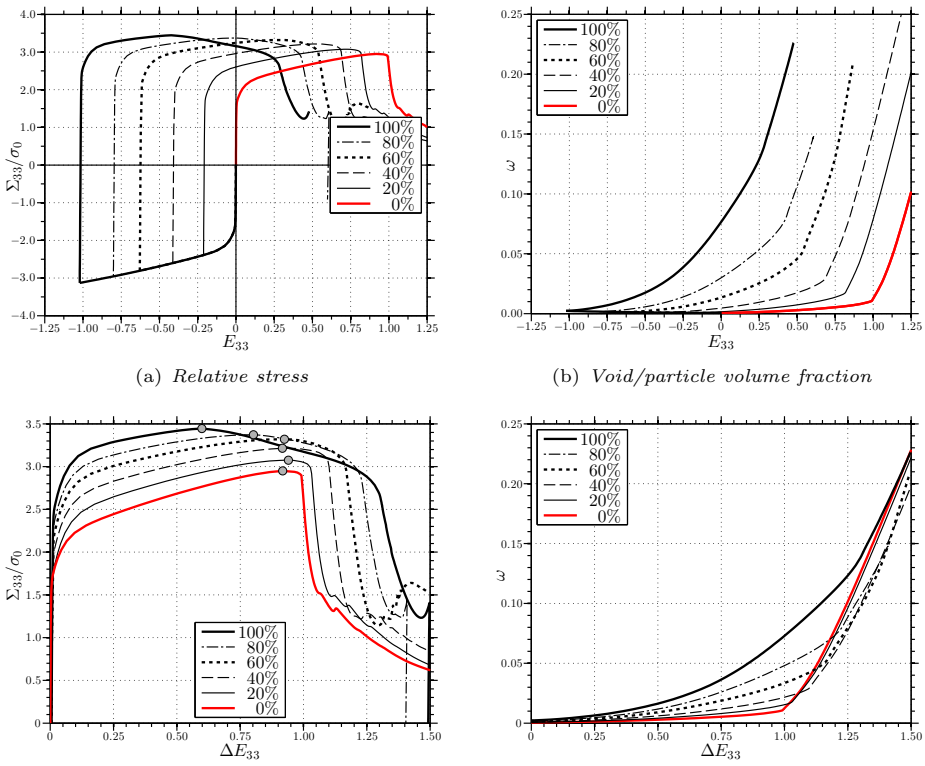

(a) *Relative stress*

(b) *Void/particle volume fraction*

(c) *Relative stress*

(d) *Void/particle volume fraction*

Figure 9.18: *Effect of increasing compression before tension, with the top row showing the entire load sequence curves taken directly from the simulations, while the bottom row shows the tensile step using the point of load reversal as the origin in each individual case.*

9.5 Discussion

The axisymmetric unit cell simulations carried out for tension only conforms with results obtained by work prior to the present [148]. In short, these are that increasing triaxiality and initial particle volume fraction, both decrease strain to fracture. Siriguet and Leblond [154] modelled a rigid particle in a non-hardening matrix with no cohesion, and showed that for $\Sigma^* < 2/3$ nucleation is incomplete due to compressive normal tractions near the mid-section. It was shown that ω

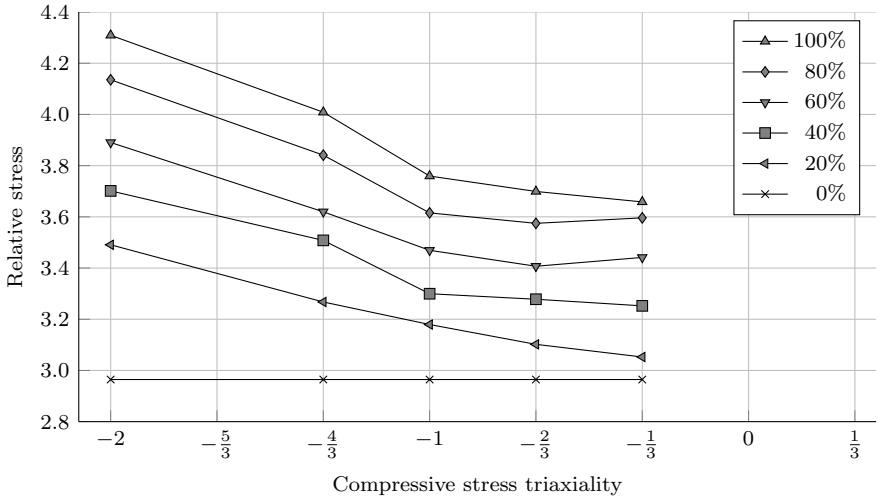

Figure 9.19: *Largest local main principal stress (relative to the yield stress) in unit cell vs. compressive triaxiality after a load sequence of compression to different levels (0%, 20%, 40%, 60%, 80% and 100%) followed by a tensile strain of* $\Delta E_{33} = 0.5$.

increases steadily but slowly.

Comparison with test data is also encouraging, as the predicted fracture strain was close to the experimental. For the results to be good, a fairly constant triaxiality in the test is required as the model is limited to exactly that – a constant triaxiality.

Basing the triaxiality applied to the unit cell on global simulations of material tests, in combination with a good estimate for the initial particle volume fraction, seems to be a worthwhile approach. Also, between the two different material models employed, little difference was observed. The main differences were in the global material simluations, where some variations in triaxiality were present due to the material model as Tables 9.1 and 9.2 will attest to.

Fleck et al. [156] showed that including the contact in the particle/matrix interaction is important, especially at negative triaxialities and this was included when the load sequence was expanded to account for compression before tension. Various coefficients of friction were tested, and seemed to exert little or no influence on the results. No cohesion between the particle and the matrix

Table 9.1: *Stress ratios ρ_c extracted from simulations of global axisymmetric material tests.*

Specimen	Mat.	Compression			Tension		
		$\rho^*_{c,\min}(\div)$	$\overline{\rho}^*_c(M)$	$\rho^*_{c,\max}(+)$	$\rho^*_{c,\min}(\div)$	$\overline{\rho}^*_c(M)$	$\rho^*_{c,\max}(+)$
Smooth	JC	-	-	-	0.0000	0.1929	0.4046
Smooth	C	-	-	-	0.0000	0.2077	0.4365
$R = 2.0$	JC	-	-	-	0.2259	0.3886	0.4348
$R = 2.0$	C	-	-	-	0.2259	0.3934	0.4345
$R = 0.8$	JC	-	-	-	0.2878	0.4715	0.4927
$R = 0.8$	C	-	-	-	0.2878	0.4778	0.5043
D1 00%	JC	-	-	-	0.2406	0.4159	0.4591
D1 00%	C	-	-	-	0.2408	0.4190	0.4572
D1 10%	JC	0.2412	0.4043	0.4356	0.3877	0.4043	0.4499
D1 10%	C	0.2412	0.3813	0.4102	0.3795	0.4124	0.4521
D1 20%	JC	0.2412	0.4017	0.4350	0.3731	0.4084	0.4554
D1 20%	C	0.2412	0.3918	0.4113	0.3655	0.4067	0.4533
D1 30%	JC	0.2413	0.3965	0.4345	0.3726	0.4052	0.4473
D1 30%	C	0.2419	0.4008	0.4199	0.3590	0.4038	0.4488
D1 40%	JC	0.2413	0.3935	0.4339	0.3526	0.4075	0.4496
D1 40%	C	0.2413	0.4035	0.4217	0.3456	0.4000	0.4538
D2 40%	JC	0.1868	0.3034	0.3438	0.2666	0.3438	0.4296
D2 40%	C	0.1868	0.3150	0.3354	0.2336	0.3363	0.4481
D2 60%	JC	0.1869	0.2926	0.3609	0.2655	0.3450	0.4321
D2 60%	C	0.1869	0.3123	0.3340	0.2118	0.3346	0.4610
D2 80%	JC	0.1866	0.2881	0.3595	0.2596	0.3339	0.3816
D2 80%	C	0.1869	0.3100	0.3322	0.2210	0.3227	0.4113
D2 90%	JC	0.1870	0.2881	0.3600	0.2548	0.3379	0.3753
D2 90%	C	0.1870	0.3098	0.3322	0.1844	0.3188	0.3975
D2 100%	JC	0.1870	0.2888	0.3596	0.2643	0.3512	0.3898
D2 100%	C	0.1870	0.3102	0.3312	0.2154	0.3363	0.4174

is included as the bonding between the two was very weak in the X65 material (see Chapter 5).

The compression-tension unit cell simulations of the material tests were also in decent agreement with the experimental values (provided a somewhat constant triaxiality). When applying a range of different compressive triaxialities before tension, the lower triaxialities caused higher stress in the cell and also a lower strain to failure after load reversal.

Increasing compression also leads to higher stress, but an increased strain increment to failure was observed when the load was reversed, contrary to the experimental data. This can, perhaps, be ameliorated by encompassing a stress based fracture criteria for brittle fracture, as this was also observed experimentally for large compression before tension (see e.g. Fig. 5.23 on page 144).

For future work, the matrix may be modelled using a Gurson type model [157]

Table 9.2: *Stress triaxialities calculated by Eq.* (9.3) *using the stress ratios in Table 9.1.*

Specimen	Mat.	Compression			Tension		
		$\sigma^*_{\min}(\div)$	$\overline{\sigma}^*(M)$	$\sigma^*_{\max}(+)$	$\sigma^*_{\min}(\div)$	$\overline{\sigma}^*(M)$	$\sigma^*_{\max}(+)$
Smooth	JC	-	-	-	0.3333	0.5723	1.0128
Smooth	C	-	-	-	0.3333	0.5955	1.1079
$R = 2.0$	JC	-	-	-	0.6252	0.9688	1.1025
$R = 2.0$	C	-	-	-	0.6252	0.9820	1.1018
$R = 0.8$	JC	-	-	-	0.7374	1.2254	1.3046
$R = 0.8$	C	-	-	-	0.7374	1.2236	1.3506
D1 00%	JC	-	-	-	0.6501	1.0453	1.1841
D1 00%	C	-	-	-	0.6505	1.0545	1.1756
D1 10%	JC	−0.6512	−1.0121	−1.1051	0.9666	1.0245	1.1513
D1 10%	C	−0.6512	−0.9496	−1.0289	0.9449	1.0352	1.1585
D1 20%	JC	−0.6513	−1.0048	−1.1033	0.9286	1.0238	1.1696
D1 20%	C	−0.6513	−0.9776	−1.0321	0.9093	1.0214	1.1624
D1 30%	JC	−0.6513	−0.9902	−1.1016	0.9273	1.0146	1.1428
D1 30%	C	−0.6524	−1.0021	−1.0573	0.8934	1.0107	1.1477
D1 40%	JC	−0.6514	−0.9821	−1.0999	0.8779	1.0212	1.1501
D1 40%	C	−0.6514	−1.0098	−1.0627	0.8615	1.0001	1.1641
D2 40%	JC	−0.5631	−0.7688	−0.9009	0.6968	0.8574	1.0864
D2 40%	C	−0.5631	−0.7932	−0.8379	0.6381	0.8401	1.1453
D2 60%	JC	−0.5631	−0.7470	−0.8980	0.6948	0.8600	1.0943
D2 60%	C	−0.5631	−0.7875	−0.8348	0.6021	0.8361	1.1888
D2 80%	JC	−0.5627	−0.7380	−0.8945	0.6839	0.8346	0.9505
D2 80%	C	−0.5632	−0.7826	−0.8308	0.6170	0.8097	1.0321
D2 90%	JC	−0.5633	−0.7379	−0.8959	0.6753	0.8438	0.9342
D2 90%	C	−0.5633	−0.7821	−0.8308	0.5594	0.8014	0.9931
D2 100%	JC	−0.5633	−0.7395	−0.8948	0.6926	0.8748	0.9721
D2 100%	C	−0.5633	−0.7831	−0.8286	0.6079	0.8401	1.0498

to account for small, secondary pores, although the compression may stagger the subsequent development of such pores. A wide variety of such models are available (see e.g. Ref. [148]). Further, unit cell simulations may also be extended to 3D, in stacked or staggered arrays for periodicity [158].

In any case, decent predictions were made for the tension tests with fairly constant triaxiality, whereas predicting fracture for non-proportional loading is somewhat more difficult. Some insight has at least been gained to how such a fracture mechanism behaves.

Chapter 10

Summary, conclusions and recommandations

10.1 Summary

The study presented has been a substantial expansion on the initial work on two-step loading of pipeline strips conducted by Manes et al. [5]. A better understanding of the mechanisms at play regarding pipe impact has been achieved through material and component tests in combination with numerical simulations. All tests showed good repeatability, with well defined geometry and boundary conditions. Metallurgical investigations have also been an integral part of the study, and has contributed indispensably to further enlightenment.

Both dynamic and quasi-static tests have been carried out to evaluate the effects of the problem being dynamic. Further, tensile axial loads have been applied to pipes being deformed transversely, while simultaneously applying pressure (all quasi-statically). Simulations using different element types and different constitutive relations for the material in these component tests have been conducted with decent results. Global results are in general quite good, while estimates of local strains and in turn fracture can and should be improved upon.

10.2 Conclusions

The following conclusions may be drawn from the work presented.

Results from the material tests gave indications that:

- The material in these seamless pipes is isotropic.
- The material is homogeneous across the cross-section.
- As seen by many others, sensitivity to a triaxial state of stress is registered, with higher stress triaxiality leading to lower fracture strain, whereas the stress at fracture is of the same order.
- Increasing the strain rate leads to an increase in flow stress, while the fracture strain is unaltered.
- Compression before tension appears to reduce both the absolute and relative strain to fracture.

Experimental work on component tests showed that:

- The test setup in the pendulum accelerator produced consistent, repeatable results.
- Impact velocity, and hence initial kinetic energy, determines the level of both local and global deformation in the pipe.
- The force level during stretching after impact was highly dependent on initial deformation.
- Surface cracks or through-thickness cracks were always produced during stretching after impact, depending on initial deformation.
- Fracture can occur from impact only, and most likely initiates during springback directly after the impact.
- Quasi-static tests with equivalent boundary conditions to the impact tests show that a higher force level is registered dynamically, meaning that a higher deformation is required to absorb the same energy quasi-statically.
- No fracture was seen after the quasi-static test, even after the largest deformation. This indicates that the dynamic springback is the critical phase.

- Filling the pipes with water and leaving them open did not cause any noticeable change in impact behaviour.
- Sealing the opening with a deformable end cap resulted in a pressure build-up, a bulging membrane, and a stiffer response.

Further experimental work using the stretch-bending rig revealed that:

- Applying an axial tensile load to the pipe increases its transverse stiffness.
- Local deformations are not much affected by the axial load.
- Adding internal pressure reduced the squashing of the cross-section of the pipe.
- Pressure causes a more localised deformation profile along the pipe's longitudinal axis.
- A higher force level was required to attain the same deformation when pressure was included.

Using optical microscopes and scanning electron microscopes to perform metallurgical examinations showed that:

- Fracture surfaces in tension only are ductile, with nucleation, void growth and coalescence as the major fracture mechanism.
- There are two types of particles in the material, angular and spherical.
- The angular particles bonded well with the matrix and the spherical poorly.
- A ductile-to-brittle transition of the fracture arises from high compression before tension in the component tests.
- Cleavage fracture surface can be produced by compressing specimens to high strain levels before exposing them to tension.
- Large scale plastic deformation can precede cleavage fracture.
- Particles can crack under compression.
- Fracture seems to initiate within the pipe wall during impact and springback.

From the finite elements simulations of the component tests the main conclusion are that:

- The main physical mechanisms are adequately captured in the simulations.
- Of the material models employed, there was no marked difference in global response.
- The global response is predicted well for the impact, but the force is slightly overestimated during stretching.
- For global response calculations, shell elements seem to be sufficient.
- Local strains are difficult to predict accurately due to high gradients across the pipe wall thickness and non-proportional loading.
- Commonly employed fracture criteria do not account for the effect of compression before tension.
- A very fine mesh is required for sufficiently accurate descriptions of the local strain field as fracture initiates at scales much smaller than the size of the elements typically used in global simulations.

The fluid-structure interaction simulations provided evidence that:

- The pipes were not completely full of water in the experiments.
- The global response is well captured.
- Pressure build-up is captured in the simulations.
- Correct choice of discretisation technique and fluid-structure coupling for the task at hand is crucial.

Scaling down a few levels to unit cell simulations showed that:

- The unit cell simulations herein reproduced results already verified by others.
- There was no particularly marked difference between the two material models used, except perhaps in the area around re-yielding.
- Using a global simulation to provide boundary conditions for a unit cell gave good results in tension as long as the triaxiality was fairly constant globally.
- Increased compression leads to increased stress locally in the cell, and accelerated void growth in tension. The local stress was found to be more than four times the yield stress, which is an indication that brittle fracture may be a problem.

- Lower compressive triaxiality also leads to increased stress locally in the cell.
- Higher compression seemed to delay the onset of coalescence in tension despite accelerated void growth, contrary to experimental evidence.

10.3 Recommandations for further work

The most obvious challenge is to make further attempts at capturing the initiation of fracture after the impact phase, and the path seems to be to go down in scale. Using global simulations of the material tests to generate boundary conditions (in terms of triaxiality) for a unit cell was promising, and this approach could perhaps be employed on component tests as well, along with a stress based fracture criterion as suggested earlier. A stress based criterion could also improve the global analyses of the entire pipe, as the local stresses were found to be very high here as well.

Experimentally, additional compression-tension tests could provide some more insight. Then an intermediate cross-sectional diameter compared with the two diameters used herein should be employed, as tendencies to barrelling was observed for the most compressed specimens.

As for component tests, the programme carried out in this thesis is quite complete. Any further tests could perhaps investigate the effect of retaining a certain amount of kinetic energy while increasing the velocity and decreasing the mass. Additional experiments on closed, water-filled pipes would also be beneficial if the pressure was measured during impact. This should then be recreated numerically. Dynamic tests with pressurised pipes could also provide additional insight, and measures to improve the DIC measurements should also be taken as this can be a quite useful tool.

Bibliography

[1] N. Jones. Inelastic response of structures due to large impact and blast loadings. *Journal of Strain Analysis for Engineering Design*, 45:451–464, 2010.

[2] Petroleumstilsynet. *Damage and incidents involving load-bearing structures and pipeline systems.* Petroleum Safety Authority Norway, Cited 27.10.2014. `http://www.ptil.no/news/damage-and-incidents-involving-load-bearing-structures-and-pipeline-systems-article4306-79.html?lang=en_US`.

[3] Statoil ASA. *Small gas leak from Kvitebjørn pipeline*, Cited 27.10.2014. `http://www.statoil.com/en/NewsAndMedia/News/2008/Pages/gasleakkvitebjorn.aspx`.

[4] N. Jones and R.S. Birch. Influence of internal pressure on the impact behaviour of steel pipelines. *International Journal of Pressure Vessel Technology*, 118:464–471, 1996.

[5] A. Manes, R. Porcaro, H. Ilstad, E. Levold, M. Langseth, and T. Børvik. The behaviour of an offshore steel pipeline material subjected to stretching and bending. *Ships and Offshore Structures*, 7:371–387, 2012.

[6] S. Kyriakides and T.A. Netto. On the dynamics of propagating buckles in pipelines. *International Journal of Solids and Structures*, 37:6843–6867, 2000.

[7] R. Ramasamy and T.M.Y.S. Tuan Ya. Nonlinear finite element analysis of collapse and post-collapse behaviour in dented submarine pipelines. *Applied Ocean Research*, 46:116–123, 2014.

[8] S. Fareed and I. May. Response of mild steel pipes under high mass low velocity impacts. *Proceedings of the ASME 2014 33rd International Conference on Ocean, Offshore and Arctic Engineering*, 2014.

[9] N. Jones, S.E. Birch, R.S. Birch, L. Zhu, and M. Brown. An experimental study on the lateral impact of fully clamped mild steel pipes. *Proceedings of the Institution of Mechanical Engineers, Part E: Journal of Process Mechanical Engineering*, pages 111–127, 1992.

[10] K. Chen and W.Q. Shen. Further experimental study on the failure of fully clamped steel pipes. *International Journal of Impact Engineering*, 21:177–202, 1998.

[11] W.Q. Shen and D.W. Shu. A theoretical analysis on the failure of unpressurised and pressurised pipelines. *Proceedings of the Institution of Mechanical Engineers 216 (E)*, pages 151–165, 2002.

[12] C.S. Ng and W.Q. Shen. Effect of lateral impact loads on failure of pressurised pipelines supported by foundation. *Proceedings of the Institution of Mechanical Engineers 220 (E)*, pages 193–206, 2006.

[13] N. Jones and R.S. Birch. Low-velocity impact of pressurised pipelines. *International Journal of Impact Engineering*, 37:207–219, 2010.

[14] C.-K. Oh, Y.-J. Kim, J.-H. Baek, Y.-P. Kim, and W.-S. Kim. Ductile failure of API X65 pipes with notch-type defects using a local fracture criterion. *International Journal of Pressure Vessels and Piping*, 84:512–525, 2007.

[15] S.G. Thomas, S.R. Reid, and W. Johnson. Large deformations of thin-walled circular tubes under transverse loading – I: An experimental survey of the bending of simply supported tubes under a central load. *International Journal of Mechanical Sciences*, 18:325–333, 1976.

[16] A.R. Watson, S.R. Reid, and W. Johnson. Large deformations of thin-walled circular tubes under transverse loading—II: Experimental study of the crushing of circular tubes by centrally applied opposed wedge-shaped indenters. *International Journal of Mechanical Sciences*, 18:387–397, 1976.

[17] A.R. Watson, S.R. Reid, and W. Johnson. Large deformations of thin-walled circular tubes under transverse loading - III: Further experiments on the bending of simply supported tubes. *International Journal of Mechanical Sciences*, 18:501–509, 1976.

[18] C.G. Soares and T.H. Søreide. Plastic Analysis of Laterally Loaded Circular Tubes. *Journal of Structural Engineering*, 109:451–467, 1983.

[19] P. Mohseni. *Brittle and Ductile Fracture of X80 Arctic Steel*. PhD thesis, Norwegian University of Science and Technology, 2012.

[20] DNV. *Offshore standard DNV-OSS-301: Certification and verification of pipelines*. Det Norske Veritas, 2000.

[21] DNV. *Offshore standard DNV-OS-F101: Submarine pipeline systems*. Det Norske Veritas, 2008.

[22] DNV. *Offshore standard DNV-RP-F111: Interference between trawl gear and pipelines*. Det Norske Veritas, 2010.

[23] B. Liu, R. Villavicencio, and C.G. Soares. Experimental and numerical plastic response and failure of pre-notched transversely impacted beams. *International Journal of Mechanical Sciences*, 77:314–332, 2013.

[24] V. Longva, S. Sævik, E. Levold, and H. Ilstad. Dynamic simulation of subsea pipeline and trawl board pull-over interaction. *Marine Structures*, 34:156–184, 2013.

[25] A.J. Neilson, W.D. Howe, and G.P. Garton. Impact resistance of mild steel pipes: An experimental study. *Safety Experiments and Analysis Group, Safety and Engineering Science Division AEE Winfrith, AEEW – R 2125*, 1987.

[26] Q.H. Shah. Experimental and numerical study on the orthogonal and oblique impact on water filled pipes. *International Journal of Impact Engineering*, 38:330–338, 2011.

[27] C.-K. Oh, Y.-J. Kim, J.-H. Baek, and W.-S. Kim. Development of stress-modified fracture strain for ductile failure of API X65 steel. *International Journal of Fracture*, 143:119–133, 2007.

[28] Tenaris. *Production processes*, Cited 23.01.2013. `http://www.tenaris.com/AboutUs/ProductionProcesses.aspx`.

[29] M. Kristoffersen, T. Børvik, I. Westermann, M. Langseth, and O.S. Hopperstad. Impact against X65 steel pipes — An experimental investigation. *International Journal of Solids and Structures*, 50:3430–3445, 2013.

[30] M. Kristoffersen, F. Casadei, T. Børvik, M. Langseth, and O.S. Hopperstad. Impact against empty and water-filled X65 steel pipes – Experiments and simulations. *International Journal of Impact Engineering*, 71:73–88, 2014.

[31] M. Kristoffersen, T. Børvik, M. Langseth, H. Ilstad, E. Levold, and O.S. Hopperstad. Damage and failure in an X65 steel pipeline caused by trawl gear impact. *Proceedings of the ASME 2013 32nd International Conference on Ocean, Offshore and Arctic Engineering*, 2013.

[32] M. Kristoffersen, F. Casadei, T. Børvik, M. Langseth, G. Solomos, and O.S. Hopperstad. Numerical simulations of submerged and pressurised X65 steel pipes. *XII International Conference on Computational Plasticity, Barcelona, Spain*, 2013.

[33] K. Slåttedalen and A. Ørmen. Impact against offshore pipelines – Experiments and numerical simulations. Master's thesis, Norwegian University of Science and Technology, 2010.

[34] J.G. Fornes and S. Gabrielsen. Impact against offshore pipelines. Master's thesis, Norwegian University of Science and Technology, 2011.

[35] V. Aune and M.S. Hovdelien. Impact against offshore pipelines. Master's thesis, Norwegian University of Science and Technology, 2012.

[36] T.I. Asheim and I. Mogstad. Impact against offshore pipelines. Master's thesis, Norwegian University of Science and Technology, 2013.

[37] E. Jakobsen. Deformation of Pressurized Pipelines. Master's thesis, Norwegian University of Science and Technology, 2013.

[38] E. Digerud and K. Lofthaug. Bending of X65 Offshore Steel Pipes. Master's thesis, Norwegian University of Science and Technology, 2014.

[39] DNV. *Offshore standard DNV-RP-F107: Risk assessment of pipeline protection.* Det Norske Veritas, 2010.

[40] *N-004: Design of steel structures.* NORSOK, 2013.

[41] J. Amdahl, R. Watan, Z. Hu, and T. Holmås. Broad side ship collision with jacket legs: Examination of Norsok N-004 analysis procedure. *Proceedings of the ASME 2012 31st International Conference on Ocean, Offshore and Arctic Engineering*, 2012.

[42] *NS-EN 1991-1-7: Actions on structures - Accidental actions.* Standard Norge, 2008.

[43] *NS-EN 1993-4-3: Design of steel structures - Pipelines.* Standard Norge, 2009.

[44] T.H. Søreide. *Ultimate load analysis of marine structures.* Tapir Forlag, second edition, 1981.

[45] C.P. Ellinas and A.C. Walker. Damage on offshore tubular bracing members. *IABSE colloquium on ship collision with ridges and offshore structures*, pages 253–261, 1983.

[46] J.G. de Oliveira, T. Wierzbicki, and W. Abramowicz. Plastic behaviour of tubular members under lateral concentrated loading. Technical report, 1982.

[47] T.H. Søreide and J. Amdahl. Deformation characteristics of tubular members with reference to impact loads from collision or dropped objects. *Norwegian Maritime research paper*, 2:3–12, 1982.

[48] Pipeline engineering web apps. *Pipe Dent Assessment Calculators*, Cited 28.07.2014. `http://http://pipeng.com/index.php/ts/itdmotdiam014a`.

[49] N. Jones and W.Q. Shen. A theoretical study of the laterial impact of fully clamped pipelines. *Proceedings of the Institution of Mechanical Engineers, Part E: Journal of Process Mechanical Engineering*, 1992.

[50] A. Ghiotti, S. Fanini, S. Bruschi, and P.F. Bariani. Modelling of the Mannesmann effect. *CIRP Annals - Manufacturing Technology*, 58:255–258, 2009.

[51] J.-H. Baek, Y.-P. Kim, W.-S. Kim, J.-M. Koo, and C.-S. Seok. Load bearing capacity of API X65 pipe with dent defect under internal pressure and in-plane bending. *Materials Science and Engineering A*, 540:70–82, 2012.

[52] A. Fragiel, R. Schouwenaarf, R. Guardián, and R. Pérez. Microstructural characteristics of different commercially available API 5L X65 steels. *Journal of New Materials for Electrochemical Systems*, 8:115–119, 2005.

[53] M. Fourmeau, T. Børvik, A. Benallal, and O.S. Hopperstad. Anisotropic failure modes of high-strength aluminium alloy under various stress states. *International Journal of Plasticity*, 48:34–53, 2013.

[54] T.H. Hyde, R. Luo, and A.A. Becker. Elastic-plastic analysis of offset indentations on unpressurised pipes. *International Journal of Solids and Structures*, 44:399–418, 2007.

[55] R. Hill. *The Mathematical Theory of Plasticity*. Oxford University Press, 1950. ISBN 0-19-856162-8.

[56] Y. Chen, A.H. Clausen, O.S. Hopperstad, and M. Langseth. Application of a split-Hopkinson tension bar in a mutual assessment of experimental tests and numerical predictions. *International Journal of Impact Engineering*, 38:824–836, 2011.

[57] H. Kolsky. *Stress waves in solids*. Dover Publications, 1963.

[58] C. Albertini and M. Montagnani. Dynamic material properties of several steels for fast breeder reactor safety analysis. Technical report, Ispra, Italy: Applied Mechanics Division, Joint Research Centre, 1977.

[59] B.S. Opheim. *Bending of thin-walled aluminium extrusions*. PhD thesis, Norwegian University of Science and Technology, 1996.

[60] Y. Bao and R. Treitler. Ductile crack formation on notched Al2024-T351 bars under compression-tension loading. *Materials Science and Engineering*, 384:385–394, 2004.

[61] P.O. Bouchard, L. Bourgeon, H. Lachapele, E. Maire, C. Verdu, R. Forestier, and R.E. Loge. On the influence of particle distribution and reverse loading on damage mechanisms of ductile steels. *Materials Science and Engineering A*, 496:223–233, 2008.

[62] G. Gruben, E. Fagerholt, O.S. Hopperstad, and T. Børvik. Fracture characteristics of a cold-rolled dual-phase steel. *European Journal of Mechanics A/Solids*, 30:204–218, 2011.

[63] T. Børvik, O.S. Hopperstad, T. Berstad, and M. Langseth. A computational model of viscoplasticity and ductile damage for impact and penetration. *European Journal of Mechanics A/Solids*, 20:685–712, 2001.

[64] J.R. Rice and D.M. Tracey. On the ductile enlargement of voids in triaxial stress fields. *Journal of Mechanics and Physics of Solids*, 17:201–217, 1969.

[65] V. Tvergaard and A. Needleman. Analysis of the cup-cone fracture in a round tensile bar. *Acta Metallurgica*, 32:157–169, 1984.

[66] J.-H. Baek, Y.-P. Kim, W.-S. Kim, and C.-S. Seok. Effects of pre-strain on the mechanical properties of API 5L X65 pipe. *Materials Science and Engineering A*, 527:1473–1479, 2010.

[67] A. Sabih and J.A. Nemes. Internal ductile failure mechanisms in steel cold heading process. *Journal of Materials Processing Technology*, 209: 4292–4311, 2009.

[68] A.G. Hanssen, T. Auestad, T. Tryland, and M. Langseth. The kicking machine: A device for impact testing of structural components. *International Journal of Crashworthiness*, 8:385–392, 2003.

[69] A.H. Clausen. *Stretch Bending of Aluminium Extrusions*. PhD thesis, Norwegian University of Science and Technology, 1999.

[70] A. Palmer, A. Neilson, and S. Sivadasan. Pipe perforation by medium-velocity impact. *International Journal of Impact Engineering*, 32:1145–1157, 2006.

[71] A.G. Hanssen, T. Auestad, M. Langseth, and T. Tryland. Development of a 3-component load cell for structural impact testing. *International Journal of Mechanics and Materials in Design*, 2:15–22, 2005.

[72] E. Fagerholt. *Field measurements in Mechanical Testing Using Close-Range Photogrammetry and Digital Image Analysis*. PhD thesis, Norwegian University of Science and Technology, 2012.

[73] K.G. Rakvåg, N.J. Underwood, G.K. Schleyer, T. Børvik, and O.S. Hopperstad. Transient pressure loading of clamped metallic plates with preformed holes. *International Journal of Impact Engineering*, 53:44–55, 2013.

[74] Z. Marciniak, J. Duncan, and S. Hu. *Mechanics of sheet metal forming*. Oxford: Butterworth-Heinemann, 2002.

[75] N. Jones. *Structural Impact*. Cambridge University Press, 1989. ISBN 0-521-30180-7.

[76] M. Zeinoddini, J.E. Harding, and G.A.R. Parke. Effect of impact damage on the capacity of tubular steel members of offshore structures. *Marine Structures*, 11:141–157, 1998.

[77] I.B. Iflefel, D.G. Moffat, and J. Mistry. The interaction of pressure and bending on a dented pipe. *International Journal of Pressure Vessels and Piping*, 82:761–769, 2005.

[78] T.L. Anderson. *Fracture mechanics - Fundamentals and applications*. Taylor and Francis Group, third edition, 2005. ISBN 0-8493-1656-1.

[79] P.F. Thomason. As assessment of plastic-stability models of ductile fracture. *Acta Metallurgica*, 30:279–284, 1982.

[80] V. Tvergaard and J.W. Hutchinson. Two mechanisms of ductile fracture: void by void growth versus multiple void interaction. *International Journal of Solids and Structures*, 39:3581–3597, 2002.

[81] R. Tian, S. Chan, S. Tang, A.M. Kopacz, J.-S. Wang, H.-J. Jou, L. Siad, L.-E. Lindgren, G.B. Olson, and W.K. Liu. A multiresolution continuum simulation of the ductile fracture process. *Journal of Mechanics and Physics of Solids*, 58:1681–1700, 2010.

[82] R. Ghajar, G. Mirone, and A. Keshavarz. Ductile failure of X100 pipeline steel – Experiments and fractography. *Materials and Design*, 43:513–525, 2013.

[83] A.H. Cottrell. *Fracture*. Wiley, New York, 1959.

[84] E. Smith. Cleavage fracture in mild steel. *International Journal of Fracture Mechanics*, 4:131–145, 1968.

[85] S.H. Goods and L.M. Brown. The nucleation of cavities by plastic deformation. *Acta Metallurgica*, 27:1–15, 1979.

[86] C.J. McMahon and M. Cohen. Initiation of fracture in polycrystalline iron. *Acta Metallurgica*, 13:591–604, 1965.

[87] X. Gao, C.F. Shih, V. Tvergaard, and A. Needleman. Constraint effects on the ductile-brittle transition in small scale yielding. *Journal of Mechanics and Physics of Solids*, 44:1255–1282, 1996.

[88] F.A. McClintock. Local criteria for ductile fracture. *International Journal of Fracture Mechanics*, 4:101–130, 1968.

[89] R.G. Hoagland, A.R. Rosenfield, and G.T. Hahn. Mechanisms of fast fracture and arrest in steels. *Metallurgical Transactions*, 3:123–136, 1972.

[90] T. Antretter and F.D. Fischer. Particle cleavage and ductile crack growth in a two-phase composite on a microscale. *Computational Materials Science*, 13:1–7, 1998.

[91] *Abaqus analysis user's manual version 6.11.* SIMULIA, 2013.

[92] F. Irgens. *Continuum mechanics.* Springer Verlag, 2008. ISBN 978-3-540-74297-5.

[93] *Theory manual: SIMLab Metal Model.* Stuctural Impact Laboratory (SIMLab), Norwegian University of Science and Technology, Cited 30.03.2014.

[94] G.R. Johnson and W.H. Cook. A constitutive model and data for metals subjected to large strains, high strain rates and high temperatures. *Proceedings of the 7th International Symposium on Ballistics*, pages 541–547, 1983.

[95] G.R. Johnson and W.H. Cook. Fracture characteristics of three metals subjected to various strains, strain rates, temperatures and pressures. *Engineering Fracture Mechanics*, 21:31–48, 1985.

[96] M.G. Cockcroft and D.J. Latham. Ductility and the workability of metals. *Journal of the Institute of Metals*, 96:33–39, 1968.

[97] G. Gruben, O.S. Hopperstad, and T. Børvik. Evaluation of uncoupled ductile fracture criteria for the dual-phase steel Docol 600DL. *International Journal of Mechanical Sciences*, 62:133–146, 2012.

[98] G. Le Roy, J.D. Embury, and M.F. Ashby. A model of ductile fracture based on the nucleation and growth of voids. *Acta Metallurgica*, 29:1509–1522, 1981.

[99] H. Anton and C. Rorres. *Elementary linear algebra*. John Wiley & Sons Inc., New York, ninth edition, 2005. ISBN 0-471-44902-4.

[100] N. Stander, W. Roux, T. Goel, T. Eggleston, and K. Craig. *LS-OPT 4.2 User's Manual*. Livermore Software Technology Corporation, 2012.

[101] S. Dey. *High-strength Steel Plates Subjected to Projectile Impact*. PhD thesis, Norwegian University of Science and Technology, 2004.

[102] R.D. Cook, D.S. Malkus, M.E. Plesha, and R.J. Witt. Concepts and applications of finite element analysis. 2002.

[103] C.-S. Oh, N.-H. Kim, Y.-J. Kim, J.-H. Baek, and Y.-P. Kim. A finite element ductile failure simulation method using stress-modified fracture strain model. *Engineering Fracture Mechanics*, 78:124–137, 2011.

[104] C.-K. Oh, Y.-J. Kim, J.-H. Baek, Y.-P. Kim, and W.-S. Kim. A phenomenological model of ductile fracture of API X65 steel. *International Journal of Mechanical Sciences*, 49:1399–1412, 2007.

[105] *Salome Documentation*. Open CASCADE, Cited 27.03.2012. `http://www.salome-platform.org/user-section/online-documentation`.

[106] R.O. Ritchie, J.F. Knott, and J.R. Rice. On the relationship between critical tensile stress and fracture toughness in mild steel. *Journal of Mechanics and Physics of Solids*, 21:395–410, 1973.

[107] F. Casadei, M. Larcher, and N. Leconte. Strong and weak forms of a fully non-conforming FSI algorithm in fast transient dynamics for blast loading of structures. *III ECCOMAS Thematic Conference on Computational Methods in Structural Dynamics and Earthquake Engineering, Corfu, Greece*, May 2011.

[108] F. Casadei. *Numerical simulation of fast transient dynamic phenomena in fluid-structure systems*, May 2011. Lecture notes from course held in Barcelona.

[109] T. Belytschko, W.K. Liu, and B. Moran. *Nonlinear Finite Elements for Continua and Structures*. John Wiley & Sons Ltd., 2000. ISBN 0-471-98774-3.

[110] J. Donea, A. Huerta, J.-Ph. Ponthot, and A. Rodriguez-Ferran. Arbitrary Lagrangian-Eulerian methods. *Encyclopedia of Computational Mechanics*, 2004.

[111] *Europlexus user's manual*. Joint Research Centre, Cited 30.08.2013. `http://europlexus.jrc.ec.europa.eu/public/manual_pdf/manual.pdf`.

[112] J. Donea, S. Giuliani, and J.P. Halleux. An arbitrary Lagrangian-Eulerian finite element method for transient dynamic fluid-structure interactions. *Computer Methods in Applied Mechanics and Engineering*, 33:689–723, 1982.

[113] F. Casadei and N. Leconte. Coupling finite elements and finite volumes by Lagrange multipliers for explicit dynamic fluid-structure interaction. *International Journal for Numerical Methods in Engineering*, 86:1–17, 2011.

[114] A.J. Smits. *A Physical Introduction to Fluid Mechanics*. John Wiley & Sons Ltd., 2000. ISBN 0-471-25349-9.

[115] F. Casadei. Implementation of Compressible Fluid Models in PLEXIS-3C. Technical report, Ispra, Italy: Safety Technology Institute, Joint Research Centre, 1998.

[116] F. Casadei and J-P. Halleux. An algorithm for permanent fluid-structure interaction in explicit transient dynamics. *Computer Methods in Applied Mechanics and Engineering*, 128:231–289, 1995.

[117] F. Casadei, J.P. Halleux, A. Sala, and F. Chille. Transient fluid-structure interaction algorithms for large industrial applications. *Computer Methods in Applied Mechanics and Engineering*, 190:3081–3110, 2001.

[118] F. Casadei and S. Potapov. Permanent fluid-structure interaction with non-conforming interfaces in fast transient dynamics. *Computer Methods in Applied Mechanics and Engineering*, 193:4157–4194, 2004.

[119] A. Soria and F. Casadei. Arbitrary Lagrangian-Eulerian multi-component compressible flow with fluid-structure interaction. *International Journal for Numerical Methods in Fluids*, 25:1263–1284, 1997.

[120] A. Sala, F. Casadei, and A. Soria. A 3D finite volume numerical model of compressible multicomponent flow for fluid-structure interaction applications. *4th Congreso de Méto-dos Numéricos en Ingenieria, Sevilla, Spain*, June 1999.

[121] S. Giuliani. An algorithm for continuous rezoning of the hydrodynamic grid in Arbitrary Lagrangian Eulerian computer codes. *Nuclear Engineering and Design*, 72:205–212, 1982.

[122] F. Casadei. Fast transient fluid-structure interaction with failure and fragmentation. *8-th World Congress on Computational Mechanics (WCCM8), Venice, Italy*, June 30–July 5 2008.

[123] R.A. Gingold and J.J. Monaghan. Smoothed particle hydrodynamics: theory and application to non-spherical stars. *Monthly Notices of the Royal Astronomical Society*, 181:375–389, 1977.

[124] L.B. Lucy. A numerical approach to the testing of the fission hypothesis. *The Astronomical Journal*, 82:1013–1024, 1977.

[125] J.J. Monaghan. An introduction to SPH. *Computer Physics Communications*, 48:89–96, 1988.

[126] K. Hughes, R. Vignjevic, J. Campbell, T. De Vuyst, N. Djordjevic, and L. Papagiannis. From aerospace to offshore: Bridging the numerical simulation gaps – Simulation advancements for fluid structure interaction problems. *International Journal of Impact Engineering*, 61:48–63, 2013.

[127] J.J. Monaghan. Why particle methods work. *SIAM Journal of Scientific and Statistical Computing*, 3:422–433, 1982.

[128] J.J. Monaghan. Smoothed particle hydrodynamics. *Reports on Progress in Physics*, 68:1703–1759, 2005.

[129] A.S. Tijsseling. Fluid-structure interaction in liquid-filled pipe systems: A review. *Journal of Fluids and Structures*, 10:109–146, 1996.

[130] R. Mohammad, A. Kotousov, and J. Codrington. Analytical modelling of a pipe with flowing medium subjected to an impulse load. *International Journal of Impact Engineering*, 38:115–122, 2011.

[131] B. Moras. Constitutive Equations of Strain Rate Sensitive Metals for the Automotive Industry. Technical report, Structural Mechanics Unit, Joint Research Centre, Ispra, Italy, 1999.

[132] T. Belytschko and M.O. Neal. Contact-impact with the pinball algorithm with penalty and Lagrangian methods. *International Journal for Numerical Methods in Engineering*, 31:547–572, 1991.

[133] V. Faucher and S. Kokh. Extended Vofire algorithm for fast transient fluid-structure dynamics with liquid-gas flows and interfaces. *Journal of Fluids and Structures*, 39:102–125, 2013.

[134] G. Moe. Forces on slender structures, 2007. Compendium from TBA4265 at the Norwegian University of Science and Technology.

[135] M. Zheng, C. Hu, Z.J. Luo, and X. Zheng. Further study of thenew damage model by negative stress triaxiality. *International Journal of Fracture*, 63: R15–R19, 1993.

[136] Y. Bao and T. Wierzbicki. On fracture locus in the equivalent strain and stress triaxiality space. *International Journal of Mechanical Sciences*, 46: 81–98, 2004.

[137] L. Xue. Damage accumulation and fracture initiation in uncracked ductile solids subject to triaxial loading. *International Journal of Solids and Structures*, 44:5163–5181, 2007.

[138] K. Nahson and J.W. Hutchinson. Modification of the Gurson Model for shear failure. *European Journal of Mechanics A/Solids*, 27:1–17, 2008.

[139] K.L. Nielsen and V. Tvergaard. Effect of a shear modified Gurson model on damage development in a FSW tensile specimen. *International Journal of Solids and Structures*, 46:587–601, 2009.

[140] V. Tvergaard. Shear deformation of voids with contact modelled by internal pressure. *International Journal of Mechanical Sciences*, 50:1459–1465, 2008.

[141] V. Tvergaard. Behaviour of voids in a shear field. *International Journal of Fracture*, 158:41–49.

[142] S. Kweon. Damage at negative triaxiality. *European Journal of Mechanics A/Solids*, 31:203–212, 2012.

[143] A. Needleman. A numerical study of necking in circular cylindrical bars. *Journal of the Mechanics and Physics of Solids*, 20:111–127, 1972.

[144] V. Tvergaard. Influence of voids on shear band instabilities under plane strain conditions. *International Journal of Fracture*, 17:389–407, 1981.

[145] V. Tvergaard. On localization in ductile materials containing spherical voids. *International Journal of Fracture*, 18:237–252, 1982.

[146] J. Koplik and A. Needleman. Void growth and coalescence in porous plastic solids. *International Journal of Solids and Structures*, 24:835–853, 1988.

[147] A. Needleman. A continuum model for void nucleation by inclusion debonding. *Journal of Applied Mechanics*, 54:525–531, 1987.

[148] A.A. Benzerga and J.-B. Leblond. Ductile fracture by Void Growth to Coalescence. *Advances in Applied Mechanics*, 44:174–304, 2010.

[149] V. Tvergaard. Material failure by void growth to coalescence. *Advances in Applied Mechanics*, 27:83–151, 1990.

[150] D. Steglich and W. Brocks. Micromechanical modelling of the behaviour of ductile materials including particles. *Computational Materials Science*, 9:7–17, 1997.

[151] E. Riks. An incremental approach to the solution of snapping and buckling problems. *International Journal of Solids and Structures*, 150:529–551, 1979.

[152] *Python Documentation*. Python Software Foundation, Cited 27.03.2012. `http://www.python.org/doc/`.

[153] A.S. Argon, J. Im, and R. Safoglu. Cavity formations from inclusions in ductile fracture. *Metallurgical Transactions*, 6A:825–837, 1975.

[154] K. Siriguet and J.-B. Leblond. Effect of void locking by inclusion upon the plastic behavior of porous ductile solids – I: theoretical modeling and numerical study of void growth. *International Journal of Plasticity*, 20: 225–254, 2004.

[155] G.E. Dieter. *Mechanical Metallurgy*. McGraw Hill Higher Education, 1989. ISBN 0-07-100406-8.

[156] N.A. Fleck, J.W. Hutchinson, and V. Tvergaard. Softening by void nucleation and growth in tension and shear. *Journal of the Mechanics and Physics of Solids*, 37:515–540, 1989.

[157] A.L. Gurson. Continuum theory of ductile rupture by void nucleation and growth: Part 1 – Yield criteria and flow rules for porous ductile media. *Journal of Engineering Material and Technology*, 99:2–15, 1977.

[158] A.S. Ognedal. *Large-Deformation Behaviour of Thermoplastics at Various Stress States*. PhD thesis, Norwegian University of Science and Technology, 2012.

Appendices

Appendix A

Derivation of analytical pipe dent approach

This appendix contains the derivation of the analytical method for pipe denting outlined by Søreide [44]. Its intention is to estimate load-displacement curves for tubular members of a platform, intended to absorb the kinetic energy of a ship collision.

No fenders and no coating of the tubes are assumed. The tubes are further assumed to have uniform thickness t and mean diameter D (mean radius R), and a perfectly plastic material with yield stress σ_0. Also, no global bending or axial stretching is accounted for, only denting. The plastic moment capacity per unit length m_p of a rectangular cross-section of height t is

$$m_p = \frac{1}{4}\sigma_0 t^2 \tag{A.1}$$

Fig. A.1 shows a tube in which a dent has formed. The energy is then absorbed by the plastic hinges that form with the deformation. The total plastic work W_p is then equal to the sum of the work W_r along the lines forming the central rectangle of the dent in Fig. A.1, and the work W_t along the lines forming the triangles. To estimate the total work, the rotation of the hinges has to be

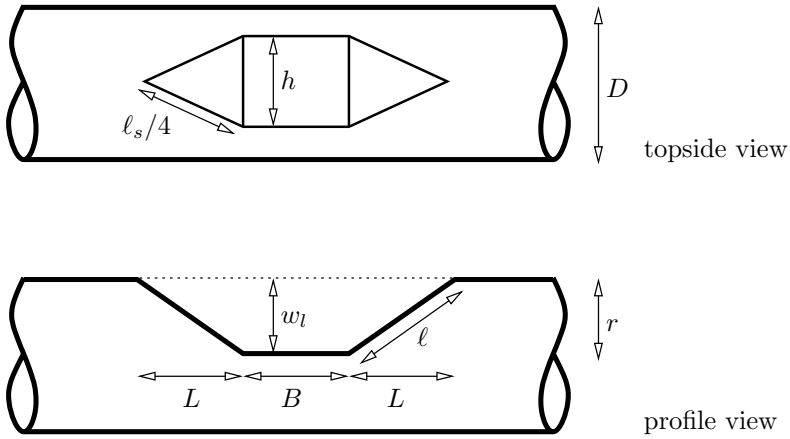

Figure A.1: *Overview of dent from top and in profile, with some measurements.*

found. This is done through some geometric considerartions during the course of deformation.

Rotation around the lines of length B in Fig. A.1 is needed for W_r. From Fig. A.2, which shows a cross-section of the bottom of the dent, it is seen that

$$\sin\alpha = \frac{r - w_l}{r} = 1 - \frac{w_l}{r} \tag{A.2}$$

The angle of rotation γ_r is then found through

$$\gamma_r = \frac{\pi}{2} - \alpha = \frac{\pi}{2} - \arcsin\left(1 - \frac{w_l}{r}\right) \tag{A.3}$$

Finally, the plastic work W_r is determined by

$$\begin{aligned} W_r &= 2m_p B\gamma_r \\ &= \frac{1}{2}\sigma_0 B t^2 \cdot \left(\frac{\pi}{2} - \arcsin\left(1 - \frac{w_l}{r}\right)\right) \end{aligned} \tag{A.4}$$

in which w_l is the only unknown.

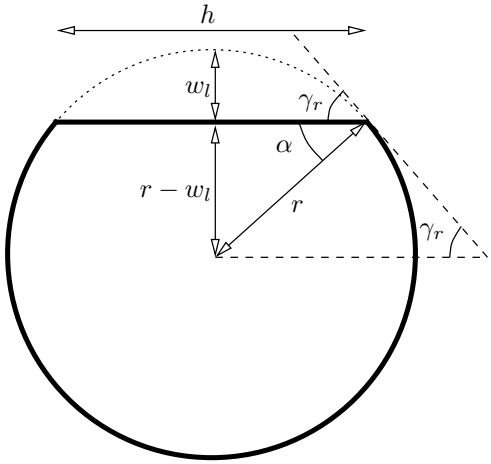

Figure A.2: *Cross-section of middle part of dent, with some measurements.*

Next, an expression for W_t in terms of γ_t is needed. This is somewhat more complicated due to the inclination, but still quite straight forward. A cross-section perpendicular to the inclined part of the dent in two directions (see dashed lines in left part of Fig. A.3) has an elliptic base shape. The desired angle γ_t is equal to $\theta_1 + \theta_2$, for each of which an explicit solution is sought. An ellipse is parametrised in the xy-plane by $t_e \in [0, 2\pi]$ as

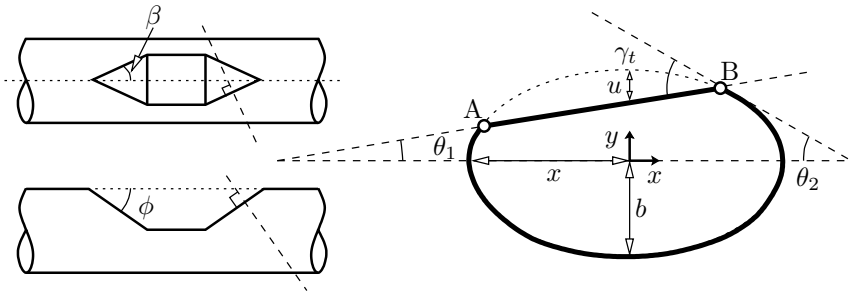

Figure A.3: *Cross-section (right) of slanted part of dent along the dashed lines on the overview sketch (left), with some measurements.*

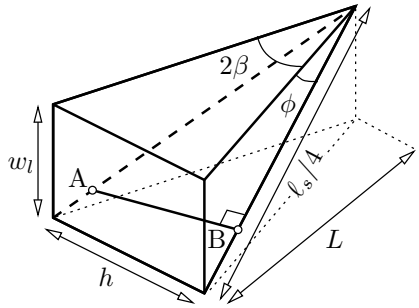

Figure A.4: *Some geometric relations in the triangular part of the dent.*

$$x = a\cos t_e \ , \qquad y = b\sin t_e \tag{A.5}$$

By using the angles β and ϕ from Fig. A.3, a and b can be expressed in terms of the mean radius r,

$$a = \frac{r}{\cos\beta} \ , \qquad b = \frac{r}{\cos\phi} \tag{A.6}$$

Considering the geometric relations in Fig. A.4, following expressions for β and ϕ are obtained

$$\cos\beta = \frac{L}{\sqrt{\left(\frac{\ell_s}{4}\right)^2 - w_l^2}} \ , \qquad \cos\phi = \frac{\sqrt{\left(\frac{\ell_s}{4}\right)^2 - w_l^2}}{\ell_s/4} \tag{A.7}$$

The length of the edge of the plastic hinge $\ell_s/4$ can be found through the Pythagorean relation

$$\left(\frac{\ell_s}{4}\right)^2 - w_l^2 = L^2 + \left(\frac{h}{2}\right)^2 \tag{A.8}$$

Further, h can be expressed by (see Fig. A.2)

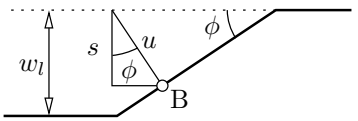

Figure A.5: *Profile of dent showing some measurements needed in the calculation.*

$$(r - w_l)^2 + \left(\frac{h}{2}\right)^2 = r^2$$

$$h = 2w_l\sqrt{\frac{2r}{w_l} - 1} \tag{A.9}$$

Inserting Eq. (A.9) into Eq. (A.7) yields

$$\cos\beta = \frac{1}{\sqrt{1 + \left(\frac{w_l}{L}\right)^2\left(\frac{2r}{w_l} - 1\right)}}\,, \qquad \cos\phi = \sqrt{\frac{1 + \left(\frac{w_l}{L}\right)^2\left(\frac{2r}{w_l} - 1\right)}{1 + \frac{2rw_l}{L^2}}} \tag{A.10}$$

Using Eq. (A.10) in Eq. (A.6), and inserting the resulting expressions into the parametrisation in Eq. (A.5) gives explicit expressions of x and y on the ellipse. The gradient of the line tangential to the ellipse is then obtained by

$$\frac{\mathrm{d}y}{\mathrm{d}x} = \frac{\mathrm{d}y}{\mathrm{d}t_e}\frac{\mathrm{d}t_e}{\mathrm{d}x} = \frac{-\cos\beta}{\cos\phi \cdot \tan t_e} \tag{A.11}$$

Fig. A.5 shows a profile skectch of the dent's inclination, showing point B from Fig. A.3. The variable t_e can now be eliminated from Eq. (A.11),

$$y = b - u = b - \frac{s}{\cos\phi} = b\sin t_e$$

$$\sin t_e = 1 - \frac{s}{b\cos\phi} = 1 - \frac{s}{r}$$

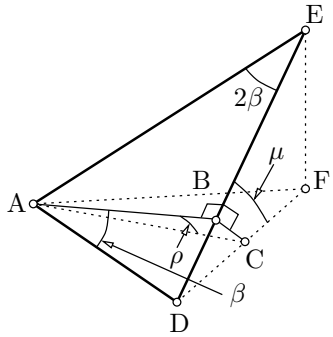

Figure A.6: *Slanted triangular part of dent, including some key points.*

$$\tan t_e = \frac{\sin t_e}{\cos t_e} = \frac{\sin t_e}{\sqrt{1-\sin^2 t_e}}$$

$$= \frac{1-\frac{s}{r}}{\sqrt{1-\left(1-\frac{s}{r}\right)^2}} \tag{A.12}$$

Eq. (A.12) is then inserted into Eq. (A.11) which comes out as

$$\frac{\mathrm{d}y}{\mathrm{d}x} = \frac{-\sqrt{\left(1+\frac{2rw_l}{L^2}\right)\left(\frac{s}{r}\left(2-\frac{s}{r}\right)\right)}}{\left(1+\frac{2rw_l}{L^2}-\left(\frac{w_l}{L}\right)^2\right)\left(1-\frac{s}{r}\right)} \tag{A.13}$$

The angle θ_2 can now be aquired by taking $\arctan\left(-\mathrm{d}y/\mathrm{d}x\right)$

$$\theta_2 = \arctan\left(\frac{\sqrt{\left(1+\frac{2rw_l}{L^2}\right)\left(\frac{s}{r}\left(2-\frac{s}{r}\right)\right)}}{\left(1+\frac{2rw_l}{L^2}-\left(\frac{w_l}{L}\right)^2\right)\left(1-\frac{s}{r}\right)}\right) \tag{A.14}$$

Moving on to θ_1, it observed that the gradient of line AB is needed. By examining Fig. A.6, the following relation is established,

$$\tan\rho = \frac{\ell_{\mathrm{BC}}}{\ell_{\mathrm{AC}}} = \frac{\ell_{\mathrm{BC}}}{\sqrt{\ell_{\mathrm{AB}} - \ell_{\mathrm{BC}}}} = \frac{1}{\sqrt{\left(\frac{\ell_{\mathrm{AB}}}{\ell_{\mathrm{BC}}}\right)^2 - 1}} \tag{A.15}$$

in which ℓ_{AB} means the distance from point A to point B, ℓ_{BC} the distance from B to C and so on[1]. Still using Fig. A.6, an expression for $\ell_{\mathrm{AB}}/\ell_{\mathrm{BC}}$ is sought. The angles μ and β in the figure can be expressed as

$$\tan\mu = \frac{\ell_{\mathrm{BC}}}{\ell_{\mathrm{BD}}} = \frac{w_l}{\sqrt{L^2 + \left(\frac{h}{2}\right)^2}} = \frac{w_l/L}{\sqrt{1 + \left(\frac{w_l}{L}\right)^2 \left(\frac{2r}{w_l} - 1\right)}}$$

$$\tan\beta = \frac{\frac{1}{2}\cdot\ell_{\mathrm{AD}}}{\ell_{\mathrm{AE}}} = \frac{h/2}{\sqrt{w_l^2 + L^2}} = \frac{w_l}{L}\cdot\sqrt{\frac{\frac{2r}{w_l} + 1}{1 + \left(\frac{w_l}{L}\right)}} = \frac{\ell_{\mathrm{BD}}}{\ell_{\mathrm{AB}}}$$

$$\frac{\ell_{\mathrm{AB}}}{\ell_{\mathrm{BC}}} = \frac{\ell_{\mathrm{AB}}}{\ell_{\mathrm{BD}}}\cdot\frac{\ell_{\mathrm{BD}}}{\ell_{\mathrm{BC}}} = \frac{1}{\tan\beta}\cdot\frac{1}{\tan\mu}$$

$$\frac{\ell_{\mathrm{AB}}}{\ell_{\mathrm{BC}}} = \left(\frac{L}{w_l}\right)^2 \sqrt{\frac{\left(1 + \left(\frac{w_l}{L}\right)^2\right)\left(1 + \left(\frac{w_l}{L}\right)^2 \left(\frac{2r}{w_l} - 1\right)\right)}{\frac{2r}{w_l} - 1}} \tag{A.16}$$

Thus, an expression for $\ell_{\mathrm{AB}}/\ell_{\mathrm{BC}}$ has been obtained, and the gradient for line AB can be found. Squaring Eq. (A.16) and inserting it into Eq. (A.15) and using that $\theta_1 = \rho$ yields

$$\tan\theta_1 = \left(\frac{w_l}{L}\right)^2 \sqrt{\frac{\frac{2r}{w_l} - 1}{1 + \left(\frac{w_l}{L}\right)^2 \left(\frac{2r}{w_l}\right)}}$$

[1] This means that $\ell_{\mathrm{AB}} = \ell_{\mathrm{BA}}$.

$$\theta_1 = \arctan\left(\left(\frac{w_l}{L}\right)^2 \cdot \sqrt{\frac{\frac{2r}{w_l} - 1}{1 + \left(\frac{2rw_l}{L^2}\right)}}\right) \tag{A.17}$$

Finally γ_t is found by summation of Eqs. (A.14) and (A.17),

$$\gamma_t = \theta_1 + \theta_2$$

and the total plastic work is then $W_t = m_p \ell_s \gamma_t$. As γ_t depends on s from Fig. A.5, an average between the values at $s = 0$ and at $s = w_l$ is used,

$$\bar{\gamma}_t = \frac{\gamma_t\,(s = 0) + \gamma_t\,(s = w_l)}{2}$$

which replaces γ_t in the plastic work, $W_t = m_p \ell_s \bar{\gamma}_t$.

By inserting the values zero and w_l for s into $\bar{\gamma}_t$ and writing out W_t the following, rather cumbersome, expression is obtained;

$$\begin{aligned} W_t =& \sigma_0 t^2 w_l \cdot \sqrt{\frac{2r}{w_l} + \left(\frac{L}{w_l}\right)^2} \cdot \left[\arctan\left(\left(\frac{w_l}{L}\right)^2 \cdot \sqrt{\frac{\frac{2r}{w_l} - 1}{1 + \left(\frac{2rw_l}{L^2}\right)}}\right)\right. \\ &\left. + \frac{1}{2}\arctan\left(\frac{\sqrt{\left(1 + \frac{2rw_l}{L^2}\right)\left(\frac{w_l}{r}\left(2 - \frac{w_l}{r}\right)\right)}}{\left(1 + \frac{2rw_l}{L^2} - \left(\frac{w_l}{L}\right)^2\right)\left(1 - \frac{w_l}{r}\right)}\right)\right] \end{aligned} \tag{A.18}$$

At last, the total plastic work W_p in both the rectangle W_r and triangle W_t amounts to

$$W_p = W_r + W_t$$

Appendix B

Material inpection certificate

This appendix contains the material inspection certificate from the pipe manufacturer Tenaris in Argentina. It provides nominal values for yield stress, ultimate tensile strength, Charpy impact test values, chemical composition of alloy, etc. The ID for the pipeline in question is "Heat 34571" which is convieniently marked with yellow. From the page numbering of this attached document, it is evident that some pages are missing. These pages are connected with testing of other pipelines, and are therefore omitted.

Tenaris

INSPECTION CERTIFICATE

(EN 10204 3.1B - ISO 10474 3.1B)

Siderca S.A.I.C.
Dr. Jorge A. Simini 250
B2804AAH) Campana
Buenos Aires - Argentina
(54) 3489 433100 Int
(54) 3489 433405 Fax

Cliente / Customer	Expediente/ Manufacturing Order	Número / Number	Fecha / Date	Pág./Page
STATOIL	5f1174.01	231949	17/11/2004	1 / 21
Producto / Product	Orden de Compra/ Purchase Order	Item	Referencia del Cliente / Customer Reference	
SMLS LINE PIPE TO BE COATED/GALVANIZED	4500754339	1	NORME SAT PROJECT	
Norma / Standard	Grado / Grade		Extremos / Ends	
DNV RULES OS-F101-2000 /QCP 2384 Rev. 0 + PMDS. for Norne Satellites (+)	SML 450PPD		SQUARE CUT END	
Dimensiones / Dimensions — Schedule / Peso Nominal / Nominal Weight	Longitud / Length	Superficie Externa / External Surface	Cantidades / Quantities	
141.30 x 9.50 mm — 30.97 KG/MT	11.17/12.7 m	WITHOUT PROTECTION-BARE	1089 Pc — 13621.93 m — 421282 Kg	
5 9/16 x 0.374 inches — 20.78 LB/FT			1089 Pcs — 44691.37 Ft — 928768 Lb	

ENSAYOS DE TRACCION / TENSILE TEST

Colada	Nº de Ensayo	Condición de la probeta					Temp de Ens	Dimensiones		Sección	Fluencia / Yield Strength						Rotura/U.T.S			Relación F/R	Alargamiento Elongation			Red. de area		Dureza / Hardness Tipo / type:			
		Specimen condition						Size		Area	Offset Method			EUL Method						YS/UTS Ratio	Lo (*)			Area Red.		V. Obt.		
Heat	Test Nº	Zona Zone	Estado	Ext.	Nº P/T	Tipo Type	Ori.	Test Temp	mm	mm2	Req. Min 0.2%	V. obt.	EUL	Req. Min	V. obt.	Req. Max	Req. Min	V. obt.	Req. Max	Req. Max	Obt.	mm	%	Rec. Min	%	Req. Min	Req. Max	Req. Max
											N/mm2		%	N/mm2			N/mm2											
33652	445286	C/B	PRO	O	15	ST	L	TART	12.54 X 9.96	120.07			0.5	450	473.1	570	535	574.7		0.92	0.82	61.9	18.0	29.6				
33652	445286	C/B	PRO	O	102	ST	L	TART	12.48 X 9.94	119.24			0.5	450	494.0	570	535	569.6		0.92	0.84	61.7	18.0	28.0				
33652	445290	C/B	PRO	E	52	ST	L	TART	12.68 X 9.57	121.54			0.5	450	497.0	570	535	591.6		0.92	0.84	62.3	18.0	29.5				
33652	445288	C/B	PRO	E	5	ST	L	TART	12.71 X 9.38	119.41			0.5	450	488.6	570	535	562.9		0.92	0.83	61.7	18.0	28.9				
33652	458836	C/B	PRO	O	1902	ST	L	TART	13.50 X 9.25	125.10			0.5	450	543.6	570	535	622.7		0.92	0.87	63.2	18.0	24.5				
33652	458837	C/B	PRO	E	1911	ST	L	TART	13.33 X 9.69	129.39			0.5	450	513.2	570	535	593.5		0.92	0.86	64.3	18.0	23.1				
34571	455724	C/B	PRO	O	1361	ST	L	TART	13.47 X 9.51	128.32			0.5	450	516.9	570	535	591.5		0.92	0.87	64.0	18.0	24.0				
34571	455732	C/B	PRO	E	1407	ST	L	TART	13.22 X 9.30	123.15			0.5	450	536.7	570	535	604.9		0.92	0.89	62.7	18.0	25.7				
34571	455783	C/B	PRO	O	1471	ST	L	TART	13.37 X 9.44	126.43			0.5	450	498.3	570	535	566.1		0.92	0.85	63.5	18.0	24.6				
34571	455847	C/B	PRO	O	1705	ST	L	TART	13.18 X 9.24	121.89			0.5	450	505.8	570	535	570.5		0.92	0.89	62.4	18.0	36.2				
64287	455537	C/B	PRO	E	806	ST	L	TART	12.50 X 9.19	115.05			0.5	450	498.3	570	535	563.2		0.92	0.88	60.6	18.0	23.6				
64287	455538	C/B	PRO	O	851	ST	L	TART	12.52 X 9.88	120.12			0.5	450	487.8	570	535	560.3		0.92	0.87	61.9	18.0	27.7				

TEST TECNOLOGICO / TECHNOLOGICAL TEST

Aplastamiento Flattening Test		Curvado Bend test		Abocardado Flaring Test		Pestañado Flange Test		Ens. De anillo expandido Ring expanding Test		Ens. De Tracción de anillo Ring tensile Test		NOTA / NOTE:
N.A		N.A		N.A		N.A		N.A		N.A		

Pro = Proceso/ Process
N = Normalizado/ Normalized
DST = Distensionado y Stress Relief
Q & T = Templado y Revenido/ Quenched & Tempered
TART = Temp. Ambiental/ Room Temperature

RE = Rectangular
CI = Cilindrical/Cylindrical
ST = Segmento Tubular / Tubular segmen
TU = Transversal

C/B = Cuerpo / Body
R/U = Recalque / Upset
P / A = Promedio / Average
Min = Mínimo / minimum
Max = Máximo / Maximum

L = Longitudinal
T = Transversal
P/T = Tubo/ Pipe
EXT = Extremo/ End
M = Medio/ Middle

V.Obt. = Valor Obtenido/ Obtained value
E = Comienzo de marcación/ Stenciling starting
O = Extremo opuesto al E/ Opposite extreme to E
(**) = 5,65 * √So

CALI 17994

Tenaris

INSPECTION CERTIFICATE

(EN 10204 3.1B - ISO 10474 3.1B)

Siderca S.A.I.C
Dr Jorge A. Simini 250
(B2804MHA) Campana
Buenos Aires, Argentina
(54) 3489 433100 tel
(54) 3489 433405 fax

Cliente / Customer	Expediente/ Manufacturing Order	Número / Number	Fecha / Date	Pág./Page
STATOIL	5/1174.01	231949	17/11/2004	4 / 21
Producto / Product	**Orden de Compra/ Purchase Order**	**Item**	**Referencia del Cliente / Customer Reference**	
SMLS LINE PIPE TO BE COATED/GALVANIZED	4500754339	1	NORNE SAT PROJECT	
Norma / Standard	**Grado / Grade**		**Extremos / Ends**	
DNV RULES OS-F101-2000 /QCP 2384 Rev. 0 + PMDS. for Norne Satellites (+)	SML 450IPFD		SQUARE CUT END	

Dimensiones / Dimensions	Schedule	Peso Nominal / Nominal Weight	Longitud / Length	Superficie Externa / External Surface	Cantidades / Quantities
141.30 x 9.50 mm 5 9/16 x 0.374 inches		30.97 KG/MT 20.78 LB/FT	11.7/12.7 m	WITHOUT PROTECTION-BARE	1089 Pz 13621.93 m 421282 Kg 1089 Pcs 44691.37 Ft 928768 Lb

ENSAYOS QUIMICOS / CHEMICAL ANALYSES

			% C	% Si	% Mn	% Cr	% Mo	% W	% Cd	% P	% S	% Ni	% V	% Al	% Sn	% Cu	% As	% Nb	% Ti	% Pb	% Sb	% Co	% Zr	% Bi	% Ca	% B	% N	% O	% Mg	% H	% C.e 1	% C.e 2	% Pcm	% Sum 1	% Sum 2	% Sum 3	R 1	R 2	R 3
			x 100							x 1000													x 10000							*	x 100				x 1000				
Colada	Heat	Max	12	35	160	20	13			15	3	300	100	50	20	350	30	50	40	10	10			100	60	5	100				38		22	120					
Heat		Min	7	15	100		5							15																									
Ensayo	Prod	Max	12	35	160	20	13			15	3	300	100	50	20	350	30	50	40	10	10			100	60	5	100				38		22	120				2.0	
Test		Min	7	15	100		5							15																									
33652	Heat		11	28	112	4	12	0		7	1	36	54	23	5	70	3	1	15	1	1	5	20	14	21	1	54		1		35		20	70				4.2	
(445286)	Prod		11	26	111	5	12			8	1	34	51	21	4	63	1	1	14	1	2	3	10	11	19	1	52		5		35		19	66				4.0	
(445288)	Prod		11	26	111	5	12			8	1	35	51	22	4	62	1	1	15	1	2	3	10	11	24	1	51		5		35		19	67				4.3	
(445290)	Prod		11	28	111	5	12			7	1	35	52	25	5	63	2	1	15	1	1	4	20	11	22	1	55		5		35		19	68				4.5	
(445388)	Prod		10	27	110	5	12			7	1	35	52	24	5	64	1	1	14	1	3	3	10	11	21	1	55		6		33		18	67				4.3	
(458836)	Prod		10	26	112	4	11	0		7	2	35	56	24	6	79	3	1	14	1	1	6	20	10	18	1	53		1		34		18	70				4.5	
(458837)	Prod		10	27	113	4	11	0		7	2	35	56	23	6	79	3	1	14	1	1	6	20	14	19	1	58		1		34		19	71				3.9	
34571	Heat		9	25	113	4	9	0		8	1	38	62	15	7	85	5	1	13	1	1	7	10	1	16	1	58		1		32		17	76				2.5	
(455724)	Prod		9	27	110	4	10	0		10	1	45	60	20	8	81	3	1	13	1	1	4	10	1	20	1	60		4		32		17	74				3.3	
	Prod		9	24	110	4	9	0		9	1	36	60	16	6	66	1	1	11	1	1	4	10	1	21	1	60		3		32		17	72				2.6	
(455732)	Prod		9	24	110	4	9	0		9	1	36	60	16	5	66	2	1	12	1	1	4	10	1	17	1	60		3		32		17	73				2.6	
(455783)	Prod		9	25	110	4	10	0		9	1	38	60	17	7	71	3	1	12	1	1	4	10	1	18	1	60		3		32		17	73				2.8	
	Prod		9	24	110	4	9	0		9	1	35	60	16	6	66	2	1	12	1	1	4	10	1	18	1	60		3		32		17	73				2.6	
(455947)	Prod		10	24	113	4	9	0		9	1	35	62	18	6	86	2	1	13	1	1	4	10	1	18	1	60		3		33		18	76				3.0	
64267	Heat		10	29	110	4	10	0		10	1	49	67	30	10	101	6	1	15	1	1	7	10	1	21	1	63		1		33		19	83				4.7	

NOTAS / NOTES: H = Análisis de colada / Heat Analysis. P = Análisis de producto / Product Analysis C.e = Carbono Equivalente/Equivalent Carbon R = Ratio * = PPM / Part per million

CEQ 1 = C+(MN/6)+(CR+MO+V)/5+(NI+CU)/15

CEQ 2 =

PCM = C+(SI/30)+(MN+CR+CU)/20+(NI/60)+(MO/15)+(V/10)+(5*B)

Sum 1 = NB+V+TI

SUM 2 =

SUM 3 =

R 1 = AL/N

R 2 =

R 3 =

CAU 17/04

Tenaris

INSPECTION CERTIFICATE

(EN 10204 3.1B - ISO 10474 3.1B)

Siderca S.A.I.C.
Dr. Jorge A. Sabato 350
B1607EWV Campana
Buenos Aires, Argentina
(54) 3489 433108 tel
(54) 3489 433405 fax

Cliente / Customer	Expediente/ Manufacturing Order	Número / Number	Fecha / Date	Pag./Page
STATOIL	571174.01	231949	17/11/2004	8 / 21
Producto / Product	Orden de Compra/ Purchase Order	Ítem	Referencia del Cliente / Customer Reference	
SMLS LINE PIPE TO BE COATED/GALVANIZED	4500754339	1	NORNE SAT PROJECT	
Norma / Standard	Grado / Grade		Extremos / Ends	
DNV RULES OS-F101-2000 /QCP 2384 Rev. 0 + PMDS. for Norne Satellites (+)	SML 450PPD		SQUARE CUT END	
Dimensiones / Dimensions — Schedule — Peso Nominal / Nominal Weight	Longitud / Length	Superficie Externa / External Surface	Cantidades / Quantities	
141.30 x 9.50 mm — 30.97 KG/MT	11.7/12.7 m	WITHOUT PROTECTION-BARE	1089 Pz — 13621.93 m — 421282 Kg	
5 9/16 x 0.374 inches — 20.78 LB/FT			1089 Pcs — 44691.37 Ft — 928768 Lb	

ENSAYOS DE IMPACTO / IMPACT TEST

Colada Heat	Ensayo Test	Condición de la probeta / Specimen condition					Temper. °C		Energía Absorbida / Absorbed Energy:										Area dúctil / Shear Area (%)							Expansión Lateral/Lateral Exp. (Mil)						
		Zona Zone	Método Method	Entalla Notch	Dimensiones Size mm		Orient.		Unidad Unit	Req.		V.Obt/Obtained Values							Req.		V.Obt/Obtained Values					Req.		V.Obt./Obtained Values				
												Sample Nº									Sample Nº							Sample Nº				
							Req.	T/E		Min	P/A	1	2	3		Min	P/A		Min	P/A	1	2	3		Min	P/A	1	2	3		Min	P/A
33652	445286	C/B	CHARPY	V	10,00	x 7,50	L	-33	Joules	57,0	67,5	283,2	283,3	278,9	278,8	281,5															
33652	445288	C/B	CHARPY	V	10,00	x 7,50	L	-33	Joules	57,0	67,5	262,0	255,4	254,9	254,0	257,1															
33652	445290	C/B	CHARPY	V	10,00	x 7,50	L	-33	Joules	57,0	67,5	259,4	259,4	279,3	259,2	266,0															
33652	445288	C/B	CHARPY	V	10,00	x 7,50	L	-33	Joules	57,0	67,5	252,7	272,6	252,7	252,7	259,4															
33652	458836	C/B	CHARPY	V	10,00	x 7,50	L	-33	Joules	57,0	67,5	269,8	276,9	256,3	256,3	267,6															
33652	458837	C/B	CHARPY	V	10,00	x 7,50	L	-33	Joules	57,0	67,5	258,3	267,4	256,7	256,7	267,5															
34571	455734	C/B	CHARPY	V	10,00	x 7,50	L	-33	Joules	57,0	67,5	325,5	333,1	340,6	325,5	333,0															
34571	455732	C/B	CHARPY	V	10,00	x 7,50	L	-33	Joules	57,0	67,5	324,7	312,6	353,4	312,6	323,5															
34571	455783	C/B	CHARPY	V	10,00	x 7,50	L	-33	Joules	57,0	67,5	312,6	345,3	312,6	312,6	323,5															
34571	455947	C/B	CHARPY	V	10,00	x 7,50	L	-33	Joules	57,0	67,5	303,0	309,6	303,8	303,0	305,1															
64267	455937	C/B	CHARPY	V	10,00	x 7,50	L	-33	Joules	57,0	67,5	307,0	285,1	301,6	285,1	297,9															
64267	455938	C/B	CHARPY	V	10,00	x 7,50	L	-33	Joules	57,0	67,5	336,2	321,3	323,3	321,3	327,0															
64267	455940	C/B	CHARPY	V	10,00	x 7,50	L	-33	Joules	57,0	67,5	286,7	312,4	325,3	286,7	308,1															
64267	455959	C/B	CHARPY	V	10,00	x 7,50	L	-33	Joules	57,0	67,5	325,9	315,8	310,0	310,0	317,2															
64267	458835	C/B	CHARPY	V	10,00	x 7,50	L	-33	Joules	57,0	67,5	276,3	296,4	283,9	276,3	285,5															
64267	458838	C/B	CHARPY	V	10,00	x 7,50	L	-33	Joules	57,0	67,5	276,9	285,3	265,8	265,8	269,3															
64268	455940	C/B	CHARPY	V	10,00	x 7,50	L	-33	Joules	57,0	67,5	302,4	303,4	300,4	300,4	302,0															
64268	455941	C/B	CHARPY	V	10,00	x 7,50	L	-33	Joules	57,0	67,5	314,2	322,0	325,5	322,0	313,9															
64268	455943	C/B	CHARPY	V	10,00	x 7,50	L	-33	Joules	57,0	67,5	333,3	307,2	303,2	303,2	314,5															
64268	455944	C/B	CHARPY	V	10,00	x 7,50	L	-33	Joules	57,0	67,5	281,7	325,1	298,8	281,7	301,9															
64268	455945	C/B	CHARPY	V	10,00	x 7,50	L	-33	Joules	57,0	67,5	302,0	312,6	256,1	256,1	303,6															
64269	455476	C/B	CHARPY	V	10,00	x 7,50	L	-33	Joules	57,0	67,5	287,5	302,4	314,2	287,5	301,3															

NOTE: Req = Requisitos / Requirements C/B = Cuerpo / Body R/U = Recalque / Upset Orient = Orientación / Orientation V = Valor / Value P/A = Promedio / Average Min = Mínimo / Minimum T/E = Temp. Ens. / Test Temp.

CAU 17004

Tenaris

INSPECTION CERTIFICATE

(EN 10204 3.1B - ISO 10474 3.1B)

Siderca S.A.I.C
Dr Jorge A. Simini 250
(B2804MHA) Campana
Buenos Aires, Argentina
(54) 3489 433100 tel
(54) 3489 433405 fax

Cliente / Customer		Expediente/ Manufacturing Order	Número / Number	Fecha / Date	Pág./Page
STATOIL		5/1174.01	231949	17/11/2004	11 / 21
Producto / Product		Orden de Compra/ Purchase Order	Item	Referencia del Cliente / Customer Reference	
SMLS LINE PIPE TO BE COATED/GALVANIZED		4500754339	1	NORNE SAT PROJECT	
Norma / Standard		Grado / Grade		Extremos / Ends	
DNV RULES OS-F101-2000 /QCP 2384 Rev. 0 + PMDS. for Norne Satellites (+)		SML 450IPFD		SQUARE CUT END	
Dimensiones / Dimensions	Schedule	Peso Nominal / Nominal Weight	Longitud / Length	Superficie Externa / External Surface	Cantidades / Quantities
141.30 x 9.50 mm 5 9/16 x 0.374 inches		30.97 KG/MT 20.78 LB/FT	11.7/12.7 m	WITHOUT PROTECTION-BARE	1089 Pz 13621.93 m 421282 Kg 1089 Pcs 44691.37 Ft 928768 Lb

Valores Requeridos / Required Values	Individuales / Individuals			Promedios / Average			Tipo de dureza / Hardness type
	Max	Min	Var	Max	Min	Var	VICKERS HV10
	260						

ENSAYO DE DUREZA/ HARDNESS TEST

Cuadrante / Quadrant			Obtenidos/ Obtained — Valor individual/ Individual Value							
	Colada/ Heat	33652								
	Ensayo/ Test	458836								
	Tubo/ Pipe	1902	1	2	3	4	Max	Min	P/A	Var
1	Extremo / End	O								
	Diametro Ext./ External Diam.		199	195	196	195	199.0	195.0	196.3	
	Centro/ Mid-wall		207	200	192	194	207.0	192.0	198.3	3.8
	Diametro Int./ Internal Diam.		198	190	195	195	198.0	190.0	194.5	

Cuadrante / Quadrant			Obtenidos/ Obtained — Valor individual/ Individual Value							
	Colada/ Heat	33652								
	Ensayo/ Test	458837								
	Tubo/ Pipe	1911	1	2	3	4	Max	Min	P/A	Var
1	Extremo / End	E								
	Diametro Ext./ External Diam.		193	194	193	190	194.0	190.0	192.5	
	Centro/ Mid-wall		198	195	193	206	206.0	193.0	198.3	5.8
	Diametro Int./ Internal Diam.		192	192	193	195	195.0	192.0	193.0	

Cuadrante / Quadrant			Obtenidos/ Obtained — Valor individual/ Individual Value							
	Colada/ Heat	34571								
	Ensayo/ Test	455724								
	Tubo/ Pipe	1361	1	2	3	4	Max	Min	P/A	Var
1	Extremo / End	O								
	Diametro Ext./ External Diam.		194	193	193	207	207.0	193.0	196.5	
	Centro/ Mid-wall		196	185	181	180	196.0	180.0	185.5	16.3
	Diametro Int./ Internal Diam.		176	181	184	181	184.0	176.0	180.5	

Cuadrante / Quadrant			Obtenidos/ Obtained — Valor individual/ Individual Value							
	Colada/ Heat	34571								
	Ensayo/ Test	455732								
	Tubo/ Pipe	1407	1	2	3	4	Max	Min	P/A	Var
1	Extremo / End	E								
	Diametro Ext./ External Diam.		219	203	199	198	219.0	198.0	204.8	
	Centro/ Mid-wall		190	187	185	186	190.0	185.0	187.0	26.0
	Diametro Int./ Internal Diam.		179	171	179	186	186.0	171.0	178.8	

Ind = Individual Val. = Valor/ Value Min = Mínimo/ Minimum Max = Máximo/ Maximum P/A = Promedio/ Average Var. = Variación/ Variation
E = Comienzo de la marcación/ Stenciling starting O = Extremo opuesto al E/ Opposite end to E M = Medio/ Middle

CALI 17504

Tenaris

Siderca S.A.I.C.
Dr. Jorge A. Simini 250
B2804EHA Campana
Buenos Aires - Argentina
(54) 3489 433100 tel
(54) 3489 433405 fax

INSPECTION CERTIFICATE

(EN 10204 3.1B - ISO 10474 3.1B)

Cliente / Customer	Expediente/ Manufacturing Order	Número / Number	Fecha / Date	Pág./Page
STATOIL	511174.01	231949	17/11/2004	12 / 21
Producto / Product	Orden de Compra/ Purchase Order	Ítem	Referencia del Cliente / Customer Reference	
SMLS LINE PIPE TO BE COATED/GALVANIZED	4500754339	1	NORNE SAT PROJECT	
Norma / Standard	Grado / Grade		Extremos / Ends	
DNV RULES OS-F101-2000 /QCP 2384 Rev. 0 + PMDS. for Norne Satellites (*)	SML 450PFD		SQUARE CUT END	
Dimensiones / Dimensions Schedule / Peso Nominal / Nominal Weight / Longitud / Length / Superficie Externa / External Surface / Cantidades / Cuantities				
141.30 x 9.50 mm 30.97 KG/MT 11.7/12.7 m WITHOUT PROTECTION-BARE 1089 Pz 13621.93 m 421282 Kg				
5 9/16 x 0.374 inches 20.78 LB/FT 1089 Pcs 44691.37 Ft 928768 Lb				

ENSAYO DE DUREZA/ HARDNESS TEST

Valores Requeridos / Required Values	Individuales Individuals Max	Mín	Var	Promedios Average Max.	Mín.	Var.	Tipo de dureza Hardness type
	260						VICKERS HV10

Cuadrante	Colada/ Heat	34571	Obtenidos/ Obtained						
	Ensayo/ Test	455783	Valor individual/ Individual Value						
Quadrant	Tubo/ Pipe	1471	1	2	3	4	Max	Min	P/A	Var
	Extremo / End	O								
1	Diametro Ext./ External Diam.		198	192	185	192	198.0	185.0	191.8	9.0
	Centro/ Mid-wall		188	187	184	187	188.0	184.0	186.5	
	Diametro Int./ Internal Diam.		185	186	182	178	186.0	178.0	182.8	

Cuadrante	Colada/ Heat	64267	Obtenidos/ Obtained						
	Ensayo/ Test	455537	Valor individual/ Individual Value						
Quadrant	Tubo/ Pipe	808	1	2	3	4	Max	Min	P/A	Var
	Extremo / End	E								
1	Diametro Ext./ External Diam.		201	205	203	197	205.0	197.0	201.5	9.8
	Centro/ Mid-wall		211	207	208	202	211.0	202.0	207.0	
	Diametro Int./ Internal Diam.		216	209	212	208	216.0	208.0	211.3	

Cuadrante	Colada/ Heat	34571	Obtenidos/ Obtained						
	Ensayo/ Test	455847	Valor individual/ Individual Value						
Quadrant	Tubo/ Pipe	1705	1	2	3	4	Max	Min	P/A	Var
	Extremo / End	O								
1	Diametro Ext./ External Diam.		185	189	189	187	189.0	187.0	188.5	8.2
	Centro/ Mid-wall		187	187	183	190	190.0	183.0	186.8	
	Diametro Int./ Internal Diam.		192	196	194	198	198.0	192.0	195.0	

Cuadrante	Colada/ Heat	64267	Obtenidos/ Obtained						
	Ensayo/ Test	455538	Valor individual/ Individual Value						
Quadrant	Tubo/ Pipe	851	1	2	3	4	Max	Min	P/A	Var
	Extremo / End	O								
1	Diametro Ext./ External Diam.		167	176	168	170	176.0	167.0	170.3	6.0
	Centro/ Mid-wall		174	174	176	174	176.0	174.0	174.5	
	Diametro Int./ Internal Diam.		175	176	177	177	177.0	175.0	176.3	

Ind = Individual Val. = Valor/ Value Mín = Mínimo/ Minimum Max = Máximo/ Maximum P/A = Promedio/ Average Var = Variación/ Variation
E = Comienzo de la marcación/ Stenciling starting O = Extremo opuesto al E/ Opposite end to E M = Medio/ Middle

CAU 17904

Appendix C

Measurements of pipes

This section contains the thickness and inner diameter measurements of the pipes tested. A portable ultrasound device has been used to conduct the measurements. This has been calibrated on several occasions, and the accuracy when measuring the same point multiple times was adequate. The standard deviation from 30 measurements on the same point, conducted at five different different locations (150 measurements in total), was about 0.03 mm. The curved surface of the pipe was a bit tricky to measure accurately, but this confirms that the measurements are reasonably accurate.

Table C.1: *Measurements of pipe A.*

Position	**1**	**2**	**3**	**4**	**5**	**Avg.**	**Sdev.**	**Var.**
North	4.10	3.97	3.83	3.86	4.09	3.97	0.126	0.016
Northeast	-	3.56	3.40	3.54	-	3.50	0.087	0.008
East	3.67	3.63	3.54	3.44	3.37	3.53	0.126	0.016
Southeast	-	3.49	3.60	3.60	-	3.56	0.064	0.004
South	3.50	3.77	3.79	3.83	3.97	3.77	0.171	0.029
Southwest	-	4.41	4.52	4.59	-	4.51	0.091	0.008
West	4.23	4.02	4.18	4.20	4.41	4.21	0.139	0.019
Northwest	-	4.13	4.11	4.27	-	4.17	0.087	0.009
Avg.	3.88	3.87	3.87	3.92	3.96	**3.89**	-	-
Sdev.	0.346	0.316	0.376	0.403	0.435	-	**0.349**	-
Var.	0.120	0.100	0.141	0.163	0.189	-	-	**0.122**

Table C.2: *Measurements of pipe B.*

Position	**1**	**2**	**3**	**4**	**5**	**Avg.**	**Sdev.**	**Var.**
North	4.23	4.00	3.93	3.95	4.09	4.04	0.123	0.015
Northeast	-	3.56	3.54	3.44	-	3.51	0.064	0.004
East	3.56	3.56	3.44	3.40	3.31	3.45	0.108	0.012
Southeast	-	3.51	3.47	3.47	-	3.48	0.023	0.001
South	3.63	3.70	3.70	3.88	3.79	3.74	0.097	0.009
Southwest	-	4.20	4.32	4.62	-	4.38	0.216	0.047
West	4.18	4.06	4.06	4.20	4.25	4.15	0.086	0.007
Northwest	-	4.20	4.13	4.20	-	4.18	0.040	0.002
Avg.	3.90	3.85	3.82	3.90	3.86	**3.86**	-	-
Sdev.	0.354	0.297	0.333	0.439	0.413	-	**0.343**	-
Var.	0.125	0.088	0.111	0.193	0.171	-	-	**0.118**

Table C.3: *Measurements of pipe C.*

Position	**1**	**2**	**3**	**4**	**5**	**Avg.**	**Sdev.**	**Var.**
North	4.39	4.25	4.16	4.06	3.95	4.16	0.170	0.029
Northeast	-	4.11	3.97	3.74	-	3.94	0.187	0.035
East	3.83	3.83	3.93	3.79	3.79	3.83	0.057	0.003
Southeast	-	3.79	3.95	3.93	-	3.89	0.087	0.008
South	3.86	3.88	3.95	4.06	4.20	3.99	0.141	0.020
Southwest	-	4.25	4.11	4.34	-	4.23	0.116	0.013
West	4.16	4.16	4.02	4.00	4.20	4.11	0.091	0.008
Northwest	-	4.25	4.09	4.18	-	4.17	0.080	0.006
Avg.	4.06	4.07	4.02	4.01	4.04	**4.04**	-	-
Sdev.	0.266	0.200	0.087	0.197	0.201	-	**0.175**	-
Var.	0.071	0.040	0.008	0.039	0.041	-	-	**0.031**

Table C.4: *Measurements of pipe D.*

Position	**1**	**2**	**3**	**4**	**5**	**Avg.**	**Sdev.**	**Var.**
North	3.97	4.02	3.81	3.83	3.60	3.85	0.164	0.027
Northeast	-	3.70	3.74	3.93	-	3.79	0.123	0.015
East	3.86	4.02	4.13	4.34	4.11	4.09	0.175	0.031
Southeast	-	4.06	4.29	4.50	-	4.28	0.220	0.048
South	4.71	4.64	4.80	4.80	5.07	4.80	0.163	0.027
Southwest	-	4.80	4.73	4.62	-	4.72	0.091	0.008
West	4.45	4.45	4.34	4.25	4.25	4.35	0.100	0.010
Northwest	-	4.25	4.16	4.06	-	4.16	0.095	0.009
Avg.	4.25	4.24	4.25	4.29	4.26	**4.26**	-	-
Sdev.	0.401	0.366	0.382	0.340	0.609	-	**0.376**	-
Var.	0.161	0.134	0.146	0.116	0.371	-	-	**0.141**

Table C.5: *Measurements of pipe E.*

Position	**1**	**2**	**3**	**4**	**5**	**Avg.**	**Sdev.**	**Var.**
North	3.72	3.83	4.13	4.06	3.88	3.92	0.168	0.028
Northeast	-	3.65	3.70	3.83	-	3.73	0.093	0.009
East	3.83	3.86	3.93	4.06	3.93	3.92	0.089	0.008
Southeast	-	4.23	4.16	4.32	-	4.24	0.080	0.006
South	4.50	4.55	4.41	4.36	4.27	4.42	0.111	0.012
Southwest	-	4.91	4.82	4.57	-	4.77	0.176	0.031
West	4.16	4.40	4.43	4.29	4.18	4.29	0.123	0.015
Northwest	-	4.39	4.39	4.20	-	4.33	0.110	0.012
Avg.	4.05	4.23	4.25	4.21	4.07	**4.19**	-	-
Sdev.	0.352	0.423	0.344	0.227	0.189	-	**0.316**	-
Var.	0.124	0.179	0.119	0.051	0.036	-	-	**0.100**

Table C.6: *Measurements of pipe F.*

Position	**1**	**2**	**3**	**4**	**5**	**Avg.**	**Sdev.**	**Var.**
North	3.90	3.54	3.63	3.95	3.90	3.78	0.186	0.034
Northeast	-	3.83	3.72	3.83	-	3.79	0.064	0.004
East	4.06	4.11	3.97	4.06	4.20	4.08	0.084	0.007
Southeast	-	4.39	4.20	4.30	-	4.30	0.095	0.009
South	4.20	4.52	4.39	4.20	4.11	4.28	0.167	0.028
Southwest	-	4.78	4.80	4.50	-	4.69	0.168	0.028
West	3.83	4.06	4.06	4.16	3.90	4.00	0.134	0.018
Northwest	-	3.74	3.86	4.20	-	3.93	0.239	0.057
Avg.	4.00	4.12	4.08	4.15	4.03	**4.09**	-	-
Sdev.	0.166	0.420	0.382	0.207	0.152	-	**0.300**	-
Var.	0.027	0.177	0.146	0.043	0.023	-	-	**0.090**

Table C.7: *Measurements of pipe G.*

Position	**1**	**2**	**3**	**4**	**5**	**Avg.**	**Sdev.**	**Var.**
North	3.72	4.10	4.12	4.28	4.28	4.10	0.229	0.052
Northeast	-	4.12	4.26	4.30	-	4.23	0.095	0.009
East	3.83	3.72	3.72	3.95	3.77	3.80	0.096	0.009
Southeast	-	3.77	3.74	3.90	-	3.80	0.085	0.007
South	4.10	4.08	4.10	3.97	4.12	4.07	0.060	0.004
Southwest	-	4.35	4.12	4.01	-	4.16	0.173	0.030
West	4.19	4.12	4.35	4.17	4.35	4.24	0.107	0.011
Northwest	-	4.26	4.39	4.35	-	4.33	0.067	0.004
Avg.	3.96	4.07	4.10	4.12	4.13	**4.08**	-	-
Sdev.	0.221	0.218	0.253	0.179	0.259	-	**0.215**	-
Var.	0.049	0.048	0.064	0.032	0.067	-	-	**0.046**

Table C.8: *Measurements of pipe H.*

Position	**1**	**2**	**3**	**4**	**5**	**Avg.**	**Sdev.**	**Var.**
North	4.04	4.17	4.46	4.62	4.51	4.36	0.244	0.060
Northeast	-	4.28	4.46	4.66	-	4.47	0.190	0.036
East	3.81	3.88	3.77	3.90	4.21	3.91	0.174	0.030
Southeast	-	3.72	3.59	3.72	-	3.68	0.075	0.006
South	4.12	3.77	3.84	3.77	3.77	3.85	0.152	0.023
Southwest	-	3.90	3.86	3.59	-	3.78	0.169	0.028
West	4.04	4.10	4.19	3.95	3.86	4.03	0.128	0.016
Northwest	-	4.37	4.66	4.45	-	4.49	0.150	0.022
Avg.	4.00	4.02	4.10	4.08	4.09	**4.06**	-	-
Sdev.	0.134	0.242	0.392	0.428	0.340	-	**0.322**	-
Var.	0.018	0.058	0.154	0.183	0.115	-	-	**0.103**

Table C.9: *Measurements of pipe I.*

Position	**1**	**2**	**3**	**4**	**5**	**Avg.**	**Sdev.**	**Var.**
North	3.77	3.66	3.95	3.99	4.17	3.91	0.199	0.039
Northeast	-	3.59	3.63	3.72	-	3.65	0.067	0.004
East	3.81	3.77	3.60	3.95	3.99	3.82	0.155	0.024
Southeast	-	4.17	3.96	4.17	-	4.10	0.121	0.015
South	4.01	4.39	4.15	3.95	3.90	4.08	0.197	0.039
Southwest	-	4.36	4.33	4.21	-	4.30	0.079	0.006
West	4.20	4.17	4.26	4.17	4.08	4.18	0.065	0.004
Northwest	-	3.95	4.21	4.26	-	4.14	0.166	0.028
Avg.	3.95	4.01	4.01	4.05	4.04	**4.02**	-	-
Sdev.	0.198	0.311	0.279	0.182	0.116	-	**0.230**	-
Var.	0.039	0.097	0.078	0.033	0.014	-	-	**0.053**

Table C.10: *Measurements of pipe J.*

Position	**1**	**2**	**3**	**4**	**5**	**Avg.**	**Sdev.**	**Var.**
North	4.48	4.72	4.60	4.59	4.51	4.58	0.094	0.009
Northeast	-	4.15	4.21	4.22	-	4.19	0.038	0.001
East	4.12	3.77	4.04	3.92	4.06	3.98	0.139	0.019
Southeast	-	3.81	4.04	3.99	-	3.95	0.121	0.015
South	3.83	3.90	3.68	3.77	3.97	3.83	0.112	0.013
Southwest	-	4.24	4.08	4.17	-	4.16	0.080	0.006
West	4.17	4.33	4.12	4.30	3.99	4.18	0.138	0.019
Northwest	-	4.57	4.44	4.47	-	4.49	0.068	0.005
Avg.	4.15	4.19	4.15	4.18	4.13	**4.16**	-	-
Sdev.	0.266	0.349	0.278	0.278	0.255	-	**0.276**	-
Var.	0.071	0.122	0.077	0.077	0.065	-	-	**0.076**

Table C.11: *Measurements of pipe K.*

Position	**1**	**2**	**3**	**4**	**5**	**Avg.**	**Sdev.**	**Var.**
North	4.10	4.07	3.96	3.90	3.50	3.91	0.241	0.058
Northeast	-	4.20	4.08	3.99	-	4.09	0.105	0.011
East	4.03	4.05	3.85	3.71	3.78	3.88	0.141	0.020
Southeast	-	4.47	4.42	4.31	-	4.40	0.082	0.007
South	4.26	4.27	4.19	4.20	4.39	4.26	0.080	0.006
Southwest	-	4.64	4.69	4.60	-	4.64	0.045	0.002
West	3.96	4.03	4.06	4.15	4.02	4.04	0.069	0.005
Northwest	-	4.01	3.95	4.06	-	4.01	0.055	0.003
Avg.	4.09	4.21	4.15	4.12	3.92	**4.12**	-	-
Sdev.	0.128	0.235	0.279	0.270	0.377	-	**0.265**	-
Var.	0.016	0.055	0.078	0.073	0.142	-	-	**0.070**

Table C.12: *Measurements of pipe L.*

Position	**1**	**2**	**3**	**4**	**5**	**Avg.**	**Sdev.**	**Var.**
North	4.20	3.98	3.71	3.70	3.78	3.87	0.214	0.046
Northeast	-	4.07	3.93	4.02	-	4.01	0.071	0.005
East	4.60	4.29	4.33	4.52	4.67	4.48	0.166	0.028
Southeast	-	4.48	4.79	4.90	-	4.72	0.218	0.047
South	4.22	4.30	4.43	4.46	4.36	4.35	0.097	0.009
Southwest	-	4.31	4.48	4.40	-	4.40	0.085	0.007
West	3.93	3.97	3.85	3.71	3.53	3.80	0.180	0.032
Northwest	-	4.00	3.82	3.62	-	3.81	0.190	0.036
Avg.	4.24	4.18	4.17	4.17	4.09	**4.17**	-	-
Sdev.	0.275	0.193	0.391	0.471	0.522	-	**0.358**	-
Var.	0.076	0.037	0.153	0.221	0.273	-	-	**0.128**

Table C.13: *Measurements of pipe M.*

Position	**1**	**2**	**3**	**4**	**5**	**Avg.**	**Sdev.**	**Var.**
North	3.55	3.47	3.57	3.56	3.72	3.57	0.091	0.008
Northeast	3.68	3.54	3.41	3.47	3.63	3.55	0.111	0.012
East	4.13	4.10	3.99	3.90	3.86	4.00	0.119	0.014
Southeast	4.12	3.90	3.89	3.81	3.75	3.89	0.140	0.020
South	4.31	4.30	4.20	4.07	3.82	4.14	0.203	0.041
Southwest	3.72	3.51	3.58	3.56	3.40	3.55	0.116	0.013
West	3.81	3.58	3.63	3.60	3.68	3.66	0.092	0.008
Northwest	3.64	3.43	3.55	3.45	3.62	3.54	0.096	0.009
Avg.	3.87	3.73	3.73	3.68	3.69	**3.74**	-	-
Sdev.	0.278	0.328	0.269	0.223	0.143	-	**0.253**	-
Var.	0.077	0.108	0.072	0.050	0.020	-	-	**0.064**

Table C.14: *Measurements of pipe N.*

Position	**1**	**2**	**3**	**4**	**5**	**Avg.**	**Sdev.**	**Var.**
North	4.15	4.10	4.26	4.54	4.54	4.31	0.215	0.046
Northeast	3.82	3.76	3.87	3.97	4.07	3.90	0.123	0.015
East	3.90	3.79	3.72	3.70	3.99	3.82	0.123	0.015
Southeast	3.54	3.54	3.45	3.48	3.58	3.52	0.052	0.003
South	3.89	3.68	3.54	3.67	3.65	3.69	0.127	0.016
Southwest	4.00	3.95	3.80	3.88	3.86	3.90	0.078	0.006
West	4.11	4.11	4.02	4.00	4.03	4.05	0.052	0.003
Northwest	3.85	3.96	4.30	3.99	4.10	4.04	0.170	0.029
Avg.	3.91	3.86	3.87	3.90	3.98	**3.90**	-	-
Sdev.	0.187	0.203	0.310	0.317	0.298	-	**0.258**	-
Var.	0.035	0.041	0.096	0.100	0.089	-	-	**0.067**

Table C.15: *Measurements of pipe 1.*

Position	**1**	**2**	**3**	**4**	**5**	**Avg.**	**Sdev.**	**Var.**
North	3.55	3.80	3.96	4.01	3.94	3.85	0.188	0.035
Northeast	3.68	3.86	4.10	3.91	3.81	3.87	0.154	0.024
East	4.21	4.37	4.50	4.26	4.18	4.30	0.131	0.017
Southeast	4.45	4.57	4.44	4.29	4.35	4.42	0.107	0.011
South	4.62	4.58	4.50	4.48	4.69	4.57	0.086	0.007
Southwest	4.30	4.20	4.13	4.30	4.43	4.27	0.114	0.013
West	4.15	3.97	4.06	4.24	4.43	4.17	0.177	0.031
Northwest	3.59	3.59	3.69	3.91	3.88	3.73	0.155	0.024
Avg.	4.07	4.12	4.17	4.18	4.21	**4.15**	-	-
Sdev.	0.410	0.370	0.289	0.206	0.314	-	**0.313**	-
Var.	0.168	0.137	0.083	0.043	0.098	-	-	**0.097**

Table C.16: *Measurements of pipe 2.*

Position	**1**	**2**	**3**	**4**	**5**	**Avg.**	**Sdev.**	**Var.**
North	3.71	3.91	3.97	3.88	3.74	3.84	0.112	0.013
Northeast	3.97	4.07	4.12	3.94	3.83	3.99	0.114	0.013
East	4.10	4.14	4.15	3.95	3.97	4.06	0.095	0.009
Southeast	4.31	4.26	4.14	4.06	4.24	4.20	0.101	0.010
South	3.90	3.80	3.77	3.85	4.07	3.88	0.118	0.014
Southwest	3.82	3.66	3.79	3.81	4.09	3.83	0.157	0.025
West	3.60	3.62	3.76	3.90	3.94	3.76	0.156	0.024
Northwest	3.63	3.75	3.78	3.94	3.81	3.78	0.112	0.012
Avg.	3.88	3.90	3.94	3.92	3.96	**3.92**	-	-
Sdev.	0.244	0.234	0.180	0.076	0.167	-	**0.182**	-
Var.	0.059	0.055	0.032	0.006	0.028	-	-	**0.033**

Table C.17: *Measurements of pipe 3.*

Position	**1**	**2**	**3**	**4**	**5**	**Avg.**	**Sdev.**	**Var.**
North	3.96	3.66	3.83	3.95	3.96	3.87	0.131	0.017
Northeast	4.09	4.05	4.25	4.29	4.12	4.16	0.104	0.011
East	4.10	4.41	4.49	4.42	4.15	4.31	0.176	0.031
Southeast	3.97	4.44	4.50	4.34	4.15	4.28	0.218	0.047
South	3.93	4.18	4.17	4.11	4.08	4.09	0.101	0.010
Southwest	4.13	4.06	3.93	3.92	4.20	4.05	0.123	0.015
West	3.82	3.61	3.48	3.45	3.90	3.65	0.201	0.040
Northwest	3.92	3.63	3.62	3.72	3.93	3.76	0.152	0.023
Avg.	3.99	4.01	4.03	4.03	4.06	**4.02**	-	-
Sdev.	0.107	0.339	0.382	0.332	0.115	-	**0.268**	-
Var.	0.011	0.115	0.146	0.110	0.013	-	-	**0.072**

Table C.18: *Measurements of pipe 4.*

Position	**1**	**2**	**3**	**4**	**5**	**Avg.**	**Sdev.**	**Var.**
North	4.08	3.98	3.92	4.10	4.17	4.05	0.099	0.010
Northeast	4.62	4.48	4.35	4.28	4.46	4.44	0.130	0.017
East	4.45	4.39	4.12	4.10	4.33	4.28	0.159	0.025
Southeast	4.46	4.48	4.42	4.21	4.26	4.37	0.123	0.015
South	4.11	4.32	4.26	4.17	4.01	4.17	0.122	0.015
Southwest	3.99	4.12	4.30	4.19	3.99	4.12	0.133	0.018
West	3.80	3.83	4.01	4.12	4.01	3.95	0.135	0.018
Northwest	4.08	3.99	4.08	4.30	4.32	4.15	0.147	0.022
Avg.	4.20	4.20	4.18	4.18	4.19	**4.19**	-	-
Sdev.	0.280	0.252	0.176	0.077	0.177	-	**0.194**	-
Var.	0.078	0.063	0.031	0.006	0.031	-	-	**0.038**

Table C.19: *Measurements of pipe 5.*

Position	**1**	**2**	**3**	**4**	**5**	**Avg.**	**Sdev.**	**Var.**
North	4.66	4.66	4.48	4.35	4.39	4.51	0.147	0.021
Northeast	4.30	4.47	4.39	4.30	4.19	4.33	0.106	0.011
East	4.04	4.17	4.30	4.21	4.08	4.16	0.104	0.011
Southeast	3.69	3.86	3.97	4.06	3.90	3.90	0.138	0.019
South	3.91	3.86	4.06	4.15	4.21	4.04	0.151	0.023
Southwest	3.89	3.69	3.74	3.90	4.07	3.86	0.150	0.023
West	4.48	4.19	4.24	4.28	4.48	4.33	0.137	0.019
Northwest	4.63	4.44	4.24	4.20	4.37	4.38	0.172	0.030
Avg.	4.20	4.17	4.18	4.18	4.21	**4.19**	-	-
Sdev.	0.369	0.344	0.241	0.146	0.194	-	**0.259**	-
Var.	0.136	0.118	0.058	0.021	0.038	-	-	**0.067**

Table C.20: *Measurements of pipe 6.*

Position	**1**	**2**	**3**	**4**	**5**	**Avg.**	**Sdev.**	**Var.**
North	4.08	4.17	4.29	4.39	4.46	4.28	0.155	0.024
Northeast	4.04	3.86	3.95	4.15	4.26	4.05	0.158	0.025
East	4.46	4.12	4.08	4.08	4.21	4.19	0.160	0.026
Southeast	4.08	3.95	3.69	3.63	3.86	3.84	0.185	0.034
South	4.08	4.05	4.01	3.78	3.86	3.96	0.130	0.017
Southwest	3.72	3.89	3.78	3.68	3.70	3.75	0.085	0.007
West	4.08	4.26	4.39	4.38	4.12	4.25	0.143	0.021
Northwest	3.88	4.05	4.21	4.35	4.21	4.14	0.180	0.032
Avg.	4.05	4.04	4.05	4.06	4.09	**4.06**	-	-
Sdev.	0.210	0.139	0.243	0.319	0.254	-	**0.228**	-
Var.	0.044	0.019	0.059	0.102	0.065	-	-	**0.052**

Appendix D

Bulging of circular membrane

This appendix explains the procedure based on Ref. [74] used to estimate the pressure arising in the impact experiment on closed water filled pipes. More specifically, pipe I in Section 4.3. One thick (rigid) and one thin (deformable) end cap were used to contain the water within the pipe, and the height h of the thin, deformed end cap was used in the calculation.

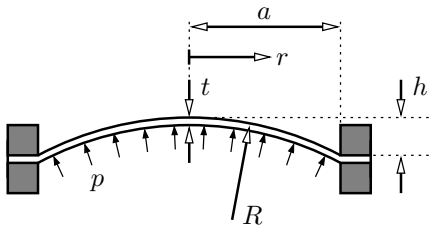

Figure D.1: *Measurements used when determining pressure based on bulging of circular membrane.*

Starting from Fig. D.1, which shows the cross-section of a clamped, axisymmetric membrane of thickness t and radius a, it is seen that a certain pressure p gives rise to a deformation h of the membrane, assumed to deform into an arc with radius R (or rather, a spherical shell in full 3D). Here, r is the measure

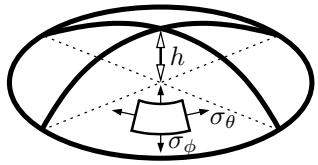

Figure D.2: *Dome arising from pressure applied to circular membrane.*

from the axis of symmetry towards the edge, meaning that $r \in [0, a]$. Details on the geometry of the can be found in Section 4.3.

Further, a plane stress condition is assumed. Considering a piece of the "dome" formed due to the pressure, two main stresses, denoted σ_θ and σ_ϕ, act on it as indicated by the arrows. By symmetry $\sigma_\theta = \sigma_\phi$, so the von Mises equivalent stress σ_{eq} becomes

$$\sigma_{\text{eq}} = \sqrt{\sigma_1^2 - \sigma_1\sigma_2 + \sigma_2^2} = |\sigma_\phi| \tag{D.1}$$

in which σ_1 and σ_2 are the principal stresses. The equivalent strain ε_{eq} is expressed via the principal strains ε_1, ε_2 and ε_3,

$$\varepsilon_{\text{eq}} = \sqrt{\frac{2}{3}\left(\varepsilon_1^2 + \varepsilon_2^2 + \varepsilon_3^2\right)} = \sqrt{\frac{2}{3}\left(\varepsilon_\theta^2 + \varepsilon_\phi^2 + \varepsilon_t^2\right)}$$

where ε_θ and ε_ϕ are rather self-explanatory, while ε_t is the strain in the thickness direction,

$$\varepsilon_t = \ln\left(\frac{t}{t_0}\right) = -\ln\left(\frac{t_0}{t}\right) \tag{D.2}$$

with t being the current thickness and t_0 the initial thickness. Symmetry conditions give $\varepsilon_\theta = \varepsilon_\phi$, and by assuming conservation of volume $\varepsilon_t = -2\varepsilon_\phi$, yielding

$$\varepsilon_{\text{eq}} = \sqrt{\frac{2}{3}\left(\varepsilon_\phi^2 + \varepsilon_\phi^2 + 4\varepsilon_\phi^2\right)} = 2\varepsilon_\phi = -\varepsilon_t \tag{D.3}$$

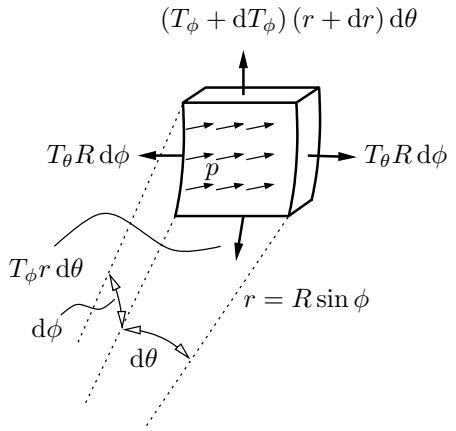

Figure D.3: *Forces acting on small part of the cylindrical shell.*

Now consider a small element of the shell and the forces acting on it as shown in Fig. D.3. T_ϕ and T_θ are tractions, given by $T_\phi = \sigma_\phi t$ and $T_\theta = \sigma_\theta t$. Equilibrium along the surface normal of the element is

$$\begin{aligned} p\,(r\mathrm{d}\theta)\,(R\mathrm{d}\phi) &= T_\theta R\,\mathrm{d}\phi\,\mathrm{d}\theta \cdot \sin\phi + T_\phi r\,\mathrm{d}\theta\,\mathrm{d}\phi \\ p\,(R\sin\phi)\,(R\mathrm{d}\phi) &= T_\theta R\,\mathrm{d}\phi \cdot \sin\phi + T_\phi\,(R\sin\phi)\,\mathrm{d}\phi \\ pR &= T_\theta + T_\phi = 2T_\phi = 2\sigma_\phi t \end{aligned}$$

thus providing an expression for the pressure as a function of the stress, thickness and arc (sphere) radius,

$$p = \frac{2t\sigma_\phi}{R} \tag{D.4}$$

all of which are unknown quantities. First, R is easily obtained by the geomtic relation

$$R = \frac{a^2 + h^2}{2h} \tag{D.5}$$

Then t is determined through the preservation of volume assumption

$$\pi a^2 \cdot t_0 = 2\pi R \cdot ht$$
$$\Rightarrow t = t_0 \cdot \frac{a^2}{2Rh} \tag{D.6}$$

The stress is determined through a constitutive relation, and a simple one-term power law has been chosen to this end, $\sigma_{\text{eq}} = K \cdot \varepsilon_{\text{eq}}^n$, where K and n are material constants determined from material tests. Inserting Eq. (D.6) into Eq. (D.4) provides

$$p = 2t_0 \cdot \frac{a^2}{2Rh} \cdot \frac{\sigma_\phi}{R} \tag{D.7}$$

Then, using $\varepsilon_{\text{eq}} = \ln(t_0/t)$ with Eq. (D.6) in the constitutive relation with $\sigma_{\text{eq}} = |\sigma_\phi|$ and inserting Eq. (D.5) yields a final estimate for the pressure p as a function of the measured dome height h,

$$p = \frac{4t_0 h}{a}\left(\frac{h}{a}\right) \cdot \frac{1}{\left(1+\frac{h^2}{a^2}\right)^2} \cdot K\left[\ln\left(1+\frac{h^2}{a^2}\right)\right]^n \tag{D.8}$$

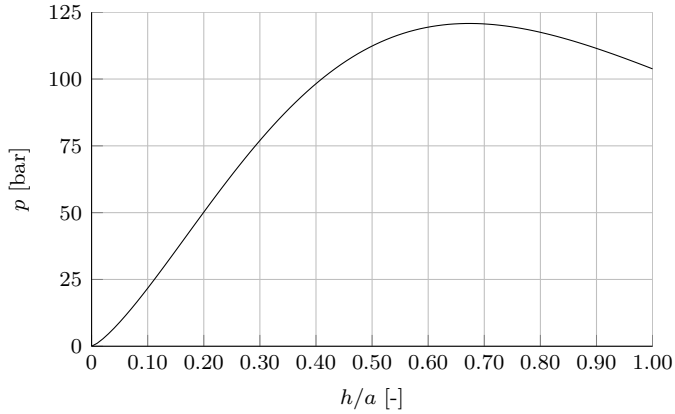

Figure D.4: *Bulging pressure in Bar as function of dome height relative to the radius.*

Using $t_0 = 0.7$ mm, $a = 63.3$ mm, $K = 990.8$ MPa and $n = 0.148$, the bulging pressure is plotted in Fig. D.4 as a function of dome height h normalised by r. For large values of h/a, Eq. (D.8) will cease to be valid as the material will most like fail before such values are attained. With the measured bulging deformation $h = 14$ mm ($h/a \approx 0.22$) from the component test, the estimated pressure becomes approximately 56 Bar.

Appendix E

Calibrations for stretch-bending rig

This appendix contains the current calibration data for the measuring equipment used in the stretch bending rig. The calibration data for the vertical load cell is provided by the vendor and given in Italian. The remainder of the calibrations were done by the lab in the in the period 19.11.2012 to 18.03.2013, and are given in Norwegian.

Data from the calibration procedures is presented as following:

Table E.1: Vertical load cell
Table E.2: Vertical position
Table E.3: Horizontal load cell – this was later adjusted according to the findings in Section 4.5
Table E.4: Horizontal position 1
Table E.5: Horizontal position 2
Table E.6: Angle at rotation point 1
Table E.7: Angle at rotation point 2
Table E.8: Vertical amplifier

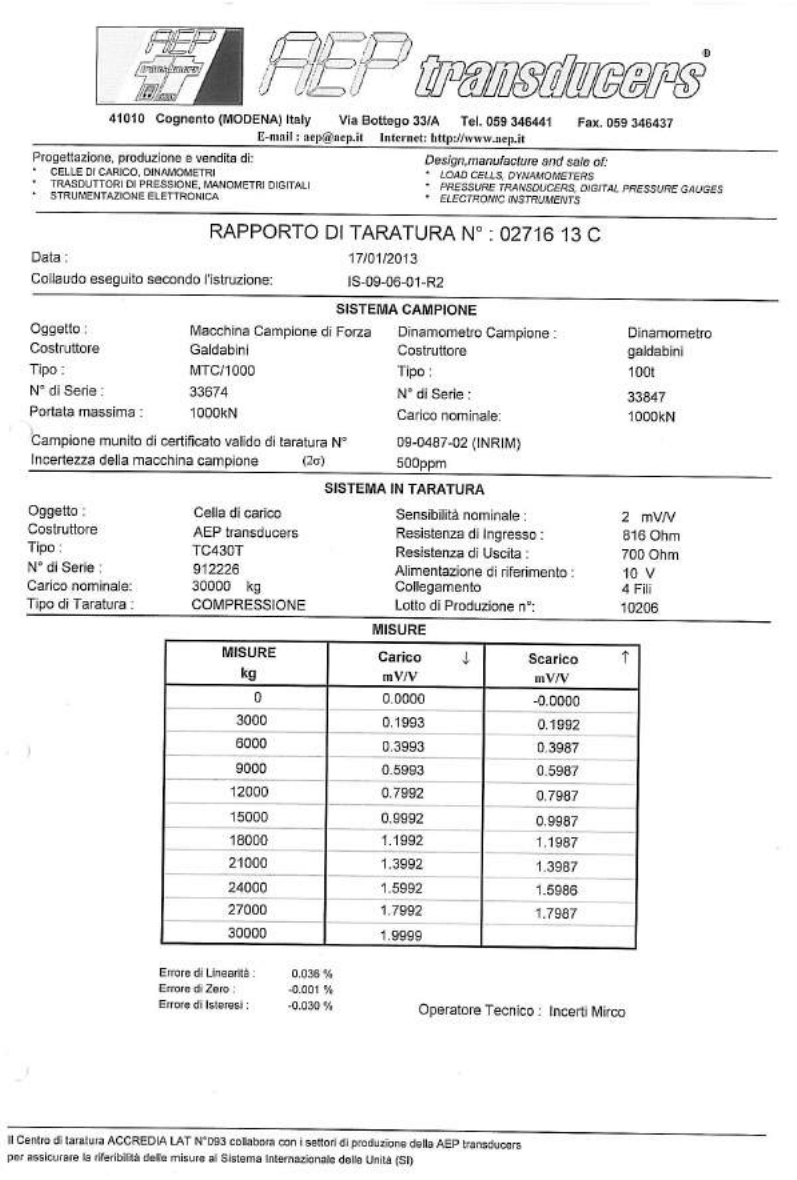

AEP transducers®

41010 Cognento (MODENA) Italy Via Bottego 33/A Tel. 059 346441 Fax. 059 346437
E-mail : aep@aep.it Internet: http://www.aep.it

Progettazione, produzione e vendita di:
* CELLE DI CARICO, DINAMOMETRI
* TRASDUTTORI DI PRESSIONE, MANOMETRI DIGITALI
* STRUMENTAZIONE ELETTRONICA

Design,manufacture and sale of:
* *LOAD CELLS, DYNAMOMETERS*
* *PRESSURE TRANSDUCERS, DIGITAL PRESSURE GAUGES*
* *ELECTRONIC INSTRUMENTS*

RAPPORTO DI TARATURA N° : 02716 13 C

Data : 17/01/2013

Collaudo eseguito secondo l'istruzione: IS-09-06-01-R2

SISTEMA CAMPIONE

Oggetto :	Macchina Campione di Forza	Dinamometro Campione :	Dinamometro
Costruttore	Galdabini	Costruttore	galdabini
Tipo :	MTC/1000	Tipo :	100t
N° di Serie :	33674	N° di Serie :	33847
Portata massima :	1000kN	Carico nominale:	1000kN

Campione munito di certificato valido di taratura N° 09-0487-02 (INRIM)
Incertezza della macchina campione (2σ) 500ppm

SISTEMA IN TARATURA

Oggetto :	Cella di carico	Sensibilità nominale :	2 mV/V
Costruttore	AEP transducers	Resistenza di Ingresso :	816 Ohm
Tipo :	TC430T	Resistenza di Uscita :	700 Ohm
N° di Serie :	912226	Alimentazione di riferimento :	10 V
Carico nominale:	30000 kg	Collegamento	4 Fili
Tipo di Taratura :	COMPRESSIONE	Lotto di Produzione n°:	10206

MISURE

MISURE kg	Carico ↓ mV/V	Scarico ↑ mV/V
0	0.0000	-0.0000
3000	0.1993	0.1992
6000	0.3993	0.3987
9000	0.5993	0.5987
12000	0.7992	0.7987
15000	0.9992	0.9987
18000	1.1992	1.1987
21000	1.3992	1.3987
24000	1.5992	1.5986
27000	1.7992	1.7987
30000	1.9999	

Errore di Linearità : 0.036 %
Errore di Zero : -0.001 %
Errore di Isteresi : -0.030 %

Operatore Tecnico : Incerti Mirco

Il Centro di taratura ACCREDIA LAT N°093 collabora con i settori di produzione della AEP transducers per assicurare la riferibilità delle misure al Sistema Internazionale delle Unità (SI)

Figure E.1: *Calibration data for vertical load cell*

Kalibrering vertikalposisjon

Dato: 19.11.2012

Målt mm	Forskøvet mm	Målt V
418	-229	-9.00
469	-178	-7.00
519	-128	-5.00
570	-77	-3.00
621	-26	-1.00
647	0	0.00
673	26	1.00
724	77	3.00
775	128	5.00
825	178	7.00
877	230	9.00

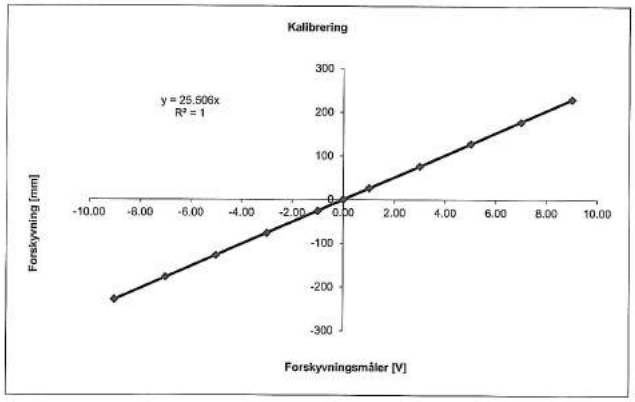

Faktor: 10V = 255.06mm

Figure E.2: *Calibration data for vertical position.*

Kalibrering horisontal lastcelle

Dato: 11.03.2013
Ref Celle: NKT584 (300kN)

Ønsket	Referanse Lastcelle	Målt	Korrigert 0.9856	
	0.7	0.9	0.9	0.98561009
10	10.1	10.1	10.0	
30	20.5	20.7	20.4	
30	30.9	31.4	30.9	
40	41.4	42.2	41.6	
50	51.8	52.8	52.0	
75	78.1	79.7	78.6	
100	104.5	106.3	104.8	
125	130.7	132.7	130.8	
150	157.2	159.6	157.3	
175	183.8	186.3	183.6	
190	199.9	202.4	199.5	

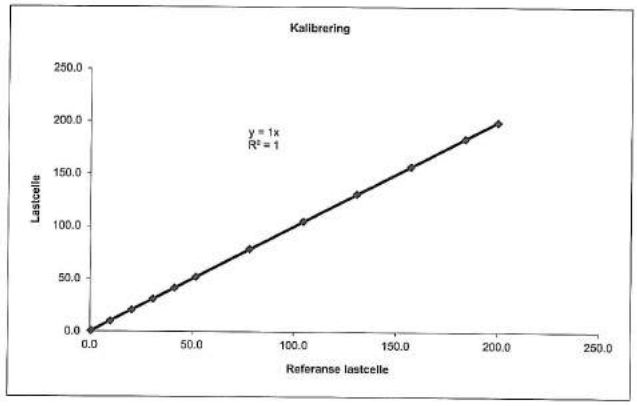

Faktor: 10V = 325.2kN

Figure E.3: *Calibration data for horizontal load cell.*

Kalibrering horisontalposisjon X1

Dato: 19.11.2012

Målt mm	Forskøvet mm	Målt V
579	-138	-9.00
549	-108	-7.01
519	-78	-5.00
488	-47	-3.00
457	-16	-1.00
441	0	0.00
426	15	1.00
395	46	3.00
363	78	5.01
332	109	7.01
302	139	9.01

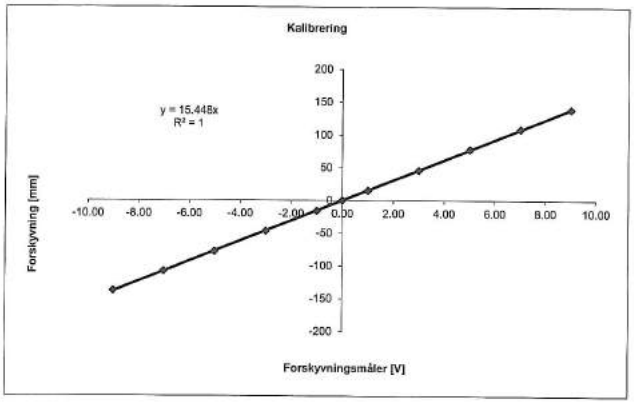

Faktor: 10V = 154.48mm

Figure E.4: *Calibration data for horizontal position 1.*

Kalibrering horisontalposisjon X2

Dato: 19.11.2012

Målt mm	Forskøvet mm	Målt V
543	-140	-9.01
512	-109	-7.01
481	-78	-5.00
450	-47	-3.00
419	-16	-1.00
403	0	0.00
388	15	1.01
357	46	3.01
325	78	5.02
295	108	7.01
264	139	9.02

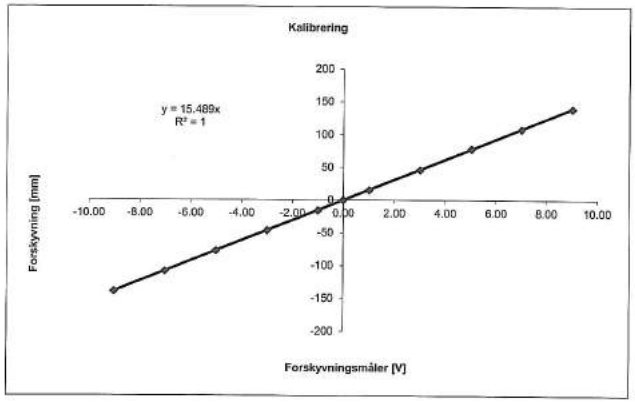

Faktor: 10V = 154.89mm

Figure E.5: *Calibration data for horizontal position 2.*

Kalibrering Vinkel X1

Dato: 19.11.2012

Målt Deg	Målt V
-15.8	-1.02
-1.9	-0.19
4.6	0.21
11.1	0.61
17.5	0.99
23.6	1.36
28.6	1.67
32.9	1.92

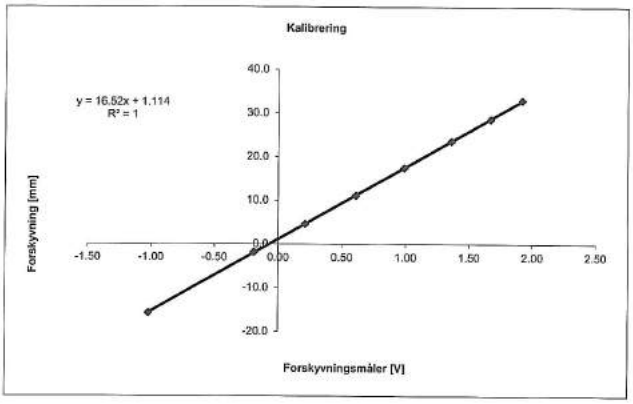

Faktor: 1V = 16.52Deg

Figure E.6: *Calibration data for angle at rotation point 1.*

Kalibrering Vinkel X2

Dato: 19.11.2012

Målt Deg	Målt V
-12.2	-0.75
-1.9	-0.13
3.2	0.18
8.4	0.49
13.6	0.81
18.7	1.11
23.0	1.37
30.3	1.80

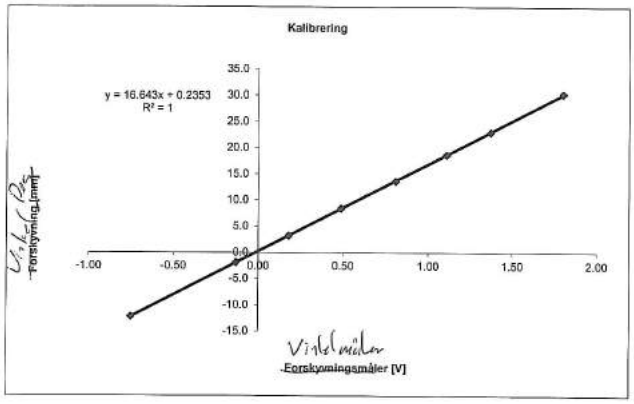

Faktor: 1V = 16.64Deg

Figure E.7: *Calibration data for angle at rotation point 2.*

Kalibrering vertikal forsterker

Dato: 18.03.2013

Referanse mV/V	Målt V	Korrigert
-2.00	-10.394	-10.457
-0.50	-2.542	-2.605
-0.20	-0.977	-1.040
-0.10	-0.456	-0.519
-0.05	-0.195	-0.258
0.00	0.063	0.000
0.05	0.325	0.262
0.10	0.586	0.523
0.20	1.107	1.044
0.50	2.672	2.609
2.00	10.508	10.445

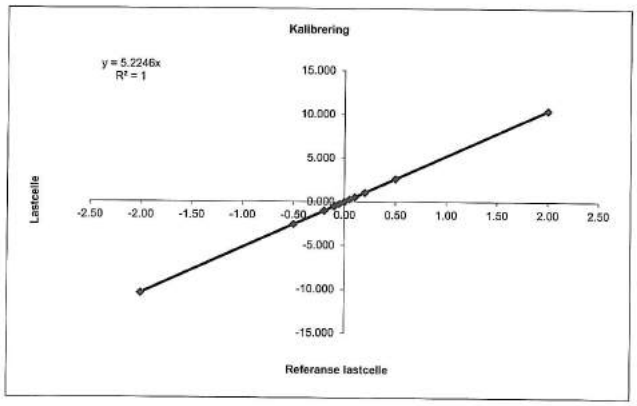

Faktor: 2mv/V celle ganges med 0.957 for maks utslag

50 kN: 10V= 47.85kN

300kN: 10V= 287.1kN

Figure E.8: *Calibration data for vertical amplifier.*

Appendix F

Drawings for stretch-bending rig

Presented herein are the drawings for the modification of the stretch-bending rig. These drawings are made by Olav Fismen. A list of the drawings, eight in total, are presented below:

Fig. F.1: Overview of stretch-bending rig
Fig. F.2: Pipe with connections
Fig. F.3: Pipe with flanges
Fig. F.4: Flanges
Fig. F.5: Forks
Fig. F.6: Connecting steel piece
Fig. F.7: Axle connecting steel piece and fork
Fig. F.8: System for applying pressure

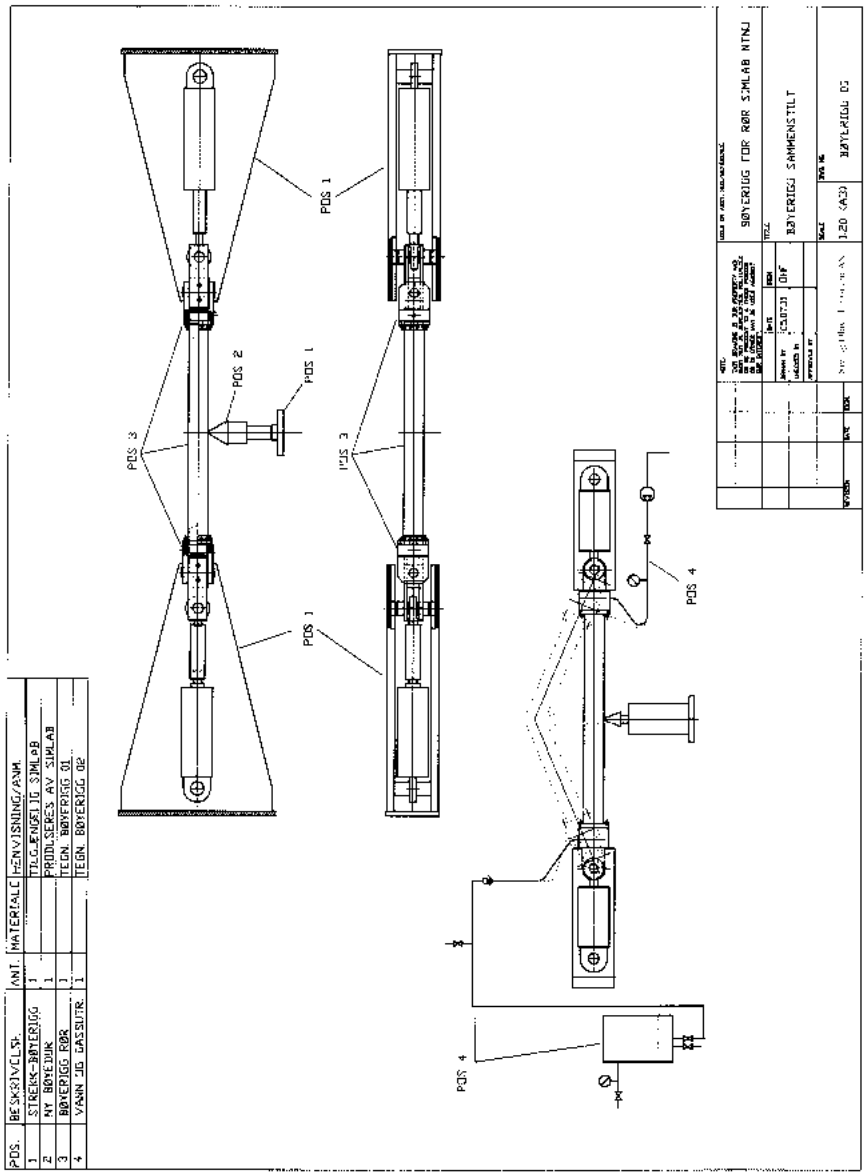

Figure F.1: *Overview of stretch-bending rig.*

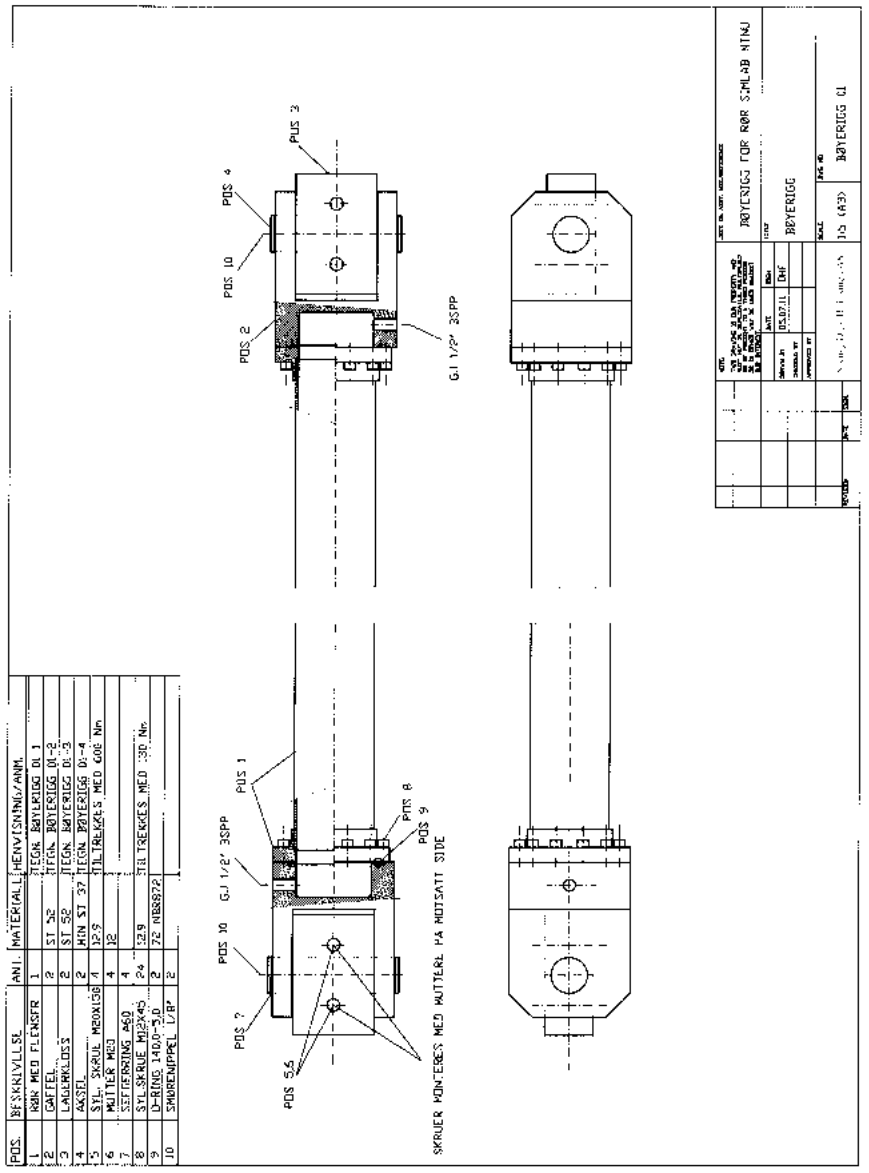

Figure F.2: *Pipe with connections.*

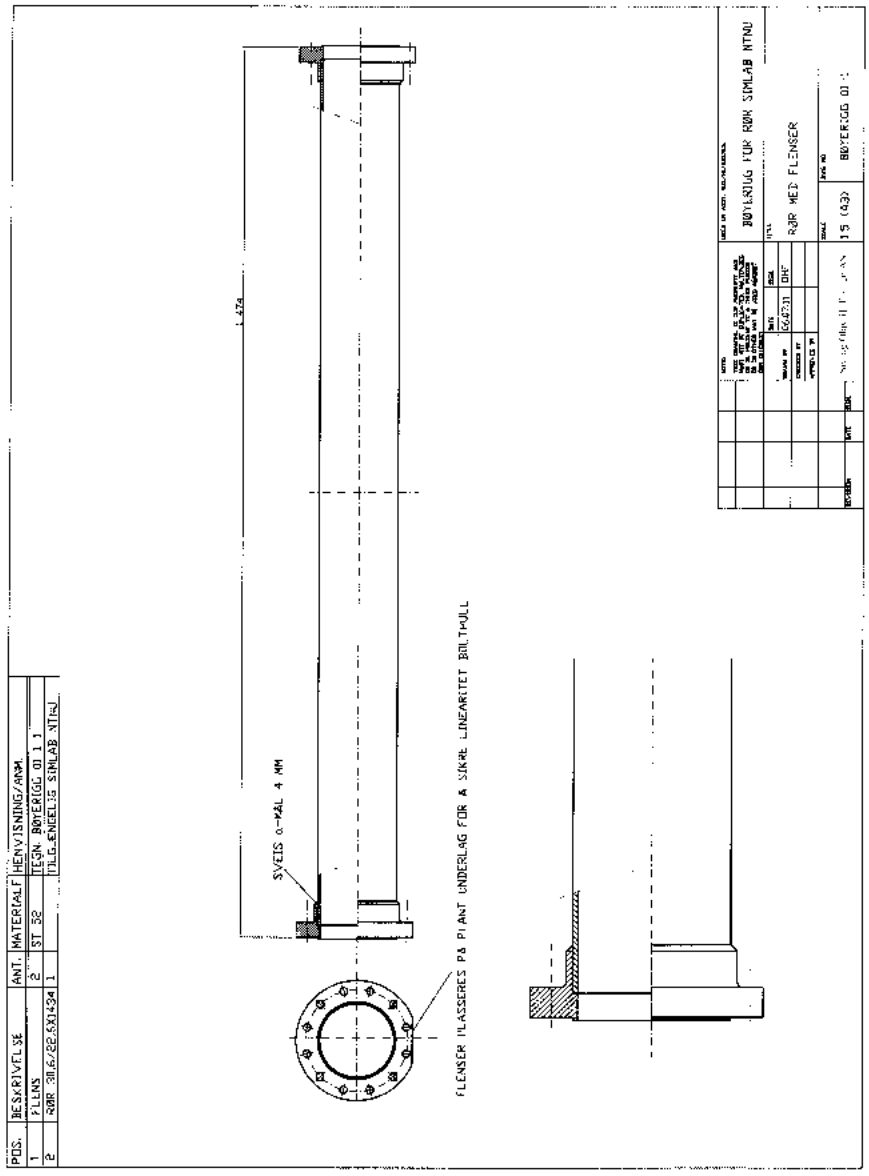

Figure F.3: *Pipe with flanges.*

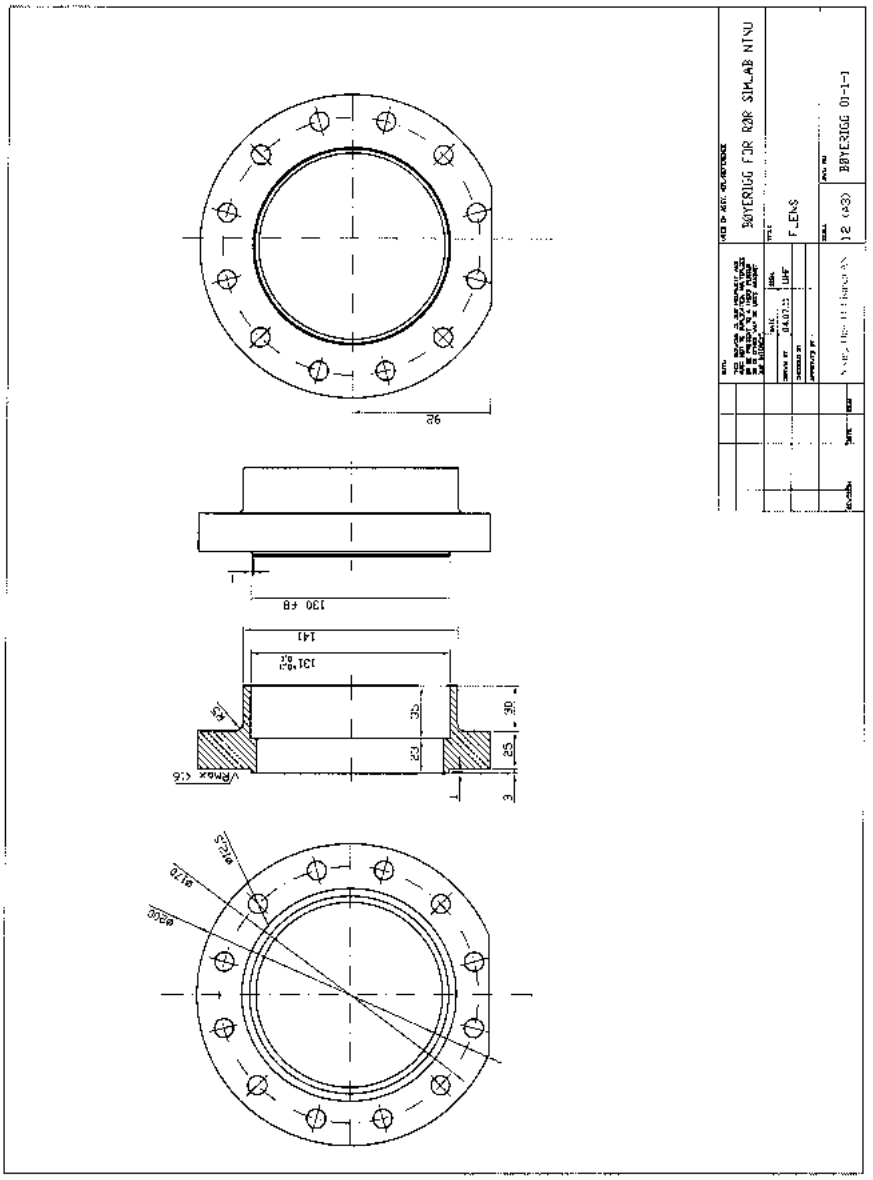

Figure F.4: *Flanges.*

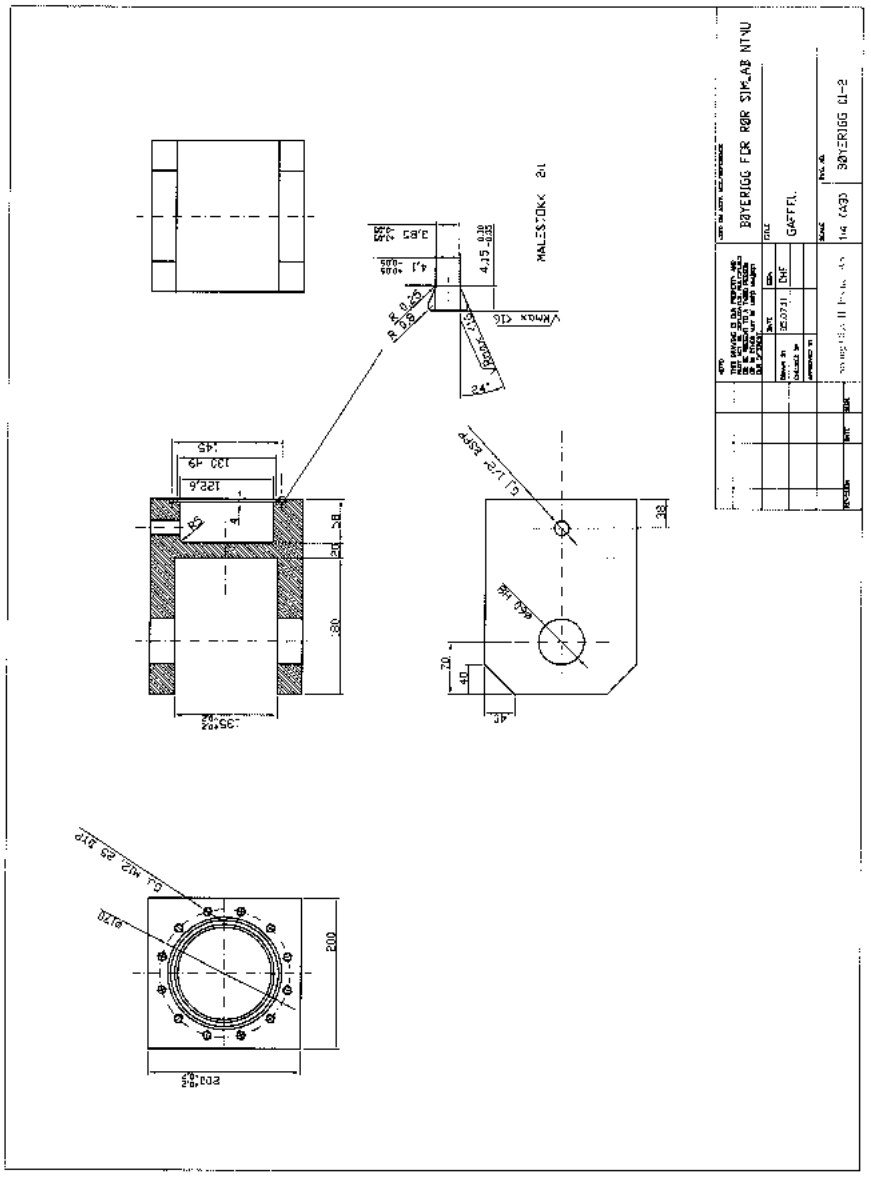

Figure F.5: *Forks.*

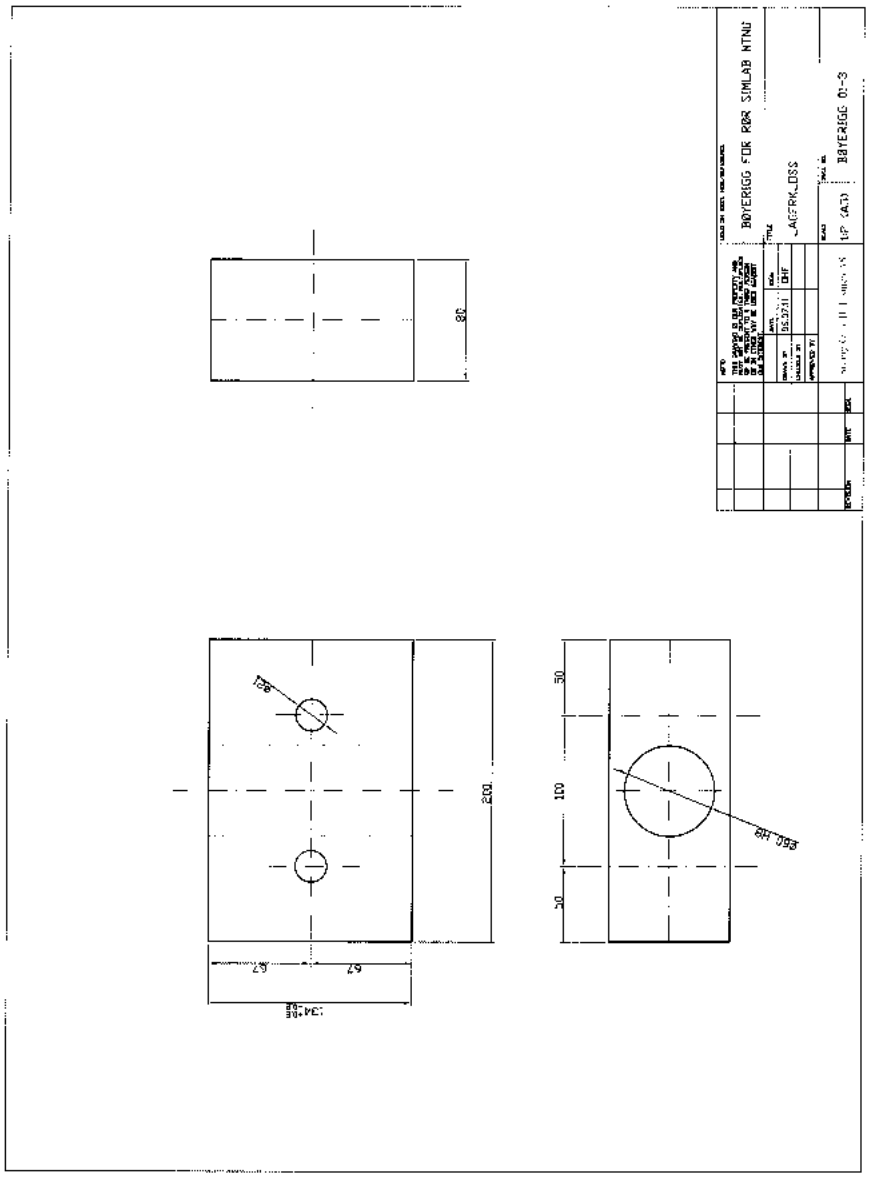

Figure F.6: *Connecting steel piece.*

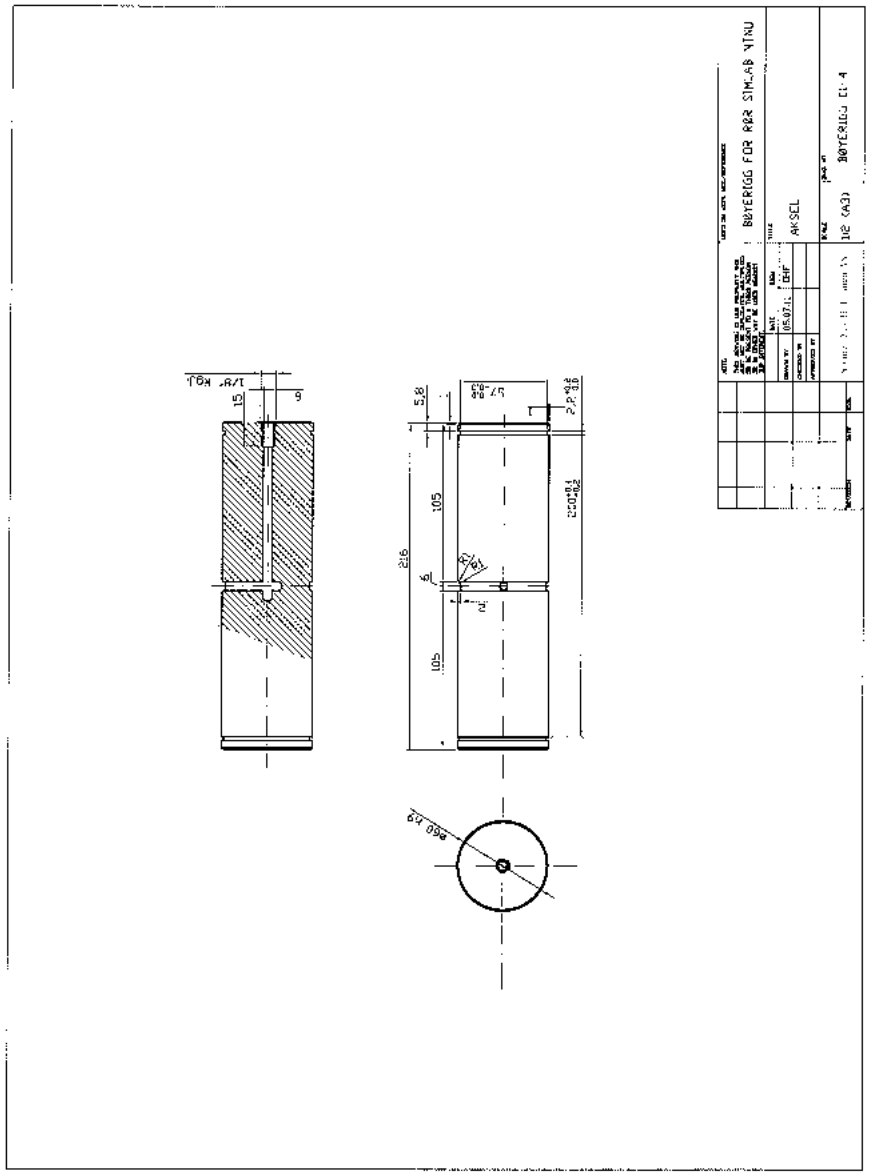

Figure F.7: *Axle connecting steel piece and fork.*

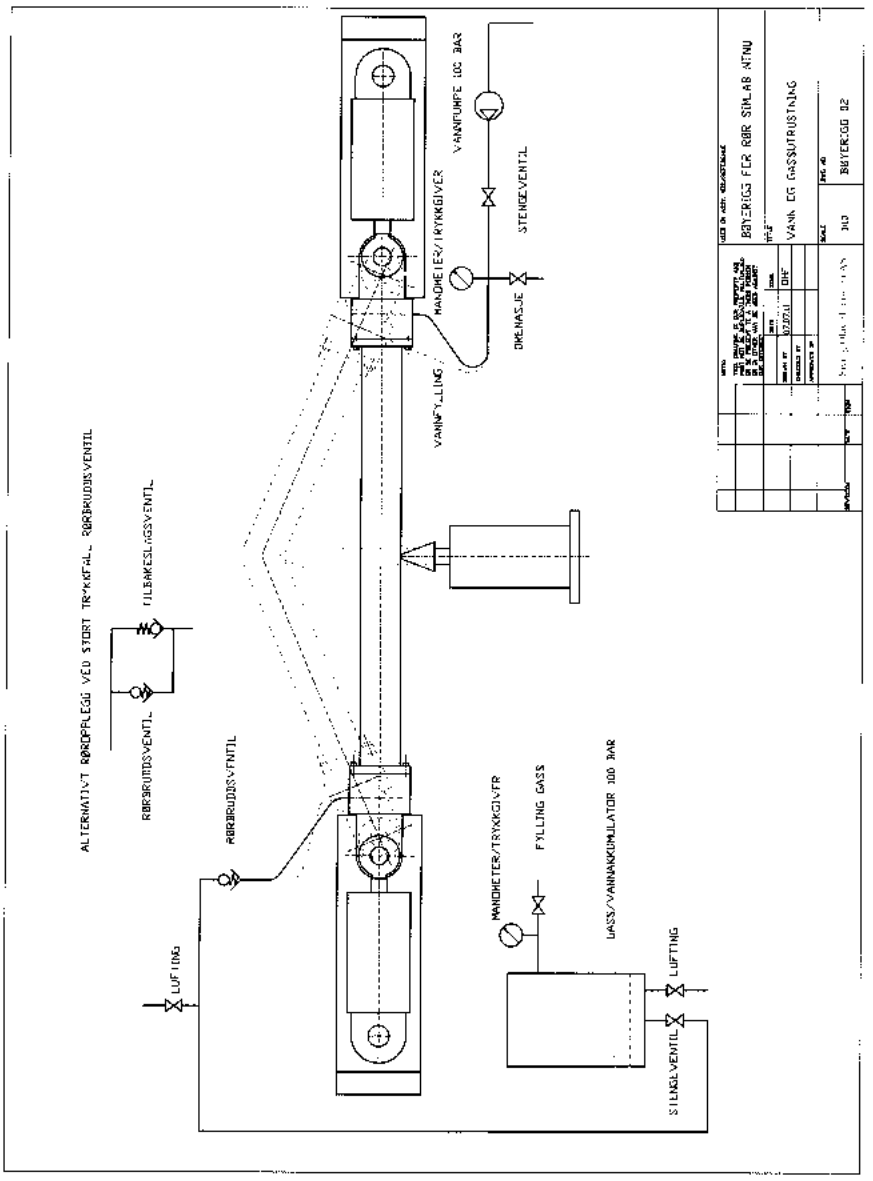

Figure F.8: *System for applying pressure.*

Index

ALE, 200

barrelling, 51
Bauschinger effect, 49, 53
buckling, 51

CEN, 18
component tests, 61
    impact, 67
    impact, water-filled, 80
    overview, 65
    quasi static, 88
    stretching, 67
    stretching and bending, 94
constitutive relation, 157
    calibration, 161
    constants, 164
    Johnson-Cook, 157
contact
    penalty, 172
    pinball, 227

deformation capacity, 20
deformation gradient, 154
denting, 10, 73, 173
Det Norske Veritas, 9
    DNV-OS-F101, 10
    DNV-OSS-301, 10
    DNV-RP-F111, 10
    Offshore service specifications, 10
    Offshore standards, 10
    Recommended practices, 10
deviatoric stress, *see* stress
diameter reduction measurement, 38
dislocation, 52
DNV, *see* Det Norske Veritas
ductile-to-brittle transition, 51

EDS, 34, 123
energy-dispersive X-ray spectroscopy, *see* EDS
equation of state, 204
equivalent static load, 19, 92
Eulerian coordinates, 200
Euler equations, 203
    modified, 204
Eurocode, 18
    NS-EN 1991-1-7, 19
    NS-EN 1993-4-3, 19
Europlexus, 199

FLSR algorithm, **218**, 229
FLSW algorithm, 220
fluid-structure interaction, *see* FSI

fluid-structure interface, 199
fracture
    cleavage, 126
    ductile, 128
    ductile-to-brittle, 149
fracture criteria, 159
    calibration, 164
    Cockcroft-Latham, 160
    constants, 166
    Extended Cockcroft-Latham, 160
    Johnson-Cook, 159
fracture surface
    tensile specimens, 40
fracture strain, 48
    abolute, 150
    average, 41
    relative, 150
FSA algorithm, **208**, 228
FSI, **199**, 226
    ALE, 231
    embedded, 234
    Lagrangian, 230
    results, 230
    SPH, 238

global displacement, 75

hard impact, *see* impact
hardening
    isotropic, 48
    kinematic, 48
homogeneity
    of material, 41
hooking, 11

impact
    against pipeline, 10
    hard impact, 19
    soft impact, 19
impact simulations, 174
initial simulations, 170
    results, 173
    setup, 170
ISO, 18
isotropic hardening, *see* hardening
isotropy
    of material, 41

kicking machine, 63
kinematic hardening, *see* hardening
Kvitebjørn accident, 1

Lagrangian coordinates, 200
local displacement, 75

Mannesmann effect, 33
material inspection certificate, 305
material model, *see* constitutive relation
material tests, 33
    dynamic uniaxial, 44
    notched compression-tension, 51
    notched tension, 42
    quasi-static notched, 42
    quasi-static uniaxial, 37
    reversed loading, 48
mesh sensitivity, 179
most critical element, 180

NORSOK, 14
    N-004, 14

overall permanent displacement, 27

peak true stress, 41
pendulum accelerator, 63
pinball method, 227
pipe
    production of, 33

pipeline impact, *see* impact
Ptil, 1
pull-over, 10

rate-of-deformation tensor, 154
    corotational, 154
rezoning, 213

scanning electron microscopy, *see* SEM
SEM, 34, 123
SHTB, *see* split Hopkinson bar
soft impact, *see* impact
SPH, 229
split Hopkinson bar, 44
Standard Norge, 18
strain wave, 45
stress
    deviatoric, 156
    equivalent, 155
    von Mises, 155
stress tensor
    Cauchy, 154
    corotational, 154
stretch bending rig, 65
stretch simulations, 175
submodel, 185

Tenaris, 34, 305
true strain, 39
true stress, 39

ultimate tensile strength, 34
    average, 41
unit cell, 139, 243
    mesh, 246
    procedure, 248
    results, 249
    strain, 246
    stress, 245

wave propagation velocity, 45

yield stress, 34
yield stress
    average, 40
Young's modulus, 34
    corrected, 46

DEPARTMENT OF STRUCTURAL ENGINEERING
NORWEGIAN UNIVERSITY OF SCIENCE AND TECHNOLOGY

N–7491 TRONDHEIM, NORWAY
Telephone: +47 73 59 47 00 Telefax: +47 73 59 47 01

"Reliability Analysis of Structural Systems using Nonlinear Finite Element Methods",
C. A. Holm, 1990:23, ISBN 82-7119-178-0.

"Uniform Stratified Flow Interaction with a Submerged Horizontal Cylinder",
Ø. Arntsen, 1990:32, ISBN 82-7119-188-8.

"Large Displacement Analysis of Flexible and Rigid Systems Considering Displacement-Dependent Loads and Nonlinear Constraints",
K. M. Mathisen, 1990:33, ISBN 82-7119-189-6.

"Solid Mechanics and Material Models including Large Deformations",
E. Levold, 1990:56, ISBN 82-7119-214-0, ISSN 0802-3271.

"Inelastic Deformation Capacity of Flexurally-Loaded Aluminium Alloy Structures",
T. Welo, 1990:62, ISBN 82-7119-220-5, ISSN 0802-3271.

"Visualization of Results from Mechanical Engineering Analysis",
K. Aamnes, 1990:63, ISBN 82-7119-221-3, ISSN 0802-3271.

"Object-Oriented Product Modeling for Structural Design",
S. I. Dale, 1991:6, ISBN 82-7119-258-2, ISSN 0802-3271.

"Parallel Techniques for Solving Finite Element Problems on Transputer Networks",
T. H. Hansen, 1991:19, ISBN 82-7119-273-6, ISSN 0802-3271.

"Statistical Description and Estimation of Ocean Drift Ice Environments",
R. Korsnes, 1991:24, ISBN 82-7119-278-7, ISSN 0802-3271.

“Properties of concrete related to fatigue damage: with emphasis on high strength concrete”,
G. Petkovic, 1991:35, ISBN 82-7119-290-6, ISSN 0802-3271.

"Turbidity Current Modelling",
B. Brørs, 1991:38, ISBN 82-7119-293-0, ISSN 0802-3271.

"Zero-Slump Concrete: Rheology, Degree of Compaction and Strength. Effects of Fillers as Part Cement-Replacement",
C. Sørensen, 1992:8, ISBN 82-7119-357-0, ISSN 0802-3271.

"Nonlinear Analysis of Reinforced Concrete Structures Exposed to Transient Loading",
K. V. Høiseth, 1992:15, ISBN 82-7119-364-3, ISSN 0802-3271.

"Finite Element Formulations and Solution Algorithms for Buckling and Collapse Analysis of Thin Shells",
R. O. Bjærum, 1992:30, ISBN 82-7119-380-5, ISSN 0802-3271.

"Response Statistics of Nonlinear Dynamic Systems",
J. M. Johnsen, 1992:42, ISBN 82-7119-393-7, ISSN 0802-3271.

"Digital Models in Engineering. A Study on why and how engineers build and operate digital models for decisison support",
J. Høyte, 1992:75, ISBN 82-7119-429-1, ISSN 0802-3271.

"Sparse Solution of Finite Element Equations",
A. C. Damhaug, 1992:76, ISBN 82-7119-430-5, ISSN 0802-3271.

"Some Aspects of Floating Ice Related to Sea Surface Operations in the Barents Sea",
S. Løset, 1992:95, ISBN 82-7119-452-6, ISSN 0802-3271.

"Modelling of Cyclic Plasticity with Application to Steel and Aluminium Structures",
O. S. Hopperstad, 1993:7, ISBN 82-7119-461-5, ISSN 0802-3271.

"The Free Formulation: Linear Theory and Extensions with Applications to Tetrahedral Elements
with Rotational Freedoms",
G. Skeie, 1993:17, ISBN 82-7119-472-0, ISSN 0802-3271.

"Høyfast betongs motstand mot piggdekkslitasje. Analyse av resultater fra prøving i Veisliter'n",
T. Tveter, 1993:62, ISBN 82-7119-522-0, ISSN 0802-3271.

"A Nonlinear Finite Element Based on Free Formulation Theory for Analysis of Sandwich Structures",
O. Aamlid, 1993:72, ISBN 82-7119-534-4, ISSN 0802-3271.

"The Effect of Curing Temperature and Silica Fume on Chloride Migration and Pore Structure of High Strength Concrete",
C. J. Hauck, 1993:90, ISBN 82-7119-553-0, ISSN 0802-3271.

"Failure of Concrete under Compressive Strain Gradients",
G. Markeset, 1993:110, ISBN 82-7119-575-1, ISSN 0802-3271.

"An experimental study of internal tidal amphidromes in Vestfjorden",
J. H. Nilsen, 1994:39, ISBN 82-7119-640-5, ISSN 0802-3271.

"Structural analysis of oil wells with emphasis on conductor design",
H. Larsen, 1994:46, ISBN 82-7119-648-0, ISSN 0802-3271.

"Adaptive methods for non-linear finite element analysis of shell structures",
K. M. Okstad, 1994:66, ISBN 82-7119-670-7, ISSN 0802-3271.

"On constitutive modelling in nonlinear analysis of concrete structures",
O. Fyrileiv, 1994:115, ISBN 82-7119-725-8, ISSN 0802-3271.

"Fluctuating wind load and response of a line-like engineering structure with emphasis on motion-induced wind forces",
J. Bogunovic Jakobsen, 1995:62, ISBN 82-7119-809-2, ISSN 0802-3271.

"An experimental study of beam-columns subjected to combined torsion, bending and axial actions",
A. Aalberg, 1995:66, ISBN 82-7119-813-0, ISSN 0802-3271.

"Scaling and cracking in unsealed freeze/thaw testing of Portland cement and silica fume concretes",
S. Jacobsen, 1995:101, ISBN 82-7119-851-3, ISSN 0802-3271.

"Damping of water waves by submerged vegetation. A case study of laminaria hyperborea",
A. M. Dubi, 1995:108, ISBN 82-7119-859-9, ISSN 0802-3271.

"The dynamics of a slope current in the Barents Sea",
Sheng Li, 1995:109, ISBN 82-7119-860-2, ISSN 0802-3271.

"Modellering av delmaterialenes betydning for betongens konsistens",
Ernst Mørtsell, 1996:12, ISBN 82-7119-894-7, ISSN 0802-3271.

"Bending of thin-walled aluminium extrusions",
Birgit Søvik Opheim, 1996:60, ISBN 82-7119-947-1, ISSN 0802-3271.

"Material modelling of aluminium for crashworthiness analysis",
Torodd Berstad, 1996:89, ISBN 82-7119-980-3, ISSN 0802-3271.

"Estimation of structural parameters from response measurements on submerged floating tunnels",
Rolf Magne Larssen, 1996:119, ISBN 82-471-0014-2, ISSN 0802-3271.

“Numerical modelling of plain and reinforced concrete by damage mechanics”,
Mario A. Polanco-Loria, 1997:20, ISBN 82-471-0049-5, ISSN 0802-3271.

“Nonlinear random vibrations - numerical analysis by path integration methods”,
Vibeke Moe, 1997:26, ISBN 82-471-0056-8, ISSN 0802-3271.

“Numerical prediction of vortex-induced vibration by the finite element method”,
Joar Martin Dalheim, 1997:63, ISBN 82-471-0096-7, ISSN 0802-3271.

“Time domain calculations of buffeting response for wind sensitive structures”,
Ketil Aas-Jakobsen, 1997:148, ISBN 82-471-0189-0, ISSN 0802-3271.

"A numerical study of flow about fixed and flexibly mounted circular cylinders",
Trond Stokka Meling, 1998:48, ISBN 82-471-0244-7, ISSN 0802-3271.

“Estimation of chloride penetration into concrete bridges in coastal areas”,
Per Egil Steen, 1998:89, ISBN 82-471-0290-0, ISSN 0802-3271.

“Stress-resultant material models for reinforced concrete plates and shells”,
Jan Arve Øverli, 1998:95, ISBN 82-471-0297-8, ISSN 0802-3271.

“Chloride binding in concrete. Effect of surrounding environment and concrete composition”,
Claus Kenneth Larsen, 1998:101, ISBN 82-471-0337-0, ISSN 0802-3271.

“Rotational capacity of aluminium alloy beams”,
Lars A. Moen, 1999:1, ISBN 82-471-0365-6, ISSN 0802-3271.

“Stretch Bending of Aluminium Extrusions”,
Arild H. Clausen, 1999:29, ISBN 82-471-0396-6, ISSN 0802-3271.

“Aluminium and Steel Beams under Concentrated Loading”,
Tore Tryland, 1999:30, ISBN 82-471-0397-4, ISSN 0802-3271.

"Engineering Models of Elastoplasticity and Fracture for Aluminium Alloys",
Odd-Geir Lademo, 1999:39, ISBN 82-471-0406-7, ISSN 0802-3271.

"Kapasitet og duktilitet av dybelforbindelser i trekonstruksjoner",
Jan Siem, 1999:46, ISBN 82-471-0414-8, ISSN 0802-3271.

“Etablering av distribuert ingeniørarbeid; Teknologiske og organisatoriske erfaringer fra en norsk ingeniørbedrift”,
Lars Line, 1999:52, ISBN 82-471-0420-2, ISSN 0802-3271.

“Estimation of Earthquake-Induced Response”,
Símon Ólafsson, 1999:73, ISBN 82-471-0443-1, ISSN 0802-3271.

“Coastal Concrete Bridges: Moisture State, Chloride Permeability and Aging Effects”
Ragnhild Holen Relling, 1999:74, ISBN 82-471-0445-8, ISSN 0802-3271.

”Capacity Assessment of Titanium Pipes Subjected to Bending and External Pressure”,
Arve Bjørset, 1999:100, ISBN 82-471-0473-3, ISSN 0802-3271.

“Validation of Numerical Collapse Behaviour of Thin-Walled Corrugated Panels”,
Håvar Ilstad, 1999:101, ISBN 82-471-0474-1, ISSN 0802-3271.

“Strength and Ductility of Welded Structures in Aluminium Alloys”,
Miroslaw Matusiak, 1999:113, ISBN 82-471-0487-3, ISSN 0802-3271.

“Thermal Dilation and Autogenous Deformation as Driving Forces to Self-Induced Stresses in High Performance Concrete”,
Øyvind Bjøntegaard, 1999:121, ISBN 82-7984-002-8, ISSN 0802-3271.

“Some Aspects of Ski Base Sliding Friction and Ski Base Structure”,
Dag Anders Moldestad, 1999:137, ISBN 82-7984-019-2, ISSN 0802-3271.

"Electrode reactions and corrosion resistance for steel in mortar and concrete",
Roy Antonsen, 2000:10, ISBN 82-7984-030-3, ISSN 0802-3271.

"Hydro-Physical Conditions in Kelp Forests and the Effect on Wave Damping and Dune Erosion. A case study on Laminaria Hyperborea",
Stig Magnar Løvås, 2000:28, ISBN 82-7984-050-8, ISSN 0802-3271.

"Random Vibration and the Path Integral Method",
Christian Skaug, 2000:39, ISBN 82-7984-061-3, ISSN 0802-3271.

"Buckling and geometrical nonlinear beam-type analyses of timber structures",
Trond Even Eggen, 2000:56, ISBN 82-7984-081-8, ISSN 0802-3271.

”Structural Crashworthiness of Aluminium Foam-Based Components”,
Arve Grønsund Hanssen, 2000:76, ISBN 82-7984-102-4, ISSN 0809-103X.

“Measurements and simulations of the consolidation in first-year sea ice ridges, and some aspects of mechanical behaviour”,
Knut V. Høyland, 2000:94, ISBN 82-7984-121-0, ISSN 0809-103X.

”Kinematics in Regular and Irregular Waves based on a Lagrangian Formulation”,
Svein Helge Gjøsund, 2000-86, ISBN 82-7984-112-1, ISSN 0809-103X.

”Self-Induced Cracking Problems in Hardening Concrete Structures”,
Daniela Bosnjak, 2000-121, ISBN 82-7984-151-2, ISSN 0809-103X.

"Ballistic Penetration and Perforation of Steel Plates",
Tore Børvik, 2000:124, ISBN 82-7984-154-7, ISSN 0809-103X.

"Freeze-Thaw resistance of Concrete. Effect of: Curing Conditions, Moisture Exchange and Materials",
Terje Finnerup Rønning, 2001:14, ISBN 82-7984-165-2, ISSN 0809-103X

"Structural behaviour of post tensioned concrete structures. Flat slab. Slabs on ground",
Steinar Trygstad, 2001:52, ISBN 82-471-5314-9, ISSN 0809-103X.

"Slipforming of Vertical Concrete Structures. Friction between concrete and slipform panel",
Kjell Tore Fosså, 2001:61, ISBN 82-471-5325-4, ISSN 0809-103X.

"Some numerical methods for the simulation of laminar and turbulent incompressible flows",
Jens Holmen, 2002:6, ISBN 82-471-5396-3, ISSN 0809-103X.

“Improved Fatigue Performance of Threaded Drillstring Connections by Cold Rolling”, Steinar Kristoffersen, 2002:11, ISBN: 82-421-5402-1, ISSN 0809-103X.

"Deformations in Concrete Cantilever Bridges: Observations and Theoretical Modelling",
Peter F. Takâcs, 2002:23, ISBN 82-471-5415-3, ISSN 0809-103X.

"Stiffened aluminium plates subjected to impact loading",
Hilde Giæver Hildrum, 2002:69, ISBN 82-471-5467-6, ISSN 0809-103X.

"Full- and model scale study of wind effects on a medium-rise building in a built up area",
Jónas Thór Snæbjørnsson, 2002:95, ISBN82-471-5495-1, ISSN 0809-103X.

“Evaluation of Concepts for Loading of Hydrocarbons in Ice-infested water”,
Arnor Jensen, 2002:114, ISBN 82-417-5506-0, ISSN 0809-103X.

”Numerical and Physical Modelling of Oil Spreading in Broken Ice”,
Janne K. Økland Gjøsteen, 2002:130, ISBN 82-471-5523-0, ISSN 0809-103X.

”Diagnosis and protection of corroding steel in concrete”,
Franz Pruckner, 20002:140, ISBN 82-471-5555-4, ISSN 0809-103X.

“Tensile and Compressive Creep of Young Concrete: Testing and Modelling”,
Dawood Atrushi, 2003:17, ISBN 82-471-5565-6, ISSN 0809-103X.

“Rheology of Particle Suspensions. Fresh Concrete, Mortar and Cement Paste with Various Types of Lignosulfonates”,
Jon Elvar Wallevik, 2003:18, ISBN 82-471-5566-4, ISSN 0809-103X.

“Oblique Loading of Aluminium Crash Components”,
Aase Reyes, 2003:15, ISBN 82-471-5562-1, ISSN 0809-103X.

“Utilization of Ethiopian Natural Pozzolans”,
Surafel Ketema Desta, 2003:26, ISSN 82-471-5574-5, ISSN:0809-103X.

“Behaviour and strength prediction of reinforced concrete structures with discontinuity regions”, Helge Brå, 2004:11, ISBN 82-471-6222-9, ISSN 1503-8181.

“High-strength steel plates subjected to projectile impact. An experimental and numerical study”, Sumita Dey, 2004:38, ISBN 82-471-6282-2 (printed version), ISBN 82-471-6281-4 (electronic version), ISSN 1503-8181.

“Alkali-reactive and inert fillers in concrete. Rheology of fresh mixtures and expansive reactions.”
Bård M. Pedersen, 2004:92, ISBN 82-471-6401-9 (printed version), ISBN 82-471-6400-0 (electronic version), ISSN 1503-8181.

“On the Shear Capacity of Steel Girders with Large Web Openings”.
Nils Christian Hagen, 2005:9 ISBN 82-471-6878-2 (printed version), ISBN 82-471-6877-4 (electronic version), ISSN 1503-8181.

”Behaviour of aluminium extrusions subjected to axial loading”.
Østen Jensen, 2005:7, ISBN 82-471-6873-1 (printed version), ISBN 82-471-6872-3 (electronic version), ISSN 1503-8181.

”Thermal Aspects of corrosion of Steel in Concrete”.
Jan-Magnus Østvik, 2005:5, ISBN 82-471-6869-3 (printed version), ISBN 82-471-6868 (electronic version), ISSN 1503-8181.

”Mechanical and adaptive behaviour of bone in relation to hip replacement.” A study of bone remodelling and bone grafting.
Sébastien Muller, 2005:34, ISBN 82-471-6933-9 (printed version), ISBN 82-471-6932-0 (electronic version), ISSN 1503-8181.

“Analysis of geometrical nonlinearities with applications to timber structures”.
Lars Wollebæk, 2005:74, ISBN 82-471-7050-5 (printed version), ISBN 82-471-7019-1 (electronic version), ISSN 1503-8181.

“Pedestrian induced lateral vibrations of slender footbridges”,
Anders Rönnquist, 2005:102, ISBN 82-471-7082-5 (printed version), ISBN 82-471-7081-7 (electronic version), ISSN 1503-8181.

“Initial Strength Development of Fly Ash and Limestone Blended Cements at Various Temperatures Predicted by Ultrasonic Pulse Velocity”,
Tom Ivar Fredvik, 2005:112, ISBN 82-471-7105-8 (printed version), ISBN 82-471-7103-1 (electronic version), ISSN 1503-8181.

“Behaviour and modelling of thin-walled cast components”,
Cato Dørum, 2005:128, ISBN 82-471-7140-6 (printed version), ISBN 82-471-7139-2 (electronic version), ISSN 1503-8181.

“Behaviour and modelling of selfpiercing riveted connections”,
Raffaele Porcaro, 2005:165, ISBN 82-471-7219-4 (printed version), ISBN 82-471-7218-6 (electronic version), ISSN 1503-8181.

”Behaviour and Modelling og Aluminium Plates subjected to Compressive Load”,
Lars Rønning, 2005:154, ISBN 82-471-7169-1 (printed version), ISBN 82-471-7195-3 (electronic version), ISSN 1503-8181.

”Bumper beam-longitudinal system subjected to offset impact loading”,
Satyanarayana Kokkula, 2005:193, ISBN 82-471-7280-1 (printed version), ISBN 82-471-7279-8 (electronic version), ISSN 1503-8181.

“Control of Chloride Penetration into Concrete Structures at Early Age”,
Guofei Liu, 2006:46, ISBN 82-471-7838-9 (printed version), ISBN 82-471-7837-0 (electronic version), ISSN 1503-8181.

“Modelling of Welded Thin-Walled Aluminium Structures”,
Ting Wang, 2006:78, ISBN 82-471-7907-5 (printed version), ISBN 82-471-7906-7 (electronic version), ISSN 1503-8181.

”Time-variant reliability of dynamic systems by importance sampling and probabilistic analysis of ice loads”,
Anna Ivanova Olsen, 2006:139, ISBN 82-471-8041-3 (printed version), ISBN 82-471-8040-5 (electronic version), ISSN 1503-8181.

“Fatigue life prediction of an aluminium alloy automotive component using finite element analysis of surface topography”.
Sigmund Kyrre Ås, 2006:25, ISBN 82-471-7791-9 (printed version), ISBN 82-471-7791-9 (electronic version), ISSN 1503-8181.

”Constitutive models of elastoplasticity and fracture for aluminium alloys under strain path change”,
Dasharatha Achani, 2006:76, ISBN 82-471-7903-2 (printed version), ISBN 82-471-7902-4 (electronic version), ISSN 1503-8181.

“Simulations of 2D dynamic brittle fracture by the Element-free Galerkin method and linear fracture mechanics”,
Tommy Karlsson, 2006:125, ISBN 82-471-8011-1 (printed version), ISBN 82-471-8010-3 (electronic version), ISSN 1503-8181.

“Penetration and Perforation of Granite Targets by Hard Projectiles”,
Chong Chiang Seah, 2006:188, ISBN 82-471-8150-9 (printed version), ISBN 82-471-8149-5 (electronic version), ISSN 1503-8181.

“Deformations, strain capacity and cracking of concrete in plastic and early hardening phases”,
Tor Arne Hammer, 2007:234, ISBN 978-82-471-5191-4 (printed version), ISBN 978-82-471-5207-2 (electronic version), ISSN 1503-8181.

“Crashworthiness of dual-phase high-strength steel: Material and Component behaviour”, Venkatapathi Tarigopula, 2007:230, ISBN 82-471-5076-4 (printed version), ISBN 82-471-5093-1 (electronic version), ISSN 1503-8181.

“Fibre reinforcement in load carrying concrete structures”,
Åse Lyslo Døssland, 2008:50, ISBN 978-82-471-6910-0 (printed version), ISBN 978-82-471-6924-7 (electronic version), ISSN 1503-8181.

“Low-velocity penetration of aluminium plates”,
Frode Grytten, 2008:46, ISBN 978-82-471-6826-4 (printed version), ISBN 978-82-471-6843-1 (electronic version), ISSN 1503-8181.

“Robustness studies of structures subjected to large deformations”,
Ørjan Fyllingen, 2008:24, ISBN 978-82-471-6339-9 (printed version), ISBN 978-82-471-6342-9 (electronic version), ISSN 1503-8181.

“Constitutive modelling of morsellised bone”,
Knut Birger Lunde, 2008:92, ISBN 978-82-471-7829-4 (printed version), ISBN 978-82-471-7832-4 (electronic version), ISSN 1503-8181.

“Experimental Investigations of Wind Loading on a Suspension Bridge Girder”,
Bjørn Isaksen, 2008:131, ISBN 978-82-471-8656-5 (printed version), ISBN 978-82-471-8673-2 (electronic version), ISSN 1503-8181.

“Cracking Risk of Concrete Structures in The Hardening Phase”,
Guomin Ji, 2008:198, ISBN 978-82-471-1079-9 (printed version), ISBN 978-82-471-1080-5 (electronic version), ISSN 1503-8181.

“Modelling and numerical analysis of the porcine and human mitral apparatus”,
Victorien Emile Prot, 2008:249, ISBN 978-82-471-1192-5 (printed version), ISBN 978-82-471-1193-2 (electronic version), ISSN 1503-8181.

“Strength analysis of net structures”,
Heidi Moe, 2009:48, ISBN 978-82-471-1468-1 (printed version), ISBN 978-82-471-1469-8 (electronic version), ISSN1503-8181.

“Numerical analysis of ductile fracture in surface cracked shells”,
Espen Berg, 2009:80, ISBN 978-82-471-1537-4 (printed version), ISBN 978-82-471-1538-1 (electronic version), ISSN 1503-8181.

“Subject specific finite element analysis of bone – for evaluation of the healing of a leg lengthening and evaluation of femoral stem design”,
Sune Hansborg Pettersen, 2009:99, ISBN 978-82-471-1579-4 (printed version), ISBN 978-82-471-1580-0 (electronic version), ISSN 1503-8181.

“Evaluation of fracture parameters for notched multi-layered structures”,
Lingyun Shang, 2009:137, ISBN 978-82-471-1662-3 (printed version), ISBN 978-82-471-1663-0 (electronic version), ISSN 1503-8181.

“Modelling of Dynamic Material Behaviour and Fracture of Aluminium Alloys for Structural Applications”
Yan Chen, 2009:69, ISBN 978-82-471-1515-2 (printed version), ISBN 978-82 471-1516-9 (electronic version), ISSN 1503-8181.

"Nanomechanics of polymer and composite particles"
Jianying He 2009:213, ISBN 978-82-471-1828-3 (printed version), ISBN 978-82-471-1829-0 (electronic version), ISSN 1503-8181.

"Mechanical properties of clear wood from Norway spruce"
Kristian Berbom Dahl 2009:250, ISBN 978-82-471-1911-2 (printed version) ISBN 978-82-471-1912-9 (electronic version), ISSN 1503-8181.

"Modeling of the degradation of TiB_2 mechanical properties by residual stresses and liquid Al penetration along grain boundaries"
Micol Pezzotta 2009:254, ISBN 978-82-471-1923-5 (printed version) ISBN 978-82-471-1924-2 (electronic version) ISSN 1503-8181.

"Effect of welding residual stress on fracture"
Xiabo Ren 2010:77, ISBN 978-82-471-2115-3 (printed version) ISBN 978-82-471-2116-0 (electronic version), ISSN 1503-8181.

"Pan-based carbon fiber as anode material in cathodic protection system for concrete structures"
Mahdi Chini 2010:122, ISBN 978-82-471-2210-5 (printed version) ISBN 978-82-471-2213-6 (electronic version), ISSN 1503-8181.

"Structural Behaviour of deteriorated and retrofitted concrete structures"
Irina Vasililjeva Sæther 2010:171, ISBN 978-82-471-2315-7 (printed version) ISBN 978-82-471-2316-4 (electronic version) ISSN 1503-8181.

"Prediction of local snow loads on roofs"
Vivian Meløysund 2010:247, ISBN 978-82-471-2490-1 (printed version) ISBN 978-82-471-2491-8 (electronic version) ISSN 1503-8181.

"Behaviour and modelling of polymers for crash applications"
Virgile Delhaye 2010:251, ISBN 978-82-471-2501-4 (printed version) ISBN 978-82-471-2502-1 (electronic version) ISSN 1503-8181.

"Blended cement with reducted CO_2 emission – Utilizing the Fly Ash-Limestone Synergy",
Klaartje De Weerdt 2011:32, ISBN 978-82-471-2584-7 (printed version) ISBN 978-82-471-2584-4 (electronic version) ISSN 1503-8181.

"Chloride induced reinforcement corrosion in concrete" Concept of critical chloride content – methods and mechanisms.
Ueli Angst 2011:113, ISBN 978-82-471-2769-9 (printed version) ISBN 978-82-471-2763-6 (electronic version) ISSN 1503-8181.

"A thermo-electric-Mechanical study of the carbon anode and contact interface for Energy savings in the production of aluminium".
Dag Herman Andersen 2011:157, ISBN 978-82-471-2859-6 (printed version) ISBN 978-82-471-2860-2 (electronic version) ISSN 1503-8181.

“Structural Capacity of Anchorage Ties in Masonry Veneer Walls Subjected to Earthquake”. The implications of Eurocode 8 and Eurocode 6 on a typical Norwegain veneer wall.
Ahmed Mohamed Yousry Hamed 2011:181, ISBN 978-82-471-2911-1 (printed version) ISBN 978-82-471-2912-8 (electronic ver.) ISSN 1503-8181.

“Work-hardening behaviour in age-hardenable Al-Zn-Mg(-Cu) alloys”.
Ida Westermann , 2011:247, ISBN 978-82-471-3056-8 (printed ver.) ISBN 978-82-471-3057-5 (electronic ver.) ISSN 1503-8181.

“Behaviour and modelling of selfpiercing riveted connections using aluminium rivets”.
Nguyen-Hieu Hoang, 2011:266, ISBN 978-82-471-3097-1 (printed ver.) ISBN 978-82-471-3099-5 (electronic ver.) ISSN 1503-8181.

“Fibre reinforced concrete”.
Sindre Sandbakk, 2011:297, ISBN 978-82-471-3167-1 (printed ver.) ISBN 978-82-471-3168-8 (electronic ver) ISSN 1503:8181.

“Dynamic behaviour of cablesupported bridges subjected to strong natural wind”.
Ole Andre Øiseth, 2011:315, ISBN 978-82-471-3209-8 (printed ver.) ISBN 978-82-471-3210-4 (electronic ver.) ISSN 1503-8181.

“Constitutive modeling of solargrade silicon materials”
Julien Cochard, 2011:307, ISBN 978-82-471-3189-3 (printed ver). ISBN 978-82-471-3190-9 (electronic ver.) ISSN 1503-8181.

“Constitutive behavior and fracture of shape memory alloys”
Jim Stian Olsen, 2012:57, ISBN 978-82-471-3382-8 (printed ver.) ISBN 978-82-471-3383-5 (electronic ver.) ISSN 1503-8181.

“Field measurements in mechanical testing using close-range photogrammetry and digital image analysis”
Egil Fagerholt, 2012:95, ISBN 978-82-471-3466-5 (printed ver.) ISBN 978-82-471-3467-2 (electronic ver.) ISSN 1503-8181.

“Towards a better under standing of the ultimate behaviour of lightweight aggregate concrete in compression and bending”,
Håvard Nedrelid, 2012:123, ISBN 978-82-471-3527-3 (printed ver.) ISBN 978-82-471-3528-0 (electronic ver.) ISSN 1503-8181.

“Numerical simulations of blood flow in the left side of the heart”
Sigrid Kaarstad Dahl, 2012:135, ISBN 978-82-471-3553-2 (printed ver.) ISBN 978-82-471-3555-6 (electronic ver.) ISSN 1503-8181.

“Moisture induced stresses in glulam”
Vanessa Angst-Nicollier, 2012:139, ISBN 978-82-471-3562-4 (printed ver.) ISBN 978-82-471-3563-1 (electronic ver.) ISSN 1503-8181.

“Biomechanical aspects of distraction osteogensis”
Valentina La Russa, 2012:250, ISBN 978-82-471-3807-6 (printed ver.) ISBN 978-82-471-3808-3 (electronic ver.) ISSN 1503-8181.

“Ductile fracture in dual-phase steel. Theoretical, experimental and numerical study”
Gaute Gruben, 2012:257, ISBN 978-82-471-3822-9 (printed ver.) ISBN 978-82-471-3823-6 (electronic ver.) ISSN 1503-8181.

“Damping in Timber Structures”
Nathalie Labonnote, 2012:263, ISBN 978-82-471-3836-6 (printed ver.) ISBN 978-82-471-3837-3 (electronic ver.) ISSN 1503-8181.

“Biomechanical modeling of fetal veins: The umbilical vein and ductus venosus bifurcation”
Paul Roger Leinan, 2012:299, ISBN 978-82-471-3915-8 (printed ver.) ISBN 978-82-471-3916-5 (electronic ver.) ISSN 1503-8181.

“Large-Deformation behaviour of thermoplastics at various stress states”
Anne Serine Ognedal, 2012:298, ISBN 978-82-471-3913-4 (printed ver.) ISBN 978-82-471-3914-1 (electronic ver.) ISSN 1503-8181.

“Hardening accelerator for fly ash blended cement”
Kien Dinh Hoang, 2012:366, ISBN 978-82-471-4063-5 (printed ver.) ISBN 978-82-471-4064-2 (electronic ver.) ISSN 1503-8181.

“From molecular structure to mechanical properties”
Jianyang Wu, 2013:186, ISBN 978-82-471-4485-5 (printed ver.) ISBN 978-82-471-4486-2 (electronic ver.) ISSN 1503-8181.

“Experimental and numerical study of hybrid concrete structures”
Linn Grepstad Nes, 2013:259, ISBN 978-82-471-4644-6 (printed ver.) ISBN 978-82-471-4645-3 (electronic ver.) ISSN 1503-8181.

“Mechanics of ultra-thin multi crystalline silicon wafers”
Saber Saffar, 2013:199, ISBN 978-82-471-4511-1 (printed ver.) ISBN 978-82-471-4513-5 (electronic ver). ISSN 1503-8181.

“Through process modelling of welded aluminium structures”
Anizahyati Alisibramulisi, 2013:325, ISBN 978-82-471-4788-7 (printed ver.) ISBN 978-82-471-4789-4 (electronic ver.) ISSN 1503-8181.

“Combined blast and fragment loading on steel plates”
Knut Gaarder Rakvåg, 2013:361, ISBN978-82-471-4872-3 (printed ver.) ISBN 978-82-4873-0 (electronic ver.). ISSN 1503-8181.

“Characterization and modelling of the anisotropic behaviour of high-strength aluminium alloy”
Marion Fourmeau, 2014:37, ISBN 978-82-326-0008-3 (printed ver.) ISBN 978-82-326-0009-0 (electronic ver.) ISSN 1503-8181.

“Behaviour of threated steel fasteners at elevated deformation rates”
Henning Fransplass, 2014:65, ISBN 978-82-326-0054-0 (printed ver.) ISBN 978-82-326-0055-7 (electronic ver.) ISSN 1503-8181.

“Sedimentation and Bleeding”
Ya Peng, 2014:89, ISBN 978-82-326-0102-8 (printed ver.) ISBN 978-82-326-0103-5 (electric ver.) ISSN 1503-8181.